High-Redshift Ultraluminous Quasi-Stellar Objects:
Black holes and their accretion discs

Samuel Lai

A thesis submitted for the degree of

Doctor of Philosophy

The Australian National University

Research School of Astronomy & Astrophysics

Australian
National
University

February 2024

To my cherished loved ones, whose unwavering support was critical to the completion of this work.

Declaration

I hereby declare that the work undertaken in this thesis has been conducted by me alone, except where indicated in the text. I conducted this work between March 2021 and February 2024, during which I was a PhD candidate at the Australian National University. This thesis, in whole or in part, has not been submitted to this or any other university for a degree.

This thesis has been compiled as a Thesis by Compilation in accordance with relevant ANU policies. Except where stated otherwise, each of the main chapters in this thesis has been published in peer reviewed journals. I have made significant contribution to each of these journal articles and have written the papers myself. What follows is a Statement of Contribution, which describes the degree of involvement in the listed publications.

- **Lai, S.**, Bian, F., Onken, C. A., Wolf, C., Mazzucchelli, C., Bañados, E., Bischetti, M., Bosman, S. E. I., Becker, G., Cupani, G., D'Odorico, V., Eilers, A.-C., Fan, X., Farina, E. P., Onoue, M., Schindler, J.-T., Walter, F., Wang, F., Yang, J., & Zhu, Y. (2022), *Chemical abundance of $z \sim 6$ quasar broad-line regions in the XQR-30 sample*, MNRAS, 513, 1801.

- **Lai, S.**, Wolf, C., Onken, C. A., & Bian, F. (2023), *Characterising SMSS J2157-3602, the most luminous known quasar, with accretion disc models*, MNRAS, 521, 3682.

- **Lai, S.**, Onken, C. A., Wolf, C., Bian, F., Cupani, G., Lopez, S., & D'Odorico, V. (2023), *Virial black hole mass estimates of quasars in the XQ-100 legacy survey*, MNRAS, 526, 3230.

- **Lai, S.**, Onken, C. A., Wolf, C., Bian, F., & Fan, X. (2024), *XQz5: a new ultraluminous $z \sim 5$ quasar legacy sample*, MNRAS, 527, 3912.

- **Lai, S.**, Onken, C. A., Wolf, C., Bian, F., & Fan, X. (2024), *Supermassive black holes are growing slowly by $z \sim 5$*, MNRAS, submitted.

For the above listed publications, I was the first author and primary contributor – *i.e.*, I performed all of the data analysis and wrote all of the text. I also played a major role in obtaining the data by submitting observing proposals and performing the observations for the publications based on the XQz5 sample. The co-authors reviewed the papers, providing feedback and suggestions, which have improved each of these works. Each of these publications is presented as a chapter in the thesis, with small modifications to suit the thesis format.

During the course of the PhD candidature, I have also made contributions to the

following publications as a co-author:

- Onken, C. A., **Lai, S.**, Wolf, C., Lucy, A. B., Hon, W. J., Tisserand, P., Sokoloski, J. L., Luna, G. J. M., Manick, R., Fan, X., & Bian, F. (2022), *Discovery of the most luminous quasar of the last 9 Gyr*, Publ. Astron. Soc. Australia, 39, e037.

- Tang, J.-J., Wolf, C., Tonry, J., **Lai, S.**, Yong, S. Y., & Steyn, Z. (2023), *Probing quasar viewing angle with the variability structure function*, MNRAS, 523, 4441.

- Wolf, C., **Lai, S.**, Onken, C. A., Amrutha, A., Bian, F., Hon, W. J., Tisserand, P., & Webster, R. (2024), *The accretion of a solar mass per day by a 17-billion solar mass black hole*, Nature Astronomy, accepted.

- Onken, C. A., Wolf, C., Bian, F., Fan, X., Hon, W. J., Raithel, D., Tisserand, P., & **Lai, S.** (2022), *Ultraluminous high-redshift quasars from SkyMapper - II. New quasars and the bright end of the luminosity function*, MNRAS, 511, 572.

- Zhu, Y., Becker, G. D., Bosman, S. E. I., Keating, L. C., D'Odorico, V., Davies, R. L., Christenson, H. M., Bañados, E., Bian, F., Bischetti, M., Chen, H., Davies, F. B., Eilers, A.-C., Fan, X., Gaikwad, P., Greig, B., Haehnelt, M. G., Kulkarni, G., **Lai, S.**, Pallottini, A., Qin, Y., Ryan-Weber, E. V., Walter, F., Wang, F., & Yang, J. (2022), *Long Dark Gaps in the Lyβ Forest at z < 6: Evidence of Ultra-late Reionization from XQR-30 Spectra*, ApJ, 932, 76.

- Onken, C. A., Wolf, C., Hon, W. J., **Lai, S.**, Tisserand, P., & Webster, R. (2023), *AllBRICQS: The All-sky BRIght, Complete Quasar Survey*, Publ. Astron. Soc. Australia, 40, e010.

- Satyavolu, S., Eilers, A.-C., Kulkarni, G., Ryan-Weber, E., Davies, R. L., Becker, G. D., Bosman, S. E. I., Greig, B., Mazzucchelli, C., Bañados, E., Bischetti, M., D'Odorico, V., Fan, X., Farina, E. P., Haehnelt, M. G., Keating, L. C., **Lai, S.**, & Walter, F. (2023), *New quasar proximity zone size measurements at z 6 using the enlarged XQR-30 sample*, MNRAS, 522, 4918.

- D'Odorico, V., Bañados, E., Becker, G. D., Bischetti, M., Bosman, S. E. I., Cupani, G., Davies, R., Farina, E. P., Ferrara, A., Feruglio, C., Mazzucchelli, C., Ryan-Weber, E., Schindler, J.-T., Sodini, A., Venemans, B. P., Walter, F., Chen, H., **Lai, S.**, Zhu, Y., Bian, F., Campo, S., Carniani, S., Cristiani, S., Davies, F., Decarli, R., Drake, A., Eilers, A.-C., Fan, X., Gaikwad, P., Gallerani, S., Greig, B., Haehnelt, M. G., Hennawi, J., Keating, L., Kulkarni, G., Mesinger, A., Meyer, R. A., Neeleman, M., Onoue, M., Pallottini, A.,

Qin, Y., Rojas-Ruiz, S., Satyavolu, S., Sebastian, A., Tripodi, R., Wang, F., Wolfson, M., Yang, J., & Zanchettin, M. V. (2023), *XQR-30: The ultimate XSHOOTER quasar sample at the reionization epoch*, MNRAS, 523, 1399.

- Mazzucchelli, C., Bischetti, M., D'Odorico, V., Feruglio, C., Schindler, J.-T., Onoue, M., Bañados, E., Becker, G. D., Bian, F., Carniani, S., Decarli, R., Eilers, A.-C., Farina, E. P., Gallerani, S., **Lai, S.**, Meyer, R. A., Rojas-Ruiz, S., Satyavolu, S., Venemans, B. P., Wang, F., Yang, J., & Zhu, Y. (2023), *XQR-30: Black hole masses and accretion rates of 42 $z \geq 6$ quasars*, A&A, 676, A71.

- Zhu, Y., Becker, G. D., Christenson, H. M., D'Aloisio, A., Bosman, S. E. I., Bakx, T., D'Odorico, V., Bischetti, M., Cain, C., Davies, F. B., Davies, R. L., Eilers, A.-C., Fan, X., Gaikwad, P., Haehnelt, M. G., Keating, L. C., Kulkarni, G., **Lai, S.**, Ma, H.-X., Mesinger, A., Qin, Y., Satyavolu, S., Takeuchi, T. T., Umehata, H., & Yang, J. (2023), *Probing Ultralate Reionization: Direct Measurements of the Mean Free Path over $5 < z < 6$*, ApJ, 955, 115.

- Gaikwad, P., Haehnelt, M. G., Davies, F. B., Bosman, S. E. I., Molaro, M., Kulkarni, G., D'Odorico, V., Becker, G. D., Davies, R. L., Nasir, F., Bolton, J. S., Keating, L. C., Iršič, V., Puchwein, E., Zhu, Y., Asthana, S., Yang, J., **Lai, S.**, & Eilers, A.-C. (2023), *Measuring the photoionization rate, neutral fraction, and mean free path of H I ionizing photons at $4.9 \leq z \leq 6.0$ from a large sample of XShooter and ESI spectra*, MNRAS, 525, 4093.

I contributed to each of these listed publications by generating useful discussion, providing constructive feedback on manuscript drafts, or performing part of the observations underpinning the study. My contribution to the first few listed publications, indicated by square points, are notable in that I had either written a section of the paper or performed a critical component of the data analysis.

Christian Wolf

17 January 2024

Ji-Jia Tang

17 January 2024

Samuel Lai

16 January 2024

Acknowledgements

The realisation of this body of work would not have been possible without the support, encouragement, and guidance of countless individuals who, through their contributions, no matter how subtle, have nurtured my personal and professional development. In certain respects, my development as an academic in the past few years have mirrored the exponential mass growth of the supermassive black holes that I study, yet my part pales in comparison to the contribution of those who have accepted me and taken me under their wing.

My eternal gratitude goes out to the chair of my supervisory panel, Christian Wolf, and my primary supervisor, Christopher Onken. Their knowledge and dedication to their work set them apart as inspirational academic role models. Chris Wolf, a fount of interesting scientific ideas worth pursuing, works tirelessly to advocate for his students and is genuinely invested in their progress. He has given me valuable opportunities from arranging in-situ observing at the Siding Spring Observatory prior to the automation of the 2.3m telescope to allowing me to attend the Arizona Giant Magellan Telescope conference in his place. Chris Wolf is also directly responsible for my two casual jobs, which have enabled me to obtain experience in both an administrative and a teaching role. My primary advisor, Chris Onken, practically never closes his office door and has always made himself available for the most trivial of questions, even on the weekends. He frequently offers practical and actionable advice, allowing me to make progress on multiple projects at a rapid pace. For much of my candidature, I have depended on Chris Onken for his resourcefulness and steady guidance. The final member of my committee, Fuyan Bian, also deserves significant thanks. Fuyan was instrumental in granting me an internship opportunity at the European Southern Observatory during the early days of the PhD candidacy when the global pandemic prevented me from traveling to Australia. I have benefited greatly from his input and his advocacy for me to join a larger international community of quasar researchers. Moreover, Fuyan reminds me that time taken to slow down, unwind, and de-stress is just as valuable as long working hours due to the diminishing return on time investment.

Prior to my PhD, I had the pleasure of having Kinwah Wu and Ziri Younsi as my supervisors and mentors for my MSc research. I regret, in the past, that I have not properly conveyed the gratitude that is sincerely held. I could not thank them enough for starting me down this road of black hole research and opening my eyes to the expansive world of computational astrophysics. Ambitious and highly intelligent, Kinwah and Ziri held very high expectations for my single year at University College London. This gentle pressure served as a guiding beacon through a sea of

uncertainty and self-doubt. Their confidence that I had potential for academic research is credited for my decision to re-apply for a PhD, which would have been my third and final attempt if unsuccessful. To this day, I would consider it an accomplishment to develop merely a fraction of their passion, ambition, and competence. A special acknowledgement also goes out to Siyi Xu and her mentor Michael Jura, who gave me my first research opportunities in the early undergraduate years.

Throughout the duration of the candidacy, the Australian National University supported my work with the University Research Scholarship for postgraduate research, the HDR Fee Remission Scholarship, and the ANU Supplementary Scholarship. Special thanks to Michelle Cicolini and the School Manager, Mat Malzacher, who have helped me with various aspects, from relocation to casual employment. I would also like to thank all of my co-authors who have provided advice and suggestions that have improved each of my publications. Additionally, I thank the anonymous referees who, through their constructive criticism, have further polished the quality of each study.

My loving parents, who believed in me and supported my every decision, deserve a lifetime of thanks and I would also like to extend a special thanks to Uncle Luke in Sydney who has opened his doors to my frequent comings and goings. If I have ever been a positive influence in the lives of others, it is entirely reflective of the qualities and character of my parents. I would also like to thank my siblings who, despite our many differences and infrequent in-person contact, have always maintained a special brotherly fondness. The community and cohort at the Research School of Astronomy and Astrophysics has also been incredibly welcoming. The conversations, games, and sports have shown me that there's more to the PhD experience than working tirelessly in solitude. Thanks to fellow PhD candidates Sajay, Simon, Neelesh, Hilay, Songlin, Heran, and numerous other contemporaries who have enriched the overall experience and made it all the more worthwhile.

Finally, the completion of this thesis and of my PhD journey would not have been possible without my partner Charmaine, whose daily encouragement inspires me to be the best version of myself in all of my work and interpersonal interactions. Her steadfast presence is instrumental in keeping me grounded and preserving my sanity. With each communication, I am reminded of what and who my unwavering hard work is for.

The road that has led to this point has, at times, been turbulent and from this vantage point, there's still a looming mountain ahead to climb. But with the support and kindness of these cherished individuals, the journey ahead may perhaps be manageable and even *enjoyable*.

Abstract

Over the past century, black holes transitioned from mere theoretical constructs to ubiquitous entities in the Universe. Extensive evidence supports the notion that supermassive black holes, which reside in the nuclear region of most mature galaxies, play an integral role in the assembly and dynamics of galactic material on cosmological timescales. However, the rapid evolution of supermassive black holes and their immediate environments in the early Universe ($\lesssim 1$ Gyr) is still poorly understood due to the paucity of robust constraints on physical accretion mechanisms, the limited statistical significance of available samples, and the scarcity of independent methodologies of black hole characterisation.

The work contained within this thesis endeavours to trace the evolution of supermassive black holes at high redshifts ($z \sim 5$) using highly complete quasar samples with robustly-measured spectrophotometric properties, from which characteristics of the quasar, such as the black hole mass, disc luminosity, and broad-line region metallicity can be inferred. First, I build a spectroscopic analysis tool specifically designed for quasar spectra and apply it to a literature $z \sim 4$ quasar sample, measuring emission-lines (*e.g.,* Si IV λ1398, O IV λ1402, C IV λ1549, Mg II λ2799, H$\beta\lambda$4863Å) and inferring black hole properties from mass and luminosity-sensitive features. I then build up a new sample of $z \sim 5$ quasars, XQz5, with multiwavelength spectroscopic follow-up, based on a parent sample with a well-defined completeness function, and report on the measured spectroscopic properties. Next, I analyse quasar demographics with the $z \sim 5$ sample and measure supermassive black hole growth. In the latter half of the thesis, I discuss metallicity-sensitive emission-line ratios, such as (Si IV+O IV)/C IV and N V/C IV, in a $z \sim 6$ sample from the literature. Furthermore, I showcase the utility of employing thermal accretion disc models to analyse quasar spectral energy distributions. This approach has potential as a physically-motivated independent method that can aid in constraining properties of black holes.

In summary, the results presented in this thesis are: the highly-complete spectroscopic follow-up of the most luminous quasars near $z \sim 5$ providing robustly measured spectral properties, constraints on physical accretion properties regulating $z \sim 5$ supermassive black hole growth, and the release of a quasar spectroscopic analysis code package as well as a Bayesian accretion disc modelling code package. Through modelling the growth patterns exhibited by the most luminous and massive black holes at $z \sim 5$, I show that high radiative efficiencies ($\epsilon > 0.32$) are disfavoured at a confidence level of 3σ and deduce that the growth in the early Universe must have been at least 3$\times$ more rapid to align with our observations.

Contents

List of Figures

List of Tables

Introduction

Active galactic nuclei (AGN) are a class of astrophysical objects characterised by a compact galactic nuclear region that emits significant non-stellar radiation across much of the electromagnetic spectrum, which is now known to be powered by persistent accretion onto supermassive black holes. As AGN have been observed with the energy output exceeding that of all integrated starlight from their host galaxies, they are the most luminous non-transient objects in the universe, which enables them to be observed across much of cosmic history. It's also now believed that nearly all mature galaxies contain active or quiescent supermassive black holes in their nuclear regions. Although the AGN fraction in the local Universe is estimated to be between $\sim 10 - 40\%$ (e.g. Ho 2008), depending on the classification of low-ionisation nuclear emission-line regions (LINERs; Heckman 1980), empirical correlations between the central black hole and its host galaxy properties suggest a deep interconnection facilitated by mutual feedback during the black hole's active period (see review by Kormendy & Ho 2013). Our own Milky Way Galaxy hosts a relatively quiescent black hole with a mass of $\sim 4.5 \times 10^6 \, M_\odot$, where $M_\odot$ is one solar mass (e.g. Ghez et al. 2008; Gillessen et al. 2009), but its last active phase may have been a brief flaring event which occurred as recently as 200 years ago (Marin et al. 2023).

The history of AGN characterisation began with the discovery of emission lines and astrophysical jets from distant "spiral nebulae" in the early 20th century (Fath 1909; Slipher 1917; Curtis 1918), which became the subject of the Great Shapley–Curtis Debate on the scale of the universe in 1920 (Carroll & Ostlie 1996). Later, when the extragalactic nature of these galaxies was better established, Carl Seyfert would publish observations of AGN with broad emission lines (Seyfert 1943), which would eventually become known as Seyfert galaxies. In the early 1960s, radio astronomy developments resulted in the discovery of point sources with unprecedented redshift for their time (Minkowski 1960). One source, 3C 273, was observed through a lunar occultation with the Australian Parkes station 210 foot antenna. Follow-up observations confirmed the redshift of the object by identifying the hydrogen Balmer

emission lines and discovered that the source is composed of two components: a star-like object and a faint jet (Greenstein 1963; Hazard et al. 1963; Oke 1963; Schmidt 1963). The optical luminosity of the source had to be unprecedented at the detected redshift, brighter than the starlight output the largest elliptical galaxies. On the other hand, the radio luminosity was comparable to other already discovered bright radio sources, although the surface brightness was higher than that of radio galaxies. Such objects eventually became known as quasi-stellar objects (QSOs) or quasars. Soon thereafter, quasars were recognised to be emitting from compact spatial volumes (e.g. Greenstein & Schmidt 1964), powered by accretion of material onto supermassive black holes of distant galaxies (Salpeter 1964), and a flurry of new quasars were published (e.g. Schmidt 1965), each increasing in detected redshift (see review by Shields 1999, for a more complete AGN history). At such high redshifts, quasars were quickly recognised for their importance in probing cosmological questions.

Now, a wide variety of observable phenomena are classified under the AGN umbrella and unified by a paradigm where each class is differentiated by the observer's orientation angle (e.g. Antonucci 1993; Urry & Padovani 1995). These include the aforementioned Seyfert galaxies and their subtypes, the Fanaroff-Riley radio galaxies (Fanaroff & Riley 1974), quasars, blazars, and some LINERs. One of the main AGN sub-classification quantities is the "radio-loudness", which is determined by the radio-to-optical flux density ratio. "Radio quiet" AGN, with a ratio $R < 10$, make up the vast majority ($>90\%$) of the AGN population (Padovani 2011) and the fundamental difference between the two classes is the presence of absence of a powerful relativistic jet (Padovani 2016). Another way that AGN are further classified into finer gradations is by the Seyfert sub-type, differentiated by the strength of broad to narrow emission lines and quantified by the $H\beta/[O\ \textsc{iii}]\ \lambda5007\text{Å}$ ratio (Osterbrock 1980). Under the AGN paradigm, the diversity in broad to narrow emission-line ratios is explained by the orientation-dependent visibility of the AGN broad-line region, which can be affected by varying degrees of line-of-sight obscuration due to the presence of a flared dusty torus along the AGN equatorial plane (Antonucci 1993). Quasars are much more luminous counterparts of Seyfert galaxies and exhibit many of the same characteristics, but the host galaxy is no longer clearly visible, and a blazar is a jetted AGN where the jet is pointed nearly directly at the Earth. Finally, LINERs, if indeed accretion powered, seem to be weakly accreting low luminosity AGN with properties that could sometimes be emulated by astrophysical shocks or stellar photoionisation (Ho 2008).

The picture that arises from the unified AGN paradigm is one where the observed

orientation angle has as much of an effect, if not a greater effect, on the observable outcome than the intrinsic diversity of characteristics in accreting supermassive black holes. However, we emphasise that variations driven by intrinsic differences also play a significant role as evidenced by the identification of the first eigenvector from Principal Component Analysis (Boroson & Green 1992), resulting in an AGN or quasar main sequence (e.g. Marziani et al. 2022). Regardless, the general geometrical AGN model can be described by the following physical components (Urry & Padovani 1995), assumed to be axisymmetric and roughly defined spatially in terms of gravitational radii, $R_{\mathrm{g}} = GM/c^2$, separated from the central point of symmetry:

- ($\sim 10^0\,R_{\mathrm{g}}$) The central supermassive black hole produces the gravitational potential which powers the accretion and radiative output of AGN. Critical radii of the black hole, such as the event horizon and innermost stable circular orbit (ISCO), are located at several factors of R_{g} depending on the dimensionless black hole spin, defined by $a \equiv cJ/(GM^2)$, where J is angular momentum. The ISCO defines the inner edge of the accretion disc.

- ($\sim 10^{1-2}\,R_{\mathrm{g}}$) The accretion disc is composed of diffuse material in high-velocity orbital motion around the black hole, heated to high temperatures by friction and emitting intense thermal radiation in the rest-frame optical to X-ray wavelengths. Angular momentum in the disc is likely redistributed throughout the disc material by magnetorotational instability (Balbus & Hawley 1991). The thermal radiation is anisotropic due to the geometry of the disc and general relativistic effects.

- ($\sim 10^{3-4}\,R_{\mathrm{g}}$) The broad-line region is commonly described as high-density clouds moving rapidly within the black hole's gravitational potential with Keplerian velocities from $1000 - 20000\,\mathrm{km\,s^{-1}}$ (Netzer 2015). The high densities of broad-line region clouds prevent forbidden line transitions through collision de-excitation (e.g. Osterbrock & Ferland 2006). Partial to total obscuration of broad emission lines from the broad-line region by outer elements is thought to be responsible for the Seyfert sub-type spectrum (see Maiolino & Rieke 1995, and references therein).

- ($\gtrsim 10^4\,R_{\mathrm{g}}$) The inner radius of the dusty and clumpy torus (e.g. Elitzur 2008), determined by the dust sublimation radius, is roughly coincident with the broad-line region (e.g. Rose et al. 2015). However, the torus geometry is complex and poorly constrained (Netzer 2015). As the torus obscures the inner accretion disc and broad-line region, measurements of the torus covering factor help describe the AGN anisotropy. Such measurements find a strong

anti-correlation between the covering factor and the source luminosity (e.g. Merloni et al. 2014), resulting in the idea of a "receding" torus (Lawrence 1991). The probable "clumpiness" of the obscuring torus remains a significant challenge for analytical and phenomenological models (Netzer 2015).

- ($\sim 10^{5-7}\,R_{\mathrm{g}}$) The narrow-line region is composed of lower-velocity photoionised gas clouds located further away from the central black hole. The lower density clouds produce forbidden lines, such as [O III] $\lambda 5007$Å. Due to its large spatial extent, which extends well into the galaxy at large, the narrow-line region is not obscured by the dusty torus in the unified AGN paradigm.

- ($\sim 10^{4-11}\,R_{\mathrm{g}}$) Radio jets have been observed in jetted AGN out to very large scales and are thought to play an important role as jet-driven feedback in galactic evolution (e.g. Hardcastle & Croston 2020). AGN jets also played a part in early discoveries and recognition of extragalactic sources as distant galaxies (Curtis 1918). Jets are thought to be launched by the Blandford-Znajek process (Blandford & Znajek 1977), but it is not yet clear why some AGN are jetted while the majority are not (Padovani 2017).

As an abstract framework, this unified model has been a useful classification tool with some explanatory power (e.g. presence of broad lines in type 2 Seyferts revealed through polarised light; Miller & Goodrich 1990). However, in the past decades, challenges to the unified scheme, such as the existence of "true" Seyfert 2s (e.g. Li et al. 2015; Pons & Watson 2016; XueGuang et al. 2021) and the luminosity-dependent vertical support mechanism for the obscuring torus (e.g. Netzer 2015), limit the widespread practical applicability of the model. As yet, this paradigm remains a partial description of a wide range of phenomena, all of which involve a supermassive black hole.

1.1   Quasar Cosmic Evolution

Because of their high luminosities, the properties of quasars are particularly conducive for studying evolution over cosmological timescales. In their ultraviolet and optical emission, quasars appear to have similar spectral energy distributions over multiple decades in intrinsic luminosity and throughout much of cosmic history (e.g. Elvis et al. 1994; Selsing et al. 2016), pointing to common fundamental radiative mechanisms that remain invariant over cosmic epoch. However, the jet and corona (responsible for the radio and X-ray emission, respectively) can vary considerably with the accretion behaviour (e.g. Elvis 2010). This is reflected by the dispersion in radio-loudness and the optical-to-X-ray flux ratio, α_{OX}. Nevertheless, the homo-

geneity in average quasar properties across diverse samples (e.g. Elvis et al. 1994; Dietrich et al. 2002), where a significant fraction of the residual variation can be understood in terms of Eigenvector 1 (Boroson & Green 1992), makes quasars a useful probe of cosmological environments.

One of the captivating aspects of observing quasars out to high redshifts stems from empirical correlations observed between black holes and their hosts. The earliest black hole and host correlations were found between the black hole mass and bulge luminosity, or more fundamentally, the mass of the black hole and the bulge (e.g. Magorrian et al. 1998; Kormendy & Gebhardt 2001; Merritt & Ferrarese 2001; McLure & Jarvis 2002; Marconi & Hunt 2003; Häring & Rix 2004), but historically, the correlation between the black hole mass and galaxy velocity dispersion was found to be even tighter (e.g. Ferrarese & Merritt 2000; Gebhardt et al. 2000). Now it's believed that both the black hole mass with bulge mass relation ($M_{\mathrm{BH}} - M_{\mathrm{bulge}}$) and black hole mass with velocity dispersion relation ($M_{\mathrm{BH}} - \sigma$) have similar intrinsic scatter. Weaker correlations were also found between black holes with dark matter haloes (e.g. Ferrarese 2002) and globular cluster systems (e.g. Burkert & Tremaine 2010; Harris & Harris 2011). Equally as informative and interesting are the discoveries of what galactic properties and components do not correlate with the black hole. The absence of a correlation was found between black holes with galaxy discs (e.g. Kormendy & Gebhardt 2001) and host pseudobulges (e.g. Kormendy et al. 2011). The totality of the evidence suggests that black holes coevolve with the properties of classical bulges and elliptical galaxies (but see Kormendy & Ho 2013, for a measured and conservative perspective). Therefore, studies of distant quasars provide valuable probes of the conditions and processes which prevailed in the high-redshift Universe, during the early stages of galaxy evolution.

The intense luminosity of quasars gives rise to another valuable characteristic: their sightlines, which have been used to study properties of the circumgalactic/intergalactic medium and the history of cosmic reionisation. Metal absorption lines detected along the quasar line-of-sight act as probes of the chemical composition of intervening gas, which illuminate stellar synthesis processes in early galaxies (e.g. Cooke et al. 2011; Becker et al. 2012). The dense Ly α forest observed in $z \gtrsim 5$ spectra probes the epoch of reionisation, the last major phase change in the Universe (see reviews by Becker et al. 2015; McQuinn 2016), by enabling measurements of dark gaps (e.g. Songaila & Cowie 2002; Furlanetto et al. 2004; Gallerani et al. 2008), transmission statistics (Fan et al. 2006), and constraints of the ultraviolet background (e.g. D'Odorico et al. 2008; Dall'Aglio et al. 2008; Haardt & Madau 2012). The latest studies prompted by the increasing availability of $z \sim 6$ quasar

spectra found that signatures of the reionisation process continue well below $z \sim 6$ to $z \sim 5.3$ (e.g. Zhu et al. 2021; Bosman et al. 2022), supporting a late end of reionisation.

The evolution of supermassive black holes, as observed in the brightest of high-redshift quasars, is also an unresolved matter due to their immense size and limitations imposed by the available cosmic time. Ever since the discovery of the first $z \gtrsim 6$ quasars (Fan et al. 2001), stringent constraints have been placed on the formation and growth mechanisms of supermassive black holes, which lie above the evolutionary path of Eddington-limited accretion on stellar black hole remnants (see review by Volonteri et al. 2021). The critical open question is how black holes managed to grow so quickly at high redshifts. Several exotic heavy seed formation scenarios were proposed, including gravitational collapse of Population III stars (e.g. Madau & Rees 2001; Volonteri et al. 2003), runaway mergers (e.g. Portegies Zwart et al. 2004; Seth et al. 2008; Devecchi & Volonteri 2009), hierarchical assembly (e.g. Giersz et al. 2015; Dayal et al. 2019), or direct collapse of supermassive stars (e.g. Loeb & Rasio 1994; Wise et al. 2008; Regan & Haehnelt 2009). It would also be possible for black holes to undergo phases of super-Eddington or radiatively inefficient accretion, achieved through counter-alignment of the accretion disc (e.g. King & Pringle 2006). Although mass estimations at $6.0 \gtrsim z \gtrsim 7.6$ have generally been performed consistently (e.g. Shen et al. 2019b; Onoue et al. 2019; Yang et al. 2021; Farina et al. 2022), these studies would benefit significantly from improved and independent methods of mass measurement, particularly for lower-luminosity quasars which can mask a significant number of black holes accreting at low-Eddington rates (Onoue et al. 2019).

The analyses described in this Section rely on statistically significant spectroscopically observed high-redshift quasar samples, where the progress in the past few decades have largely been driven by wide-area systematic surveys and more detailed multiwavelength follow-up. The new James Webb Space Telescope is also poised to produce many new discoveries, challenges, and opportunities.

1.1.1 High-redshift quasar samples

The majority of high-redshift quasars are discovered using colour selection, which is expressed as the difference between two magnitudes in broadband filters positioned at different wavelengths. Through this commonly used method, candidate quasars are identified by a series of colour cuts (e.g. Jiang et al. 2016; Bañados et al. 2016; Schindler et al. 2017; Wang et al. 2019; Onken et al. 2022a, 2023). The colour selection technique is effective because the intrinsic quasar spectral energy distribu-
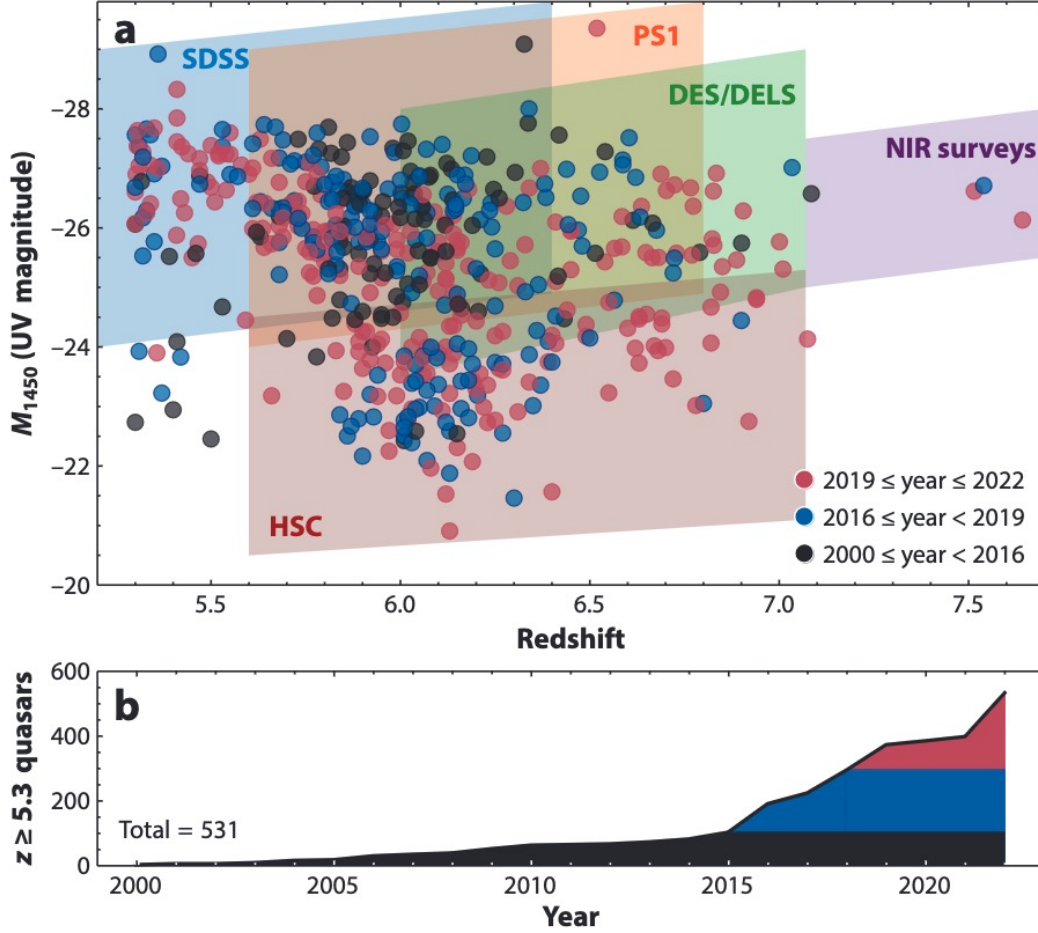
Figure 1.1: Distribution of known $z \geq 5.3$ quasars listed by redshift and absolute magnitude in the ultraviolet 1450Å wavelength. The shaded regions cover the parameter space probed by large quasar survey programs: Sloan Digital Sky Survey (SDSS; Lyke et al. 2020), Pan-STARRS1 (PS1; Chambers et al. 2016), Dark Energy Survey (DES; Abbott et al. 2021) or DESI (Dark Energy Spectroscopic Instrument) Legacy Imaging Survey (DELS; Dey et al. 2019), NIR surveys, and Hyper Suprime-Cam (HSC; e.g. Niida et al. 2020) The bottom-panel shows the cumulative number of known $z \geq 5.3$ quasars as a function of publication year up to 2022. This figure is reproduced from Fan et al. (2023).

tion is distinguishable from that of other sources. In the rest-frame ultraviolet and optical bands, the intrinsic quasar spectrum is characterised by a blue power-law continuum with embedded strong, broad emission lines. At higher redshifts ($z \gtrsim 3$), strong neutral hydrogen absorption in the intergalactic medium form the Ly α forest, which can be seen in photometric surveys when the quasar flux "drops-out" from wavelength bands bluer than the rest-frame Lyman break. The drop-out selection method was responsible for the discoveries of the first $z > 4$ quasars (e.g. Warren et al. 1987). However, simple colour selection can be affected by high contamination rates (e.g. Wang et al. 2019). Several techniques have since been implemented to improve selection efficiency, such as Bayesian model comparison (e.g. Mortlock et al. 2012; Matsuoka et al. 2022), modelling the spectral energy distribution (e.g. Reed et al. 2017), or machine learning classification (e.g. Shu et al. 2019; Wenzl et al. 2021; Chaussidon et al. 2023; Queiroz et al. 2023). While efficient, machine learning selection techniques can potentially miss highly valuable targets with unusual properties (e.g. the discovery of Wu et al. 2015). Combining colour cuts with mid-infrared colours and Gaia astrometry (Gaia Collaboration et al. 2021) is also effective at increasing selection efficiency (e.g. Calderone et al. 2019; Wolf et al. 2020; Onken et al. 2023).

Figure 1.1 presents the distribution of all known published $z \geq 5.3$ quasars up to December 2022 listed by redshift, absolute magnitude in ultraviolet 1450Å, and publication year. The parameter space probed by several major survey programs is highlighted in the top panel and the bottom panel illustrates the rapid increase in the availability of high-redshift quasar spectra due to improvements in candidates selection and spectroscopic identification. The highest redshift frontier as seen in the figure stood at $z = 7.64$ (Wang et al. 2021). Since then, data from the James Webb Space Telescope and the Chandra X-ray Observatory have resulted in discoveries up to $z \sim 10$ (Bogdán et al. 2023). As the frontier expands to higher redshifts, additional work has been put in to push lower-redshift observations to lower luminosities (e.g. Matsuoka et al. 2022) and to improve the completeness at the bright end (e.g. Onken et al. 2022a). Future surveys such as the Legacy Survey of Space and Time by the Vera C. Rubin Observatory (Ivezić et al. 2019) and the European Space Agency's Euclid mission (Euclid Collaboration et al. 2022) will provide deeper survey photometry and enable the selection and discovery of thousands additional high-redshift quasars, which would be prime targets for high-quality spectroscopic follow-up.

1.2   Spectroscopic Observations

Astronomical spectroscopy is the primary observational technique by which distant celestial objects are studied. Quasars emit radiation across the entire electromagnetic spectrum, but ground-based observatories are limited to observations in optical, near-infrared, and radio atmospheric transmission windows. Regardless, ground-based coverage enables the rest-frame ultraviolet to optical emission spectrum of quasars to be observed out to high ($z > 7.5$) redshifts, which makes quasars valuable cosmological probes that can provide important insights into the distant universe, including on the nature of the AGN (e.g. Mazzucchelli et al. 2023), chemistry of the host galaxies (e.g. Wolfe et al. 2005), and properties of intergalactic environments (e.g. D'Odorico et al. 2022).

Figure 1.2 shows a comparison of the rest-frame ultraviolet to optical (2500–5500Å) template quasar emission spectrum to Seyfert 1, Seyfert 2, and lenticular (S0) galaxy templates. The templates are sourced from the Space Telescope Science Institute AGN[1] (Francis et al. 1991) and galaxy[2] (Calzetti et al. 1994; Kinney et al. 1996) spectral atlases. Multiple prominent emission lines are labeled, from Mg II $\lambda2799$ to H$\beta\lambda4863$ and [O III] $\lambda4960$.

Accounting for 5–16% of all galaxies (Maiolino & Rieke 1995), active galaxies, quasars and Seyfert galaxies share many common spectral characteristics. In particular, Seyfert 1 galaxies are local, less luminous versions of quasars with detectable host galaxies. In contrast, the active nuclei of Seyfert 2s are thought to be obscured by orientation, with broad components that are sometimes detectable through polarised light spectroscopy (e.g. Miller & Goodrich 1990). However, we note the existence of apparent "true" Seyfert 2s with intrinsically weak broad emission lines (e.g. Li et al. 2015; Pons & Watson 2016; XueGuang et al. 2021). A typical lenticular (S0) galaxy spectrum, composed of the stellar continuum, is markedly different from the active galaxy spectra in colour and in the absence of photoionised narrow emission features.

Quasar spectra encompass a wealth of information concerning the underlying physical mechanisms and processes responsible for the observed radiation, including thermal distribution, chemical composition, photoionisation, collisional excitation, and gas kinematics. Stellar populations may also have an observable influence on spectral characteristics, particularly in lower luminosity active galaxies. Extracting physical information from spectroscopic data requires an accurate and robust modelling process.

---

[1] https://archive.stsci.edu/hlsps/reference-atlases/cdbs/grid/agn/
[2] https://archive.stsci.edu/hlsps/reference-atlases/cdbs/grid/kc96/
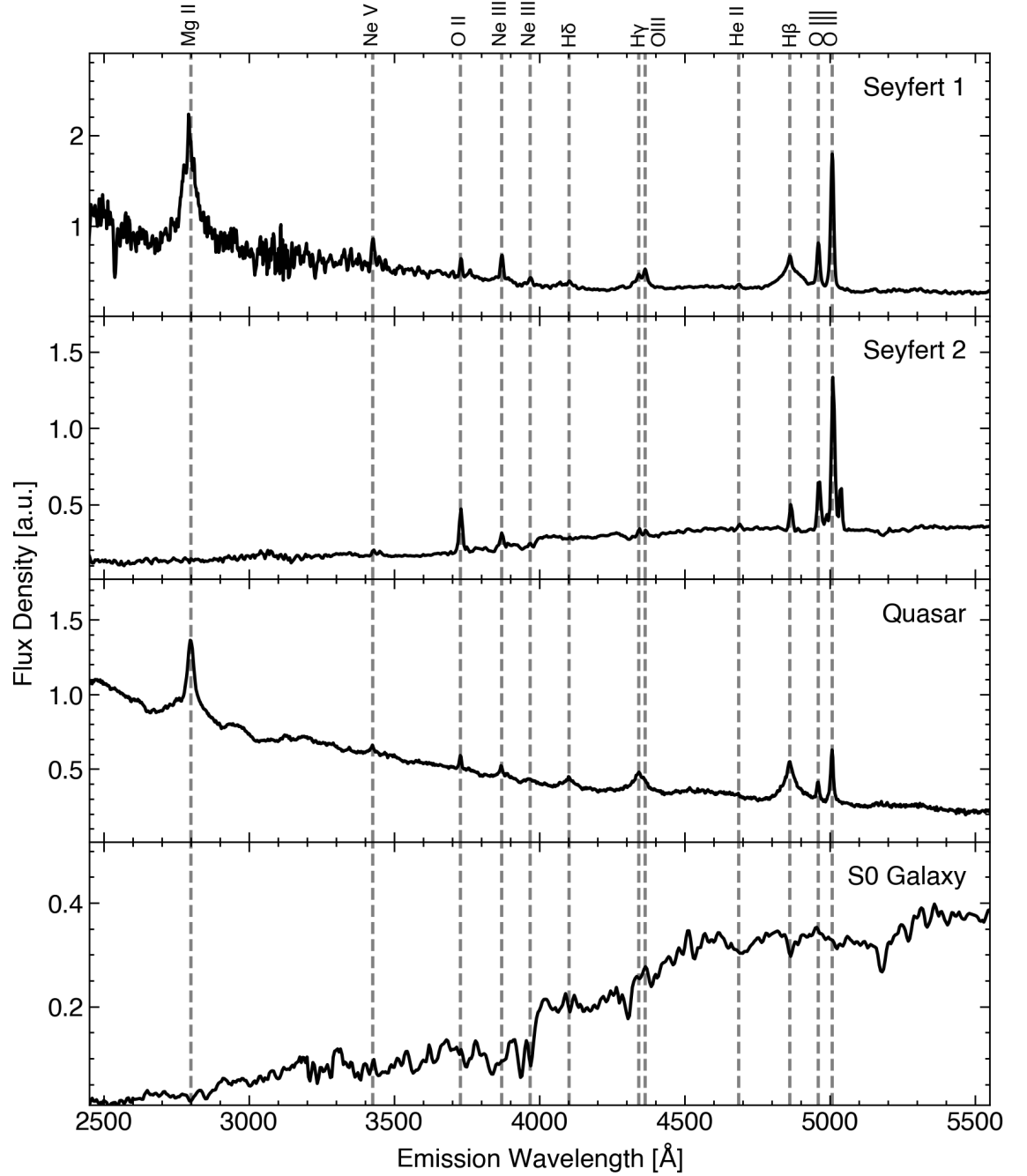
Figure 1.2: Template spectra of galaxies from top to bottom: Seyfert 1, Seyfert 2, quasar-hosting galaxy, and S0 galaxy, sourced from the Space Telescope Science Institute spectral atlases. The templates are plotted from 2500–5500Å, covering parts of the ultraviolet and optical emission spectrum and the flux density is in arbitrary units. Several prominent emission lines are labeled in the spectrum from Mg II λ2799 to H$\beta\lambda$4863 and [O III] λ4960.

1.2.1   Spectral modelling

The process of spectral decomposition in the rest-frame ultraviolet and optical quasar spectrum is a technique designed to disentangle various sources of radiation that are intertwined in the observable spectrum, such as spectral lines from the quasar continuum. Quasar emission lines can be further decomposed into broad and narrow components, which correspond to spatially and kinematically distinct gas clouds. An example of the broad and narrow dichotomy is visible in Figure 1.2 from the H$\beta\lambda$4863 and adjoining [O III] lines between the Seyfert 1/Quasar and Seyfert 2 templates. A common approach is to construct a model of the quasar continuum which is fit to selected line-free windows in the available data. In the rest-frame ultraviolet and optical spectrum, the non-stellar continuum model typically includes three components, a power-law continuum, Fe II template, and Balmer continuum. Stellar components are often ignored for high-redshift or high-luminosity quasars, but wherever the flux contribution from a stellar population is evident, the host decomposition is performed with principal component analysis (Yip et al. 2004a,b) or specialised codes, such as pPXF (Cappellari 2017). Figure 1.3 shows a deconstructed model quasar spectrum compared to the Francis et al. (1991) composite. The model components are the power-law, Balmer continuum, host galaxy, and emission lines, which also includes the Fe II continuum. The Lyα forest suppression is modelled with the Becker et al. (2013) parameterisation. The consistency between the reconstructed quasar spectrum and the Francis et al. (1991) composite highlights the uniformity of average quasar characteristics across diverse samples and supports the efficacy of the spectral decomposition technique.

The power-law continuum is predicted by a sum of blackbody components emitted from a multi-temperature accretion disc. In the simplest case of a steady-state geometrically thin and optically thick disc (Shakura-Sunyaev disc theory; Shakura & Sunyaev 1973), the radial temperature profile is (Frank et al. 2002)

$$T(R)^4 = \frac{3GM\dot{M}}{8\pi R^3 \sigma} \left[1 - \sqrt{\frac{R_*}{R}} \right] , \tag{1.1}$$

where the familiar physical constants, G, π, and σ relate the mass of the central body M, the mass accretion rate $\dot{M}$, radius R, and inner edge of the accretion disc R_* to the temperature. The total emitted spectrum can then be approximated as the blackbody spectrum of each element of area with effective temperature, $T(R)$, integrated over the face area of the accretion disc. It can then be shown that the characteristic power-law disc spectrum, $F_\nu \propto \nu^{1/3}$, is observed as long as the ratio of the hottest and coolest parts of the disc is appreciably greater than unity. However,
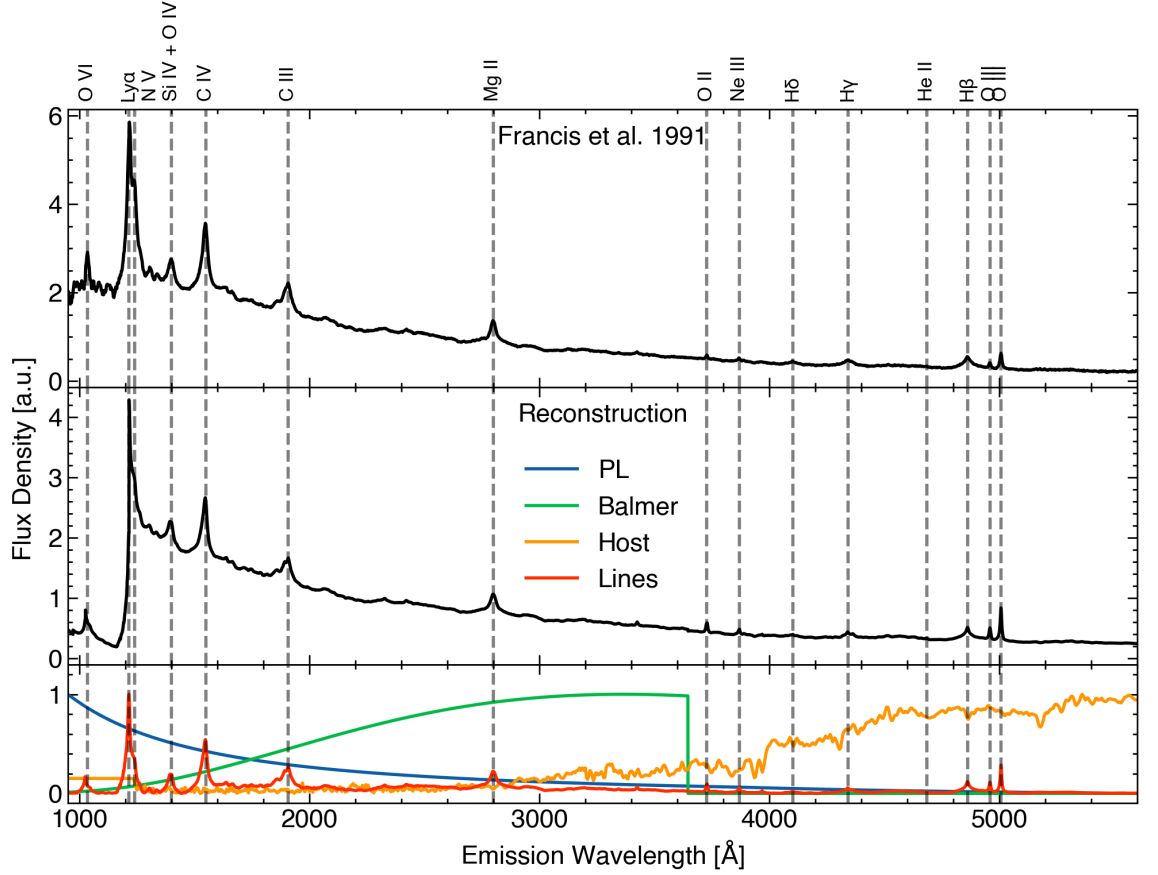
Figure 1.3: Deconstruction of a quasar spectral model into individual emission components, including a power-law continuum, Balmer continuum, host galaxy component, and emission lines. The flux density is in arbitrary units. Prominent emission lines are labeled except for the Fe II pseudo-continuum which is also part of the emission-line component. The flux of individual emission components are normalised between 0 and 1. The model spectrum, created with the help of `qsogen` (Temple et al. 2021c), is compared to the Francis et al. (1991) quasar composite.

when confronted with observation, the simplest disc model breaks down, requiring relaxation of the steady-state, geometrically thin, or optically thick assumptions and more realistic disc models. We discuss accretion disc modelling further in Section 1.4. For the purposes of the spectral decomposition, the quasar continuum is assumed to behave locally as a power-law with a wide range of possible slopes. This assumption is sufficient to fit quasar continua over an order of magnitude in wavelength range from $0.1 - 1\,\mu m$ (Selsing et al. 2016).

Due to the abundance of electron levels in iron atoms, numerous broad and blended iron emission lines are distributed throughout the rest-frame ultraviolet and optical wavelengths. Although relatively weak, this heavily blended emission forms a pseudo-continuum that raises the intrinsically emitted continuum and complicates measurements of resonance lines and non-iron features. Both empirical and theoretical iron templates have been developed to facilitate the iron spectral decomposition. Most empirical templates are based on the iron spectrum of I Zw 1 (e.g. Vestergaard & Wilkes 2001; Tsuzuki et al. 2006; Salviander et al. 2007; Mejía-Restrepo et al. 2016), which is a relatively bright narrow-line Seyfert 1 with strong iron emission. Templates based on one well-studied target are typically sufficient to subtract strong iron emission in the study of non-iron features. Therefore in practice, the iron templates are renormalised and convolved with a Gaussian kernel to match the diversity of features in observed quasars. The decomposed iron spectrum itself also has significant scientific value as the Fe II(UV)/Mg II flux ratio is sensitive to Fe and Mg abundance, which can be used to infer star formation in the early universe (e.g. Dietrich et al. 2003). In this work, it is important to recognise that the Fe II/Mg II ratio also depends on the radiation field, hydrogen density, and microturbulence. Therefore, a larger sample of iron-rich targets combined with theoretical Fe II emission spectra is critical to ensure that the chemical abundance inferences are robust against variations in photoionisation conditions.

The Balmer continuum is frequently invoked to explain the $\lambda3000\text{Å}$ bump, which is a broad hump-like feature representing excess emission above the expected disc-like power-law continuum. The feature was observed in the optical spectra of quasars and Seyfert 1 galaxies (e.g. Neugebauer et al. 1979; Richstone & Schmidt 1980) with variability behaviour that is more closely associated with quasar emission lines rather than the underlying continuum (e.g. Netzer & Davidson 1979; Schmidt & Miller 1980). Modelling efforts showed that the $\lambda3000\text{Å}$ bump is broadly consistent with Balmer continuum emission emitted from optically thick clouds heated to a uniform temperature by high energy radiation (e.g. Grandi 1982). The success of this model led to its adoption in spectral decomposition routines, where the free parameters of

the model include the normalisation, electron temperature, and optical depth.

The quasar line emission spectrum is generally thought to be the consequence of two emitting regions that are located at separate spatial scales from the central black hole with distinct dynamical properties (e.g. Peterson 2006). The broad-line region (BLR) is located in close proximity (sub-parsec scales) to the central gravitational potential, leading to Doppler-broadened emission-line profile velocity widths ranging from thousands to tens of thousands km/s. In contrast, the narrow-line region (NLR) of a quasar is emitted at dozens to thousands of parsecs away from the central black hole with emission-line velocity widths up to a few hundred km/s. Due to the difference in spatial extent, variability in the BLR occurs at much shorter timescales than in the NLR, where the variability signal is geometrically diluted. Emission lines in the NLR can be a tracer of host galaxy properties and the longer timescale quasar activity, while the BLR lines are more sensitive to properties of the central black hole and its immediate environment.

Observed emission lines, and particularly the broad emission lines, can exhibit a wide range of properties, from asymmetric wings to multiple peaks. Models of the emission-line profile must therefore have the flexibility to account for these complexities. As a consequence, multi-component line modelling is commonly adopted (e.g. Greene & Ho 2005; Shen et al. 2011; Rakshit et al. 2020; Wu & Shen 2022), decomposing emission features into NLR and BLR components.

The complete modelling exercise is then a non-linear least-squares curve fitting minimisation problem which can be solved with iterative optimisation algorithms, such as the Levenberg-Marquardt algorithm (e.g. Guo et al. 2018), or Bayesian approaches, such as the Markov chain Monte Carlo sampler (e.g. Sexton et al. 2021). In the former method, the uncertainties are estimated from multiple fits to synthetic spectra, where each spectrum is generated from randomly sampling the flux at each pixel based on the error spectrum. In the latter methods, uncertainties in model parameters are inferred from the posterior distributions.

As spectral modelling is a significant component of the work presented in this thesis, I developed a custom publicly available `Python`-based software package (`PyQSpecFit`[3]; Lai 2023b) with the express purpose of modelling quasar spectra. The underlying optimisation algorithm is the Levenberg-Marquardt algorithm, which is used to optimise the pseudo-continuum model and the line model in succession. Realistic uncertainties are generated from the Monte-Carlo random sampling approach.

---

[3]https://github.com/samlaihei/PyQSpecFit

1.2.2   Characterising black hole properties from spectra

The fundamental properties of any black hole are its mass, spin, and charge (Israel 1968), although charged black holes are likely to quickly neutralise with the surrounding accretion disc plasma. Therefore, the uncharged and spinning Kerr black hole is the most astrophysically relevant solution to Einstein's field equations. Black holes with accretion discs are also described by the Eddington ratio, which describes the ratio of the bolometric luminosity to its Eddington limit, and radiative efficiency, which relates the luminosity to the mass accretion rate. The line-of-sight to the observer can also change the black hole appearance due to the anisotropy of emission, or the presence of biconical outflows, an obscuring torus, or intervening intergalactic medium material. The mathematical description of the accretion disc also involves its own set of parameters which describe the viscosity, heating, opacity, among many other hydrodynamic fluid properties. In reality, these are further complicated by time evolution and inhomogeneities, which break down the assumptions of axial symmetry assumptions. In summary, the observable characteristics of even the simplest toy model black holes involves the interplay of all of the above parameters. Fortunately, the abundant complexity inherent in the system does not preclude us from extracting useful constraints from observed spectroscopic information.

One of the fundamental properties of a black hole, its mass, can be inferred indirectly from its gravitational influence on orbiting material. A particularly striking application of this idea comes from the multi-year observations of the "S-stars" orbiting the central supermassive black hole in the middle of the Milky Way, Sgr A* (Ghez et al. 1998). However, the concept applies just as readily to orbiting gas. Because gravity is a conservative force, the virial theorem relates the time-averaged kinetic energy to the gravitational potential energy. Virialisation is often invoked to relate the orbital kinematics of emitting gas from the BLR to the central gravitational potential, and the assumption is thought to hold as long as the system has not been recently perturbed. Under this assumption, the virial mass of a black hole can be described by (e.g. Wandel et al. 1999),

$$M_{\mathrm{BH}} = f \frac{RV^2}{G} \,, \qquad (1.2)$$

where R is the radius of the emitting gas, V is its orbital velocity, G is the gravitational constant, and f is the virial factor, which is introduced to account for uncertainties in the BLR morphology and orientation. When adopted as a constant, the virial factor, which varies from system to system, is one of the primary sources of uncertainty in the black hole mass estimate (e.g. Peterson 2010; Bennert et al.

2021). In practice, the virial factor is determined empirically by tying measured virial masses to the black hole mass-bulge stellar velocity dispersion ($M_{\mathrm{BH}} - \sigma_*$) relation (e.g. Onken et al. 2004; Woo et al. 2010; Ho & Kim 2014; Woo et al. 2015; Yu et al. 2019) and resulting mass measurements adopt the relation's intrinsic scatter of ~ 0.4 dex (e.g. Bennert et al. 2021).

The radius of the line-emitting BLR is constrained by reverberation mapping experiments (Blandford & McKee 1982; Peterson 1993), which cross-correlate observed variability behaviour in the AGN continuum with variability in the emission lines at a later time separated by the light travel time delay. The majority of the reverberation mapping work focuses on the H$\beta\lambda4863$ emission-line (e.g. Peterson & Horne 2004; Bentz et al. 2009; Denney et al. 2010; Fonseca Alvarez et al. 2020; Malik et al. 2023), observable in local AGN through ground-based optical telescopes. Other lines, including C IV $\lambda1549$ (e.g. Lira et al. 2018; Grier et al. 2019; Hoormann et al. 2019) and Mg II $\lambda2799$ (e.g. Homayouni et al. 2020; Yu et al. 2023), have also been studied, albeit with lower statistics. Reverberation mapping campaigns are expensive, particularly for high-redshift or high-luminosity quasars, due to the large broad-line region sizes and cosmological time dilation, which necessitates long-term monitoring programs. Therefore, the combined work of multiple reverberation mapping projects has amounted to mass estimates of a few hundred, mostly local AGN.

However, the reverberation mapping work has convincingly detected an empirical relationship between the radius of the BLR and the nuclear continuum luminosity (R-L relation; e.g. Kaspi et al. 2000, 2005; Bentz et al. 2006, 2013; Fonseca Alvarez et al. 2020), which allowed the continuum luminosity to act as a proxy for the BLR radius. The R-L relation can be expressed as $R_{\mathrm{BLR}}/10\,\mathrm{lt\,days} = \alpha \mathrm{L}^\beta$, where (α, β) are calibration constants, and $\beta = 0.5$ is the canonical relationship from photoionisation models (e.g. Bentz et al. 2013). With constraints on the BLR size determined by the relation, the black hole mass can then be estimated with the "single-epoch virial black hole mass estimate",

$$\left(\frac{M_{\mathrm{BH,vir}}}{M_\odot} \right) = 10^{\mathrm{a}} \left[\frac{\lambda L_\lambda}{10^{44}\,\mathrm{erg\,s^{-1}}} \right]^b \left[\frac{V}{1000\,\mathrm{km\,s^{-1}}} \right]^c , \qquad (1.3)$$

where the velocity width, V, of Doppler-broadened emission lines (e.g. Peterson et al. 2004; Peterson & Bentz 2006) is measured with the full-width at half maximum (FWHM) or the dispersion (σ_{line}) of the line profile. The constants (a, b, c) are calibrated to reverberation mapping mass estimates, where b is set to the exponent, β, in the $R - L$ relation and c is usually 2 as given by the virial theorem. Due

to its convenience and ease of application, the single-epoch mass estimate has been applied to hundreds of thousands of AGN through optical spectroscopy (e.g. Shen et al. 2011; Rakshit et al. 2020; Wu & Shen 2022), as well as many high-redshift quasars through near-infrared observations (e.g. López et al. 2016; D'Odorico et al. 2023) as emission lines are redshifted out of the optical coverage. Although single-epoch recipes have been developed for multiple emission lines (*i.e.,* C IV, Mg II, Hβ, Hα), they are calibrated to Hβ reverberation mapping experiments as its R-L relation is the most extensively studied. Single-epoch virial estimators exhibit a ~ 0.3 dex intrinsic scatter with their reverberation mapping counterparts, which results in an overall black hole mass systematic uncertainty of ~ 0.5 dex.

The relation in Equation 1.3 implies that the quasar BLR should exhibit a characteristic "breathing" anti-correlation between the emission-line velocity width and the continuum luminosity. Assuming the canonical $R \propto L^{0.5}$ relation (e.g. Bentz et al. 2013), the breathing anti-correlation can be expressed as $\Delta \log V = -0.25 \Delta \log L$, where $\Delta \log V$ and $\Delta \log L$ represent changes in the line width and continuum luminosity, respectively. Figure 1.4 shows example Hα and Hβ breathing anti-correlations for a quasar J141645.15+542540.8 based on data from the Sloan Digital Sky Survey Reverberation Mapping Project (Wang et al. 2020). The slope for the Hβ line is similar to the canonical expectation, but the Hα slope is shallower. The Mg II emission-line exhibits variability behaviour that is distinct from the expected breathing mode (e.g. Guo et al. 2019), possibly because Mg II is dominated by collisional excitation (Guo et al. 2020). C IV may even show anti-breathing behaviour (Wang et al. 2020), implying that the uncertainty in the black hole mass determination derived from C IV would be larger than for Balmer lines. Therefore, the virial approach may only be valid for other lines as a sample average, while single-epoch mass estimates of individual quasars would exhibit considerable scatter. This highlights how continued reverberation mapping experiments are necessary to further constrain the detailed BLR structure and kinematics.

AGN are notable for emitting substantial radiation over all wavelengths, as seen through compiled AGN spectral energy distributions (SEDs) from multiple telescopes to cover broad ranges in the full electromagnetic spectrum. Past work has noted a remarkable homogeneity in the averaged SEDs across large groups of samples, indicating similar underlying physical emission mechanisms (e.g. Elvis et al. 1994; Dietrich et al. 2002). A consequence of this uniformity is that a black hole's total radiative output can be estimated from single-epoch spectroscopic observations by correcting the observed monochromatic luminosity at a reference wavelength to the integrated emission from mean AGN SEDs (e.g. Richards et al. 2006; Shang
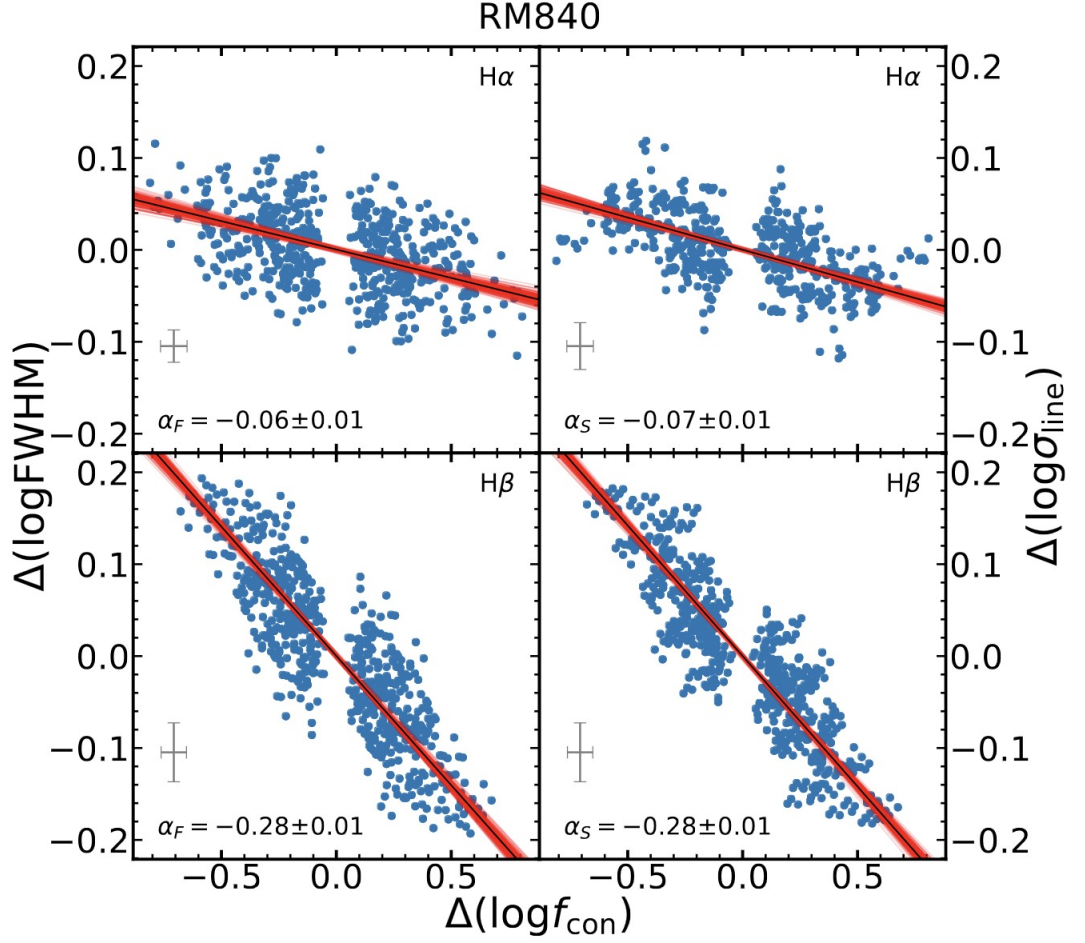
Figure 1.4: Correlations between the line widths, FWHM, and the host-subtracted continuum flux, f_{con}, for Hα and Hβ, demonstrating the BLR breathing behaviour in J141645.15+542540.8. The solid black line with red sheath is the median and 1σ confidence ranges of the linear regression, while the grey crosshairs indicate the median uncertainties of the data. The slope of the regression is indicated on the bottom-left corner of each panel. This figure is reproduced from Wang et al. (2020).

et al. 2011; Runnoe et al. 2012). The bolometric correction factor, denoted by k, can be static (e.g. Richards et al. 2006) or luminosity-dependent (e.g. Marconi et al. 2004; Runnoe et al. 2012; Trakhtenbrot & Netzer 2012; Netzer 2019). It is applied to the measured continuum monochromatic luminosity in the form $L_{\mathrm{bol}} = k\lambda L_\lambda$, and corrections for anisotropy are sometimes considered as well (Nemmen & Brotherton 2010; Runnoe et al. 2012). The expected uncertainties are as large as ~ 0.3 dex for individual AGN that may not be as well-represented by the average SED.

As both the black hole mass and bolometric luminosity can be estimated from spectroscopic analysis, it is merely a matter of algebra to derive the Eddington ratio from $\lambda \equiv L_{\mathrm{bol}}/L_{\mathrm{Edd}}$, where $L_{\mathrm{Edd}} = 1.26 \times 10^{38} \, (M_{\mathrm{BH}}/M_\odot) \, \mathrm{erg\,s^{-1}}$ is the Eddington luminosity for pure hydrogen plasma in spherical symmetry. The required radiation pressure is dependent on the material composition, *e.g.*, if the opacity was lower, as for a helium atmosphere, then the Eddington luminosity is higher. The Eddington ratio is particularly notable for its presumed role in Eigenvector 1 (Boroson & Green 1992), which is predominantly driven by the anti-correlation between Fe II emission and the [O III] line. It is also a useful quantity to assess the AGN accretion properties and one of the fundamental parameters which determines the rate at which a black hole is accreting. AGNs with accretion properties that exceed the nominal Eddington limit have been observed, but these values should be treated with caution due to the large uncertainties associated with black hole mass and bolometric luminosity estimations. Supercritical mass growth, a natural consequence of accretion disc physics under specific conditions, is expected to be short-lived due to the production of powerful jet outflows that can disrupt accretion flow (Regan et al. 2019). From observations of high-redshift targets to the local Universe, the phenomenon of "downsizing" has been noted in galaxies as well as quasars (e.g. Barger et al. 2005; Vestergaard & Osmer 2009; Kelly et al. 2010; Willott et al. 2010a), where the brightest quasars shift to lower mass black holes.

The radiative efficiency, ϵ, describes the fraction of the accreted material's gravitational potential energy that is released as radiation and it relates the bolometric luminosity to the mass accretion rate by $L_{\mathrm{bol}} = \epsilon \dot{M} c^2$. Accretion disc theory suggests that the radiative efficiency is a function of the dimensionless black hole spin, a_*, ranging from 0.057 for a Schwarzschild black hole to 0.422 for a near maximally spinning Kerr black hole (Shakura & Sunyaev 1973; Thorne 1974), but lower efficiencies can be achieved when the spin axis of the black hole and its accretion disc are misaligned (King et al. 2005). Low efficiencies are also an attractive solution to the growth of supermassive black holes at high redshifts, because under chaotic inflow scenarios, the accretion rate can be an order of magnitude higher compared to

near maximally spinning black holes (e.g. King et al. 2008; Zubovas & King 2021). The fiducial value for the radiative efficiency, $\epsilon = 0.1$, is based on the Sołtan argument (Soltan 1982) applied to the local black hole mass density (Yu & Tremaine 2002) and its value corresponds to a black hole spin of $a_* \sim 0.7$. This suggests that the local black hole population has been spun up by prolonged periods of coherent accretion. Currently, there are two main methods for constraining the spin and the radiative efficiency of individual AGN: X-ray reflection and thermal continuum modelling (Reynolds 2019, 2021).

The X-ray reflection method is based on measuring the width of high-energy spectral features emitted in close proximity to the innermost stable circular orbit (ISCO) of the black hole, where the ISCO radius is a sensitive function of black hole spin. The X-ray reflection spectrum, truncated by the ISCO, is broadened by the combined effects of Doppler and gravitational broadening, resulting in broad and highly skewed spectral features. Several dozen measurements of the strong Fe K-shell emission lines in high quality X-ray spectra have resulted in direct measurements of the black hole spin using the X-ray reflection method (Reynolds 2014; Vasudevan et al. 2016), where most measured black holes have spins of $a_* > 0.9$, which may be an overrepresentation of radiatively efficient systems in a flux-limited sample.

The second main method for constraining black hole spin is thermal continuum modelling, which is based on the spin-dependence of the accretion disc temperature. As with the X-ray reflection method, this is a consequence of the ISCO radius, which influences the inner edge of the accretion disc. Rapidly spinning black holes have a smaller ISCO radius, which heats the inner disc to higher temperatures and shifts the observed AGN SED to higher energies. This dependence can be exploited to measure properties of the black hole and I discuss the method in the context of black hole mass measurements in Section 1.4. Continuum modelling has largely been used in the context of black hole X-ray binaries, where the existing spin measurements have generally been consistent with the X-ray reflection method (see review by Reynolds 2021).

An example application of the methods discussed in this section is in the discovery and study of SMSS J114447.77−430859, the most luminous quasar in the last 9 Gyr (Onken et al. 2022b). This work, which I co-authored, demonstrates the utility of the `PyQSpecFit` package in characterising black holes from spectroscopic data. The quasar, found at a redshift of $z = 0.83$, was identified during a search for symbiotic binary stars. Optical and near-infrared spectroscopy revealed broad Mg II, Balmer lines, and Paβ, which were used to measure a black hole mass of $\log(M_{\rm BH}/M_\odot) = 9.4 \pm 0.5$ from single-epoch virial mass estimates. The bolometric luminosity of

the quasar was estimated to be $L_{\rm bol} = (4.7 \pm 1.0) \times 10^{47}\,{\rm erg\,s^{-1}}$ from bolometric corrections applied to the power-law continuum, making it the most luminous quasar in the last 9 Gyr of cosmic history. The implied Eddington ratio from the mass and luminosity estimates is $\lambda \approx 1.4$. X-ray observations were presented in Kammoun et al. (2023), where the continuum modelling method resulted in a 10 times more massive black hole and 32% higher luminosity, but no clear constraint on the black hole spin.

Further applications of these methods are described in the subsequent chapters.

1.2.3   Metallicity of the broad-line region

Spectroscopic decomposition of the AGN rest-frame ultraviolet spectrum can also probe the relative strengths of emission lines from the BLR, which are sensitive to the chemical abundance in the line-forming regions (see review by Hamann & Ferland 1999). Quasar abundance studies are motivated by the apparent coevolution observed between the central supermassive black hole and their host galaxies, as seen through the $M_{\rm BH} - M_{\rm bulge}$ relation (e.g. Magorrian et al. 1998; Greene et al. 2010), the $M_{\rm BH} - \sigma$ relation (Ferrarese & Merritt 2000; Gebhardt et al. 2000; Tremaine et al. 2002), the galaxy stellar mass - gas phase metallicity relationship (MZR; e.g. Maiolino et al. 2008; Maiolino & Mannucci 2019; Sanders et al. 2021) and the $M_{\rm BH}/M_{\rm host}$ ratio (e.g. Targett et al. 2012). Studies of high-redshift metallicities can be used to investigate chemical evolution in galactic nuclear material in the early (< 1 Gyr) Universe.

Emission-line abundance diagnostics rely on detailed photoionisation calculations to reveal line ratios with significant sensitivity to chemical abundance and little dependence on other unknown parameters. These studies generally focus on broad rest-frame ultraviolet emission line ratios, such as N V/C IV and (Si IV+O IV)/C IV, which are monotonically increasing functions of metallicity according to local optimally-emitting cloud (LOC; Baldwin et al. 1995) models implemented in `Cloudy` photoionisation simulations (Hamann et al. 2002; Nagao et al. 2006). Figure 1.5 shows various emission-line flux ratios as a function of metallicity for `Cloudy` LOC models from Nagao et al. (2006). The Fe II/Mg II flux ratio is also of particular interest among the BLR flux ratios due to the different enrichment pathways from which Mg and Fe are produced, where Mg is produced primarily through core-collapse type II supernovae (e.g. Woosley & Hoffman 1992) and Fe is produced by type Ia supernovae over longer lifetimes (e.g. Greggio & Renzini 1983). Thus, the same spectral decomposition techniques used to characterise the black hole can also be
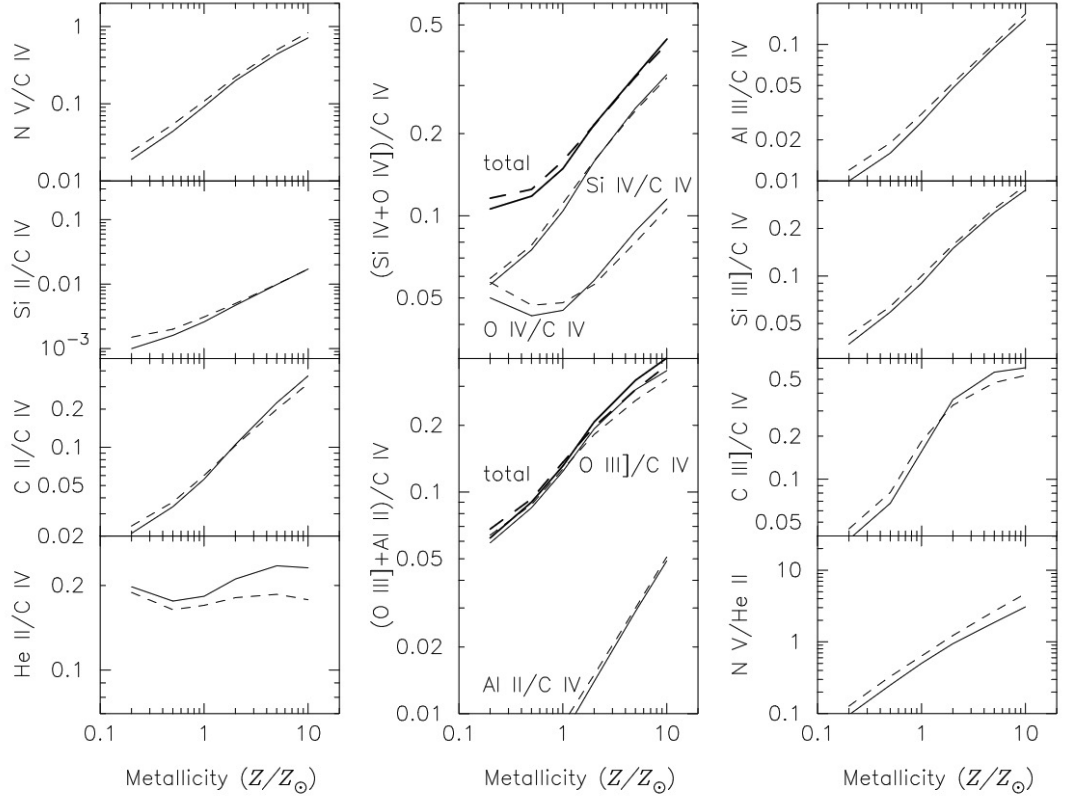
Figure 1.5: Emission-line flux ratios as a function of metallicity determined by locally optimally emitting cloud `Cloudy` photoionisation modelling. The solid and dashed lines refer to relations derived from ionising SEDs with a large or small ultraviolet thermal bump, respectively. This figure is reproduced from Nagao et al. (2006).

used to infer chemical abundances in the quasar BLR.

Existing chemical abundance studies in the literature find correlations between metallicity-sensitive line ratios with the black hole mass (e.g. Matsuoka et al. 2011; Xu et al. 2018; Wang et al. 2022), quasar luminosity (e.g. Hamann & Ferland 1993; Nagao et al. 2006), and outflow strength (e.g. Wang et al. 2012; Shin et al. 2017), with some quasars reaching $Z \sim 5 - 10\,Z_\odot$ (e.g. Juarez et al. 2009). Another notable result is that the observed line ratios appear to be independent of redshift (Pentericci et al. 2002; Xu et al. 2018), up to redshifts as high as $z = 7.64$ (Onoue et al. 2020; Yang et al. 2021), suggesting rapid chemical enrichment of the host galaxy's nuclear region as early as ~ 500 Myr after the formation of the first stars with little evolution afterwards. Other studies (e.g. Sameshima et al. 2017; Temple et al. 2021a) are critical of these results, suggesting that the diversity of emission-line properties can be explained by systematic differences in gas densities and incident ionising flux, without invoking metallicity. Because quasars at high redshift are biased towards the most luminous subset with the most massive host galaxies, future studies of

chemical abundance in quasar BLR will need to consider quasars over a broad range of luminosities, black hole mass, and redshift, alongside detailed photoionisation simulations to suggest the highest likelihood conditions which produce the observed emission properties.

1.3 Quasar Demographic Analysis

Robust measurements of the quasar population across cosmological history reveal critical information about supermassive black hole mass assembly, which can be tested against models of black hole and galaxy evolution. Recently, wide-field spectroscopic surveys compiling hundreds of thousands of quasars across a wide range of redshifts (e.g. Schneider et al. 2010; Lyke et al. 2020; Yang et al. 2023) have changed the landscape of quasar abundance analysis by enabling accurate measurements of quasar properties. The most basic demographic analysis application is the quasar luminosity function which has been measured for AGN populations across a wide range of redshifts (e.g. Jiang et al. 2016; Yang et al. 2016; Akiyama et al. 2018; Matsuoka et al. 2018b; McGreer et al. 2018; Niida et al. 2020; Kim et al. 2020; Onken et al. 2022a; Schindler et al. 2023), and recently up to $z \sim 7$ (Matsuoka et al. 2023).

Not long after the discovery of quasars, Schmidt (1968) found that the quasar spatial density increases with redshift up to $z \gtrsim 2$. It was later established by wide-field surveys, such as the Two-degree Field Galaxy Redshift Survey (2dF; Boyle et al. 2000), Classifying Objects by Medium-Band Observations – a spectrophotometryic 17-filter survey (COMBO-17; Wolf et al. 2003a,b) and SDSS (Richards et al. 2006), that the peak quasar epoch is located between $z = 2 - 3$, declining towards higher redshifts (e.g. Schmidt et al. 1995). Luminosity functions at $z \sim 5$ suggest that the AGN ionising photon density is not a major contributor to cosmic reionisation (e.g. Matsuoka et al. 2018b; Kim et al. 2020; Matsuoka et al. 2023) compared to early star-forming galaxies (Robertson et al. 2015), but see Grazian et al. (2022) for an alternate view. Early high-redshift ($z \sim 6$) quasar surveys dependent on the optical SDSS data could only probe the most luminous subset of quasars (Fan et al. 2004; Jiang et al. 2009; Willott et al. 2010b; Jiang et al. 2016). Later projects extended the $z \sim 6$ quasar sample down to significantly lower luminosities using, for example, deeper imaging data from the Subaru HSC Strategic Program Survey (SHELLQS; Matsuoka et al. 2016).

At even higher redshifts $z \gtrsim 7$, measurement of the quasar luminosity function becomes increasingly difficult due to the declining quasar spatial density, which

would require deeper wide-area surveys. Naturally, the faint-end of the luminosity function is often incomplete and the bright-end slope is significantly affected by small-number statistics. The entire $z > 9$ observable Universe may host only one $M_{1450} < -26$ quasar powered by a supermassive ($10^9 \, M_\odot$) black hole (Fan et al. 2023). Thus, although it is clear that there is a strong exponential decline in the comoving luminous quasar spatial density, the shape and evolution of the luminosity function is still uncertain. Nevertheless, the quasar luminosity function is usually parameterised as a double power-law

$$\Phi(M_{1450}, z) = \frac{\Phi^*(z)}{10^{0.4(\alpha+1)\Delta M_{1450}} + 10^{0.4(\beta+1)\Delta M_{1450}}}, \qquad (1.4)$$

where M_{1450} is the rest-frame 1450Å continuum absolute magnitude, (α, β) are power-law slopes, $\Phi^*(z)$ is a redshift-dependent normalisation, and ΔM_{1450} is $M_{1450} - M^*_{1450}$, where M^*_{1450} is the characteristic break magnitude. The luminosity function normalisation declines exponentially, as $\Phi^*(z) \propto 10^{kz}$. The luminosity function model is then fully constrained by a set of 4 parameters $(M^*_{1450}, k, \alpha, \beta)$. Jiang et al. (2016) presented their luminosity function at $z \sim 6$ using SDSS data, finding $(M^*_{1450}, k, \alpha, \beta) = (-25.1, -0.72 \pm 0.11, \text{N/A}, -2.8 \pm 0.2)$, where the faint slope, α, is unconstrained. Schindler et al. (2023) combined the lower-luminosity quasars from the SHELLQS with the bright PS1 sample at $z \sim 6$, finding $(M^*_{1450}, k, \alpha, \beta) = (-26.38^{+0.79}_{-0.60}, -0.7, -1.70^{+0.29}_{-0.19}, -3.84^{+0.63}_{-1.21})$.

A key limitation is the relatively unknown obscured fraction of quasars which would appear too reddened to be picked up by most quasar selection methods. Kato et al. (2020) discusses two dust-reddened quasars at $z > 5.6$ picked up by the deeper HSC survey extinguished by $E(B-V) > 0.1$, but the total number of known high-redshift red quasars is insufficient to produce robust conclusions on the statistical properties of obscured quasars. Simulations suggest that the intrinsic luminosity function may be 1.5 dex higher than the observed dust-extinguished luminosity function, which would mean that the majority of high-redshift AGN can be missed (Ni et al. 2020). Reliable estimates of the high-redshift obscured fraction would require multiwavelength observations extending from radio to X-ray for candidate selection and spectroscopic identification.

The luminosity function also does not directly reflect mass assembly history. The more fundamental quantity is the black hole mass function, whose selection function in flux-limited surveys is less well-defined. In principle, the quasar luminosity function is the product of the intrinsic black hole mass function convolved with its Eddington ratio distribution weighted by the quasar duty cycle, which enables the

black hole mass function to be probed by forward-modelling (e.g. Wu et al. 2022; Li et al. 2023b). One could also determine the *active* black hole mass function by quantifying observed black hole masses in a luminosity-complete sample (e.g. Vestergaard & Osmer 2009; Willott et al. 2010a; Kelly & Shen 2013). The advantage of forward-modelling techniques is that one could carefully account for uncertainties and biases in the measured quantities, but the result would be model-dependent and particularly sensitive to the shape of the Eddington ratio distribution function at the low-Eddington regime where statistics are sparse. The active black hole mass function provides a model-independent estimate based directly on observables, but the result does not necessarily reflect the intrinsic black hole population. This method is particularly useful for studies of populations of the most massive black holes, where it is expected that the intrinsic and active mass functions converge (e.g. Kelly & Shen 2013).

A unique application of the black hole mass function is presented by the Sołtan argument (Soltan 1982), which discusses how total energy production by accretion can be used to estimate the total mass contained in dead quasars. As previously discussed, a version of the argument was used to estimate the radiative efficiency using the local black hole mass density (Yu & Tremaine 2002). If accretion is the dominant mechanism by which black holes grow, the global evolution of the black hole population can be described with a continuity equation, involving the quasar duty cycle, mean Eddington ratio, and radiative efficiency. The continuity equation is described by (Shankar et al. 2013; Tucci & Volonteri 2017),

$$\frac{\delta \Phi(M_{\mathrm{BH}}, t)}{\delta t} = -\frac{\delta \left[\langle \dot{M}_{\mathrm{BH}} \rangle \Phi(M_{\mathrm{BH}}, t) \right]}{\delta M_{\mathrm{BH}}} , \qquad (1.5)$$

where the mass function, $\Phi(M_{\mathrm{BH}}, t)$, evolves as each black hole grows constantly over the period with the mean accretion rate $\langle \dot{M}_{\mathrm{BH}} \rangle$. The mean accretion rate can be expressed as,

$$\langle \dot{M}_{\mathrm{BH}} \rangle = \int d \log \lambda P(\lambda | M_{\mathrm{BH}}, z) \lambda U(M_{\mathrm{BH}}, z) \frac{M_{\mathrm{BH}}}{450 \, \mathrm{Myr}} \frac{(1 - \epsilon)}{\epsilon} , \qquad (1.6)$$

where the Eddington ratio, λ, is distributed according to $P(\lambda | M_{\mathrm{BH}}, z)$ the normalised Eddington ratio probability distribution; $U(M_{\mathrm{BH}}, z) \in [0, 1]$ is the duty cycle; and ϵ is the radiative efficiency. Using the continuity equation, one can obtain joint constraints on these three parameters by mapping the observed growth of the black hole mass function across cosmic time. Moreover, the observed mass function can be evolved back to the early Universe to gain insights on the black hole initial
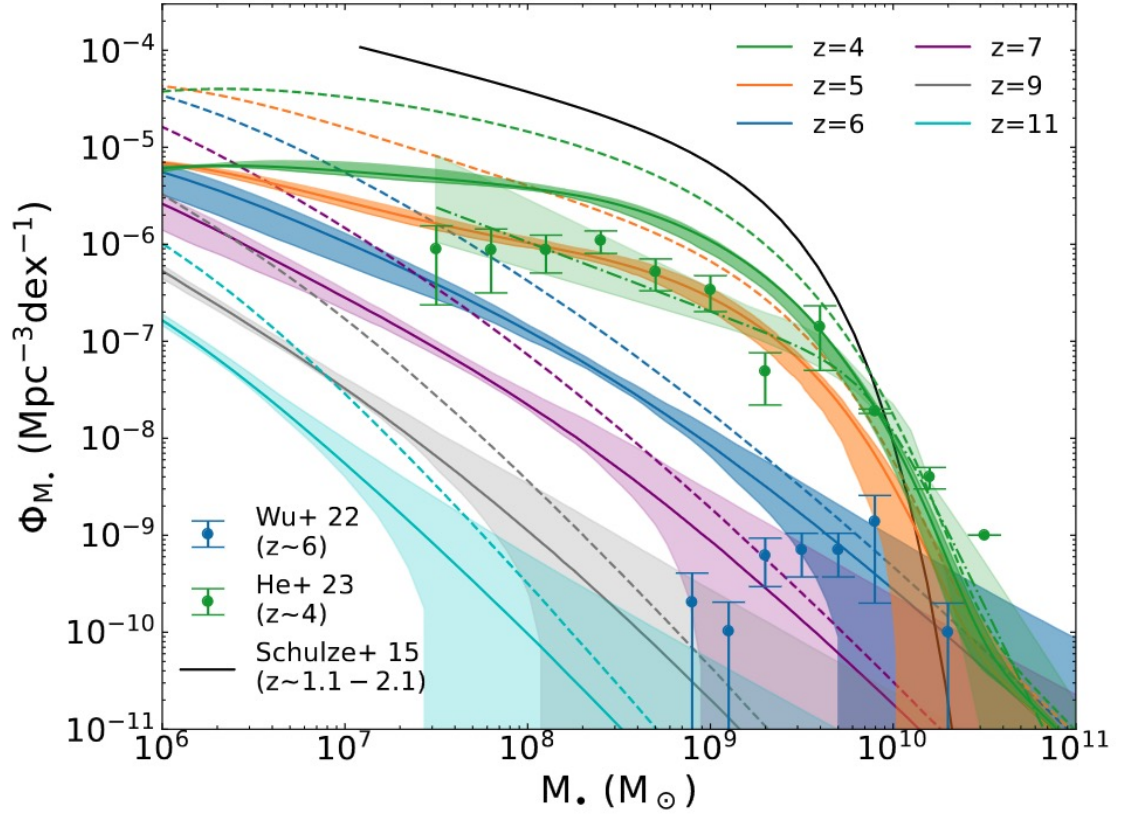
Figure 1.6: Model black hole mass functions in the redshift range, $4 \gtrsim z \gtrsim 11$, reconstructed from luminosity functions at their respective redshifts. The solid (dashed) lines represent the unobscured (total) black hole population, while the observed black hole mass functions are overlayed data points (Wu et al. 2022; He et al. 2023). The lower redshift mass function from Schulze et al. (2015) is also plotted as the black solid line. This figure is reproduced from Li et al. (2023b).

mass function and seeding mechanisms. Figure 1.6 shows black hole mass functions reconstructed from luminosity functions for the redshift range $4 \gtrsim z \gtrsim 11$ (Li et al. 2023b), alongside observed mass functions (Schulze et al. 2015; Wu et al. 2022; He et al. 2023). The black hole mass functions show a clear evolution with redshift, reflecting the cosmological mass assembly history of black holes.

Another observable characteristic of black hole mass functions across cosmic history is the phenomenon of "downsizing" or mass-dependent accretion rates (Barger et al. 2005), which describes how the brightest AGN shift to black holes with lower masses with decreasing redshift, which may be explained by black hole mass saturation at the highest masses and preferential starvation as the most massive black holes run out of readily accessible fuel to support continued accretion. This can be observed directly over a wide range of redshifts, showing that the abundance of supermassive active black holes has been declining since $z \sim 2$ (e.g. He et al. 2023), a result which

is supported by semi-analytical simulations (Shirakata et al. 2019) and is coincident with the peak quasar epoch (Schmidt et al. 1995). In Figure 1.6, downsizing can also be observed from the steepening of the mass function slope at the high-mass end over time.

The latest surveys of the ultraluminous quasar population (e.g. Schindler et al. 2017, 2019a; Boutsia et al. 2020; Cristiani et al. 2023) find a $30 - 40\%$ increase (Schindler et al. 2019b; Boutsia et al. 2021) in the number of bright quasars compared to older estimates. Consequently, quasar demographic analyses will always derive benefit from modern, wider area, and more complete surveys, which are valuable to test past predictions. Building up a highly-complete quasar sample at $z \sim 5$ with broad spectroscopic coverage is one of the primary objectives of this thesis, where Chapter 3 characterises the black holes in the sample through spectral decomposition methods and Chapter 4 presents the demographic analysis.

1.4   Accretion Disc Modelling

Classical accretion disc theory traces back to the steady-state, axially symmetric, optically thick, geometrically thin α-discs investigated by Shakura & Sunyaev (1973) and Novikov & Thorne (1973), one decade after the discovery of the first quasar, 3C 273 (Schmidt 1963). Although spherical Bondi accretion is the simplest case of accretion flow (Bondi 1952), an accretion disc is a natural outcome if the gas angular momentum, J, satisfies $J^2/GM_{\mathrm{BH}} \gg R_{\mathrm{ISCO}}$. The physical mechanism described by α defines the viscosity by $\nu = \alpha c_s h$, where the sound speed c_s is the characteristic velocity of turbulent motions and h is the vertical scale height. The viscosity mediates both the energy dissipation and angular momentum transport within a disc whose time evolution is regulated by the conservation of mass and angular momentum. The best candidate mechanism for viscosity in a black hole accretion disc is magnetorotational instability (Balbus & Hawley 1991), where magnetic field lines threading the disc can be wound up by shear forces and transport angular momentum outwards, which is a necessary component for accretion. Magnetic reconnection produces the energy dissipation and limits the growth of the field. A full discussion of accretion disc modelling theory is beyond the scope of this thesis, but see Abramowicz & Fragile (2013) for a comprehensive review.

The standard thin disc framework is a solution of the steady-state structure, solved analytically for a few physically reasonable assumptions: that the disc is thin, Keplerian, and optically thick. The viscosity also adjusts to the required mass accretion rate and the radiation pressure is generally ignored. Characteristic timescales

in the thin disc model are the viscous timescale (radial motion), t_{visc}, dynamical timescale (orbital motion), t_{dyn}, and the thermal timescale (vertical thermal balance), t_{th}, ordered as $t_{\text{visc}} > t_{\text{th}} > t_{\text{dyn}}$. If we then assume that each annulus in the disc radiates as a blackbody with a local effective temperature, the total flux can be integrated across the entire disc surface down to an innermost edge, defined by the spin-dependent ISCO. For any set of black hole parameters, synthetic accretion disc SEDs can be created by ray-tracing null geodesics from an observer placed at infinity, oriented with some inclination angle with respect to the disc. Early applications of accretion disc modelling estimated the black hole mass of 3C 273 to be $\log(M_{\text{BH}}/M_\odot) = 8.3 - 8.7$ (Malkan 1983), well before reverberation mapping estimates of $\log(M_{\text{BH}}/M_\odot) = 8.3 - 8.4$ using the FWHM from the root-mean-square spectrum or $\log(M_{\text{BH}}/M_\odot) \approx 8.7$ from the mean spectrum (Kaspi et al. 2000). Later reverberation mapping studies corrected its black hole mass higher to $\log(M_{\text{BH}}/M_\odot) = 8.8 - 9.0$ (Peterson et al. 2004), while the GRAVITY instrument (GRAVITY Collaboration et al. 2017) on the Very Large Telescope Interferometer (VLTI) spatially resolved the BLR dynamics, measuring $\log(M_{\text{BH}}/M_\odot) = 8.2 - 8.6$ (Gravity Collaboration et al. 2018). Given that the intrinsic scatter in the $M_{\text{BH}} - \sigma_*$ relation is ~ 0.4 dex (e.g. Onken et al. 2004; Bennert et al. 2021), all of the discussed black hole mass estimates are statistically consistent.

In recent years, accretion disc modelling as a method to constrain black hole properties has generally fallen out of favour in comparison to reverberation mapping and single-epoch virial black hole mass estimates. The availability of spectroscopic data on hundreds of thousands of quasars (e.g. Lyke et al. 2020) is advantageous toward spectral decomposition techniques, leading to large catalogues of quasars with measured line properties (e.g. Rankine et al. 2020; Wu & Shen 2022). Meanwhile, accretion disc modelling was beset by issues, such as its inability to reproduce other energetically significant regions of the SED besides the "big blue bump" (Shields 1978) without more complex physical processes (Koratkar & Blaes 1999) and challenges to its simplifying assumptions, such as the vanishing torque at the inner edge of the accretion disc (Gammie 1999). Figure 1.7 shows the portion of the AGN SED within the big blue bump that is characterised by thermal emission from an accretion disc model. At redder wavelengths, the dominant emission in the composite is from dust and the host galaxy. Accretion disc modelling also does not reproduce the spectral hardening or soft X-ray excess at bluer wavelengths from Comptonisation, although ad hoc methods such as the spectral hardening factor, $f_{\text{col}} \geq 1.0$, have been used to shift spectral features to higher energies.

Spectral hardening was introduced to capture the combined effects of Compton scat-

tering, absorption opacity, optical depth, and plasma density structure (e.g. Shimura & Takahara 1993; Ebisawa et al. 1993; Shimura & Takahara 1995), which helps to approximate the departure of a more realistic disc spectrum from multitemperature blackbody radiation. For X-ray binaries, the commonly adopted $f_{col} = 1.7$ (Shimura & Takahara 1995), but it's well-established that some properties of the black hole, such as its mass, are degenerate with the spectral hardening factor (e.g. Ebisawa et al. 1993; Shimura & Takahara 1995; Li et al. 2005). Studies of AGN black holes often adopt $f_{col} = 1.0$ (Vasudevan & Fabian 2007, 2009; Done et al. 2012; Calderone et al. 2013), with support from theoretical studies (Hubeny et al. 2000, 2001; Czerny et al. 2011). However, other models predict an increasing hardening factor with black hole mass (e.g. Davis & El-Abd 2019).

Given that the black hole properties are sensitive to deviations from the standard disc model and even where there is sufficient multiwavelength coverage of the big blue bump, there are parameter degeneracies that result in large uncertainties, accretion disc modelling in its more recent applications is considered to be no more accurate than a factor of ~ 5 (e.g. Calderone et al. 2013; Capellupo et al. 2016; Campitiello et al. 2020). However, Bayesian approaches are valuable in determining realistic measurement uncertainties. Accretion disc modelling has also found a niche in studies of black hole spin (e.g. Reynolds 2021) and blazars (e.g. Abdo et al. 2010), where the orientation of the accretion disc is better constrained.

The development of numerical simulation codes to include magnetohydrodynamics (MHD), such as `BlackHoleAccretionCode` (BHAC; Porth et al. 2017), `High-Accuracy Relativistic Magnetohydrodynamics` (HARM; Gammie et al. 2003), `KORAL` (Sadowski et al. 2013), and others (e.g. Londrillo & Del Zanna 2000; Anninos et al. 2005; Stone et al. 2008; Etienne et al. 2015) reflects a significant advancement in the computational resources available to researchers. Combined with relativistic radiation transport codes (e.g. Dolence et al. 2009; Narayan et al. 2016; Dexter 2016), one could produce emergent spectra with self-consistent Comptonisation and compare to observation (e.g. Yoon et al. 2020; Wielgus et al. 2022). This is a logical next step to unite observable characteristics of AGN with accretion disc structure and radiation field derived numerically from first principles. In the radio astronomy context, general relativistic magnetohydrodynamic models were able to accurately predict reconstructed black hole images from the very-long baseline interferometry data gathered by the Event Horizon Telescope Collaboration (Event Horizon Telescope Collaboration et al. 2019b, 2022b).

A shortcoming for fully three-dimensional MHD simulations is the computational expense exacted by simulations of large spatial scales. The spatial resolution re-
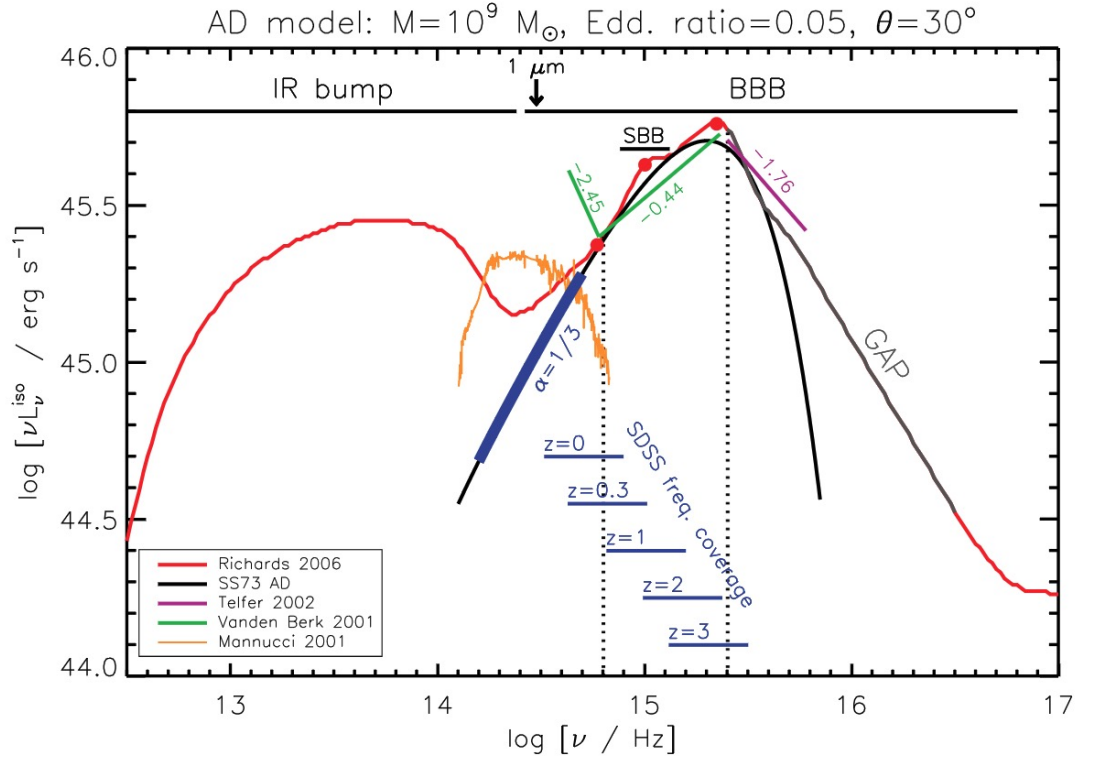
Figure 1.7: Comparison of a composite AGN SED (red) from Richards et al. (2006) and an accretion disc model from Calderone et al. (2013) with parameters listed above the figure. Also plotted are several mean spectral slopes from the literature (Vanden Berk et al. 2001; Telfer et al. 2002), the rest-frame SDSS coverage, the location of the "small blue bump" (SBB) (Wills et al. 1985), and a spiral galaxy template (orange) (Mannucci et al. 2001). The big blue bump (BBB) is the frequency range within which the accretion disc model successfully reproduces the SED shape. The figure is reproduced from Calderone et al. (2013).

quired to adequately resolve thin discs is particularly challenging (Abramowicz & Fragile 2013), which is why the focus of long-duration simulations have been on thick or puffy discs (e.g. Narayan et al. 2012). Height integrated semi-analytic α-disc models (Shakura & Sunyaev 1973; Novikov & Thorne 1973; Li et al. 2005; Sadowski 2011; Straub et al. 2011) as implemented in XSPEC (Arnaud 1996) are still used in accretion disc modelling, particularly when Comptonisation in the accretion disc atmosphere can be modelled separately (Hubeny et al. 2001). Comparisons find existing XSPEC spectral models to provide reasonable fits to synthetic observations of numerical radiative MHD simulations (e.g. Wielgus et al. 2022). Thus, there is latent potential to further explore and develop the use of XSPEC spectral models to constrain black hole properties from the broadband SED and the study presented in Chapter 6 takes advantage of this opportunity.

1.5   Motivation and Thesis Outline

The overarching objective of this thesis is to enhance the understanding of high-redshift quasars through detailed characterisation of existing samples, construction of new samples with broad spectroscopic wavelength coverage, and the development of independent tools to constrain black hole properties based on a theoretical foundation. The thesis is organised as follows.

Chapter 2 characterises black hole properties in the XQ-100 quasar legacy survey (López et al. 2016), a sample of luminous quasars in the redshift range $3.5 < z < 4.5$. Detailed characterisation of black hole properties at high-redshift enables future studies of quasar demographics and correlations with host galaxy properties. XQ-100 is a legacy survey of 100 quasars with high quality echelle spectra and resolution $R \approx 6000 - 9000$, covering a broad wavelength range from the rest-frame ultraviolet to optical. Designed primarily for galactic absorption and intergalactic medium science (e.g. Perrotta et al. 2016, 2018), the black holes contained within the sample had not been characterised independently. Using the publicly available PyQSpecFit code which I developed, I measure and compare black hole mass estimates derived from the C IV, Mg II, and Hβ emission lines. Moreover, I compare the effect of different underlying Fe II models on the resulting mass estimate. This work aids future studies of black hole and host galaxy co-evolution as well as chemical abundance studies of the broad-line region. With its high quality spectra, XQ-100 would also be a prime sample to study quasar-driven outflows and their effects on line profiles or the observed SED.

In Chapter 3, I compile and release the spectroscopic data collected from observ-

ing programs focused on a highly complete, ultraluminous quasar sample, called
XQz5, at redshift $4.5 < z < 5.3$. Observations were obtained with VLT/X-shooter,
SOAR/TripleSpec4.1, and ANU2.3m/WiFeS. This sample was compiled partially to
fill in the redshift gap between two other large publicly available X-shooter quasar
surveys: XQ-100 ($3.5 < z < 4.5$; López et al. 2016) and XQR-30 ($5.8 < z < 6.6$
D'Odorico et al. 2023). I estimate black hole masses from the Mg II line and the L_{3000}
continuum luminosity using virial relations. I also estimate bolometric luminosities
from corrections to the L_{3000} monochromatic luminosity, comparing properties to
surrounding high-redshift quasar samples with broad spectroscopic wavelength cov-
erage and luminosity-matched lower-redshift samples. This work is accompanied
with the public release of all reduced and post-processed spectroscopic data, in ad-
dition to the measured Mg II line properties and estimated black hole properties. Due
to its high completeness, this sample is well-suited for demographic analysis.

Chapter 4 performs a demographic analysis of the XQz5 sample presented in Chapter
3. I exploit the completeness of the parent sample and its spectroscopic follow-up
to derive the observed black hole mass function. I then constrain the cosmological
black hole mass growth of the brightest quasars over the ~ 200 Myr covered by
the sample and compare mass functions at different redshifts to estimate the black
hole mass evolution. This study presents a joint constraint on the quasar duty
cycle, Eddington ratio, and radiative efficiency. Moreover, the result is employed
to trace the evolution of the mass function to obtain insights on the black hole
initial mass function. This study represents the culmination of the spectral analysis
techniques developed in Chapter 2 and the compilation of a dedicated sample for
this investigation in Chapter 3.

Chapter 5 studies the chemical abundance of the quasar broad-line region at
$z \sim 6$ by measuring line flux ratios of metallicity-sensitive rest-frame ultraviolet
emission lines. Existing chemical abundance studies suggest elevated metallicities
($Z \sim 5 - 10\,Z_\odot$) even at the highest redshifts (e.g. Juarez et al. 2009), prompting
the introduction of more exotic early enrichment scenarios such as enhanced super-
nova rates (e.g. Shields 1996), star formation inside accretion discs (e.g. Toyouchi
et al. 2022), or star-less nucleosynthesis (e.g. Datta & Mukhopadhyay 2019). By
comparing the metallicity estimates I obtained at $z \sim 6$ to lower-redshift quasars, I
confirm that there is no evidence of redshift evolution in the broad-line region chem-
ical abundance. However, I demonstrate that the elevated metallicities suggested by
measurements of mass- or luminosity-binned quasars can be influenced by quasars
displaying high C IV blueshift, an indicator of outflowing material.

Chapter 6 demonstrates how synthetic spectra of thermal emission from accretion

disc models can be used to constrain black hole properties independently and potentially in the absence of spectroscopic data. As discussed in Section 1.4, `XSPEC` spectral models have the potential to constrain black hole parameters from the observed broadband SED. However, it was noted that black hole parameters in such modelling efforts suffer from degeneracy. This work relies on Bayesian inference of model parameter posteriors from the Markov-Chain Monte-Carlo sampling approach and is accompanied with the public release of an accretion disc modelling algorithm, `BADFit`[4]. Using these models, I also show calculations of the derived bolometric corrections on the observed luminosity with consideration for the effects of anisotropy.

Chapter 7 presents applications of the accretion disc modelling method in a traditional thesis format, spliced with sections of publications to which I have made significant contributions as a coauthor. This chapter discusses applications in the detailed characterisation of an individual ultraluminous quasar and in quasar orientation studies. I show how synthetic spectroscopic observations of accretion discs has extensive applications in quasar observational studies, which underscores how ongoing developments in theoretical modelling will play a central role in understanding the diversity of observable AGN properties.

Finally in Chapter 8, I present a follow-up discussion in addition to a summary of the thesis and concluding remarks. I also outline possible directions for future work.

---

[4]https://github.com/samlaihei/BADFit

Virial black hole mass estimates of quasars in the XQ-100 legacy survey

Context

This chapter is published as "Lai, S., Onken, C. A., Wolf, C., Bian, F., Cupani, G., Lopez, S., & D'Odorico, V. (2023), *Virial black hole mass estimates of quasars in the XQ-100 legacy survey*, MNRAS, 526, 3230."

Preamble

Large homogeneus samples of high quality echelle spectroscopy are rare in quasar studies, particularly as the redshift increases and the ultraviolet or optical emission-line transitions shift into the near-infrared. In order to study the absorption line diagnostics that probe conditions in early galaxies and the intergalactic medium, moderate to high spectral resolution ($R > 5000$) over a wide spectral coverage is required. A legacy survey of 100 $3.5 \lesssim z \lesssim 4.5$ quasars, called XQ-100, was produced from data obtained from an European Southern Observatory Large Programme utilising the Very Large Telescope's X-shooter instrument in order to enable studies of absorption systems along the quasar line of sight. In this chapter, we measure the black hole masses in the XQ-100 sample using rest-frame ultraviolet emission-lines of C IV $\lambda1549$ and Mg II $\lambda2799$, publicly releasing the line measurements and inferred masses to aid in future studies of galaxy and black hole co-evolution at high redshift. Furthermore, the work in this chapter establishes the foundation for quasar spectral modelling that is used in other works throughout the thesis.

Abstract

The black hole (BH) mass and luminosity are key factors in determining how a quasar interacts with its environment. In this study, we utilise data from the European Southern Observatory Large Programme XQ-100, a high-quality sample of 100 X-shooter spectra of the most luminous quasars in the redshift range $3.5 < z < 4.5$, and measure the properties of three prominent optical and ultraviolet broad emission-lines present in the wide wavelength coverage of X-shooter: C IV, Mg II, and Hβ. The line properties of all three broad lines are used for virial estimates of the BH mass and their resulting mass estimates for this sample are tightly correlated. The BH mass range is $\log\left(\mathrm{M_{BH}}/\mathrm{M_\odot}\right) = 8.6 - 10.3$ with bolometric luminosities estimated from the 3000 Å continuum in the range $\log\left(\mathrm{L_{bol}}/\mathrm{erg\,s^{-1}}\right) = 46.7 - 48.0$. Robustly determined properties of these quasars enable a variety of follow-up research in quasar astrophysics, from chemical abundance and evolution in the broad-line region to radiatively driven quasar outflows.

2.1   Introduction

Hundreds of thousands of quasar (QSO) sources have now been confirmed through massive surveys (e.g., Flesch 2015; Yao et al. 2019; Lyke et al. 2020) up to a redshift of $z = 7.642$ (Wang et al. 2021). Despite the abundance of sources, high-quality echelle spectroscopy is available for only a few thousand unique QSOs, of which only a fraction contain data in the near-infrared (NIR). As the redshift increases, more of the rest-frame ultraviolet (UV) and optical atomic transitions shift into the infrared, which renders NIR observations invaluable for QSO emission and absorption-line studies.

The European Southern Observatory Large Programme "Quasars and their absorption lines: a legacy survey of the high-redshift universe with VLT/X-shooter" (hereafter referred to as XQ-100, PI: S. López, programme number 189.A-0424) is a publicly available and high-quality sample of echelle spectra from 100 luminous QSOs in the redshift range $3.5 < z < 4.5$ (López et al. 2016). The simultaneous full spectral coverage is from 315 nm to 2500 nm with resolving power $R \sim 5400 - 8900$ and median signal-to-noise ratio (SNR) of 24, measured across the whole spectrum and entire sample of 100 QSOs. Prior to XQ-100, the largest NIR spectroscopic survey, conducted using the FIRE spectrograph at Magellan, was comprised of 50 QSOs at $2 < z < 5$ (Matejek & Simcoe 2012) with a median SNR per-pixel of 13 across the entire QSO sample. The XQ-100 survey with its high SNR and broad spectral coverage provides a unique and statistically significant sample to study the rest-frame

UV and optical spectral properties of 100 high-redshift QSOs.

Among the scientific themes of the XQ-100 programme is the study of galactic absorption. Sub-damped (subDLA) or damped Ly α systems (DLA; Wolfe et al. 2005) are used to determine the cosmic density of neutral gas as they are the main reservoirs for neutral gas in the Universe (e.g., Prochaska & Wolfe 2009; Noterdaeme et al. 2012; Sánchez-Ramírez et al. 2016; Berg et al. 2019). The same systems can be used to probe metal abundances of QSO hosts by tracing gaseous absorbers along QSO sightlines (Berg et al. 2016, 2021). Similarly, intrinsic narrow absorption lines (NALs) in XQR-30 data are probes of the physical conditions of the QSO immediate environment and energetics of its outflow (Perrotta et al. 2016), where absorption-line diagnostics indicate metallicity, absorber covering fraction, and ionisation structure (Perrotta et al. 2018). In addition, the XQ-100 spectra also addresses cosmological questions through independent constraints of the Ly α forest power spectrum at high redshift (Iršič et al. 2017; Yèche et al. 2017).

The study of active galactic nuclei (AGN) properties is also one of the scientific themes from the XQ-100 programme. The high-quality spectra can be used for accurate measurements of $z > 3.5$ black hole masses using line profiles of rest-frame UV C IV, Mg II, or rest-frame optical Hβ emission-lines and the continuum luminosity (e.g., McLure & Dunlop 2004; Greene & Ho 2005; Vestergaard & Peterson 2006; Vestergaard & Osmer 2009). Flux ratios of emission-lines in the rest-frame UV, such as N V/C IV or (Si IV+O IV)/C IV, provide estimates of the metallicity in the QSO broad-line region (BLR), which probes the chemical enrichment history in high-redshift galactic nuclear regions (e.g., Hamann & Ferland 1999; Hamann et al. 2002; Nagao et al. 2006; Wang et al. 2012; Xu et al. 2018; Wang et al. 2022; Lai et al. 2022). In the local universe, black hole masses and galactic bulge masses are strongly correlated (the $M_{BH} - M_{bulge}$ relation; Marconi & Hunt 2003; Häring & Rix 2004; Greene et al. 2010), indicating that host galaxies and their central supermassive black holes co-evolve. Determining the black hole masses of high-redshift QSOs is valuable for studies that aim to investigate how properties of host galaxies and their black holes came to be strongly coupled (e.g., Croton et al. 2006; McConnell & Ma 2013; Terrazas et al. 2020).

In this study, we estimate the black hole masses of every source in XQ-100 using single-epoch virial estimates based on the prominent broad C IV λ1549Å, Mg II λ2799Å, and H$\beta\lambda$4863Å lines. We measure emission-line properties utilising the high SNR, resolving power, and wide spectral coverage of the X-shooter data to tightly constrain the observed spectral profiles. This study produces a large catalogue of bright QSOs with robustly measured emission-line properties, black hole masses,

and luminosity estimates at high-redshift ($z > 3.5$).

The content of this paper is organised as follows: in Section 2.2, we describe the XQ-100 data and their further processing. In Section 2.3, we present our approach to modelling prominent emission-lines in the observed spectra. In Section 2.4, we describe virial mass estimates based on the measured line properties. In Section 2.5, we discuss measurements of the emission-lines, black hole mass, and QSO luminosity. We compare the different virial mass estimates against each other and contextualise our results with large low-redshift samples. We summarize and conclude in Section 2.6. Throughout the paper, we adopt a flat ΛCDM cosmology with $H_0 = 70$ km s^{-1} Mpc^{-1} and $(\Omega_{\mathrm{m}}, \Omega_{\Lambda}) = (0.3, 0.7)$. All referenced wavelengths of emission-lines are measured in vacuum.

2.2   XQ-100 Sample Data and Processing

Targets in the XQ-100 sample were initially selected from the NASA/IPAC Extragalactic Database (NED) with declinations $\delta < +15°$ and redshifts $z > 3.5$. An additional twelve targets were obtained from the literature with declination $+15° < \delta < +30°$. Deliberate steps were taken to avoid targets with known broad absorption features and to avoid intrinsic colour selection bias. A full description of the target selection process can be found in López et al. (2016).

2.2.1   Sample Description and Data Reduction

The targets span the redshifts from $z = 3.508$ to $z = 4.716$ (López et al. 2016), although all but four are within the redshift range $3.5 < z < 4.5$. The sample is biased towards bright sources, covering a magnitude range in *Gaia DR3* G_{RP} band (Gaia Collaboration et al. 2021) of 16.78 to 19.00 Vegamag. Observations were carried out between 2012 April 1, and 2014 March 26 by the X-shooter instrument (Vernet et al. 2011) on the Very Large Telescope (VLT) using all three spectroscopic arms: UVB ($300-559.5$ nm), VIS ($559.5-1024$ nm), and NIR ($1024-2480$ nm). The wide wavelength coverage ensures that the C IV and Mg II emission-lines are always observed within the VIS and NIR arms for the range of redshifts in the sample. Additional information on the requested observing conditions and instrumental setup is available in López et al. (2016). We briefly summarise the reduction and processing procedures behind the XQ-100 data products, as described in López et al. (2016).

Extraction of XQ-100 spectra was performed using an IDL-based custom pipeline (Becker et al. 2012). The strategy of the custom pipeline follows techniques described

in Kelson (2003). Flux calibration uses response curves generated from observations of spectro-photometric standard stars, observed close in time to the science frames (López et al. 2016), where a fiducial response curve was used if the temporally closest standard star observation was not optimal. Newer versions of this pipeline have been used in other QSO studies, such as XQR-30 (D'Odorico et al. 2023). While XQ-100 data from all three spectrograph arms are available, for the present study, we consider only the VIS and NIR arms, because they contain all emission-lines of interest. The velocity resolution chosen to rebin the spectra are 11 km s^{-1} and 19 km s^{-1} for the VIS and NIR arms, respectively.

The absolute flux calibration is a crucial step in determining the luminosity of the QSO continuum. A comparison between XQ-100 and Sloan Digital Sky Survey (SDSS; York et al. 2000) spectra showed a systematic underestimation of flux for the X-shooter spectra due to slit losses. However, the slit losses appear to be roughly achromatic, such that the spectral shape is correctly reconstructed, but the flux calibration should be taken as order-of-magnitude estimates (López et al. 2016). Thus, we describe our independent calibration of the XQ-100 spectra to observed photometry in Section 2.2.2.

Telluric absorption features appear prominently in both the VIS and NIR arms. Corrections to the spectra are derived using model transmission spectra based on the ESO SKYCALC Cerro Paranal Advanced Sky Model, version 1.3.5 (Noll et al. 2012; Jones et al. 2013), which are applied to individual-epoch spectra of all XQ-100 QSOs. After extraction and telluric correction, the median per-pixel SNR for the whole QSO sample are 33, 25, and 43, measured at rest-frame wavelengths 1700, 3000, and 3600 Å, respectively (López et al. 2016), computed in ± 10Å windows.

The processed XQ-100 data products, including reduced spectra and telluric models, are publicly available through the ESO Science Archive Facility. However, the spliced spectra and the multi-epoch averaged spectra are not telluric corrected.

2.2.2 Data Post-Processing

We obtain individual VIS and NIR single-epoch frames from the ESO Science Archive Facility for all XQ-100 sources and apply the following post-processing procedure:

1. We use the respective telluric model included in each frame to obtain the telluric-corrected spectra and use the emission redshift to transform the spectra into the rest-frame.

2. We identify pixels for which the per-pixel SNR is 5 or below and mask them

from further processing and modelling.

3. We apply a mask by sigma-clipping with a 3σ-threshold along a box width of 40 pixels to remove some of the narrow absorption features and noise above 3σ. The absorption features are not desired when modelling the intrinsic profile of the broad emission-lines and the sigma-clipped spectrum also helps constrain the continuum. While this procedure alone will not remove the base of absorption troughs, we follow the procedure in Shen et al. (2011), which defines our single-epoch virial mass calibration of Mg II. In Section 2.3.2, we describe an additional mask buffer window to remove the base of absorption features embedded in the C IV line profile, but this is not applied throughout the entire spectrum.

4. We crossmatch the XQ-100 sample with UKIRT Infrared Deep Sky Survey (UKIDSS; Lawrence et al. 2007) DR11, UKIRT Hemisphere Survey (UHS; Dye et al. 2018) DR1, VISTA Hemisphere Survey (VHS; McMahon et al. 2013) DR6, VISTA Kilo-degree Infrared Galaxy Survey (VIKING; Edge et al. 2013) DR5, and Two Micron All-Sky Survey (2MASS; Skrutskie et al. 2006) to obtain near-infrared J-band photometry. We also crossmatch all targets with the SkyMapper Southern Survey (SMSS; Onken et al. 2019) DR3, Panoramic Survey Telescope and Rapid Response System (Pan-STARRS; Chambers et al. 2016) DR1, Sloan Digital Sky Survey (SDSS; York et al. 2000) DR16, and Dark Energy Sky Survey (DES; Abbott et al. 2021) DR2 to obtain optical i-band photometry. We obtain the transmission profile of the broadband filters using the SVO Filter Profile Service (Rodrigo & Solano 2020) and integrate the observed-frame spectra across the profile, obtaining a flux ratio between the photometry and spectrum with an associated uncertainty, which is used to calibrate the observed spectra to the photometry. There is one target, SDSS J004219.74−102009.4, for which no publicly available J-band photometry was found in the above surveys. In this case, we scale the flux of the NIR arm to match the flux of the VIS arm within the overlapping wavelength coverage. The magnitudes used for calibration are provided in the online supplementary table. We note that the median correction required to match the spectrum to photometry is a 42% flux increase with an error of 2–3%, which is higher than the $\sim 30\%$ flux underestimation on X-shooter's part compared to SDSS spectra estimated in López et al. (2016). As the photometry is taken from a separate epoch from the spectroscopic data, the additional uncertainty from the photometric calibration is insignificant compared to QSO variability, which we quantify and discuss in Section 2.5.1.

5. We standardise the rest-frame wavelength domain for all of the spectra. Every spectrum is resampled using a flux-conserving algorithm (SPECTRES; Carnall 2017) into rest-frame bins with a common velocity dispersion of 50 km s^{-1}. The resampling calculation and error propagation are described in detail in Carnall (2017). Then the VIS and NIR arms are spliced together without rescaling, using the inverse variance weighted mean flux for the superposition between arms. In a few cases, we observe a discontinuity between the VIS and NIR arms, located between 1860Å to 2275Å for the redshift range of our sample. The median flux difference between arms as measured in the overlapping region is 0.6%, albeit with a large standard deviation of 24%. However, we emphasise that the data in the overlapping region between arms are naturally at the edge of the wavelength coverage of each arm and is particularly noisy, so the flux difference measured in this fashion can be exaggerated. Nevertheless, we flag all targets with higher than 25% flux difference between the VIS and NIR arms in the supplementary table under the column "NIR_VIS_Flag". We rely on the flux calibration in each respective arm and only use data within one arm at a time to fit the QSO continuum. Thus, the flux discontinuity between arms does not affect our continuum or emission-line models.

6. If there are repeated observations of a single source, we make use of all the available data and stack the resampled telluric-corrected spectra together, using the mean weighted by the inverse variance to define the value at each 50 km s^{-1} velocity bin and propagate the uncertainty. Because of the calibration in step (iv), the flux density at each velocity bin between repeated observations are in good agreement. The temporal separation between repeated observations range from 10 days to 1.5 years. However, we are interested in the average spectrum in order to determine representative properties of the black hole mass and luminosity. Prior to rescaling the flux level of the spectra to photometry, the median flux difference between exposures measured at every velocity bin is 7.3% with a standard deviation of 7.6%. After rescaling, our flux level is more consistent, measured at 2.3% with a standard deviation of 0.6%. We also quantify the uncertainty from QSO variability in Section 2.5.1.

7. We use $R_v = 3.1$ and the Schlegel, Finkbeiner & Davis (SFD; Schlegel et al. 1998) extinction map to apply a correction for the Milky Way extinction in the observed frame. However, the normalisation of the colour excess based on the SDSS footprint and fits to the blue tip of the stellar locus suggests that SFD systematically over-predicts $E(B - V)$ by 14%. (Schlafly et al. 2010) Thus, we apply a 14% re-calibration factor to the colour excess, such that

$$E(B - V) = 0.86 \times E(B - V)_{\mathrm{SFD}} \text{ (Schlafly \& Finkbeiner 2011).}$$

After the post-processing procedure, the median SNR per 50 km s^{-1} for the whole QSO sample measured at rest-frame 1700, 3000, and 3600 Å is 76, 52, and 74, respectively, measured from the median SNR within ± 10Å windows. Much of the increase in signal originates from the SNR floor and consolidating the flux from its native resolution into the rest frame 50 km s^{-1} grid.

For the wavelength range redder than rest-frame 3600 Å, a similar post-processing procedure is applied, but the sigma-clip mask of step (iii) is omitted to preserve narrow emission-line features of Hβ and O III]. Due to the redshift range of this sample, only a subset of sources contains the Hβ line within the X-shooter coverage. We visually inspect the data to ensure that the Hβ line is distinguishable from the additional noise of the thermal background and second-order contamination at edge of the NIR arm wavelength coverage. We also ensure that the Hβ line is observed with sufficient SNR (> 10 per resolution element), which produces a sub-sample of 21 QSOs, where the median 50 km s^{-1} SNR across all 21 QSOs is 13. In this case, the SNR of each QSO is measured from the median SNR between $5090 - 5110$ Å.

2.3   Spectral Modelling

Our objective in this study is to measure the properties of the following QSO broad emission-lines: C IV $\lambda 1549$Å, Mg II $\lambda 2799$Å, and H$\beta \lambda 4863$Å. In the XQ-100 sample, both C IV and Mg II can be located in all spectra, while Hβ is observable only in lower redshift targets with sufficient signal. In this section, we describe our approach towards modelling emission-lines, using a publicly available code (`PyQSpecFit`[1]; Lai 2023b) designed specifically for modelling QSO spectral lines.

2.3.1   Continuum Modelling

Although a continuum model is provided as part of the XQ-100 data products, we elect to use our own continuum model due to how sensitive the broad emission-line models are to the local continuum. Our model follows similar studies (e.g., Wang et al. 2009) in that the underlying continuum is built from two components: a power-law continuum and Fe II template, simultaneously fit to selected pseudo-continuum-modelled wavelength regions. We briefly comment on the Balmer continuum later in this section and quantify its effect in Appendix A.1. All components of the

---

[1]https://github.com/samlaihei/PyQSpecFit

pseudo-continuum are used in measuring the Mg II and Hβ emission-lines, but the flux contribution from the Fe II continuum is less significant in the wavelength region of C IV. Thus, we only use a power-law to constrain the continuum in the vicinity of the C IV line.

The power-law continuum is defined by the following function normalised at rest-frame 3000 Å,

$$F_{\mathrm{pl}}(\lambda; F_0, \gamma) = F_{\mathrm{pl},0} \left(\frac{\lambda}{3000\text{Å}} \right)^{\gamma} , \qquad (2.1)$$

where $F_{\mathrm{pl},0}$ and γ are the normalization and power-law slope, respectively.

The Fe II continuum is of considerable importance to the Mg II and Hβ models, as both lines are sensitive to the features of the Fe II contribution underneath the emission-line. To eliminate the Fe II emission when strong, we convolve the Fe II model with a Gaussian broadening kernel $G(\lambda, \sigma)$ of standard deviation σ in order to match the variety of features observed in our spectra. The Gaussian broadening follows,

$$F_{\mathrm{Fe}}(\lambda; \zeta_0, \delta, \sigma) = \zeta_0 \, F_{\mathrm{template}}|_{\lambda(1+\delta)} \circledast G(\lambda, \sigma) , \qquad (2.2)$$

where the free parameters of the Fe II contribution include the flux scaling factor denoted by ζ_0, the standard deviation of the broadening kernel σ, and a small multiplicative wavelength shift δ. Furthermore, we consider a variety of empirical and semi-empirical Fe II emission templates: Vestergaard & Wilkes (2001, VW01) and Mejía-Restrepo et al. (2016, M16) cover the rest-frame UV while Boroson & Green (1992, BG92) and Park et al. (2022, P22) cover the rest-frame optical. Bruhweiler & Verner (2008, BV08) and Tsuzuki et al. (2006, T06) cover both regions. We use a VW01 template spliced with the Salviander et al. (2007) template, which extrapolates underneath the Mg II line from rest-frame $2200-3090$Å. Furthermore, the wavelength range $3090-3500$Å is augmented with the T06 template (Shen & Liu 2012). This version of VW01 is also used in other QSO modelling codes such as `PyQSOFit` (Guo et al. 2018). We find the typical value of the Gaussian broadening dispersion σ to be 1600 km s^{-1} in the rest-frame UV and 1300 km s^{-1} in the rest-frame optical.

In this work, we are not concerned with the specific properties of the Fe II emission, and thus we will not discuss the physical interpretation of the dispersion and velocity shifts of the Fe II emission. The Fe II pseudo-continuum is used solely as an approximation to remove iron emission when significant in the spectra. Figure 2.1 shows the spectrum of J110352+100403 close to the Mg II region with the four UV Fe II templates models overplotted along with the resulting emission-line models in a separate panel. Properties of the Mg II line model depend sensitively on the

assumed Fe II model. In the extreme case of SDSS J093556.91+002255.6, differences in the Fe II model alone are responsible for shifting the measured full-width half-maximum (FWHM) in a range from 3700 to 5200 km s^{-1}. Similarly, the Hβ line model is also sensitive to the optical Fe II model. In Section 2.3.2, we discuss how the differences in measured line properties resulting from various Fe II models inform the measurement uncertainty.

The full pseudo-continuum is the sum of all contributing components, which is uniquely defined by 5 free parameters. All components of the continuum are fit simultaneously to selected pseudo-continuum windows close to the emission-line of interest. For each emission feature, the local underlying continuum is fit separately. We do not fit a "global" continuum across the the spectral range from C IV to Hβ in order to avoid biases due to deviations from a single power-law model, such as dust reddening (e.g., Richards et al. 2003) and host galaxy contributions (e.g., Van den Berk et al. 2001). Outside irregular circumstances, such as a discontinuity in the flux-calibrated spectrum between the VIS and NIR arms, the pseudo-continuum modelling windows are selected from: 1275–1290Å, 1348–1353Å, 1445–1455Å, 1687–1697Å, 1973–1983Å, 2200–2750Å, 2820–3300Å, 3500–3800Å, 4200–4230Å, and 4435–4700Å with occasional ±30Å deviations to suit specific features of the spectra, avoid telluric regions, or to accommodate the properties of particular emission or absorption features.

The Balmer continuum is also often included in the pseudo-continuum model when modelling QSO spectra, but it is not always well-constrained and is degenerate with the power-law and Fe II continuum (e.g., Wang et al. 2009; Shen & Liu 2012), such that the Balmer contribution is not considered for the underlying continuum in some other QSO studies (e.g., Shen et al. 2011). For the XQ-100 sample, we find that the Balmer continuum properties are not well-constrained and the broad emission-line decomposition is not strongly affected by either the inclusion or exclusion of the Balmer continuum. Therefore, in the following sections, we present our results without the Balmer continuum, but we quantify the effect of its inclusion in Appendix A.1.

2.3.2   Line Modelling

Broad emission-line profiles exhibit a wide range of properties and complexities from asymmetries to multiple peaks and plateaus, making single Gaussian models unsuitable. Instead, many QSO spectral modelling studies use a multiple Gaussian approach to fit each emission feature (e.g., Greene & Ho 2005; Shen et al. 2011; Rakshit et al. 2020). Following these studies, we fit each broad emission-line with
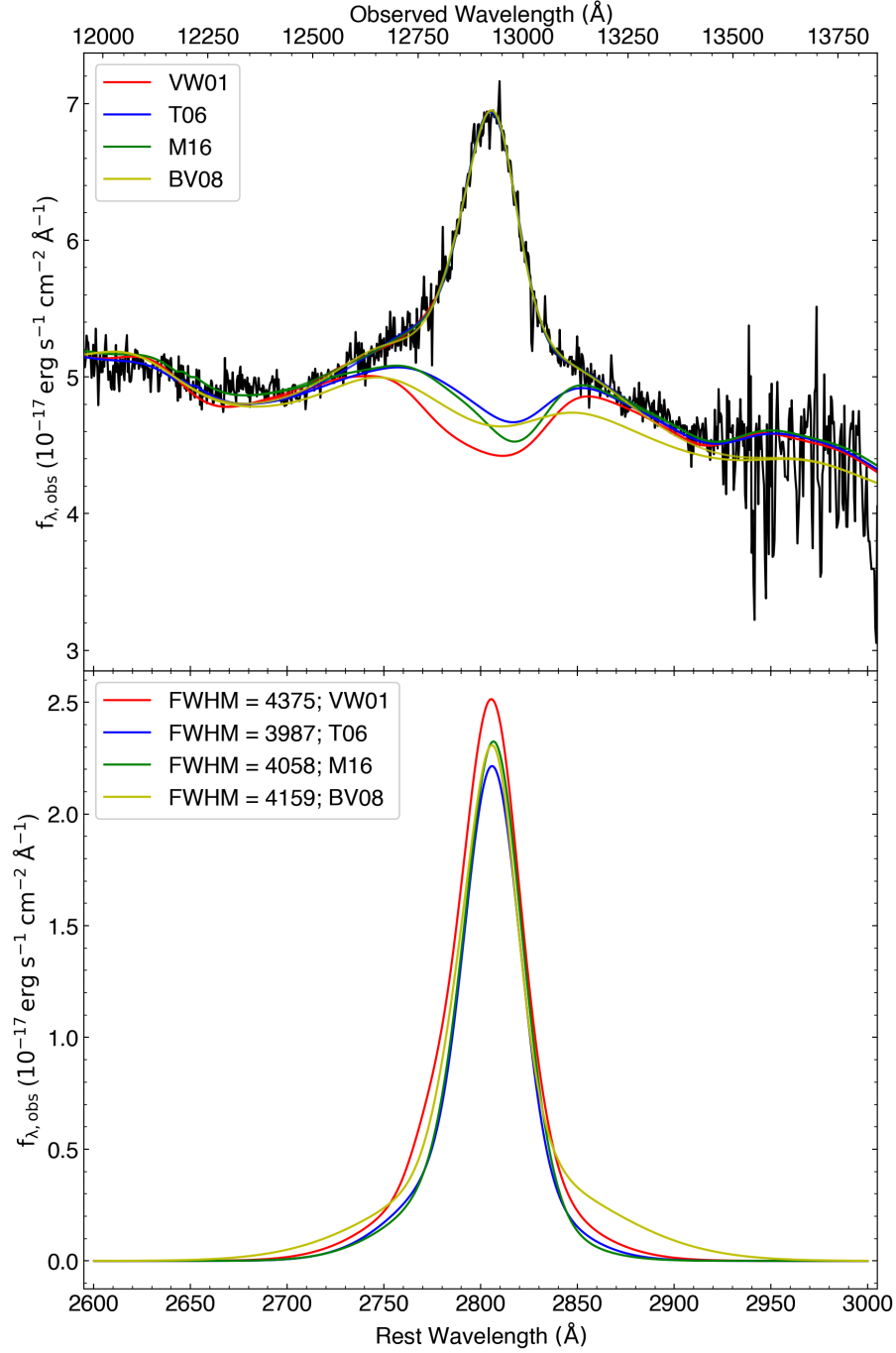
Figure 2.1: Example model of the Mg II emission feature of J110352+100403 with the combined pseudo-continuum from the power-law, Balmer, and Fe II components. The line models differ from one another by the applied Fe II template as indicated in the legend. The resulting continuum for each template is plotted in solid lines in the top panel and the continuum-subtracted line profile model is plotted in the bottom panel. In this example, the Mg II FWHM between models with different Fe II templates ranges from 4000 to 4400 km s^{-1}.

multiple (N_{gauss}) symmetric Gaussian functions having $3 \times N_{\mathrm{gauss}}$ free parameters, to obtain smooth realisations of the observed line profile. Similar to Rakshit et al. (2020), we choose $N_{\mathrm{gauss}} = (3, 4, 4)$ for C IV, Mg II, and Hβ, respectively. The 4 Gaussian components of the Mg II and Hβ lines are divided into 3 broad and 1 narrow component. For high luminosity QSOs, such as the targets in the XQ-100 sample, O III] lines with FWHMs exceeding 1000 km s^{-1} are more common (e.g. Shen & Liu 2012; Coatman et al. 2019), so we adopt a FWHM upper threshold of 1200 km s^{-1} for the Hβ narrow lines. The Mg II narrow lines are often ambiguous and poorly constrained. Thus, we further constrain the upper FWHM threshold for Mg II to 1000 km s^{-1}, ensuring that the modelled components are indeed narrow. To measure the broad-line properties of each line, we subtract the narrow-line contribution from the total line profile, using only the 3 broad components to model the emission-line.

The adjoining O III] lines can present a challenge for modelling the redder wing of the Hβ line profile, but they are also useful to constrain the width of the narrow Hβ component. However, these adjoining lines are infrequently detected in the XQ-100 spectra with J133254+005250 presented in Figure 2.2 as one of the only two cases with detectable O III], alongside J101818+054822. Without the presence of the O III] lines, the decomposition of the total Hβ line profile into its broad and narrow emission may not be unique.

While all broad emission-line profiles are affected by embedded narrow absorption features, the effect that they have on the resulting model is more significant for C IV. In order to obtain more appropriate models of the intrinsic C IV broad emission profile, we apply an additional 2500 km s^{-1} box-width sigma-clip mask with a 3σ-threshold. Every contiguous masked region has a masked buffer window of 3 pixels, equivalent to 150 km s^{-1}, applied on each end. Most broad C IV emission profiles can be fit automatically, but some QSOs contain features which are visually inspected and masked.

If not accounted for, neighbouring lines can influence the measurement of the intrinsic C IV broad-line properties. In order to disentangle the C IV line model from its neighbours, we simultaneously model the broad Si IV λ1398Å, O IV λ1402Å, N IV] λ1486Å, He II λ1640Å, and O III] λ1663Å lines, using one broad component or one broad and one narrow component to constrain each neighbouring line. We find that the C IV line properties are not sensitive to whether narrow features, if present, in adjacent lines are modelled as a separate component. The neighbouring lines are only modelled in order to account for their influence on the C IV line properties. As such, we do not tabulate properties of the neighbouring lines in our catalogue.

For both Mg II and Hβ, the final emission-line properties, tabulated in Table 2.3, are determined as the average of properties measured from the resulting line models, created by applying in turn each of the four Fe II templates. We consider two primary sources of uncertainty in the measurement of emission-line and continuum properties. One source is the uncertainty from the various Fe II emission templates and another is the measurement uncertainty. We estimate the uncertainty from the Fe II template by independently modelling each spectrum with four models; VW01, T06, BV08, and M16 at UV wavelengths and BG92, T06, P22, and BV08 at optical wavelengths. Then we measure the line properties for a given model and quote the standard deviation. We also estimate the measurement uncertainty using a Monte Carlo approach by creating 50 synthetic spectra for individual target (e.g., Shen et al. 2011), where the flux at each pixel is resampled from a symmetric distribution with a standard deviation equivalent to the pixel flux error. We assume that the noise in the spectrum follows a normal distribution. After modelling all of the synthetic spectra independently and varying the Fe II template, the final measurement uncertainty is determined from these two sources added in quadrature. Each of the two sources contributes roughly equivalent uncertainty to emission-line FWHM, but the choice of Fe II emission template dominates the variance in the measured continuum luminosity.

For the C IV line properties, we use only the Monte Carlo uncertainty estimated by modelling 50 synthetic spectra. In this case, we do not consider the uncertainty from modelling different Fe II templates, because the Fe II emission is weak in this wavelength region and it is not used to define the continuum. The different realisations of the resampled spectra and their resulting line models help to capture degeneracies in the way that flux can be distributed between C IV and its neighbouring lines, propagating that degeneracy into the uncertainty of the line properties.

We provide a data quality flag, indicated by "Quality_Flag", for each emission-line model which is used to identify where the median SNR per 50 km s^{-1} resolution element of the data within the emission-line modeling region is below 20. We manually flag additional targets with the Mg II data quality flag to indicate poor quality fits or that significant residual telluric features are evident in the spectrum. As there are no targets below the SNR threshold for the data quality flag for C IV, we instead use the flag to indicate where we have manually adjusted the fit, by choosing more appropriate continuum windows or manually masking absorption features. Additionally, we flag targets, using "Hbeta_Truncation_Flag", for which the red wings of the Hβ profile is clearly truncated by the edge of X-shooter's NIR arm wavelength coverage, which would reduce the reliability of the line model. However, we do not

exclude flagged targets from further analysis and contextualisation of the XQ-100 sample in Section 2.5.

Figure 2.2 shows samples of emission-line models of SDSS J092041.76+072544.0 and J133254+005250, which are both lower redshift for our sample and contain the Hβ emission feature. Models of C IV, Mg II, and Hβ are presented. In this figure, both Mg II and Hβ models use an underlying T06 Fe II template. Examples of all line models of C IV, Mg II, and Hβ, showing the emission-line models in greater detail, are provided as online supplementary material, where models of Mg II and Hβ are separated by Fe II template. Due to the lack of a continuum redward of Hβ, we can only use the blue side to constrain the continuum.

2.4   Single-Epoch Virial Mass Estimate

We measure the black hole mass from single-epoch spectroscopic data using the virial estimate, which is a method routinely applied to QSO spectra (e.g., Vestergaard 2002; McLure & Jarvis 2002; McLure & Dunlop 2004; Greene & Ho 2005; Vestergaard & Peterson 2006). The model assumes that the motion of gas around the black hole is virialized and its dynamics are dominated by the central gravitational field. The velocity-broadened line profile measures the gas velocity and the nuclear continuum luminosity is used as a proxy for the radius of the BLR. The radius-luminosity (R-L) relationship is an empirical correlation derived from reverberation mapping experiments which tightly links the radius of the BLR to the continuum luminosity (e.g., Kaspi et al. 2000, 2005; Bentz et al. 2006, 2013). Common emission-lines used to estimate gas velocity include Hβ, C IV, and Mg II, but the Hβ line is redshifted out of the X-shooter NIR coverage at $z \gtrsim 4$. Instead, the Mg II emission-line profile is found to generally be correlated with Hβ and can be used as its substitute in single-epoch virial black hole mass estimates (e.g., Salviander et al. 2007; Shen et al. 2008; Wang et al. 2009; Shen & Liu 2012). Additionally, there are indications that the Mg II-based estimator is more reliable for QSOs with large (> 4000 km s^{-1}) Hβ FWHM (see Marziani et al. 2013). The following equation describes the single-epoch virial mass estimate,

$$\left(\frac{M_{\rm BH,vir}}{M_\odot} \right) = 10^{\rm a} \left[\frac{\lambda L_\lambda}{10^{44}\,{\rm erg\,s^{-1}}} \right]^b \left[\frac{{\rm FWHM_{line}}}{1000\,{\rm km\,s^{-1}}} \right]^2 , \qquad (2.3)$$

where λL_λ is the monochromatic luminosity of the QSO continuum, which we measure from the power-law continuum model, and FWHM$_{\rm line}$ is the measured line full-width half-maximum of the total broad line profile. We opt to use the FWHM
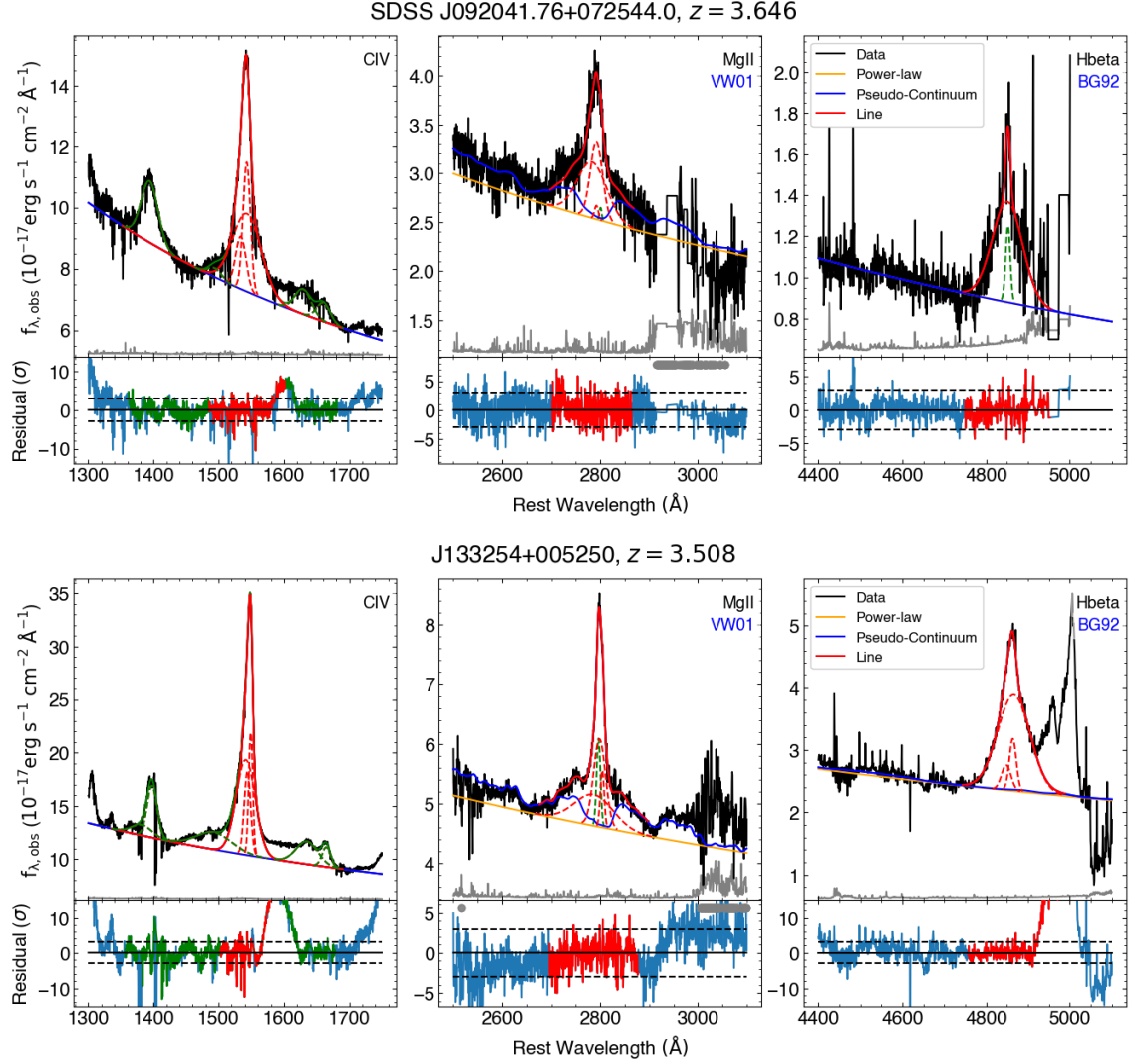
Figure 2.2: Example models of the C IV, Mg II, and Hβ emission-lines from SDSS J092041.76+072544.0 and J133254+005250. The spectroscopic data are plotted in black, its error spectrum in grey, and the power-law continuum is in orange. The error spectrum is shifted vertically such that the bottom of the panel represents zero flux error. The combined pseudo-continuum which includes a power-law and the Tsuzuki et al. (2006) Fe II template is plotted in blue. The red lines indicate the total line profile and the dashed lines are the multiple Gaussian decomposition. We show the narrow-line model with the green dotted line and in the C IV panel, green highlights the line models of neighbouring lines. The residuals are shown normalized by the flux error, σ, in order to represent the quantity minimised by the line-modelling algorithm, (data-model)/error. We represent $\pm 3\sigma$ in the residual panel with the dashed lines and we also show the result of the automated sigma-clipping in the C IV residual, where masked features remain in blue rather than red or green. Telluric absorption windows are denoted by the solid grey bar in the residual panel. These figures are available for all targets in the online supplementary material.

for the virial mass estimate instead of the line dispersion, i.e., the second moment of the line profile. Although the dispersion is well-defined for arbitrary line profiles and may have advantages over the FWHM (e.g., Fromerth & Melia 2000; Peterson et al. 2004; Collin et al. 2006; Rafiee & Hall 2011; Dalla Bontà et al. 2020), in practice, the line dispersion is sensitive to the wings of the line profile, which are naturally low in flux and can often be difficult to constrain independently from noise due to the accretion disk and Fe II continuum. We determine all line properties, including the FWHM of Mg II and Hβ, as the average of the measurements obtained from spectral decomposition using each of the all four Fe II templates. We further quantify the deviation of the measured black hole mass using each template in Appendix A.2.

The exponents (a, b) in Equation 2.3 depend on the choice of line and luminosity and are empirically calibrated by reverberation mapping experiments. For the Mg II line and a monochromatic luminosity at rest-frame 3000 Å, (a, b) are calibrated to the values (6.86, 0.5) in Vestergaard & Osmer (2009) and (6.74, 0.62) in Shen et al. (2011). On average, the differences between these different calibrations are 0.1 dex, but virial mass estimators show an intrinsic scatter of ~ 0.3 dex around their reverberation mapping counterparts (Dalla Bontà et al. 2020), while the reverberation-based estimates exhibit an intrinsic scatter of ~ 0.4 dex around the $M_{\rm BH} - \sigma_*$ relation (Bennert et al. 2021), meaning the virial mass estimates could have errors as large as ~ 0.5 dex. We adopt 0.5 dex as our single-epoch virial black hole mass uncertainty in this study. In this study, we use the Mg II-based calibration from Shen et al. (2011), which is anchored to a high-luminosity subset of local reverberation mapping determinations from Hβ, making it better suited to the XQ-100 sources. Other broad emission-lines present in our spectra can be used to obtain virial estimates of the black hole mass as well. Compared with the Mg II line, the C IV line is more likely to be affected by non-virial motions, such as the radiatively driven outflows (e.g., Proga et al. 2000; Saturni et al. 2018), making it potentially a biased black hole mass estimator (e.g., Baskin & Laor 2005; Sulentic et al. 2007; Shen et al. 2008). We provide a measure of the C IV blueshift, a signature of outflowing emission (Richards et al. 2011), in order to quantify how much the C IV-based black hole masses may be biased by non-virial components. The velocity shifts of C IV are measured relative to the systemic redshifts from López et al. (2016).

Table 2.1 presents the virial relations and specific calibrations used in this study for determining the black hole mass using C IV, Mg II, and Hβ emission-lines. Using the 3000 Å luminosity, we also estimate the bolometric luminosity by adopting a fixed bolometric correction factor of 5.15, which can lead to errors as large as 50%, or

Table 2.1: Virial relations used in this study (see Equation 2.3)

Emission-line	Luminosity	a	b	Ref
C IV	1450 Å	6.66	0.53	1
Mg II	3000 Å	6.74	0.62	2
Hβ	5100 Å	6.91	0.50	1

[1] Vestergaard & Peterson (2006) [2] Shen et al. (2011)

$\sim$0.3 dex, for individual QSOs (Richards et al. 2006).

The typical final measurement uncertainties are $\sim$240 km s^{-1} for the Mg II FWHM and 0.01 dex for the 3000 Å monochromatic luminosity, resulting in an average of 0.06 dex uncertainty in the Mg II black hole mass estimate. Similarly for Hβ, the average uncertainty is $\sim$640 km s^{-1} for the FWHM and 0.02 dex for the 5100 Å luminosity, resulting in 0.12 dex mean uncertainty in M_{BH}. Therefore, the measurement uncertainty for both estimates are well below the errors of the virial mass estimator. Without the additional uncertainties introduced by the multiple Fe II templates, the mean final measurement uncertainty in C IV FWHM is $\sim$130 km s^{-1} with negligible uncertainty in the 1450Å luminosity. The typical black hole mass uncertainty from the C IV virial estimator is thus 0.02 dex. However, line asymmetries and contribution from QSO outflows or disk winds should imply a greater uncertainty of C IV-based black hole masses.

2.5 Results and Discussion

For each of the 3 broad emission-lines (C IV, Mg II, and Hβ) used for virial black hole mass estimates in this study, we measure 6 properties of the broad line profile, described in Table 2.2. The FWHM of each line is used in the virial mass estimate. The line dispersion, Sigma, is the second moment of the line profile. We also measure the Blueshift, equivalent width (EW), and wavelength of the line profile peak (pWavelength). The blueshift is measured from the median wavelength bisecting the total flux of the line profile, and can be a useful indicator of QSO orientation, particularly with the C IV line (e.g., Richards et al. 2002; Yong et al. 2020). We measure the integrated line luminosity (iLuminosity) from the reconstructed broad emission-line profile. Ratios of the integrated luminosity may be used for chemical abundance estimates (e.g., Hamann & Ferland 1999; Hamann et al. 2002; Nagao et al. 2006), while the EWs may be used in studies of the Baldwin effect (e.g., Baldwin 1977; Patiño Álvarez et al. 2016). We present a sample of measured emission-line properties for 5 selected QSOs in Table 2.3, while the full table is available as online supplementary material.

Table 2.2: Description of measured properties for each broad emission-line.

Suffix	Description	Units
FWHM	Full-width half-maximum of profile	km s^{-1}
Sigma	Second moment of profile	km s^{-1}
Blueshift	Defined by the flux-bisecting wavelength	km s^{-1}
EW	Equivalent width in rest-frame	Å
pWavelength	Peak wavelength	Å
iLuminosity	Integrated log luminosity	erg s^{-1}

2.5.1   QSO Variability

Ever since the identification of the first QSOs, it has been recognized that QSOs are intrinsically variable (Matthews & Sandage 1963). Variations of QSO brightness occur on a large range of timescales from hours to years, where short timescales are typically associated with higher energy X-ray flux and longer timescales to the disk emission (Edelson et al. 2015; Lira et al. 2015). Models of QSO variability focus on its stochastic origin, comparing the ensemble variability structure function (SF) to damped random walk (DRW) models (e.g., Kelly et al. 2009; MacLeod et al. 2010; Kozłowski 2016; Suberlak et al. 2021).

Many studies have shown that the amplitude of QSO variability is anti-correlated with the QSO luminosity, with little apparent dependence on the redshift (e.g., Vanden Berk et al. 2004; MacLeod et al. 2010; Kozłowski 2016; Caplar et al. 2017). For a high-redshift and high-luminosity sample, such as XQ-100, the long-term asymptotic variability amplitude (SF$_\infty$) is measured to be low, from 0.1 mag (e.g., MacLeod et al. 2010; Suberlak et al. 2021) to 0.25 mag (e.g., Kozłowski 2016), where these studies made use of SDSS Stripe 82 (Jiang et al. 2014), an equatorial region imaged repeatedly during 2005, 2006, and 2007.

In this study, our sample of XQ-100 QSOs is flux calibrated to photometry observed at a separate epoch, thus our results are susceptible to QSO variability. In order to constrain variability in the XQ-100 sample, we crossmatch all sources with the Pan-STARRS DR2 detections table (Flewelling et al. 2020), removing all cases for which the number of multi-epoch i-band detections is less than 5. This results in a nearly complete sample of 82 QSOs, each with up to 33 independent i-band detections across a period of 3-5 years from 2009-2015. Models of QSO variability characteristic timescales typically find a best-fit parameter of a few hundred days for supermassive black holes in the rest-frame (e.g., MacLeod et al. 2010; Burke et al. 2021; Suberlak et al. 2021), so the Pan-STARRS detections cover little more than one rest-frame characteristic timescale. For this analysis, we estimate the observed vari-

ability amplitude using the structure function, $\mathrm{SF}_{\mathrm{obs}}(\Delta t) = \mathrm{rms}\left[\mathrm{m(t)} - \mathrm{m(t+\Delta t)}\right]$, where rms is the root-mean-square deviation. We calculate $\mathrm{SF}_{\mathrm{obs}}(\Delta t_{\mathrm{obs}})$ from the ensemble of 82 QSOs with multi-epoch photometric measurements by considering the distribution of Δm, the measured magnitude difference, for each pair of measurements separated by a time-lag, $\Delta t_{\mathrm{obs}} \sim 2, 3,$ or 4 years in the observed frame.

Using Pan-STARRS DR2 i-band detections, we find the ensemble variability amplitude of the XQ-100 sample to be $\mathrm{SF}_{\mathrm{obs}}(\Delta t_{\mathrm{obs}}) = (0.125, 0.132, 0.150)$ mag for observed frame $\Delta t_{\mathrm{obs}} \sim (2, 3, 4)$ years, which is consistent with a luminous QSO asymptotic long-term variability of $\mathrm{SF}_{\infty} < 0.20$ (MacLeod et al. 2010; Kozłowski 2016). The photometric calibrations we have used span an even wider timeframe relative to the spectroscopic observations taken between 2012–2014. Therefore, we assume the asymptotic variability as our uncertainty in the overall flux normalisation for each spectrum. A 0.20 mag variability amplitude between the X-shooter and photometric observation would manifest as < 0.1 dex uncertainty in the measured luminosities. As a consequence, we expect a black hole mass uncertainty up to ~0.05 dex may be present from variability.

2.5.2 XQ-100 Sample Properties

We now examine the black hole mass estimates from the C IV, Mg II, and Hβ-based virial estimators and contextualise the results. For both the Hβ and Mg II lines, we subtract the narrow component to obtain the pure broad emission profile (e.g., Kovačević-Dojčinović et al. 2017) and measure the broad-line properties. Figure 2.3 compares the three mass estimates to each other. As we do not exclude any flagged targets from further analysis and contextualisation, the C IV and Mg II comparison contains all 100 QSOs in the sample and the comparisons to Hβ are limited to 21 measurements. All three panels show data dispersed around the 1:1 relation denoted by the black dashed line, where the total sample variance is smaller than the adopted 0.5 dex uncertainty of the virial mass relation, which is shown for scale on the top-left of each plot. The mean differences and the standard deviation between black hole mass estimates are $\log\left(\mathrm{M}_{\mathrm{Mg\,II}}/\mathrm{M}_{\mathrm{C\,IV}}\right) = -0.05 \pm 0.34$, $\log\left(\mathrm{M}_{\mathrm{H}\beta}/\mathrm{M}_{\mathrm{C\,IV}}\right) = -0.12 \pm 0.36$, and $\log\left(\mathrm{M}_{\mathrm{Mg\,II}}/\mathrm{M}_{\mathrm{H}\beta}\right) = 0.06 \pm 0.22$. In the online supplementary table, we provide an averaged black hole mass estimate from all measured lines and determine a "Mbh_Flag" for when the averaged masses differ from the Mg II-based masses by more than 0.3 dex. Throughout the XQ-100 sample, 8% of QSOs are flagged in this way, and only one (SDSSJ1042+1957) has a Hβ virial mass estimate to shed light on the discrepancy between C IV and Mg II-based masses. For SDSSJ1042+1957, the Hβ-based mass estimate is much more consistent with

C IV than Mg II. The reason may be that the emission-lines are relatively narrow (FWHM~2000 km s^{-1}) compared to the rest of the sample, and only the Mg II line models consistently contain a narrow component.

Although the mass measurement for the XQ-100 sample relies on an extrapolation of the well-determined and lower luminosity Hβ reverberation mapping R-L relation (e.g., Bentz et al. 2013), we find all three virial estimators to remain consistent with each other within the measurement uncertainties in the high luminosity regime. This shows that the relative physical geometry of the three line-emitting regions does not change significantly with luminosity. Additionally, there are minimal systematic differences between our models to individual emission-lines and this increases our confidence in the resulting mass estimate.

In the case of outliers such as SDSSJ1202–0054, where $M_{H\beta} \sim 9.8$ and $M_{C\,IV} \sim 9.0$, or the inverse scenario for J1320299–052335, where $M_{H\beta} \sim 9.2$ and $M_{C\,IV} \sim 9.8$, their Hβ profiles are truncated and broad components are not well constrained. We present SDSSJ1202–0054 in additional detail in Appendix A.2. Other outliers, such as SDSS J074711.15+273903.3 which exhibits a > 1 dex mass difference between different lines, are characterised by relatively poor data quality in the wavelength regions surrounding the Mg II line, resulting in weaker constraints on the Fe II continuum model and a narrower emission-line FWHM. Residual telluric features from an insufficient telluric correction can corrupt the continuum model. Additionally, for targets with $3.8 \lesssim z \lesssim 4.2$, the Mg II line overlaps with a wide H$_2$O telluric absorption band at 1.4 μm which deteriorates the quality of its detection.

We compare the distribution of black hole masses and bolometric luminosities in XQ-100 to the SDSS DR7 QSO catalogue from Shen et al. (2011) in Figure 2.4, using mean masses from at least two virial mass estimates to represent the XQ-100 sample. The QSOs in the SDSS DR7 catalogue cover $0.06 < z < 5.47$ in redshift and their black hole masses are primarily based on the Mg II emission-line with the same virial mass calibration we have used, but $\sim$40% of the sample utilise either C IV or Hβ with calibrations from Vestergaard & Peterson (2006). The median black hole mass and bolometric luminosity for the SDSS DR7 QSO catalogue is $\log(M_{BH}/M_\odot) = 9.0^{+0.5}_{-0.6}$ and $\log(L_{bol}/\mathrm{erg\,s^{-1}}) = 46.4^{+0.5}_{-0.7}$, where the asymmetric dispersion is set by the 16% and 84% percentile.

We also identify the sub-sample of the SDSS DR7 QSO catalogue consisting of 3127 QSOs within the $3.5 < z < 4.5$ redshift range of the XQ-100 sample. Relative to the full catalogue of 104746 objects, the sub-sample has higher median black hole mass and luminosity with $\log(M_{BH}/M_\odot) = 9.3^{+0.5}_{-0.8}$ and $\log(L_{bol}/\mathrm{erg\,s^{-1}}) = 47.0^{+0.3}_{-0.3}$. The XQ-100 sample is more tightly distributed at the high-mass and high-luminosity tail
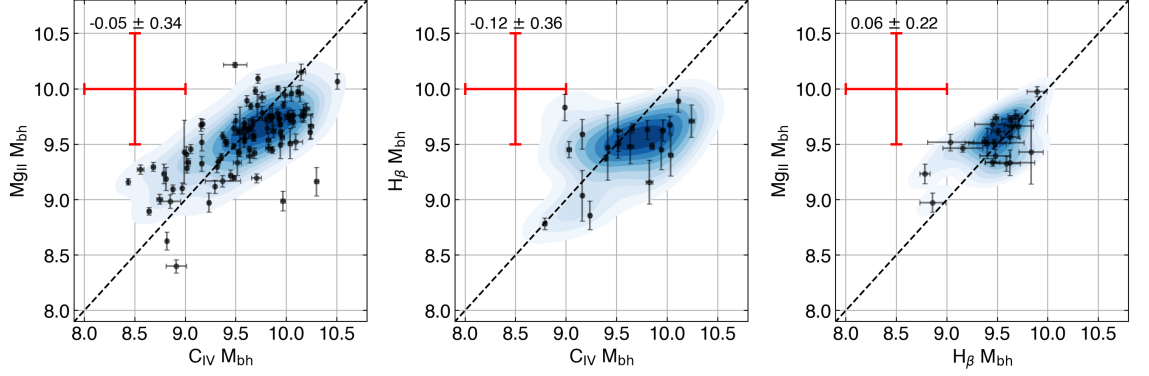
Figure 2.3: Comparison of virial black hole masses based on Mg II, C IV, and Hβ relations in Table 2.1. The blue shaded contours represent the two-dimensional continuous probability density distribution calculated with a kernel density estimator (Waskom 2021). Each subsequent contour level marks density iso-proportions increasing by an additional 10% up to 90% enclosed. The red error bars plotted on the top left of each plot show the extent of the 0.5 dex uncertainty, which is a conservative estimate of the uncertainty inherent in the virial mass estimation method. Comparisons between all three virial mass estimates are scatted around the 1:1 relation, indicated by the black dashed line. The mean and standard deviation listed in the top-left of each panel are based on the residual from the mass measure on the y-axis subtracted by the mass measure on the x-axis.

of the redshift-selected SDSS DR7 QSO sub-sample with $\log(M_{BH}/M_\odot) = 9.6^{+0.3}_{-0.4}$ and $\log(L_{bol}/erg\,s^{-1}) = 47.5^{+0.2}_{-0.2}$. A sub-sample (27%) of the XQ-100 sample exhibits mildly super-Eddington accretion rates. We also plot J2157−3602, one of the most luminous known QSO (Onken et al. 2020), which is at a comparable redshift ($z = 4.692$), with a black hole mass of $\log(M_{BH}/M_\odot) = 10.33$ and bolometric luminosity $\log(L_{bol}/erg\,s^{-1}) = 48.4$, measured with the same approach used here (Lai et al. 2023b). The full range of XQ-100 QSO properties is measured to span $\log(M_{BH}/M_\odot) = 8.6 - 10.3$ in black hole mass and $\log(L_{bol}/erg\,s^{-1}) = 46.7 - 48.0$ in bolometric luminosity, where over 85% of the sample lies within $\log(M_{BH}/M_\odot) = 9 - 10$ and $\log(L_{bol}/erg\,s^{-1}) = 47 - 48$.

We find that 55 of the targets have C IV measurements in the Shen et al. (2011) catalogue, which has also produced C IV-based virial mass estimates using the same Vestergaard & Peterson (2006) calibration. The mean and standard deviation of differences between the mass estimates from our work and from Shen et al. (2011) is $\log(M_{C\,IV}/M_{Shen}) = -0.07 \pm 0.18$ using the C IV-based mass from our sample and $\log(M_{avg}/M_{Shen}) = -0.12 \pm 0.24$ using the mean mass, which is a small systematic adjustment towards lower masses on average. We find no significant correlations between these mass differences and other measurable line properties.
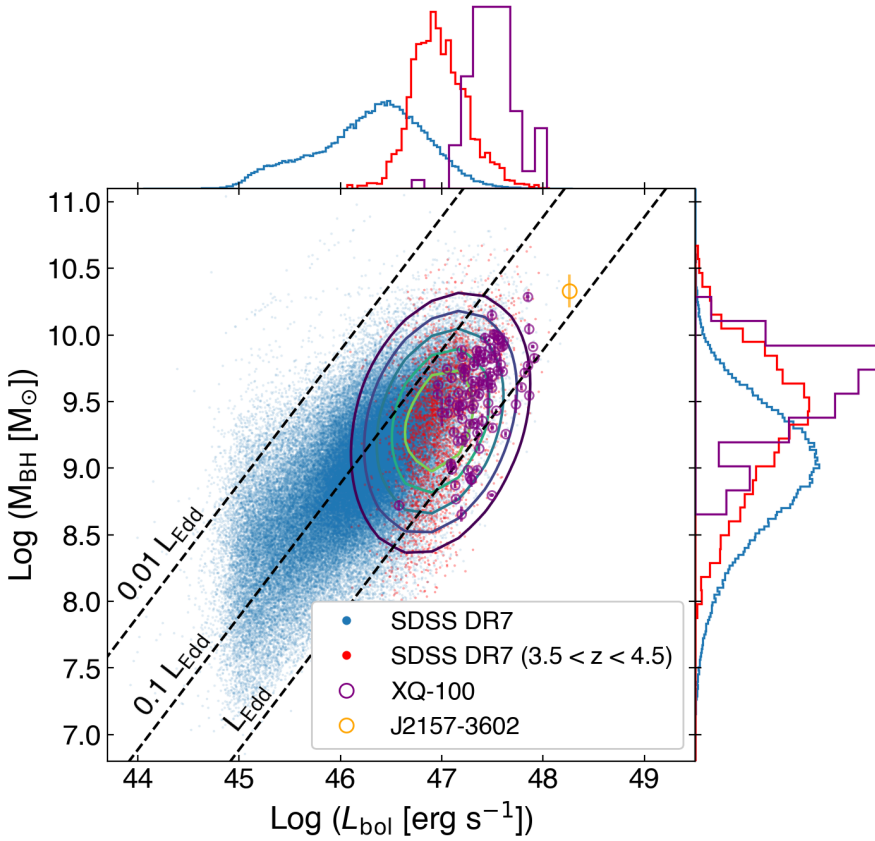
Figure 2.4: Distribution of XQ-100 black hole masses and luminosities compared to the SDSS DR7 QSO catalogue from Shen et al. (2011). The mean virial black hole mass measurements of XQ-100 are shown in purple and the SDSS DR7 data points are shown in blue. The contours delineate iso-proportions in the continuous probability distribution of the higher redshift SDSS sub-sample calculated with a kernel density estimator (Waskom 2021). Each contour encloses an additional 10% up to a 50% threshold. The black hole mass and bolometric luminosity histograms of the XQ-100 sample are normalised to the same area. Compared to the SDSS DR7 QSO catalogue, the XQ-100 sample occupies the high mass and high luminosity tail. The orange point is J2157−3602 ($z = 4.692$), one of the most luminous known QSOs (Onken et al. 2020).

Table 2.3: Measured emission-line properties of Mg II, C IV, and Hβ and continuum measurements for a selected sample of QSOs. Refer to Table 2.2 for the entry explanations. The reported uncertainties are sourced from the measurement and do not include the additional error of the virial mass method or QSO variability. The full table containing details for all XQ-100 QSOs is available as online supplementary material.

	Units	HB89 0000-263	PMN J0100-2708	BRI 0241-0146	J112634-012436	J1401+0244
OBJECT		HB89 0000-263	PMN J0100-2708	BRI 0241-0146	J112634-012436	J1401+0244
RA		00:03:22.79	01:00:12.47	02:44:01.83	11:26:34.42	14:01:46.52
Dec		-26:03:19.40	-27:08:52.10	-01:34:06.30	-01:24:38.00	02:44:37.70
redshift		4.125	3.546	4.055	3.765	4.408
Source_i		SkyMapper	SkyMapper	SkyMapper	SkyMapper	SkyMapper
imag	mag	17.075 ± 0.006	18.928 ± 0.026	18.099 ± 0.028	19.038 ± 0.071	18.395 ± 0.014
Source_J		VHS	VIKINGDR5	VHS	UKIDSS	UKIDSS
Jmag	mag	16.023 ± 0.008	17.590 ± 0.011	16.916 ± 0.015	18.053 ± 0.038	17.419 ± 0.032
CIV_FWHM	km s^{-1}	5275 ± 34	6103 ± 228	8387 ± 418	5746 ± 64	6048 ± 195
CIV_Sigma	km s^{-1}	3820 ± 91	2888 ± 367	3568 ± 229	3662 ± 134	3888 ± 276
CIV_Blueshift	km s^{-1}	1206 ± 45	1618 ± 110	1833 ± 228	2191 ± 44	821 ± 97
CIV_EW	Å	27.370 ± 0.270	23.930 ± 1.060	23.310 ± 1.100	23.270 ± 0.490	39.040 ± 0.450
CIV_pWavelength	Å	1543.380 ± 0.140	1540.830 ± 0.510	1540.860 ± 0.740	1539.290 ± 0.670	1545.790 ± 0.770
CIV_iLuminosity	erg s^{-1}	45.754 ± 0.004	44.833 ± 0.019	45.256 ± 0.021	44.819 ± 0.008	45.430 ± 0.005
CIV_PL_slope		-1.622 ± 0.008	-1.352 ± 0.020	-1.525 ± 0.016	-1.340 ± 0.025	-1.374 ± 0.008
MgII_FWHM	km s^{-1}	3396 ± 111	3599 ± 238	6378 ± 537	4574 ± 288	4319 ± 313
MgII_Sigma	km s^{-1}	3379 ± 113	2810 ± 297	3488 ± 386	3761 ± 75	3410 ± 245
MgII_Blueshift	km s^{-1}	217 ± 71	434 ± 171	-239 ± 100	-57 ± 132	-289 ± 103
MgII_EW	Å	21.620 ± 1.670	28.940 ± 3.150	40.640 ± 3.270	36.500 ± 2.280	37.360 ± 2.110
MgII_pWavelength	Å	2798.540 ± 2.310	2792.860 ± 0.990	2808.220 ± 4.840	2794.430 ± 0.650	2804.110 ± 0.450
MgII_iLuminosity	erg s^{-1}	45.210 ± 0.039	44.502 ± 0.059	45.083 ± 0.038	44.502 ± 0.028	44.961 ± 0.032
MgII_PL_slope		-1.339 ± 0.087	-1.145 ± 0.023	-1.519 ± 0.140	-1.685 ± 0.087	-1.400 ± 0.155
Hbeta_FWHM	km s^{-1}		5308 ± 924			
Hbeta_Sigma	km s^{-1}		3864 ± 637			
Hbeta_Blueshift	km s^{-1}		-634 ± 330			
Hbeta_EW	Å		86.440 ± 25.040			
Hbeta_pWavelength	Å		4856.340 ± 4.640			
Hbeta_iLuminosity	erg s^{-1}		44.494 ± 0.099			
Hbeta_PL_slope			-2.426 ± 0.395			
log_L1450	erg s^{-1}	47.522 ± 0.001	46.651 ± 0.001	47.090 ± 0.001	46.647 ± 0.001	47.038 ± 0.001
log_L3000	erg s^{-1}	47.312 ± 0.018	46.486 ± 0.021	46.907 ± 0.023	46.369 ± 0.013	46.824 ± 0.019
log_L5100	erg s^{-1}		46.240 ± 0.057			
logMBH_CIV	M$_\odot$	9.971 ± 0.006	9.636 ± 0.032	10.145 ± 0.043	9.582 ± 0.010	9.833 ± 0.028
CIV_Quality_Flag		1				
logMBH_MgII	M$_\odot$	9.855 ± 0.030	9.394 ± 0.059	10.152 ± 0.074	9.529 ± 0.055	9.762 ± 0.064
MgII_Quality_Flag				1		
logMBH_Hbeta	M$_\odot$		9.480 ± 0.154			
Hbeta_Quality_Flag			1			
logMBH_avg	M$_\odot$	9.913 ± 0.015	9.503 ± 0.056	10.148 ± 0.043	9.556 ± 0.028	9.797 ± 0.035
Mbh_Flag						
NIR_VIS_Flag						
Hbeta_Truncation_Flag			1			

2.6   Summary and Conclusion

Infrared echelle spectroscopic observations of high-redshift QSOs provide an oppor-
tunity to investigate their optical and ultraviolet atomic transitions. The XQ-100
legacy survey provides a high-quality sample of 100 QSOs in the redshift range of
$z = 3.5 - 4.5$ with high SNR, wide spectroscopic coverage between its three obser-
vation arms, and moderate resolving power.

In this study, we examine rest-frame UV and optical broad-emission-lines from all
100 QSOs in the XQ-100 legacy survey. We measure properties of the C IV, Mg II,
and Hβ emission-lines as well as the QSO continuum to estimate QSO luminosities
and black hole masses through virial relations. The main results of this study are
as follows:

- We measure the C IV and Mg II line for all 100 QSOs and the Hβ line for
  21 QSOs, using multiple templates to estimate the underlying Fe II emission.
  The virial mass estimate is based on the measured FWHM of all three broad
  emission-lines and the continuum luminosity measured near each respective
  emission-line at 1450, 3000, and 5100 Å. We provide an averaged black hole
  mass estimate from all measured emission-lines for each QSO in the online sup-
  plementary table[2] and determine the black hole masses of the XQ-100 sample
  to be $\log\left(M_{\mathrm{BH}}/M_{\odot}\right) = 8.6 - 10.3$. A comparison of mass measurements be-
  tween the Mg II virial mass estimate and the C IV and Hβ virial estimates show
  a mean difference and standard deviation of -0.05 ± 0.34 dex and 0.06 ± 0.22
  dex, respectively, which are both well below the 0.5 dex uncertainty of the
  virial estimate. There is a general consistency between the mass estimates
  derived from the C IV, Mg II, and Hβ broad emission lines. Using a fixed
  5.15 bolometric correction factor applied to the 3000 Å continuum luminos-
  ity, we estimate the bolometric luminosity range of the XQ-100 sample to be
  $\log\left(L_{\mathrm{bol}}/\mathrm{erg\,s^{-1}}\right) = 46.7 - 48.0$.

- Compared to the SDSS DR7 QSO catalogue, QSOs in the XQ-100 legacy
  survey occupy the high-mass and high-luminosity tail of the distribution. A
  sizable sub-sample consisting of 27% of the XQ-100 QSOs are accreting at
  mildly super-Eddington rates.

- For each broad emission-line from C IV, Mg II, and Hβ, we measure 6 properties
  from the broad line profile and release the full set of measurements as online
  supplementary material. The measured properties of each line include the
  full-width half maximum (FWHM), line dispersion, blueshift, equivalent width
  (EW), wavelength of the peak line profile, and integrated luminosity. We also

release example figures of all line models in the sample as online material[2].

Characterising basic properties of the XQ-100 QSOs enables a variety of follow-up research in QSO astrophysics, from chemical enrichment history using emission-line diagnostics to black hole orientation and QSO outflows. As a sample of some of the most luminous QSOs in redshift $3.5 < z < 4.5$, the XQ-100 targets are among most massive, rapidly accreting black holes in the early universe and likely harbour the most massive and active host galaxies as well. These targets can potentially be used to further investigate the relationship between black holes and their host galaxies in the high redshift universe.

Acknowledgements

---

[2]also available at https://github.com/samlaihei/XQ-100

Data Availability

The data underlying this article will be shared on reasonable request to the corresponding author. The post-processed spectra, supplementary table, and figures can be downloaded from a GitHub repository: https://github.com/samlaihei/XQ-100.

XQz5: A new ultraluminous $z \sim 5$ quasar legacy sample

Context

Preamble

The bright end of the high-redshift quasar luminosity function is continuously updated as newer, more complete quasar surveys place stronger constraints on the comoving spatial density of extreme quasars. In this chapter, we present spectroscopic follow-up observations of the brightest quasars within a highly complete range of redshifts from $4.5 < z < 5.3$, using the VLT/X-shooter, SOAR/TripleSpec4.1, and ANU2.3m/WiFeS. We apply the spectral modelling techniques presented in Chapter 2 to constrain the black hole mass from the Mg II $\lambda 2799$ emission line, publicly releasing all of the spectroscopic data and line measurements. This sample contains the most luminous quasars in its redshift range, bridges the redshift gap between other high-redshift X-shooter quasar samples, and has notable legacy significance with widespread community value. With its well-defined completeness adopted from the parent survey and robustly measured black hole properties, this sample also forms the basis of our investigation into quasar demographics at $z \sim 5$ in Chapter 4.

Abstract

Bright quasar samples at high redshift are useful for investigating active galactic nuclei evolution. In this study, we describe XQz5, a sample of 83 ultraluminous quasars in the redshift range $4.5 < z < 5.3$ with optical and near-infrared spectroscopic observations, with unprecendented completeness at the bright end of the quasar luminosity function. The sample is observed with the Southern Astrophysical Research Telescope, the Very Large Telescope, and the ANU 2.3m Telescope, resulting in a high-quality, moderate-resolution spectral atlas of the brightest known quasars within the redshift range. We use established virial mass relations to derive the black hole masses by measuring the observed Mg IIλ2799Å emission-line and we estimate the bolometric luminosity with bolometric corrections to the UV continuum. Comparisons to literature samples show that XQz5 bridges the redshift gap between other X-shooter quasar samples, XQ-100 and XQR-30, and is a brighter sample than both. Luminosity-matched lower-redshift samples host more massive black holes, which indicate that quasars at high redshift are more active than their counterparts at lower-redshift, in concordance with recent literature.

3.1   Introduction

Radiation released by actively accreting supermassive black holes can be observed across vast distances, making active galactic nuclei (AGN) and quasars some of the most luminous known non-transient astrophysical objects. Due to their potential for extreme luminosities, quasars can be observed at very early cosmic periods, into the epoch of reionisation, the last major phase change of the universe, at $z \gtrsim 6$ (e.g., Wu et al. 2015; Jiang et al. 2016; Reed et al. 2019; Shen et al. 2019a; Yang et al. 2021; D'Odorico et al. 2023). The highest redshift quasars are discovered up to $z \sim 7.5$ (e.g., Bañados et al. 2018; Yang et al. 2020; Wang et al. 2021), within the first 700 Myr since the Big Bang. Powered by supermassive black holes (SMBHs), these quasars provide stringent constraints on the size of black hole seeds and their mass evolution (e.g., Inayoshi et al. 2020; Volonteri et al. 2021; Fan et al. 2022).

Large samples of high quality luminous quasar spectra at high redshift can have significant value to the scientific community. Previous large programmes using the Very Large Telescope (VLT) instrument X-shooter (Vernet et al. 2011) have produced high quality echelle spectra of 100 quasars at redshift $3.5 < z < 4.5$ (XQ-100, López et al. 2016) and 30 quasars at redshift $5.8 < z < 6.6$ (XQR-30, D'Odorico et al. 2023). Other large samples at a similar redshift include 40 quasars at $4.6 < z < 4.9$ with Gemini/NIRI or VLT/SINFONI H-band spectroscopy (Trakhtenbrot et al. 2011)

and 50 quasars at $5.6 < z < 6.4$ with Gemini/GNIRS observations (Shen et al. 2019a).

Such samples have already been used for a wide variety of science cases. Sub-damped or damped Ly α systems in the XQ-100 sample were used to study the cosmic density of neutral gas (Sánchez-Ramírez et al. 2016; Berg et al. 2019). By tracing metal absorbers along the quasar line of sight, these systems have also been used to probe metal abundances in the host galaxy (Perrotta et al. 2016, 2018; Berg et al. 2016, 2021). In addition, cosmological questions were addressed through constraints of the matter power spectrum from the Ly α forest (Iršič et al. 2017; Yèche et al. 2017). Similarly, the XQR-30 sample, which is strategically selected from the reionisation epoch, has been the subject of numerous recent studies constraining reionisation models (Bosman et al. 2022; Zhu et al. 2021, 2022b), measurements of the quasar proximity zone (Chen et al. 2022; Satyavolu et al. 2023b), identification of metal absorption lines (Davies et al. 2023), and analyses of the black hole environment (Bischetti et al. 2022; Lai et al. 2022). Further studies are made possible by the public release of spectroscopic data with superior quality and wide spectral coverage.

In this paper, we present "XQz5", a new sample of 83 ultraluminous quasars at the redshift range $4.5 < z < 5.3$, an important epoch for studying precursors of modern massive galaxies in the post-reionisation universe. The motivation is to build a sample that is highly complete at the bright end, selecting from the brightest known Southern quasars, which reflect the most massive and rapidly accreting SMBHs. The redshift range was inherited from the sensitivity range of the SkyMapper search which formed the parent sample (Wolf et al. 2020; Onken et al. 2022a). Similar to XQ-100 and XQR-30, we observed many of our targets with the X-shooter instrument on the VLT, but we supplement our sample with TripleSpec4.1 (Wilson et al. 2004a) near-infrared (NIR) spectroscopic data from the Southern Astrophysical Research Telescope (SOAR). Designed as a legacy sample, this paper is accompanied by the public release of all reduced data products. The high SNR, moderate resolution, and wide spectral coverage of the X-shooter targets suggest that there is potential to exploit the data on the XQz5 targets for similar scientific objectives as XQ-100 and other high-redshift samples.

The NIR spectroscopic data collected for the XQz5 sample is necessary to study rest-frame UV emission-lines of high redshift quasar, which can be used to constrain metallicities in the broad-line region and black hole properties. It has been observed that in the local universe, black hole and galactic bulge masses are strongly correlated (the $M_{BH} - M_{bulge}$ relation; e.g., Marconi & Hunt 2003; Häring & Rix 2004; Greene

et al. 2010), suggesting co-evolution between host galaxies and their central SMBHs. Characterising the black hole properties at high redshifts is thus valuable for studies of how the galactic and black hole properties came to be tightly correlated (e.g., Croton et al. 2006; McConnell & Ma 2013; Terrazas et al. 2020). Therefore, in this study, we measure the Mg II $\lambda 2799$Å emission line which is observed in all 83 targets. Compared to emission lines further in the rest-frame UV which often exhibit blueshifted profiles (e.g. Shen et al. 2016), the Mg II line is typically a better tracer of the galaxy redshift at high redshifts. Using established virial mass relations and bolometric luminosity corrections, we provide robust estimates of the intrinsic black hole properties for the XQz5 sample measured in homogeneous manner.

We have organised the content of the paper as follows: in Section 3.2, we describe our z$\sim$5 quasar sample and observations. In Section 3.3, we describe the approach we adopt in modelling the quasar continuum and Mg II emission-line. We further discuss how properties of the emission-line can be used to characterise the black hole, using the single-epoch virial mass estimate. In Section 3.4, we discuss our results and contextualise our sample. We summarize and conclude in Section 3.5. Throughout the paper, we adopt a flat ΛCDM cosmology with $H_0 = 70$ km s^{-1} Mpc^{-1} and $(\Omega_{\mathrm{m}}, \Omega_{\Lambda}) = (0.3, 0.7)$. All referenced wavelengths of emission-lines are measured in vacuum.

3.2   Sample Description and Observation

Our sample is based on a collection of ultraluminous ($M_{145\mathrm{nm}} < -27.5$ AB mag) Southern quasars with unprecedented completeness from Onken et al. (2022a, hereafter O22). Using the SkyMapper Southern Survey (SMSS; Wolf et al. 2018b; Onken et al. 2019), O22 identified a sample that is 95% complete down to $z_{\mathrm{AB}} = 18.5$ mag, with an overall completeness of $\sim$80% (See Fig. 4 of O22). The completeness estimates are based on the number of known quasars eliminated by the selection criteria and the linearity of the log source number counts. This implies a 50% higher completeness at bright magnitudes than a previous reference sample from the Sloan Digital Sky Survey (SDSS) (Yang et al. 2016). These spectroscopically confirmed quasars contain some of the most massive and fastest growing SMBHs in the early Universe. About 8.5 ± 2.9% of the sample can be considered radio-loud, confirming a decrease in the radio-loud fraction with increasing redshift (Lah et al. 2023). We do not comment on the X-ray properties of the sample, but with the imminent publication of the first data release from the eROSITA All-Sky Survey (Predehl et al. 2021), a systematic investigation will become possible.

Our sample, with spectroscopic redshifts of $4.5 < z < 5.3$, serves as a high-luminosity extension of the Trakhtenbrot et al. (2011, hereafter T11) sample, partially bridging the gap between the XQ-100 Large Programme (López et al. 2016) at lower redshifts ($3.5 < z < 4.5$) and the XQR-30 Large Programme (D'Odorico et al. 2023) at higher redshifts ($5.8 < z < 6.6$). Comparisons of the quasar properties between these samples can reveal evolutionary trends in SMBH growth. We select the brightest quasars from our parent sample while aiming for a uniform distribution across redshift and perform follow-up observations with the spectroscopic instruments: SOAR/TripleSpec4.1, VLT/X-shooter, and ANU2.3m/WiFeS. All of the extracted spectra are made publicly available in a GitHub repository[1].

3.2.1 SOAR/TripleSpec4.1

TripleSpec4.1 (Wilson et al. 2004a) is a fixed-assembly cross-dispersed long-slit near-infrared imaging spectrograph with slit dimensions of 1.1" by 28" mounted on SOAR, a 4.1m aperture telescope situated in Cerro Pachón, Chile. The instrument covers a simultaneous wavelength range from 0.94 to 2.47 μm, with spectral resolution R~3500.

We observed 26 targets in the classical observing mode over 9 nights between 2021-08-22 and 2022-05-15, under the programme IDs 2021B-0036 and 2022A-389756. Using the standard ABBA observing strategy, the total integration time for each target was calculated to achieve a signal-to-noise ratio (SNR) over 20 around the Mg II emission-line. For targets in the H-band magnitude range $15.8 < H < 17.0$, the integration times ranged from 2880s to 12480s between the brightest and faintest targets. We carried out the data reduction and extraction of the infrared spectra using an adaptation of the `Spextool` IDL package (v4.1) (Cushing et al. 2004), specifically designed for TripleSpec4.1. The post-extraction flux calibration and telluric correction were performed with the `xtellcorr` IDL package (Vacca et al. 2003) using standard stars observed immediately before and after each target, which are well matched in airmass. The resulting mean $SNR_{2600} \simeq 15.8$ per 40 km s^{-1} pixel measured from the median SNR in the 100Å window between 2550–2650Å in the continuum region near the Mg II line.

3.2.2 VLT/X-shooter

VLT's X-shooter instrument (Vernet et al. 2011) is a multi-wavelength, medium resolution spectrograph with three spectroscopic arms: UVB (300–560nm), VIS

---

[1]https://github.com/samlaihei/XQz5

(550–1020nm), and NIR (1020–2480nm). We proposed observations for 40 target quasars under the programme IDs 108.22H9.001, 109.23D1.001, and 109.23D1.002. Observations were completed for 32 targets in "service mode" between 2021-10-20 and 2022-08-12, 13 of which were also observed with TripleSpec4.1. We also include one target, J2335–5901, which was observed under programme ID 0104.A-0410(A). Under service mode, we defined Observation Blocks (OBs) containing the instrument setup and requested weather conditions.

For the instrument setup, the adopted slit widths are 1.6" in the UVB, 1.5" in VIS, and 1.2" in NIR. Each slit width is the widest slit available for science observations to maximise the signal while providing a nominal resolving power of 3200, 5000, and 4300, respectively. The integration time for each target is calculated to achieve SNR > 20 around the Mg II line in the NIR arm after resampling the extracted spectra into 50 km s^{-1} velocity bins. Of the executed OBs, 71% were within observing condition specifications with an additional 5% almost within specifications, resulting in repeat observations of two targets (J091656–251146 and J121921–360933). Where the executed OBs did not meet the desired observing specifications, we manually check the data quality for each individual frame and find that despite the lower quality, all of the data could still be used for further analysis. The total VLT time investment for these new targets is 22 hours. We add two additional targets from the 0104.A-0410(A) programme which invested 0.8 hours of on-target exposure time for J215728.21–360215.1 at $z = 4.692$ and 1.6 hours for J233505–590103 at $z = 4.53$, resulting in high quality spectra (SNR$_{2600}$ ∼40/pixel).

We further supplement our sample with additional X-shooter data from the ESO Science Archive Facility of 36 targets, originating from the programmes 084.A-0574(A), 084.A-0780(B), 087.A-0125(A), 094.A-0793(A), 098.A-0111(A). We selected these additional targets from the Million Quasars (Milliquas) v7.7 Catalogue[2] (Flesch 2021), most of which are bright quasars in the redshift range $5.0 < z < 5.3$ concentrated at more northern declinations as seen in Figure 3.1. The targets from 084.A-0574(A), 087.A-0125(A), and 094.A-0793(A) were observed with slit dimensions such that the effective resolution is R = 8900, 5600 for the VIS and NIR arms, respectively. Targets from 098.A-0111(A) and 0100.A-0243(A) were observed with higher resolution NIR arm, where R = 8900, 8100, and BR 1202–0725 from 084.A-0780(B) was observed with R = 11400, 8100.

Due to the high sky-background level, extraction of the NIR spectra can be non-trivial. Although ESO provides a pipeline for X-shooter data reduction (Freudling et al. 2013), we find that the post-extraction spectra often exhibited significant sky-

---

[2]https://quasars.org/milliquas.htm
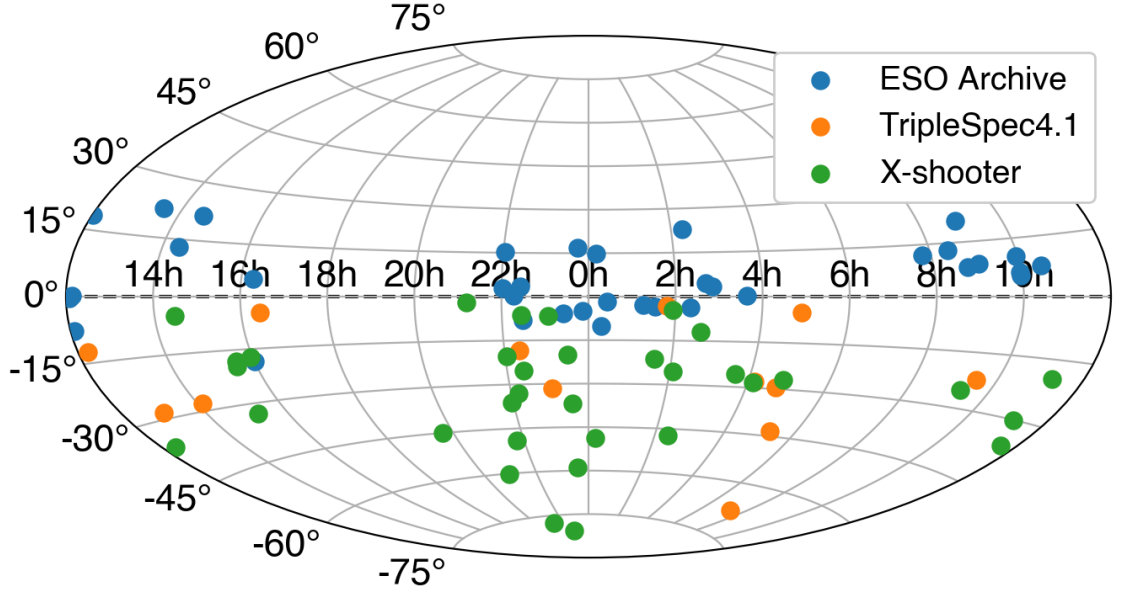
Figure 3.1: Spatial distribution of the 83 ultraluminous quasars of XQz5 in the equatorial coordinate system. The quasars are colour-coded according to the source of the data presented here. Of the 32 X-shooter targets marked in green, 13 are also observed with TripleSpec4.1 and one (J222612–061807) was later found to have existing data in the ESO Archive.

subtraction residuals. Consequently, we opted to use the semi-automated reduction procedure implemented in the `PypeIt` package (Prochaska et al. 2020a), which contains code infrastructure for X-shooter data reduction. The initial flux calibration is derived from a standard star typically observed within a day of the observation. However, the standard is not often matched to the airmass of our targets, so we later rescale the spectra to the observed photometric magnitudes as described in Section 3.2.4. Furthermore, the telluric correction algorithm in `PypeIt` utilises a large telluric grid to find the best-fitting atmospheric model in place of deriving the correction from a telluric standard.

After the extraction of the 1D spectra of all targets observed with X-shooter, the resulting mean $SNR_{1450} \simeq SNR_{2600} \simeq 16.8$ per pixel measured from the median SNR between 1400–1500Å and 2550–2650Å.

3.2.3 ANU2.3m/WiFeS

The Wide Field Spectrograph (WiFeS) instrument (Dopita et al. 2007, 2010) installed on the fully automated Australian National University 2.3m telescope is a double-beam integral field spectrograph with a wavelength coverage of 330–930 nm. For this sample, WiFeS observations are conducted on the 13 targets without

optical coverage, using R = 3000 gratings. The data reduction is performed with
the standard Python-based pipeline, `PyWiFeS` (Childress et al. 2014) and extraction
of the 1D spectra from the IFU data cubes was performed with `PySpecExtract`[3].
The resulting mean SNR_{1450} = 6.1 per 50 km s^{-1} pixel. We re-calibrate the
flux normalisation using optical photometry with the same method applied for
X-shooter data as described in the folllowing Section 3.2.4.

In Table 3.1, we list properties of all targets and extracted spectra in our sample.
The columns from left to right are the target name, coordinates, redshift derived
from the peak of the Mg II emission-line (the details of which is presented in Section
3.3), programme ID, Milky Way extinction colour excess (see Section 3.2.4), mag-
nitudes in the $i,\ z,\ H$-bands and signal-to-noise ratios in 100Å windows centered at
1450 and 2600Å. The optical i and z-band photometry are obtained from SMSS DR4
(Onken et al. in prep.), if available, or Pan-STARRS DR1 (Chambers et al. 2016).
The near-infrared H-band photometry is from one of various surveys: VISTA Hemi-
sphere Survey (VHS; McMahon et al. 2013) DR5/6, VISTA Kilo-degree Infrared
Galaxy Survey (VIKING; Edge et al. 2013) DR2, UKIRT Infrared Deep Sky Sur-
vey (UKIDSS; Lawrence et al. 2007) DR9, or Two Micron All-Sky Survey (2MASS;
Skrutskie et al. 2006). In some cases, the H-band magnitude is interpolated (using
the relations from O22) from the VHS J and K-bands or the SMSS/Pan-STARRS
z and ALLWISE/CatWISE2020 $W1$ bands (Wright et al. 2010; Cutri et al. 2013;
Marocco et al. 2021). The survey sources of the optical and near-infrared pho-
tometry are indicated in the supplementary table. The full table, extended with
associated uncertainties, is available online as supplementary material.

3.2.4   Post-Processing

Our combined sample consists of 83 ultraluminous quasars based on new observa-
tions from SOAR/TripleSpec4.1 and VLT/X-shooter alongside additional X-shooter
data from the ESO Science Archive Facility. These quasars are found in the redshift
range $4.5 < z < 5.3$ with H-band magnitudes $15.44 < H < 18.83$ and their sky
distribution in equatorial coordinates is presented in Figure 3.1. Here, we describe
the post-processing steps taken to clean the spectra and prepare them for continuum
and emission-line modelling.

1. We transform the spectrum to the rest-frame by estimating an initial redshift
   from the peak of the observed Mg II data. We then apply a per-pixel SNR
   floor of 5 and mask all data below.

---

[3]https://github.com/nishamrutha/PySpecExtract

2. We apply a sigma-clipping mask across box-widths of 40 pixels, using a 3σ threshold to remove narrow absorption features and noise above 3σ. Narrow absorption features, if left in the spectrum, can affect the modelling of the quasar continuum or intrinsic line profiles of broad emission lines.

3. The spectra are resampled from their original post-extraction resolution ($13.5/40$ km s^{-1} for X-shooter NIR/TripleSpec4.1 and $< 11.6/50$ km s^{-1} for X-shooter VIS/WiFeS) into a common wavelength grid from rest-frame 1050–3600Å using a flux-conserving algorithm, SPECTRES (Carnall 2017), with a velocity resolution of 50 km s^{-1} for each bin. Rebinning and consolidating the flux in 50 km s^{-1} bins increases the SNR of the spectral data, most notably for the X-shooter data, and standardises the output from different spectroscopic instruments for continuum and emission-line modelling.

4. As the initial X-shooter flux calibration is based on a standard that is not reliably observed in the same night or under similar conditions, we independently recalibrate the X-shooter spectra to photometry. We integrate the observed spectroscopic data over the bandpass transmission curves obtained from the SVO Filter Profile Service[4] (Rodrigo & Solano 2020) and scale the flux to match the observed magnitudes. For the X-shooter VIS arm, we use the inverse variance to weight the flux calibration between the i-band and z-band. We then scale the X-shooter NIR arm according to the calibration of the VIS arm, enforcing continuity between arms. Targets observed with TripleSpec4.1 are already calibrated to an airmass-matched standard observed immediately before or after the quasar, so we take its original calibration to be most reliable. If there is TripleSpec4.1 near-infrared spectroscopic data available for an object, then we use the TripleSpec4.1 spectrum to scale all other spectroscopic data. If we calibrated TripleSpec4.1 spectra to H-band photometry taken at a variety of different epochs, we find that the median absolute correction for the TripleSpec4.1 sample to be 15% of its original flux calibration with an additional 15% RMS deviation. In some cases, prior to the rescaling and splicing of the optical and near-infrared spectra, a discontinuity can be observed from the combined effects of chromatic slit losses and quasar variability. We note that the 15% median absolute calibration discrepancy would result in < 0.1 dex uncertainty in the estimated continuum luminosity.

5. We correct for Milky Way extinction by adopting $R_{\rm v} = 3.1$ with the Fitzpatrick (1999) extinction curve and colour excess from the Schlegel, Finkbeiner & Davis (SFD; Schlegel et al. 1998) extinction map. We then apply a suggested

---

[4]http://svo2.cab.inta-csic.es/theory/fps/

14% recalibration to the colour excess, $E(B - V) = 0.86 \times E(B - V)_{\text{SFD}}$, informed by fits to the blue tip of the stellar locus (Schlafly et al. 2010). We assume no further dust extinction from the quasar host galaxy, following the common practice for similar studies of quasar line properties, including Shen et al. (2011) – which defines our mass calibration (see Section 3.3.2) – and others (e.g., Rakshit et al. 2020; Wu & Shen 2022; Lai et al. 2023a). Furthermore, luminous quasars are intrinsically less likely to exhibit notable dust extinction, with the majority of quasars consistent with null colour excess (e.g., Krawczyk et al. 2015). Due to the ultraluminous nature of the quasars in this sample, we do not account for the starlight contribution in the spectra, which is insignificant compared to the AGN.

After post-processing of our sample, we find the median SNR = 27.2 per 50 km s^{-1} velocity bin measured from the median SNR between 2700–2750Å and 2850–2900Å. In Figure 3.2, we show our sample, XQz5, compared to other high-quality X-shooter programmes, XQ-100 and Enlarged XQR-30 Plus (E-XQR-30+), which are concentrated on lower and higher redshifts, respectively. The E-XQR-30+ sample is composed of the core 30 quasars from XQR-30 and supplemented with high-redshift literature quasars with NIR spectra as described in D'Odorico et al. (2023); in addition for this paper, we have extended E-XQR-30+ with 112 quasars listed in the Fan et al. (2022) review paper. We note that the gravitationally lensed object QSOJ0439+1634 has been removed. We also show quasars from T11, which is a lower luminosity sample at a similar redshift range, and we plot three notable quasars: J0529–4351 (Onken et al. 2023), J2157–3602 (Wolf et al. 2018a; Onken et al. 2020), and J0100+2802 (Wu et al. 2015), the three most luminous quasars in the respective redshift ranges of each sample, of which we include J2157–3602 in our sample. Other luminous quasar samples such as ELQS (Schindler et al. 2017) and QUBRICS (Cristiani et al. 2023) also reach up to $z \sim 5$, but they have not been observed with a comparable broad spectral coverage as the X-shooter samples, which include observed-frame near-infrared.

We provide all of the observed-frame telluric-corrected spectra in the supplementary material. The spectra are provided in the native resolution and do not include the post-processing steps described in this section, except for the flux re-calibration. Raw data files are available in their respective data archive facilities, the ESO Science Archive Facility[5] and NOIRLab Astro Data Archive[6].

---

[5]http://archive.eso.org/cms.html
[6]https://astroarchive.noirlab.edu/
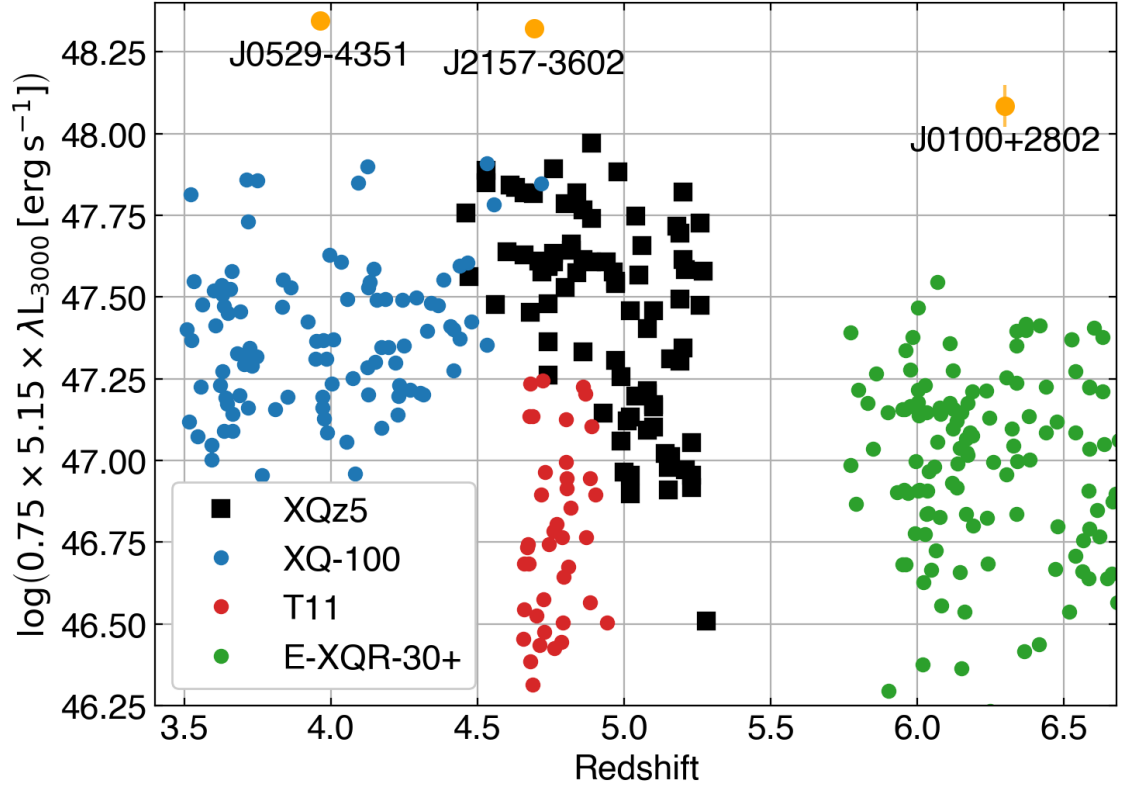
Figure 3.2: Our sample, XQz5 (black), flanked by two other X-shooter programmes, one at lower redshift, XQ-100 (red), and one at higher redshift, E-XQR-30+ (orange). XQz5 serves as a high luminosity extension of the SDSS-selected T11 sample (green) at a similar redshift, where the luminosity is measured from the 3000Å monochromatic flux of the power-law continuum. The three named targets are the brightest known quasars in the three redshift ranges, with J0529–4351 and J2157–3602 as the current first and second most luminous known quasars, respectively.

Table 3.1: Properties of the quasars and their spectra in the XQz5 sample. The text contains a description of the table columns.

Name	RA (J2000)	Dec (J2000)	$z_{\text{Mg\,II}}$[a]	PID	E(B-V)	i_{AB}[a]	z_{AB}[a]	H_{Vega}[a]	SNR_{1450}	SNR_{2600}
SDSS J001115.23+144601.8	00:11:15.23	14:46:01.81	4.97	X_3	0.045	18.28	18.10	16.53	122.8	63.5
J001225−484830	00:12:25.02	−48:48:30.10	4.62	X_8	0.007	17.80	17.72	16.01	11.6	13.6
SDSS J001714.67−100055.4	00:17:14.68	−10:00:55.43	5.02	X_5	0.034	19.57	19.62	17.57	14.8	12.2
SDSS J002526.84−014532.5	00:25:26.84	−01:45:32.52	5.06	X_5	0.027	17.97	18.07	16.26	16.7	16.9
SDSS J011546.27−025312.2	01:15:46.27	−02:53:12.24	5.08	X_5	0.031	20.05	19.82	17.98	10.9	4.5
SDSS J013127.34−032100.1	01:31:27.35	−03:21:00.07	5.20	X_5	0.029	18.28	18.01	16.00	14.3	19.9
J013539−212628	01:35:39.29	−21:26:28.39	4.90	X_8	0.015	17.97	17.82	15.84	14.0	23.0
J014742−030248	01:47:41.53	−03:02:47.88	4.80	T_1	0.021	18.42	18.00	16.29	4.7	12.9
J015619−044140	01:56:18.99	−04:41:39.84	4.93	X_8	0.020	19.20	19.06	17.27	8.9	10.8
J020437−252315	02:04:36.67	−25:23:15.44	4.87	X_8,T_1	0.012	18.29	18.35	16.59	6.2	10.2
SDSS J021624.16+230409.4	02:16:24.16	23:04:09.47	5.23	X_5	0.094	20.11	19.74	18.04	10.7	8.1
SDSS J022112.62−034252.2	02:21:12.62	−03:42:52.24	5.02	X_5	0.019	19.42	19.59	17.75	11.5	5.5
J022307−470902	02:23:06.76	−47:09:02.73	5.00	X_8	0.016	17.98	17.72	15.94	10.7	19.5
J023649−114734	02:36:48.57	−11:47:33.58	5.20	X_9,T_1	0.021	18.80	18.37	16.84	10.8	15.9
SDSS J024152.92+043553.4	02:41:52.92	04:35:53.46	5.19	X_6	0.042	19.86	19.76	17.63	11.0	8.5
SDSS J025121.33+033317.4	02:51:21.33	03:33:17.42	4.99	X_5	0.058	19.29	19.31	17.35	14.7	15.9
J033703−254832	03:37:03.06	−25:48:31.55	5.11	X_8	0.013	18.63	18.39	16.59	19.2	27.2
SDSS J033829.30+002156.2	03:38:29.31	00:21:56.26	5.02	X_5	0.077	20.10	19.90	18.19	14.3	11.5
J040733−281031	04:07:32.97	−28:10:31.26	4.74	X_8	0.026	18.63	18.50	16.91	7.2	7.8
J040915−275633	04:09:14.88	−27:56:32.90	4.48	T_1	0.032	17.94	17.77	16.20	6.2	6.4
J044433−292419	04:44:32.52	−29:24:19.19	4.82	T_1	0.023	18.57	18.60	16.74	4.0	12.6
J045057−265541	04:50:57.38	−26:55:41.44	4.77	X_8	0.031	18.74	18.48	16.43	9.6	12.0
J045428−050049	04:54:27.95	−05:00:49.46	4.83	T_1	0.027	18.46	18.46	16.56	5.7	16.7
J051509−431854	05:15:08.93	−43:18:53.64	4.61	T_1	0.022	18.52	18.35	16.25	6.5	9.2
J072012−675632	07:20:11.67	−67:56:31.56	4.62	T_1	0.117	18.39	18.09	16.22	1.9	18.9
SDSS J074749.18+115352.4	07:47:49.17	11:53:52.48	5.26	X_5	0.026	18.77	18.38	16.39	18.0	34.1
SDSS J082454.01+130216.9	08:24:54.02	13:02:16.98	5.21	X_4	0.030	20.03	19.55	17.89	23.5	17.0
SDSS J084627.84+080051.7	08:46:27.84	08:00:51.73	5.02	X_5	0.062	20.10	19.84	17.97	9.7	6.9
SDSS J085430.37+205650.8	08:54:30.37	20:56:50.84	5.17	X_5	0.023	19.42	19.75	17.66	11.3	7.8
SDSS J090245.76+085115.9	09:02:45.76	08:51:15.92	5.22	X_6	0.044	20.17	20.20	18.24	8.8	5.6
J091656−251146	09:16:55.68	−25:11:45.79	4.85	X_8,T_2	0.118	17.33	17.28	15.45	14.1	25.0
J093033−221208	09:30:32.57	−22:12:07.75	4.89	T_1	0.058	18.22	18.23	16.49	5.6	25.4
SDSS J095707.67+061059.5	09:57:07.67	06:10:59.52	5.17	X_5	0.024	19.27	19.10	17.34	13.3	11.7
SDSS J095712.20+101618.5	09:57:12.69	10:16:21.78	5.13	X_6	0.036	20.22	20.11	18.23	4.8	4.8
SDSS J095727.86+051905.2	09:57:27.93	05:19:05.70	5.19	X_4	0.043	18.64	18.26	18.18	7.5	4.3
SDSS J102833.45+074618.9	10:28:33.46	07:46:18.96	5.17	X_4	0.022	20.25	19.97	18.38	8.2	5.7
J111055−301130	11:10:54.69	−30:11:29.94	4.78	X_8,T_2	0.049	17.38	17.20	15.55	9.1	31.8
J111520−193506	11:15:20.31	−19:35:06.25	4.66	X_8,T_2	0.049	18.40	18.36	16.75	23.0	17.0
J113522−354839	11:35:21.99	−35:48:38.84	4.97	X_8,T_2	0.080	18.27	18.17	16.72	17.3	18.0
SDSS J120055.61+181733.0	12:00:55.62	18:17:33.01	5.00	X_5	0.021	19.71	19.60	17.97	16.5	13.8
SDSS J120441.73−002149.6	12:04:41.73	−00:21:49.54	5.09	X_4	0.022	19.05	19.35	17.40	22.6	14.5
BR 1202−0725	12:05:23.14	−07:42:32.76	4.69	X_2	0.032	17.94	17.85	16.22	59.9	71.4
SDSS J12083+0010	12:08:23.83	00:10:27.60	5.28	X_1	0.020	20.68	20.36	18.82	32.9	18.3
J121402−123548	12:14:02.71	−12:35:48.75	4.75	T_2	0.041	18.61	18.43	16.80	4.0	17.8
J121921−360933	12:19:21.12	−36:09:33.13	4.80	X_8	0.068	18.96	18.52	16.51	8.0	22.3

[a]Uncertainties in the full table available as supplementary material.

X_1 − 084.A-0574(A); X_2 − 084.A-0780(B); X_3 − 087.A-0125(A); X_4 − 094.A-0793(A); X_5 − 098.A-0111(A); X_6 − 0100.A-0243(A);

X_7 − 0104.A-0410(A); X_8 − 108.22H9.001; X_9 − 109.23D1.001; X_{10} − 109.23D1.002; T_1 − 2021B-0036; T_2 − 2022A-389756

Table 3.1: (Continued)

Name	RA (J2000)	Dec (J2000)	z_{MgII}	PID	E(B-V)	i_{AB}	z_{AB}	H_{Vega}	SNR_{1450}	SNR_{2600}
J130031−282931	13:00:31.13	−28:29:30.99	4.71	T_1	0.069	18.34	18.03	16.35	4.2	20.1
SDSS J133257.45+220835.9	13:32:57.44	22:08:35.86	5.11	X_6	0.010	19.22	19.29	17.33	14.4	9.3
J140802−275820	14:08:01.82	−27:58:20.36	4.47	T_2	0.043	17.83	17.67	16.05	11.7	11.7
SDSS J142325.92+130300.7	14:23:25.92	13:03:00.70	5.04	X_5	0.019	19.56	19.39	17.62	18.2	16.7
J142721−050353	14:27:21.56	−05:03:53.04	5.09	X_9	0.051	19.24	18.87	17.21	6.0	11.4
SDSS J143605.00+213239.2	14:36:05.00	21:32:39.25	5.23	X_5	0.024	20.08	19.70	17.95	14.8	9.9
J151443−325024	15:14:43.82	−32:50:24.92	4.83	X_{10},T_2	0.300	18.01	17.83	15.82	5.0	11.0
J153241−193033	15:32:41.40	−19:30:32.79	4.69	X_9,T_2	0.111	19.03	18.80	16.65	10.7	12.2
J153359−181027	15:33:59.76	−18:10:27.20	5.01	X_9	0.091	19.22	19.04	16.91	4.5	11.7
J155657−172107	15:56:57.36	−17:21:07.51	4.75	X_9,T_2	0.175	18.60	18.46	16.66	5.8	19.6
SDSS J160111.16−182835.0	16:01:11.17	−18:28:35.09	5.05	X_5	0.363	19.98	19.46	17.34	12.5	21.2
SDSS J161622.10+050127.7	16:16:22.11	05:01:27.72	4.87	X_3	0.059	18.93	18.78	17.24	114.9	106.8
J162551.54−043049.4	16:25:51.55	−04:30:49.52	5.20	T_1,T_2	0.186	18.69	18.40	16.54	2.7	15.5
J194124−450023	19:41:24.59	−45:00:23.77	5.21	X_9,T_2	0.067	18.43	18.19	16.45	11.6	17.6
J205559−601147	20:55:59.23	−60:11:47.42	4.97	X_9	0.045	18.78	18.87	17.22	15.5	19.3
J211105−015604	21:11:05.61	−01:56:04.21	4.89	X_9	0.043	18.00	17.88	16.39	12.6	15.6
J211921−772253	21:19:20.86	−77:22:53.27	4.56	X_{10},T_2	0.093	17.96	17.61	16.03	7.4	4.6
J214608−485819	21:46:08.22	−48:58:19.59	5.16	X_9,T_2	0.023	18.39	18.28	16.44	10.7	12.4
J215728.21−360215.1	21:57:28.23	−36:02:15.21	4.70	X_7	0.015	17.26	17.07	14.80	52.0	83.7
SDSS J220106.63+030207.7	22:01:06.63	03:02:07.67	5.09	X_5	0.039	19.37	19.24	17.30	23.8	17.1
J220159−202627	22:01:58.60	−20:26:27.38	4.74	X_9	0.026	18.49	18.13	16.42	12.5	9.6
SDSS J220226.77+150952.3	22:02:26.77	15:09:52.38	5.08	X_5	0.041	18.89	18.68	17.10	17.7	8.4
J221112−330246	22:11:11.55	−33:02:45.91	4.65	X_8	0.018	18.35	18.08	15.94	11.7	17.6
SDSS J221644.01+001348.1	22:16:44.02	00:13:48.12	5.01	X_4	0.052	20.37	20.29	18.60	15.3	8.7
J222153−182603	22:21:52.88	−18:26:02.93	4.53	T_1	0.033	17.63	17.36	15.78	17.1	17.6
J222358−252634	22:23:57.88	−25:26:34.40	4.80	X_8	0.020	18.78	18.72	16.96	6.7	7.6
SDSS J222514.38+033012.5	22:25:14.38	03:30:12.50	5.26	X_5	0.086	18.65	18.25	17.99	9.8	15.5
J222612−061807	22:26:12.42	−06:18:07.37	5.10	X_8	0.052	18.67	18.78	17.09	9.9	9.2
SDSS J222845.14−075755.3	22:28:45.15	−07:57:55.38	5.16	X_6	0.042	20.05	20.06	17.94	13.5	10.4
J223419−804013	22:34:19.12	−80:40:13.30	4.97	X_9	0.111	18.74	18.70	17.22	11.9	7.1
J230349−063343	23:03:49.20	−06:33:43.18	4.74	X_{10},T_1	0.037	18.26	17.83	15.96	4.8	13.7
J230430−313427	23:04:29.89	−31:34:27.11	4.87	T_1	0.022	17.73	17.73	16.13	5.4	17.0
SDSS J232536.64−055328.3	23:25:36.64	−05:53:28.43	5.23	X_6	0.030	19.75	19.10	17.68	10.7	7.5
J232953−200039	23:29:52.78	−20:00:39.19	5.04	X_9	0.028	18.52	18.39	16.55	11.4	14.4
J233435−365709	23:34:35.30	−36:57:08.99	4.72	X_9	0.014	19.27	18.90	16.51	9.3	16.7
J233505−590103	23:35:05.90	−59:01:03.39	4.53	X_7	0.012	17.58	17.57	15.92	60.1	45.4
SDSS J234433.50+165316.4	23:44:33.50	16:53:16.56	4.99	X_5	0.052	18.65	18.74	16.86	6.6	5.8
SDSS J235124.31−045907.3	23:51:24.31	−04:59:07.30	5.25	X_6	0.030	20.41	20.07	18.36	10.8	7.0

Table 3.2: Description of measured properties from modelling the spectral continuum and Mg II broad emission-line.

Property	Description	Units
Redshift	Defined by the peak flux of the line model	
FWHM	Full-width half-maximum of profile	km s^{-1}
Sigma	Second moment of profile	km s^{-1}
Blueshift	Defined by the flux-bisecting wavelength	km s^{-1}
EW	Equivalent width in rest-frame	Å
log iLuminosity	Integrated log line luminosity	erg s^{-1}
log L$_{3000}$	Power-law continuum luminosity at 3000Å	erg s^{-1}
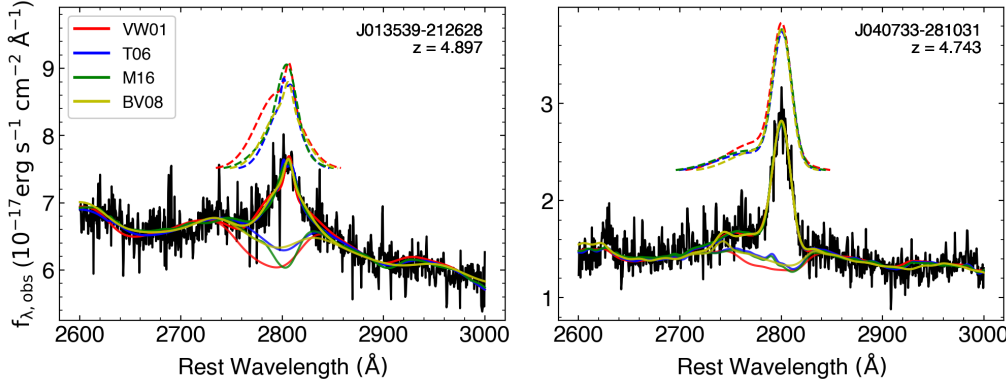
Figure 3.3: Example models of the Mg II line for J013539–212628 (left) and J040733–281031 (right), where the adopted underlying Fe II continuum model is varied between the four templates discussed in Section 3.3.1. The continuum and line models between templates are differentiated by colour and the continuum-subtracted broad line model is represented with the dashed lines, vertically shifted for visibility. The targets in each panel show the wide range in responsiveness of the Mg II profile to the choice of Fe II template: the target on the left panel shows a highly sensitive line model whereas the line model on the right is robust.

3.3   Spectral Modelling

We measure the properties of the Mg II $\lambda2799$ emission feature to constrain the redshifts of our target quasars and determine black hole masses from the velocity broadening. Here, we describe our emission-line modelling approach, which utilises a publicly available code (`PyQSpecFit`[7]; Lai 2023b) designed for modelling quasar spectral lines, including the components of our continuum and emission-line models. More information on the code and each of these components can be found in Lai et al. (2023a), which is a study of the black hole properties in the XQ-100 quasar legacy survey.

3.3.1   Continuum Modelling

Before we model the Mg II line, we first subtract a model of the quasar continuum. Our quasar continuum model is composed of two components: a power law and Fe II template, which is altogether called the pseudo-continuum. The pseudo-continuum is then uniquely defined by five free parameters and is fit simultaneously to the spectroscopic data contained within selected rest-frame windows: 1973–1983Å, 2060–2340Å, 2600–2740Å, and 2840–3100Å, chosen to minimise contribution from strong emission-lines while also covering wavelength regions in close proximity to the Mg II line with a wide diversity of expected Fe II flux.

---

[7]https://github.com/samlaihei/PyQSpecFit

The Mg II feature is sensitive to the Fe II continuum emission, which extends underneath the emission-line, and it has previously been established that the choice of Fe II template can bias the result. Notably, adopting the Vestergaard & Wilkes (2001) template, which is often used to calibrate the Mg II-based single-epoch virial black hole mass estimate (e.g., Vestergaard & Osmer 2009; Shen et al. 2011), results in larger line widths than with other models of the Fe II emission (Schindler et al. 2020; Lai et al. 2023a). Thus, we rely on four empirical and semi-empirical Fe II templates: Vestergaard & Wilkes (2001, VW01), Tsuzuki et al. (2006, T06), Bruhweiler & Verner (2008, BV08), and Mejía-Restrepo et al. (2016, M16) to minimise bias induced by any single template. The templates are renormalised and broadened with a Gaussian kernel to match the features of each observed spectrum.

A third potential component to the pseudo-continuum, the Balmer continuum, is sometimes introduced in similar studies of the Mg II emission-line in AGN (e.g., Wang et al. 2009). However, the flux of the Balmer continuum decreases continuously on the blue side of the Balmer edge located at 3645Å, and is relatively weak near the Mg II line (Vestergaard & Wilkes 2001; Dietrich et al. 2002). We also note that the Balmer continuum flux can be degenerate with the other pseudo-continuum components. Thus, despite an improved global continuum fit, the isolation of the Mg II emission-line profile is often independent of a reasonably constrained Balmer continuum model (e.g., Shen & Liu 2012; Lai et al. 2023a). Therefore, we do not include the Balmer continuum in our pseudo-continuum model, although we note that the exclusion of the Balmer continuum can change the flux of the power-law and Fe II components.

Even though we do not observe evidence of a strong Balmer flux contribution across the Balmer edge in the luminous quasar spectra of XQ-100 (Lai et al. 2023a), we estimate the systematic uncertainty related to the exclusion of the Balmer contribution to the continuum model. A common model of the Balmer continuum, adopted in other studies (e.g. Dietrich et al. 2003; Kurk et al. 2007; De Rosa et al. 2011; Shin et al. 2019), normalises the flux at the Balmer edge to 30% the flux of the power-law component at 3675Å, where the Fe II emission is absent. We assume a lower normalisation of 10% that is also commonly used in the literature (Calderone et al. 2017; Rakshit et al. 2020). Following these studies, we adopt the same electron temperature ($T_e = 15,000$ K) and optical depth ($\tau_\lambda = 1$), finding that the Balmer flux contribution at 3000Å would be between 7–8% of the power-law flux, depending on the power-law slope, where we have used the 16th and 84th percentiles of all measured slopes from our sample, $\gamma = -1.36^{+0.40}_{-0.33}$. Thus, the power-law flux at 3000Å could be overestimated by up to 10% depending on how the Balmer flux is

proportioned between the power-law and Fe II components. We later quantify on
how this could affect our results.

3.3.2   Mg II Modelling

Broad emission-line profiles can be found with a wide range of properties and mor-
phological complexities, which render emission-line models described by a single ana-
lytical function unsuitable, particularly with a Doppler broadened doublet emission-
line like Mg II. As such, quasar spectral modelling studies typically utilise a multiple
Gaussian approach to fit each individual emission feature (e.g., Greene & Ho 2005;
Shen et al. 2011; Rakshit et al. 2020; Wu & Shen 2022). Accordingly, we model the
Mg II broad emission-line with three Gaussian components and use an additional
component to fit the narrow line, if present. The maximum width of the narrow
component is set at 1000 km s^{-1}.

After subtracting the pseudo-continuum model, we fit the Mg II line model within
rest-frame 2730–2870Å. We then determine the Mg II emission-line properties from
the total line profile composed of the three broad components. The final mean
line properties and measurement uncertainties are determined from the emergent
emission-line models assuming the four different Fe II templates. We further add
in quadrature the additional uncertainty measured by fitting 50 synthetic spectra,
which are generated by randomly redistributing the flux in each fixed-velocity bin
according to its Gaussian uncertainties.

In Table 3.2, we describe each of the line properties measured from the quasar
continuum and Mg II broad emission-line model. For each target, we update the
measured redshift based on the wavelength of the peak flux in the reconstructed
Mg II line profile. From the combined broad emission-line profile, we measure the
Mg II FWHM and line dispersion, Sigma, which is the second moment of the line
profile. The blueshift of the line is measured from the flux-bisecting wavelength,
as

$$\frac{\text{Blueshift}}{\text{km s}^{-1}} \equiv c \times (\lambda_{\text{ref}} - \lambda_{\text{med}})/\lambda_{\text{ref}} \,, \tag{3.1}$$

where λ_{ref} is the vacuum wavelength of the Mg II doublet which is set to 2799.117Å,
and λ_{med} is the wavelength bisecting the total continuum-subtracted emission-line
flux. We also measure the line rest-frame equivalent width (EW) and integrated
luminosity. The monochromatic luminosity at 3000Å is measured from the power-
law continuum model. For the 14 targets with more than one spectrum, the final
line properties are measured from the weighted average of multiple observations. In
our sample, we find one target, J051509–431854, with clear Mg II absorption, which

is a common characteristic of low-ionisation broad absorption line (LoBAL) quasars. This is consistent with the expectation that quasar with BAL outflows are found in less than 20% of quasars (e.g. Gibson et al. 2009) and LoBAL outflows are even rarer, consisting of 10–15% of BAL quasars. However, there is some evidence that the BAL fraction increases with redshift (Bischetti et al. 2023). A more detailed analysis of the BAL quasar fraction will be in an separate forthcoming study.

In Figure 3.3, we show two targets which represent a range of line model susceptibility to the Fe II template. The target on the left panel (J013539–212628) is highly sensitive to the Fe II model, with a Mg II FWHM that varies from 2910–5400 km s^{-1}. In contrast, the target on the right panel (J040733–281031) is minimally affected as a result of its weak Fe II emission. Its Mg II FWHM range is from 2420–2540 km s^{-1}.

Single-Epoch Virial Mass Estimate

We use the version of the Mg II single-epoch virial mass estimate from Shen et al. (2011), which is calibrated to a high-luminosity subset from the local reverberation mapping AGN sample using the H$\beta\lambda$4863 line,

$$\left(\frac{\mathrm{M_{BH,vir}}}{\mathrm{M_\odot}}\right) = 10^{6.74} \left[\frac{\mathrm{L(3000)}}{10^{44}\,\mathrm{erg\,s^{-1}}}\right]^{0.62} \left[\frac{\mathrm{FWHM_{Mg\,II}}}{1000\,\mathrm{km\,s^{-1}}}\right]^2, \tag{3.2}$$

where $L(3000)$ is the monochromatic luminosity (λL_λ) of the quasar continuum at 3000Å and $\mathrm{FWHM_{Mg\,II}}$ is the measured line full-width at half-maximum of the Mg II broad line profile. Systematic errors from the single-epoch virial black hole mass estimate can be as high as 0.5 dex due to the combined effects of a 0.3 dex scatter around their reverberation mapping counterparts (Dalla Bontà et al. 2020) and a 0.4 dex intrinsic scatter of reverberation-based estimates around the $M_{\mathrm{BH}} - \sigma_*$ relation (Bennert et al. 2021). We adopt 0.5 dex as our single-epoch virial black hole mass uncertainty in this study. A possible 25% overestimation in L(3000) as suggested in Section 3.3.1 would overestimate the black hole mass by 0.075 dex, which is insignificant compared to the systematic uncertainties of the method.

Although we measure the line dispersion, we opt to use the FWHM in the determination of black hole mass. The line dispersion may have advantages over the FWHM (e.g., Fromerth & Melia 2000; Peterson et al. 2004; Collin et al. 2006), but in practice, it is sensitive to the wings of the line profile, which are naturally low in flux and difficult to disentangle from the pseudo-continuum model. For the XQz5 sample, we find that the fractional uncertainty for the line dispersion is typically higher than that of the FWHM.
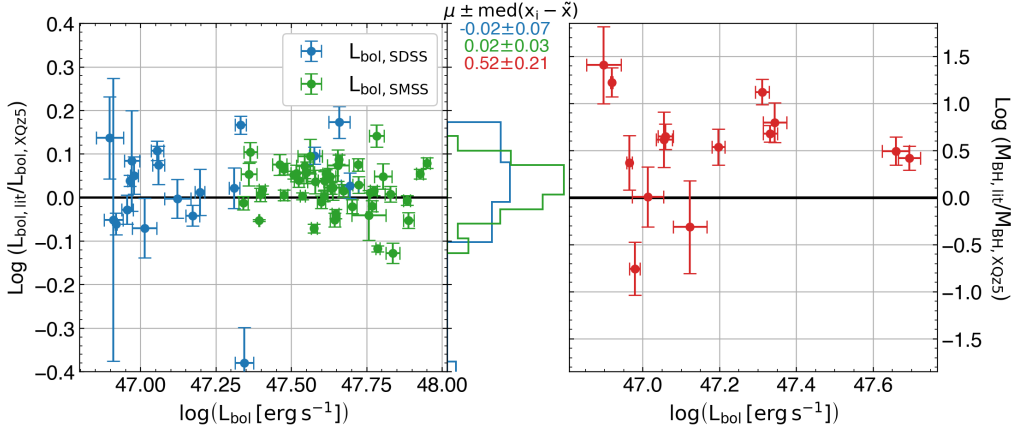
Figure 3.4: Comparisons of estimated bolometric luminosity (left) and black hole masses (right) between XQz5 measurements and the existing literature for a subset of the XQz5 with SDSS DR16Q measurements (Wu & Shen 2022) or O22 luminosities. The SDSS bolometric luminosities are estimated with the bolometric correction factor $k_{1350} = 3.81$, while the SMSS and XQz5 luminosities are estimated with $k_{3000} = 5.15$. The black hole masses from SDSS are measured from C IV. The mean and median absolute deviation of the residual for each measured quantity is listed There is a tight agreement with literature bolometric luminosities, but the C IV-based virial mass estimates from SDSS are overestimated compared to XQz5 Mg II-based M_{BH} measurements.

With the single-epoch virial mass estimate, the typical black hole mass measurement uncertainty in our sample is 0.11 dex, based on statistical uncertainties in the measured FWHM and L(3000). The error in both of these quantities is composed of the measured variance from adopting different Fe II models and fitting synthetic spectra.

3.4   Results and Discussion

The results for the parameters given in Table 3.2 are provided in a supplementary file, which is also available in a public repository[8] and a sample of the measured properties is shown in Table 3.3. We present fits of the Mg II line for all 83 quasars in Appendix B.1. Although some targets from the ESO Science Archive Facility have existing Mg II-based black hole mass estimates, such as SDSS J013127.34–032100.1 (Yi et al. 2014) and SDSS J161622.10+050127.7 (T11), we remeasure the black hole mass in a homogeneous fashion and place them in context within the larger sample. The estimated black hole mass range of the XQz5 sample is $\log(M_{BH}/M_\odot) = 8.5 - 10.4$.

---

[8]https://github.com/samlaihei/XQz5
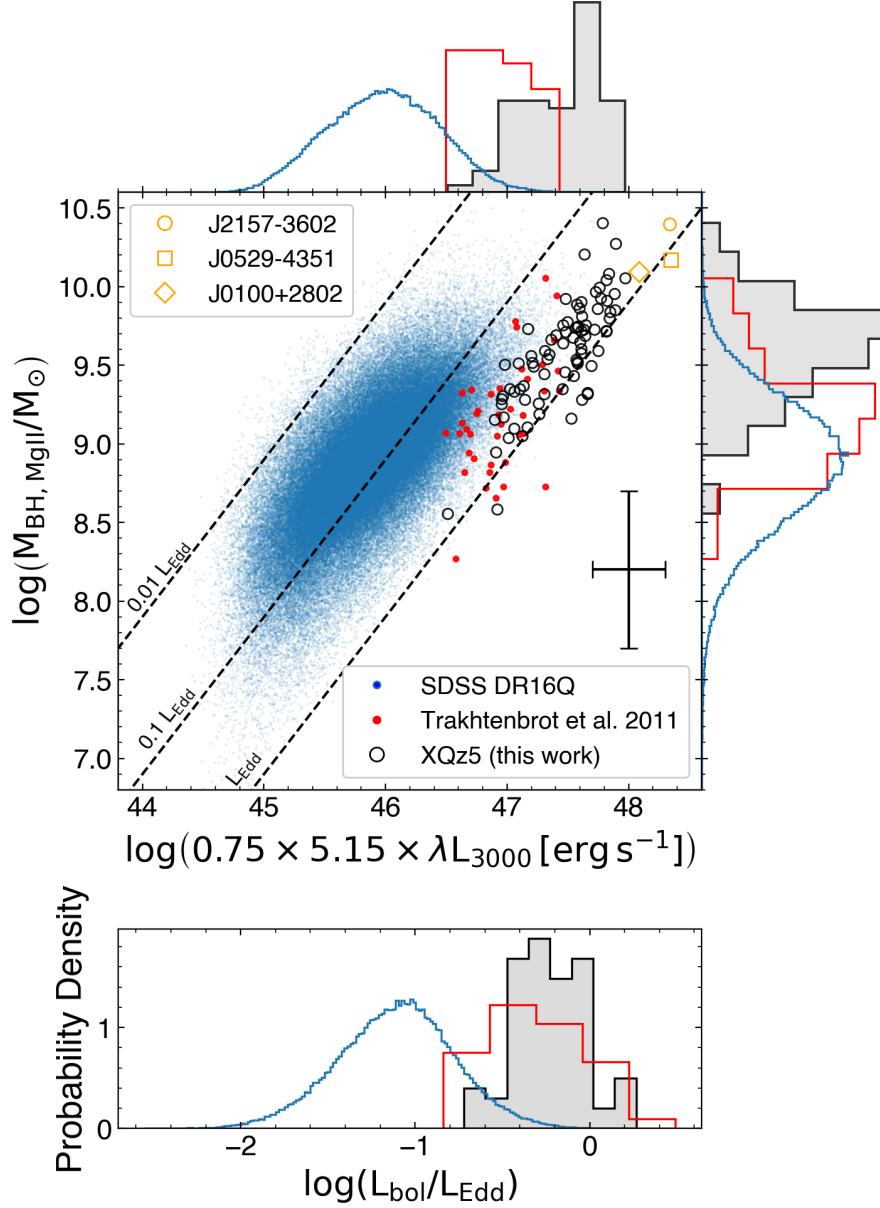
Figure 3.5: Black hole mass and bolometric luminosity density distributions as measured from k-corrections to the observed 3000Å monochromatic luminosity. Our sample, XQz5 (black open circles and shaded histograms), is compared to the SDSS DR16Q sample (blue points and histograms; Wu & Shen 2022) with Mg II measurements (at z = 0.35 – 2.3) and the T11 sample (red points and histograms), which is at a comparable redshift. By construction, XQz5 is the highest luminosity sample at this redshift range and we found it to be skewed towards higher black hole masses. However, the Eddington ratio distribution is not statistically different from the T11 sample. We assume typical systematic errors of $\Delta \log M = 0.5$ and $\Delta \log L_{\rm bol} = 0.3$, which is shown with the cross. We have also reproduced the three notable quasars presented in Figure 3.2 (open orange symbols in the $\rm M_{BH} - L_{bol}$ panel).

Table 3.3:   Examples of the measured properties from the model of the quasar continuum and Mg II line. Table 3.2 presents a description of the columns. The full tabulated results are provided in a supplementary file.

ID	FWHM	Sigma	Blueshift	EW	$\log$ iLuminosity	$\log$ L(3000)	$\log$ M$_{BH}$
J040733-281031	2485 ± 92	2515 ± 232	205 ± 57	37.66 ± 2.63	44.80 ± 0.03	46.67 ± 0.01	9.19 ± 0.03
J091656-251146	3057 ± 174	1793 ± 133	-62 ± 101	15.61 ± 2.02	45.09 ± 0.05	47.32 ± 0.01	9.77 ± 0.05
J211105-015604	3821 ± 378	2392 ± 193	130 ± 92	24.73 ± 2.13	45.11 ± 0.03	47.15 ± 0.01	9.86 ± 0.09

In this section, we discuss the corrections used to estimate bolometric luminosity from the observed spectrum and its associated uncertainties. We then compare the derived quantities between quasar samples collected at similar redshifts, and luminosity-matched samples at different redshifts. We also compare the measured properties to other high-quality X-shooter samples, XQ-100 and XQR-30.

3.4.1   Bolometric Luminosity

To measure the bolometric luminosity of a quasar exactly, it is necessary to observe the quasar at all wavelengths from all possible viewing angles and have an understanding of the source component decomposition for the observed luminosity at different wavelengths. Because that is not feasible, it is common among studies of quasars to apply a first-order correction to the observed monochromatic luminosity in the form, $L_{bol} = k_{\lambda} L(\lambda)$, where k_{λ} is the bolometric correction factor and $L(\lambda)$ represents the monochromatic luminosity, λL_{λ} at rest wavelength λ.

The bolometric correction factor, k_{λ}, is calibrated for a mean quasar spectral energy distribution (SED), integrated across a particular wavelength range. In this study, we use $k_{3000} = 5.15$, a first-order correction from Richards et al. (2006) that is calibrated to the mean SED of 259 SDSS Type 1 quasars, integrated from 100 μm to 10 keV and assumed to be emitting isotropically. However, as the Type 1 quasars used to construct the mean SED are likely to be biased towards face-on orientations, the resulting luminosity will be overestimated. Thus, we adopt the model presented in Lai et al. (2023b) and assume that the maximum opening angle of the obscuring torus for our sample, which defines the boundary between a Type 1 and Type 2 quasar classification, is 65°. We then use a thin disc model (Li et al. 2005) to estimate the correction between the observed and bolometric luminosities, assuming the quasars are randomly distributed in observed orientations and black hole spins. Using this method, the mean correction factor for anisotropy is calculated to be a 25% luminosity suppression to the observed luminosity, which is consistent with the correction in Runnoe et al. (2012), derived from similar arguments. Thus, for this study, we adopt $L_{bol} = 0.75 \times 5.15 \times L(3000)$ and we use this bolometric

correction consistently for the comparison with literature samples, unless otherwise stated. Due to the spectral diversity of quasars, the systematic uncertainty from deriving the assuming a mean SED can be as high as 50% (Richards et al. 2006), and so a systematic error of $\Delta \log L_{bol} = 0.3$ is assumed. We further note that the bolometric correction is expected to be mass or luminosity-dependent (e.g. Runnoe et al. 2012; Netzer 2019). For an ultraluminous 24 billion solar mass black hole, the bolometric correction factor at 3000Å could be as low as $k_{3000} = 1.62$ (Lai et al. 2023b), which is less than half of the bolometric luminosity derived with this method. An additional 0.05 dex adjustment may also result from a 10% overestimation of continuum flux by not explicitly modelling the Balmer component as cautioned in Section 3.3.1 and calibration errors may contribute up to 0.1 dex, but these corrections are not as significant as the assumed systematic error. We emphasise the possibility that the brightest and most massive black holes in this sample could have overestimated bolometric luminosities, but we adopt a consistent correction for all targets to facilitate comparison.

Using $k_{3000} = 5.15$ with a 0.75 anisotropy correction factor, the estimated bolometric luminosity range occupied by the XQz5 sample is then $\log(L_{bol}/\mathrm{erg\,s^{-1}}) = 46.5 - 48.34$ with Eddington ratios spanning nearly an order of magnitude from 0.19–1.8.

3.4.2   Comparison with literature samples

In this section, we place our black hole mass, luminosity, and Eddington ratio estimates in context with the literature. First, we compare the measurements obtained from the SDSS quasars in our sample with the results from the C IV-based virial estimator from SDSS DR16Q (Wu & Shen 2022). We also compare our estimates of bolometric luminosity with those from O22[9], which derived its L_{3000} luminosity estimates by matching each target's photometric information to a composite spectrum of bright quasars from $z = 1 - 2$ (Selsing et al. 2016). These comparisons are presented in Figure 3.4, from which we observe that the bolometric luminosity estimates between XQz5 and the literature are in tight agreement, despite the fact that the DR16Q estimates come from a different wavelength regime as $L_{bol} = 3.81 L_{1350}$. The literature luminosity of one outlier (not shown), identified as SDSS J001714.67–100055.4, is 0.7 dex lower than our measured luminosity and we found its continuum model in DR16Q to have been affected by a broad absorption feature. As for the measured black hole masses, the C IV-based virial mass estimator applied to SDSS data significantly overestimates the M_{BH} for our sample on average. When the 1690–

---

[9]O22 does not include black hole mass estimates
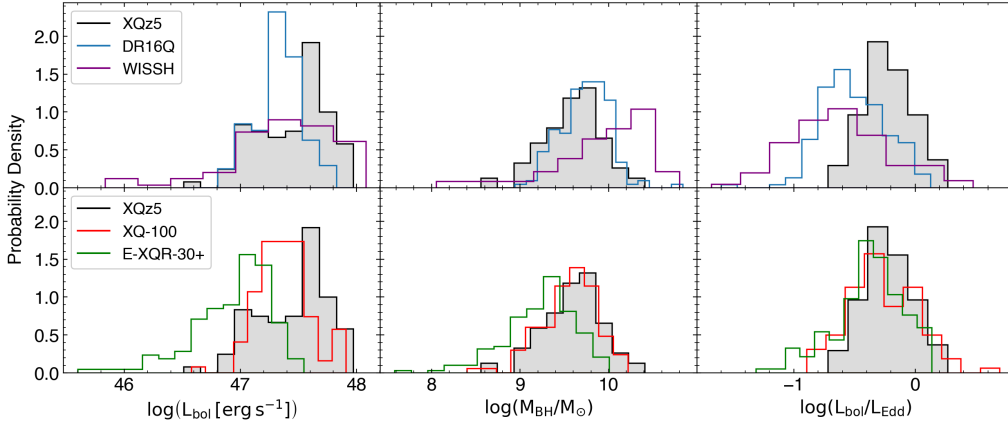
Figure 3.6: Bolometric luminosity (left), black hole mass (middle), and Eddington ratio (right) distributions for XQz5 (shaded) in comparison to two lower-redshift samples (SDSS DR16Q and WISSH) of similar luminosity (top) and two other brightness-selected quasar samples (XQ-100 and E-XQR-30+) with NIR spectroscopic data at lower and higher redshifts (bottom). The version of DR16Q plotted here (in blue) is a luminosity-matched subset of SDSS DR16Q. WISSH (in purple) is a high-luminosity SDSS and WISE-selected sample designed to reflect the most luminous known AGN in the universe. Both XQ-100 and E-XQR-30+ are bright quasar samples with high-quality spectra from X-shooter.

1705Å continuum fitting window falls near the red end of the wavelength coverage affected by enhanced sky background and molecular oxygen skylines, there is no anchor point for the continuum model on the red side of C IV. For this overlapping sample, we find that the cubic polynomial continuum model component adopted in (Wu & Shen 2022) significantly underestimates the continuum underneath the C IV line when fitted only to the blue side of C IV, which results in inflated C IV FWHMs and overestimated black hole masses.

Before comparing the XQz5 to other quasar samples, we first caution that systematic biases can arise from heterogeneous subsample selection criteria, as even well-defined subsamples can be biased if the sample completeness is unknown (Shen & Kelly 2012; Kelly & Shen 2013; Wu et al. 2022). Furthermore, we have defined the bolometric luminosity estimate using a static correction to the UV continuum luminosity. Implicitly, this assumes a consistent overall mean SED (Richards et al. 2006), which could again be a source of bias between heterogeneously selected samples. However, as XQz5 is a well-defined sample with high completeness at the bright end, we make these comparisons in order to examine relative distributions of other quasar samples compared to our sample. We include our 0.75 anisotropy correction factor consistently in our comparisons to literature estimates of bolometric luminosity.

We first construct a comparison to the T11 sample in Figure 3.5, using their Mg II measurements that we have rescaled to the Shen et al. (2011) calibration. Both XQz5 and the flux-limited T11 sample constructed from SDSS DR6 are biased towards high Eddington ratios with similar Eddington ratio distributions. However, the XQz5 targets are measured to be both more luminous and have higher mass black holes than T11. Both samples occupy the high mass and bright end of the subsample of SDSS DR16Q with well-constrained continuum luminosities and Mg II-based mass measurements between z = 0.35 – 2.3. In total, we find 11 targets in XQz5 with mildly super-Eddington luminosity.

Using SDSS DR16Q quasars with Mg II measurements as the parent sample, we construct a luminosity-matched sample by collecting two quasars with the closest matching luminosity to each quasar in XQz5, resulting in a subsample composed of 164 quasars in the redshift range $0.6 < z < 2.0$. The median L_{bol} difference of a selected SDSS DR16Q quasar and its associated XQz5 quasar is ~ 0.19 dex. Despite this, due to the scarcity of high luminosity SDSS quasars, the exact luminosity distribution of XQz5 could not be reproduced. In the top panels of Figure 3.6, we compare the luminosity, black hole mass, and Eddington ratio distribution between XQz5, the luminosity-matched DR16Q subsample, and the WISSH sample (Bischetti et al. 2017; Vietri et al. 2018), which is a high-luminosity SDSS and WISE-selected set of quasars across a wide range of redshifts ($1.8 < z < 4.7$) designed to reflect the most luminous known AGN in the universe. The black hole parameters of the WISSH sample are typically derived from the C IV emission line and L(1350), which are inter-calibrated to the results from the Mg II and Hβ line but contribute additional scatter due to their weak correlation with other virial mass estimators (e.g., Baskin & Laor 2005; Shen & Liu 2012). Nevertheless, we find in Figure 3.6, that both of the luminosity-matched lower redshift samples host black holes with higher mass than in XQz5. Statistical analysis of the XQz5 and lower-redshift mass distributions with the Kolmogorov-Smirnov (KS) test yields p-values less than 1%, indicating a statistically significant difference in the parent population. This also implies that ultraluminous quasars observed at lower redshift are generally less active with lower Eddington ratios than their counterparts at higher redshift, which is in concordance with recent literature (e.g., Yang et al. 2021; Farina et al. 2022). The mean Eddington ratio difference between XQz5 and the two lower-redshift samples is $\Delta\lambda_{Edd} \sim 0.3$

When comparing XQz5 with high-quality brightness-selected X-shooter quasar samples (XQ-100 and E-XQR-30+) in the bottom panels of Figure 3.6, we find all samples to be distributed towards high Eddington ratios, suggesting that all three

samples are composed of rapidly accreting massive quasars. The mean(median) Eddington ratio of XQz5 is $\sim 0.59(0.58)$, which is the highest mean(median) value of the three samples. The E-XQR-30+ sample has a long low-luminosity tail which consists entirely of literature quasars compiled in the Fan et al. (2022) database. Unlike XQz5 and XQ-100, these quasars are not preferentially selected from the bright quasar population. By excluding the low luminosity tail of E-XQR-30+ such that the distribution better reflects the brightest known quasars at $5.8 < z < 6.6$, we find that the three Eddington ratio distributions are not statistically different as measured by the KS test.

In this comparison, we find XQz5 to be the brightest X-shooter quasar sample by proportion and by number of quasars brighter than $\log{(L_{\rm bol}[{\rm ergs}^{-1}])} = 47.3$. As both XQz5 and XQR-30 are selected from the brightest known quasars at the time each sample was constructed, they are highly complete at the bright end of the quasar luminosity function. In particular, the completeness of the parent sample suggests that it is unlikely that a sample of brighter targets would exist within the redshift range of XQz5.

From XQR-30 at $z \sim 6.1$ to the later cosmic epoch of XQz5 at $z \sim 5.0$, we observe a significant increase in luminosity with decreasing redshift and a milder boost in black hole mass over a period of ~ 260 Myr. This reflects an underlying population of quasars that are on a rising branch stage of their cosmic evolution, as their SMBHs have been feeding continuously from an earlier seed. A forthcoming paper will model and examine the exponential mass growth of quasars at this redshift range.

3.5   Summary and Conclusion

In this study, we described XQz5, a sample composed of 83 quasars with spectroscopic redshifts $4.5 < z < 5.3$. Selected from the brightest known quasars in a Southern sample of unprecedented completeness (Onken et al. 2022a), we have compiled high quality, moderate resolution spectra in the observed frame optical and near-infrared. The median reduced and post-processed SNR = 27.2 measured per 50 km s^{-1} resolution element between 2700–2750Å and 2850–2900Å. Using the near-infrared observations, we examine the broad Mg II emission-line visible in rest-frame UV spectra and we measure properties of the black hole from the emission-line and the quasar continuum using established virial relations (Shen et al. 2011). The main results are as follows:

- By measuring the Mg II line present in all 83 quasar spectra and adopting virial relations from Shen et al. (2011), we find that the black hole mass range

of our sample is $\log(M_{BH}/M_\odot) = 8.5 - 10.4$. We also estimate the bolometric luminosity by applying a fixed bolometric correction of $k_{3000} = 5.15$ (Richards et al. 2006), with an anisotropy correction factor of 0.75 (Runnoe et al. 2012; Lai et al. 2023b), finding the majority of targets in our sample to occupy the bolometric luminosity range $\log(L_{bol}/\mathrm{erg\,s^{-1}}) = 47.0 - 48.0$, making it the brightest quasar sample among other high-redshift X-shooter surveys, XQ-100 (López et al. 2016) and XQR-30 (D'Odorico et al. 2023). The luminosity of 10 quasars in our sample appear mildly super-Eddington.

- XQz5 is a brighter sample with a 0.6 dex higher median luminosity and 0.4 dex more massive black holes compared to T11, a large sample at a similar redshift range from the literature. However, the Eddington ratio distributions occupy a similar range, with both distributions skewed towards high Eddington ratios.

- Compared to a lower-redshift SDSS DR16Q (Wu & Shen 2022) subset with Mg II measurements, XQz5 quasars occupy the high-mass and high-luminosity tail of the distribution, but when a luminosity-matched sample is constructed, the SDSS DR16Q black holes are more massive, indicating that ultraluminous quasars observed at higher redshift are generally more active than their lower-redshift counterparts, in agreement with recent literature (e.g., Yang et al. 2021; Farina et al. 2022).

Due to the high completeness of this sample at the bright end of the quasar luminosity function, this sample has notable legacy significance, as it is improbable that a brighter sample of a similar size could be constructed at this redshift range. Furthermore, as a sample that bridges the gap between XQ-100 (López et al. 2016) and XQR-30 (D'Odorico et al. 2023), this sample has widespread community value. We have made the reduced spectra available in the supplementary material and in a publicly accessible repository.

Acknowledgements

Data Availability

The data underlying this article will be shared on reasonable request to the corresponding author. Reduced spectra can be downloaded from this GitHub repository: https://github.com/samlaihei/XQz5.

Supermassive black holes are growing slowly by z~5

Context

This chapter is composed entirely of material from a paper that has been submitted to MNRAS as, "Lai, S., Onken, C. A., Wolf, C., Bian, F., & Fan, X. (2024), *Supermassive black holes are growing slowly by $z \sim 5$*, MNRAS, submitted."

Preamble

The XQz5 sample presented in Chapter 3 forms the basis for a study of quasar demographics at $z \sim 5$. In this chapter, we collect all of the quasars with spectroscopic follow-up observations and accurately measured black hole masses within the footprint of the parent survey with well-defined completeness. We use standard methods to estimate the $z \sim 5$ quasar mass function, using literature models at lower redshift to constrain the low-mass end. We then estimate the evolution in the mass function and present a simultaneous joint constraint on the duty cycle, radiative efficiency, and Eddington ratio of accretion-dominated mass assembly. This chapter is the culmination of the work presented in previous chapters, including time spent on submitting observing proposals and executing hands-on observations. This work makes a statement on the observed cosmic mass growth between $z = 5 - 4$, and the growth rate is used to comment on the black hole initial mass function, finding more rapid growth at higher redshift to be probable in order to develop the supermassive black holes observed at $z \sim 5$.

Abstract

We investigate the black hole mass function at $z \sim 5$ using XQz5, our recent sample of the most luminous quasars between the redshifts $4.5 < z < 5.3$. We include 72 quasars with robustly-measured black hole masses in the footprint of a highly complete parent survey. The completeness-corrected mass function is modelled as a double power-law model, and its evolution across redshift is fit assuming accretion-dominated mass growth. We estimate the evolution of the mass function between $z = 5 - 4$, presenting joint constraints on accretion properties through the measured dimensionless growth parameter, $k_{\rm ef} \equiv \langle \lambda \rangle U(1 - \epsilon)/\epsilon = 1.62 \pm 0.06$, where $\langle \lambda \rangle$ is the mean Eddington ratio, U is the duty cycle, and ϵ is the radiative efficiency. Notably, the measured growth is inconsistent with Eddington-limited accretion with radiative efficiencies $\epsilon > 0.34$ at 3σ confidence. If these supermassive black holes were to form from seeds smaller than $10^8 \, M_\odot$, the growth rate must have been considerably faster at $z \gg 5$ than observed between $z = 5 - 4$. A growth rate exceeding $3\times$ the observed rate would reduce the initial heavy seed mass to $10^{5-6} \, M_\odot$, aligning with supermassive star direct collapse seed masses. Stellar mass ($10^2 \, M_\odot$) black hole seeds would require $\gtrsim 4.5\times$ the observed growth rate at $z \gg 5$ to reproduce the observed black hole mass function. In any of these scenarios involving more rapid mass evolution, accreting black holes with low radiative efficiency are essential to produce the most extreme quasars, suggesting black holes with low angular momentum or photon trapping in supercritically accreting thick discs.

4.1 Introduction

The radiative output of accreting supermassive black holes (SMBHs), which reside in the centres of massive galaxies, is powered by gravitational energy associated with infalling material within the central potential well (e.g. Rees 1984), allowing them to outshine their hosts by orders of magnitude. The extreme luminosities reached by these systems enable them to be observed across cosmological distances, up to $z \sim 7.5$ (e.g., Bañados et al. 2018; Yang et al. 2020; Wang et al. 2021), when the age of the Universe was less than 700 Myr. It is now widely believed that these SMBHs play an important role in regulating host galaxy evolution (see review by Kormendy & Ho 2013), as evidenced by strong correlations between SMBH mass and velocity dispersion (e.g. Magorrian et al. 1998; Ferrarese & Merritt 2000; Gebhardt et al. 2000; Merritt & Ferrarese 2001; Kormendy et al. 2011), bulge mass (e.g. Kormendy & Richstone 1995; Marconi & Hunt 2003; Häring & Rix 2004; Peng et al. 2006; Greene et al. 2010) or total stellar mass (e.g. Cisternas et al. 2011; Reines &

Volonteri 2015; Davis et al. 2019; Ding et al. 2020; Smethurst et al. 2023). These tight relations leave little doubt of the existence of feedback mechanisms controlling the host galaxy and SMBH co-evolution. Understanding this co-evolution would aid in the development of a coherent model of galaxy formation and evolution.

In the study of host galaxy and SMBH co-evolution, the black hole mass is an important parameter that is correlated with other galactic properties. However, the best estimates of SMBH mass suggest that the most massive of them are $\gtrsim 10^9 M_\odot$ even at early cosmic times, raising questions about the SMBH cosmic mass assembly and the size of black hole seeds (see review by Volonteri et al. 2021). Accretion-dominated mass assembly implies exponential growth with an e-folding time of $450\lambda^{-1}\epsilon(1-\epsilon)^{-1}$ Myr, where ϵ is the radiative efficiency and λ is the Eddington ratio, $L_{\rm bol}/L_{\rm edd}$, with $L_{\rm edd} = 1.26 \times 10^{38} M_{\rm BH}/M_\odot \,{\rm erg\,s^{-1}}$. In order to grow $10^9 M_\odot$ black holes by 1 Gyr through accretion, $> 10^2 M_\odot$ black hole seeds would be required by 300 Myr ($z \sim 14$), assuming uninterrupted Eddington accretion with the fiducial $\epsilon = 0.1$ radiative efficiency based on the Sołtan argument (Yu & Tremaine 2002). Other than accretion, black hole mergers also contribute to the evolution of black hole mass. Large-scale hydrodynamical simulations suggest that the role of mergers in the total SMBH mass budget is secondary to growth by accretion (e.g. Dubois et al. 2014; Kulier et al. 2015; Martin et al. 2018). However, at late times when galaxies are comparatively gas-poor, the merger contribution to the total mass budget can increase, especially for the highest mass black holes (e.g. Shankar et al. 2013; Dubois et al. 2014; Kulier et al. 2015). The role of mergers at high-redshift may be illuminated by the next-generation of gravitational wave interferometers which will extend the redshift horizon and significantly improve the sensitivity to probe mergers of intermediate-mass black holes (Punturo et al. 2010; Amaro-Seoane et al. 2017; Reitze et al. 2019).

In order to explain the observed high-redshift black hole masses, SMBHs must have formed and grown rapidly (e.g. Volonteri & Bellovary 2012). Proposed black hole seeding mechanisms in the early Universe include gravitational collapse of Population III stars (e.g. Madau & Rees 2001; Volonteri et al. 2003), runaway merging (e.g. Portegies Zwart et al. 2004; Seth et al. 2008; Devecchi & Volonteri 2009), hierarchical assembly (e.g. Giersz et al. 2015; Dayal et al. 2019), or direct collapse (e.g. Loeb & Rasio 1994; Wise et al. 2008; Regan & Haehnelt 2009). Phases of super-Eddington growth or radiatively inefficient accretion can also help alleviate constraints on heavy black hole seeds (e.g. Madau et al. 2014; Inayoshi et al. 2016; Lupi et al. 2016). This can be achieved through counter-alignment of the angular momentum vectors of the accretion disc and black hole or uncorrelated mass injection (e.g. King & Pringle

2006; Zubovas & King 2021).

Observations of high-redshift SMBHs and reliable black hole mass measurements are necessary to study quasar demographics and cosmic mass assembly. Large sky surveys have improved sample statistics across a wide range of luminosities and redshifts (e.g. Shen et al. 2011; Rakshit et al. 2020; Flesch 2021; Wu & Shen 2022), while focused surveys of the ultraluminous quasar subset have directly probed the most massive black hole population and provided the most stringent constraints on their evolution (e.g. Trakhtenbrot et al. 2011; López et al. 2016; Bischetti et al. 2017; Schindler et al. 2017; Onken et al. 2022a; Cristiani et al. 2023; D'Odorico et al. 2023). Follow-up spectroscopic observations can be used to estimate black hole masses using the "single-epoch virial mass estimators" (e.g. Vestergaard & Peterson 2006; Shen 2013), which are based on empirical relationships from reverberation mapping experiments (e.g. Kaspi et al. 2000, 2005). This has enabled direct measurements of the black hole mass function and its cosmic evolution (e.g. Greene & Ho 2005; Vestergaard & Osmer 2009).

Using a spectroscopic follow-up of the most luminous and complete sample of quasars between $4.5 < z < 5.3$ (XQz5; Lai et al. 2024) supplemented by literature quasars in the same survey footprint, we present direct measurements of the active black hole mass function at $z \sim 5$. We measure the mass evolution observed between $z \sim 5$ and $z \sim 4$ mass functions, as well as within the ~ 240 Myr covered by the sample. We discuss the implications of our result on the quasar duty cycle, the spin-dependent radiative efficiency, and the size of black hole seeds at earlier cosmic epochs.

The content of this paper is organised as follows: in Section 4.2, we describe our method, beginning with a description of the $z \sim 5$ quasar sample and its parent survey. We then discuss our approach to measuring and modelling the black hole mass distribution function with the completeness correction of the sample. In Section 4.3, we apply our method to measure the black hole mass function for $z \sim 5$ and measure its redshift evolution with literature mass functions at different redshifts. We also discuss measuring the mass evolution within the $z \sim 5$ sample using a Monte Carlo method with a mock universe model. We present a summary and conclusion in Section 4.4. For this study, we adopt a standard flat ΛCDM cosmology with $H_0 = 70$ km s^{-1} Mpc^{-1} and $(\Omega_{\mathrm{m}}, \Omega_{\Lambda}) = (0.3, 0.7)$.

4.2   Method

The sample used in our analysis, XQz5 (Lai et al. 2024), is based on a survey of Southern quasars with unprecedented completeness (Onken et al. 2022a, hereafter

O22). From this parent survey, we construct a spectral atlas of ultraluminous $z \sim 5$ quasars composed of optical and near-infrared spectroscopic follow-up observations of the brightest 83 quasars in the O22 survey between the redshift range $4.5 < z < 5.3$. The spectroscopic follow-up was performed with the following instruments: SOAR/TripleSpec4.1, VLT/X-shooter, and ANU2.3m/WiFeS, and the reduced data have been made publicly available. A full description of the observations and the data reduction was published by Lai et al. (2024).

4.2.1 Sample completeness

The O22 parent sample utilises the SkyMapper Southern Survey Data Release 3 (SMSS DR3; Wolf et al. 2018b; Onken et al. 2019) in combination with precision astrometry from Gaia DR2/eDR3 as well as infrared photometric suveys from Two Micron All-Sky Survey (2MASS; Skrutskie et al. 2006), the VISTA Hemisphere Survey (VHS; McMahon et al. 2013) DR6, VISTA Kilo-Degree Infrared Galaxy Survey (VIKING; Edge et al. 2013) DR5, AllWISE (Wright et al. 2010; Cutri et al. 2013), and CatWISE2020 (Marocco et al. 2021). The full survey covers 14,486 deg^2 of the sky, including all known quasars in the search area as listed in Milliquas v7.1 and 126 newly identified luminous ($M_{1450} < -27$ mag) quasars. The magnitude-dependent completeness, defined in Figure 4 of O22 as a function of the SMSS z-band, declines from 95% at $z = 17.5$ and 90% at $z_{\mathrm{PSF}} = 18.4$ mag to 78% at $z_{\mathrm{PSF}} = 18.7$ mag. The survey is assumed to be complete up to $z = 5.4$, where the redshift constraints are imposed by the absence of signal in the Gaia G-passband at high redshift from which astrometric measurements are made (O22).

The full completeness correction in our study, $\Omega(L, z)$, is the Hadamard product of the 1-D magnitude-dependent completeness of O22 converted to luminosity, $\Omega_{\mathrm{phot}}(L, z)$, and the completeness of the spectroscopic follow-up, $\Omega_{\mathrm{spec}}(L, z)$, described by

$$\Omega(L, z) = \Omega_{\mathrm{phot}}(L, z) \odot \Omega_{\mathrm{spec}}(L, z), \tag{4.1}$$

where $\Omega_{\mathrm{spec}}(L, z)$ is estimated in a 2-D grid of luminosity and redshift. In Figure 4.1, we show the 2-D completeness function on a grid of L_{3000} monochromatic luminosity and redshift. The z-band completeness function is converted to L_{3000} using the observed H-band magnitudes to scale a composite spectrum of bright $z = 1 - 2$ quasars (Selsing et al. 2016). We show the parent sample as grey points and observed sample as green squares, where the spectroscopic completeness is determined by the fraction of quasars in O22 that have been observed with spectroscopic follow-up, smoothly interpolated over the grid. We also plot a high-redshift comparison sample as red stars, which is a combination of E-XQR-30 D'Odorico et al. (2023)

augmented by the database of Fan et al. (2023) into a compilation we refer to as
E-XQR-30+. We also show the sample from He et al. (2023), hereafter H23, which
is a study of the $z \sim 4$ mass function based on a sample of 52 quasars from the
Hyper Suprime-Cam Subaru Strategic Program and 1462 quasars from the Sloan
Digital Sky Survey (SDSS) DR7 quasar catalogue.

We choose to define the completeness function based on L_{3000}, because it is the
quantity that is relevant for black hole mass estimation as defined in Section 4.2.2.
However, variations in the spectral slope can contribute to an uncertainty in the
completeness correction. We find the residual standard (median absolute) deviation
in the measured and predicted L_{3000} to be 0.09 (0.06) dex, where large deviations
of ~ 0.3 dex are only seen for the faintest quasars in our sample. Therefore, there
is little variation in the completeness of quasars in our sample if we had derived the
completeness function from the observed z_{PSF}-mag instead of L_{3000}, particularly at
the bright end.

Our analysis is primarily focused on the high luminosity quasars between redshifts
$4.5 < z < 5.3$, for which we have 80–95% completeness for a select region and
where 54/84 of the XQz5 quasars are in the survey area. We further supplement the
sample with 9 additional quasars from Trakhtenbrot et al. (2011), hereafter T11,
and 8 quasars from López et al. (2016), hereafter XQ100, for a total of 72 quasars
in the dataset. The T11 and López et al. (2016) quasars supplement the lower-
luminosity and lower-redshift ends of the sample, respectively. These additional
quasars are targets which were already observed with spectroscopic follow-up within
the footprint of O22 and we require that they are located within a region of $\geq 25\%$
completeness. We present all 72 quasars used in our demographic analysis in Table
4.1 and we refer to the expanded dataset as XQz5+. In the following section, we
discuss how the completeness correction is used to measure the observed black hole
mass distribution function.

4.2.2 Black hole mass function

Constraining the shape and evolution of the black hole mass function is observation-
ally expensive, due to the requirement of collecting samples with high completeness
and obtaining high signal-to-noise spectroscopic data, which are necessary to obtain
reliable black hole mass measurements. Furthermore, the completeness correction
of the black hole mass function, particularly for lower masses, is not as easily ascer-
tained, as the mass on its own is not sufficient to adequately constrain the intrinsic
luminosity, and hence the observed source brightness (on which the completeness
estimate relies). Nevertheless, the cosmic evolution of the black hole mass function

Table 4.1: Properties of quasars in XQz5+ used in the demographic analysis.

ID	RA (J2000)	Dec (J2000)	Redshift	$\log L_{3000}/\mathrm{erg\,s^{-1}}$	$\log M_{\mathrm{BH}}/M_\odot$	$\log L_{\mathrm{bol}}/L_{\mathrm{Edd}}$	Source
000651−620803	1.71502	-62.13430	4.44	46.787 ± 0.029	9.73 ± 0.05	-0.45 ± 0.05	XQ100
001225−484829	3.10424	-48.80830	4.62	47.256 ± 0.019	9.80 ± 0.05	-0.06 ± 0.05	XQz5
001714−100055	4.31113	-10.01536	5.02	46.547 ± 0.023	9.37 ± 0.10	-0.34 ± 0.11	XQz5
002526−014532	6.36181	-1.75905	5.06	47.072 ± 0.036	9.33 ± 0.05	0.23 ± 0.06	XQz5
003525+004002	8.85542	0.66750	4.76	46.380 ± 0.150	8.49 ± 0.44	0.38 ± 0.46	T11
011546−025312	18.94274	-2.88676	5.08	46.505 ± 0.005	9.51 ± 0.07	-0.52 ± 0.07	XQz5
013127−032059	22.86391	-3.34998	5.20	47.108 ± 0.029	9.50 ± 0.10	0.10 ± 0.10	XQz5
013539−212628	23.91370	-21.44118	4.90	47.385 ± 0.011	10.05 ± 0.26	-0.18 ± 0.26	XQz5
014741−030247	26.92301	-3.04659	4.80	47.199 ± 0.007	10.41 ± 0.04	-0.72 ± 0.04	XQz5
015618−044139	29.07906	-4.69444	4.93	46.557 ± 0.024	9.28 ± 0.11	-0.24 ± 0.11	XQz5
020436−252315	31.15277	-25.38757	4.87	46.965 ± 0.016	9.24 ± 0.04	0.21 ± 0.05	XQz5
021043−001818	32.67984	-0.30510	4.71	46.040 ± 0.080	9.09 ± 0.40	-0.56 ± 0.41	T11
022112−034252	35.30259	-3.71447	5.02	46.535 ± 0.044	9.05 ± 0.17	-0.03 ± 0.18	XQz5
022306−470902	35.77812	-47.15069	5.00	47.297 ± 0.018	9.96 ± 0.08	-0.17 ± 0.09	XQz5
023648−114733	39.20236	-11.79268	5.20	46.890 ± 0.013	9.77 ± 0.12	-0.39 ± 0.12	XQz5
030722−494548	46.84538	-49.76336	4.72	47.261 ± 0.019	10.07 ± 0.07	-0.32 ± 0.07	XQ100
033119−074142	52.83191	-7.69525	4.73	46.550 ± 0.040	8.83 ± 0.11	0.21 ± 0.12	T11
033703−254831	54.26273	-25.80878	5.11	46.872 ± 0.025	9.64 ± 0.10	-0.28 ± 0.10	XQz5
040732−281031	61.88725	-28.17531	4.74	46.675 ± 0.010	9.19 ± 0.03	-0.03 ± 0.03	XQz5
040914−275632	62.31198	-27.94248	4.48	46.975 ± 0.040	9.74 ± 0.17	-0.28 ± 0.17	XQz5
044432−292419	71.13547	-29.40534	4.82	46.988 ± 0.010	9.89 ± 0.06	-0.41 ± 0.06	XQz5
045057−265541	72.73904	-26.92817	4.77	47.021 ± 0.027	9.72 ± 0.11	-0.21 ± 0.11	XQz5
045427−050049	73.61643	-5.01375	4.83	47.057 ± 0.016	9.76 ± 0.12	-0.21 ± 0.12	XQz5
051508−431853	78.78722	-43.31493	4.61	47.051 ± 0.028	9.69 ± 0.34	-0.15 ± 0.35	XQz5
052915−352603	82.31632	-35.43436	4.42	46.690 ± 0.018	9.22 ± 0.05	-0.04 ± 0.05	XQ100
071431−645510	108.63081	-64.91962	4.46	47.019 ± 0.012	9.61 ± 0.07	-0.11 ± 0.07	XQ100
072011−675631	110.04869	-67.94215	4.62	47.249 ± 0.023	10.08 ± 0.06	-0.35 ± 0.06	XQz5
091655−251145	139.23200	-25.19607	4.85	47.317 ± 0.012	9.77 ± 0.05	0.04 ± 0.05	XQz5
093032−221207	142.63577	-22.20213	4.89	47.022 ± 0.012	9.90 ± 0.06	-0.40 ± 0.06	XQz5
095500−013006	148.75040	-1.50189	4.42	46.814 ± 0.021	9.65 ± 0.04	-0.35 ± 0.05	XQ100
103623−034318	159.09895	-3.72192	4.53	46.766 ± 0.011	9.46 ± 0.03	-0.20 ± 0.03	XQ100
111054−301129	167.72790	-30.19164	4.78	47.335 ± 0.011	10.29 ± 0.05	-0.47 ± 0.05	XQz5
111520−193506	168.83470	-19.58506	4.66	47.019 ± 0.012	9.71 ± 0.07	-0.21 ± 0.07	XQz5
113522−354838	173.84172	-35.81076	4.97	46.952 ± 0.008	9.67 ± 0.03	-0.23 ± 0.04	XQz5

Table 4.1: (Continued)

ID	RA (J2000)	Dec (J2000)	Redshift	$\log L_{3000}/\mathrm{erg\,s^{-1}}$	$\log M_{\mathrm{BH}}/M_\odot$	$\log L_{\mathrm{bol}}/L_{\mathrm{Edd}}$	Source
120441−002149	181.17393	-0.36373	5.09	46.585 ± 0.023	9.73 ± 0.06	-0.66 ± 0.07	XQz5
120523−074232	181.34642	-7.70907	4.69	47.229 ± 0.015	10.04 ± 0.09	-0.33 ± 0.09	XQz5
121402−123548	183.51130	-12.59683	4.75	46.777 ± 0.022	9.66 ± 0.09	-0.40 ± 0.10	XQz5
121921−360933	184.83801	-36.15917	4.80	47.046 ± 0.014	10.21 ± 0.02	-0.67 ± 0.03	XQz5
130031−282931	195.12973	-28.49195	4.71	47.023 ± 0.021	9.58 ± 0.14	-0.07 ± 0.14	XQz5
132853−022441	202.22366	-2.41157	4.66	46.280 ± 0.080	9.08 ± 0.24	-0.31 ± 0.25	T11
134134+014157	205.39250	1.69939	4.69	46.730 ± 0.080	9.82 ± 0.24	-0.60 ± 0.25	T11
140801−275820	212.00757	-27.97228	4.47	47.170 ± 0.057	9.99 ± 0.10	-0.34 ± 0.11	XQz5
142721−050353	216.83984	-5.06477	5.09	46.618 ± 0.015	9.51 ± 0.06	-0.41 ± 0.06	XQz5
151443−325024	228.68260	-32.84022	4.83	47.151 ± 0.025	9.36 ± 0.04	0.28 ± 0.05	XQz5
153241−193032	233.17252	-19.50910	4.69	46.871 ± 0.024	9.35 ± 0.05	0.01 ± 0.05	XQz5
153359−181027	233.49907	-18.17420	5.01	46.870 ± 0.041	9.75 ± 0.13	-0.40 ± 0.14	XQz5
155657−172107	239.23904	-17.35207	4.75	46.901 ± 0.009	9.72 ± 0.08	-0.33 ± 0.08	XQz5
160111−182834	240.29657	-18.47638	5.05	46.981 ± 0.019	9.54 ± 0.10	-0.07 ± 0.10	XQz5
194124−450023	295.35245	-45.00656	5.21	47.158 ± 0.016	9.86 ± 0.07	-0.22 ± 0.08	XQz5
205559−601147	313.99682	-60.19648	4.97	46.961 ± 0.015	9.43 ± 0.12	0.01 ± 0.12	XQz5
205724−003018	314.35062	-0.50522	4.68	46.830 ± 0.080	9.23 ± 0.24	0.09 ± 0.25	T11
211105−015604	317.77335	-1.93449	4.89	47.155 ± 0.013	9.86 ± 0.09	-0.22 ± 0.09	XQz5
211920−772253	319.83676	-77.38142	4.56	46.954 ± 0.011	9.96 ± 0.14	-0.52 ± 0.14	XQz5
215728−360215	329.36758	-36.03752	4.69	47.672 ± 0.000	10.33 ± 0.12	-0.17 ± 0.12	XQz5
220008+001744	330.03607	0.29580	4.80	46.510 ± 0.080	8.82 ± 0.24	0.18 ± 0.25	T11
220158−202627	330.49408	-20.44092	4.74	47.014 ± 0.028	9.65 ± 0.09	-0.15 ± 0.09	XQz5
221111−330245	332.79813	-33.04606	4.65	47.231 ± 0.011	9.72 ± 0.06	-0.00 ± 0.06	XQz5
221644+001348	334.18340	0.23001	5.01	46.377 ± 0.007	9.30 ± 0.04	-0.44 ± 0.04	XQz5
221651−671443	334.21664	-67.24540	4.48	46.838 ± 0.020	9.79 ± 0.07	-0.46 ± 0.08	XQ100
221705−001307	334.27374	-0.21870	4.68	46.280 ± 0.150	8.63 ± 0.44	0.14 ± 0.46	T11
222152−182602	335.47037	-18.43412	4.53	47.302 ± 0.018	9.85 ± 0.10	-0.06 ± 0.10	XQz5
222357−252634	335.99112	-25.44284	4.80	46.942 ± 0.026	9.16 ± 0.16	0.27 ± 0.16	XQz5
222509−001406	336.28827	-0.23523	4.89	46.700 ± 0.040	9.27 ± 0.11	-0.08 ± 0.12	T11
222612−061807	336.55173	-6.30200	5.10	46.516 ± 0.015	9.35 ± 0.05	-0.35 ± 0.05	XQz5
222845−075755	337.18805	-7.96533	5.16	46.323 ± 0.032	8.95 ± 0.07	-0.14 ± 0.08	XQz5
223953−055220	339.97360	-5.87223	4.56	47.197 ± 0.012	9.64 ± 0.05	0.04 ± 0.05	XQ100
230349−063343	345.95496	-6.56195	4.74	47.052 ± 0.014	9.89 ± 0.09	-0.35 ± 0.09	XQz5
230429−313426	346.12454	-31.57416	4.87	47.181 ± 0.013	9.93 ± 0.13	-0.26 ± 0.13	XQz5
232536−055328	351.40268	-5.89114	5.23	46.998 ± 0.015	9.75 ± 0.13	-0.26 ± 0.13	XQz5
232952−200039	352.46988	-20.01085	5.04	47.162 ± 0.011	9.59 ± 0.06	0.06 ± 0.06	XQz5
233435−365708	353.64703	-36.95247	4.72	46.990 ± 0.019	9.51 ± 0.29	-0.04 ± 0.29	XQz5
233505−590103	353.77440	-59.01755	4.53	47.262 ± 0.010	9.84 ± 0.06	-0.09 ± 0.06	XQz5
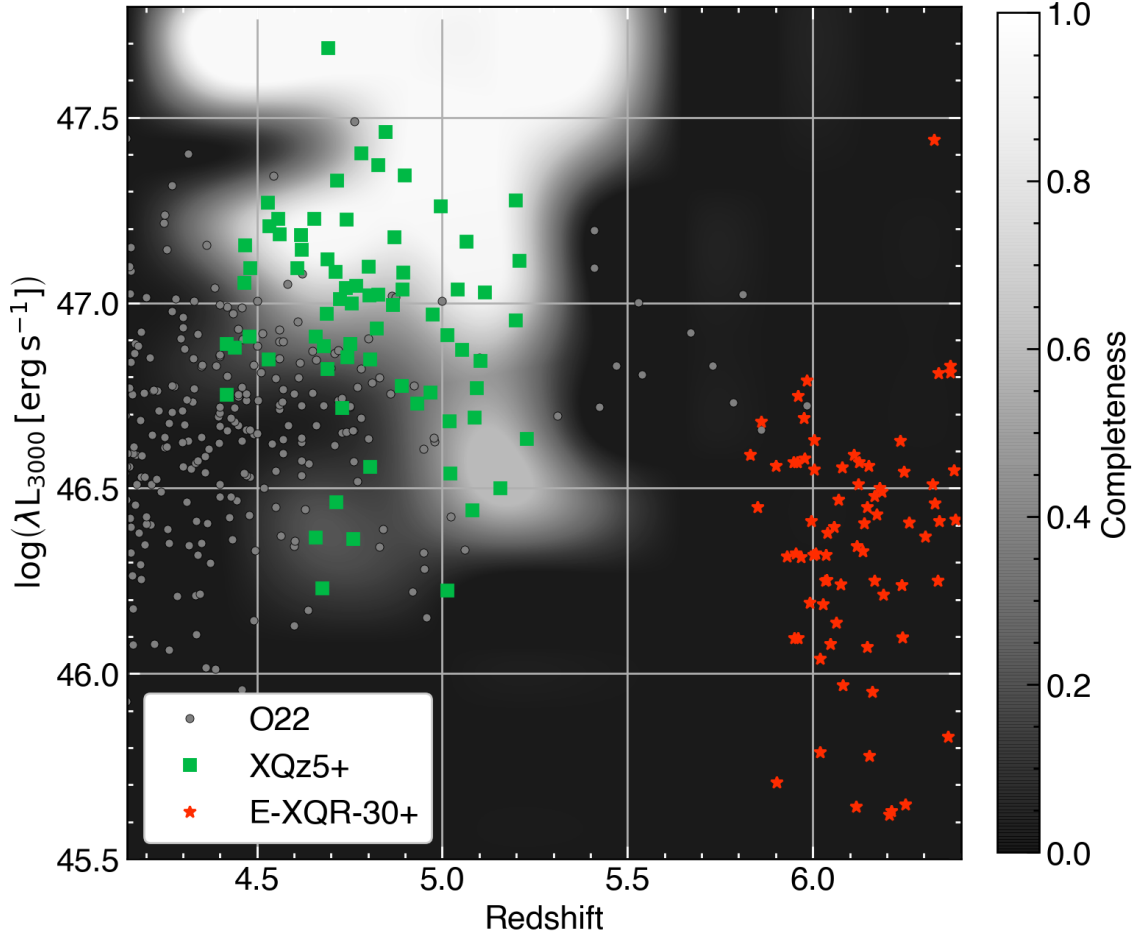
Figure 4.1: Completeness function on a 2-D grid of luminosity and redshift, where the photometric and spectroscopic completeness is mapped onto the parameter space in grayscale. Each quasar in the O22 parent sample is shown with a gray point, and the quasars with spectroscopic follow-up that we use in the $z \sim 5$ analysis are overplotted as green squares. We estimate the completeness of the spectroscopic follow-up down to $z = 5.4$, where the parent sample is assumed to be incomplete. We show E-XQR-30+ with red stars as a high-redshift comparison sample.

is a key component in the developing picture of supermassive black hole origins and growth mechanisms. Here, we describe the method used in this study to measure and parameterise the observed black hole mass function.

In the XQz5+ sample, black hole masses are estimated from near-infrared spectroscopic observations of the Mg II $\lambda2799$ broad emission line with the single-epoch virial mass estimator of Shen et al. (2011), which is calibrated to the H$\beta\lambda4863$ line in a high-luminosity subset of the local AGN reverberation mapping sample. The single-epoch virial mass equation takes the form,

$$\left(\frac{M_{\mathrm{BH,vir}}}{M_\odot}\right) = 10^a \left[\frac{L(3000)}{10^{44}\,\mathrm{erg\,s^{-1}}}\right]^b \left[\frac{\mathrm{FWHM_{Mg\,II}}}{1000\,\mathrm{km\,s^{-1}}}\right]^c , \tag{4.2}$$

where $L(3000)$ is the monochromatic luminosity (λL_λ) of the quasar continuum model at 3000Å and $\mathrm{FWHM_{Mg\,II}}$ is the measured full-width at half-maximum of the Mg II broad line profile. The calibration from Shen et al. (2011) is $(a, b, c) = (6.74, 0.62, 2.00)$. Intrinsic scatter of the virial mass estimator is ~ 0.3 dex compared to their reverberation mapping counterparts (Dalla Bontà et al. 2020) and this systematic uncertainty is typically more significant than the measurement uncertainties propagated from the FWHM and continuum luminosity.

The binned black hole mass function between $z_{\min} < z < z_{\max}$ is defined following the commonly used $1/V_{\max}$ method (Schmidt 1968; Avni & Bahcall 1980; Page & Carrera 2000),

$$\Phi(M_{\mathrm{BH}}, z) = \frac{1}{\Delta \log M_{\mathrm{BH}}} \sum_{i=1}^{N_{\mathrm{BH}}} \frac{f_{\mathrm{obs}}^{-1}}{\int_{z_{\min}}^{z_{\max}} \Omega(L_i, z)\frac{dV}{dz} dz} , \tag{4.3}$$

where $f_{\mathrm{obs}} \sim 0.351$ is the sky area coverage of our parent sample, $\Omega(L, z)$ is the 2-D completeness correction from Equation 4.1, and dV/dz is the differential comoving volume element. We estimate Poisson statistical uncertainties for each point in the binned mass function.

Black hole luminosity functions are often parameterised as a double power-law (e.g. Yang et al. 2016; Akiyama et al. 2018; Matsuoka et al. 2018b; Niida et al. 2020; Onken et al. 2022a; Matsuoka et al. 2023), tracing back to earlier studies (Boyle et al. 2000) that observe a flattening of the luminosity function at fainter magnitudes. We choose to parameterise the observed mass function at redshift z with the same double power-law described by,

$$\Phi_z(M_{\mathrm{BH,z}}) = \frac{\Phi(M_{\mathrm{BH}}^*)}{(M_{\mathrm{BH,z}}/M_{\mathrm{BH}}^*)^{-(\alpha+1)} + (M_{\mathrm{BH,z}}/M_{\mathrm{BH}}^*)^{-(\beta+1)}} , \tag{4.4}$$

where M_{BH}^* is the turnover black hole mass, $(\alpha',\ \beta')$ are the low- and high-mass slopes, and $\Phi(M_{\mathrm{BH}}^*)$ is the normalisation. We translate the observed mass function to other redshifts through the continuity equation described in Section 4.2.3. Model parameters can be derived from fitting the $1/V_{\mathrm{max}}$ binned mass function.

We note that the $1/V_{\mathrm{max}}$ approach does not consider the error function in the virial black hole mass estimates or black hole mass selection incompleteness, because the selection function is luminosity-dependent. The $1/V_{\mathrm{max}}$ approach will also exhibit a heavy bias due to a steep intrinsic mass function or a wide error distribution. Therefore, we caution that the derived mass function and its model does not necessarily reflect the intrinsic black hole mass function. However, two intrinsic mass functions separated by a measurable evolution would be equally transformed by convolution with homoscedastic error distributions. Therefore, a study of the differential mass evolution is unaffected by this bias.

The $1/V_{\mathrm{max}}$ method produces a model-independent estimate and as such, the results are not sensitive to assumptions of the error function or the Eddington ratio distribution. The Eddington ratio is the luminosity of the quasar as a fraction of its Eddington luminosity, defined as $\lambda \equiv L_{\mathrm{bol}}/L_{\mathrm{Edd}}$, where $L_{\mathrm{Edd}} = 1.26 \times 10^{38}\,(M_{\mathrm{BH}}/M_\odot)\,\mathrm{erg\,s^{-1}}$. In this study, we estimate $L_{\mathrm{bol}} = 0.75 \times k_{\mathrm{BC}} \times L_{3000}$ based on a quasar mean spectral energy distribution (SED) ($k_{\mathrm{BC}} = 5.15$; Richards et al. 2006) and a 25% anisotropy correction (Runnoe et al. 2012). We caution that L_{3000}-dependent bolometric correction factors as low as $k_{\mathrm{BC}} = 2.5$ for $\log(L_{3000}/\mathrm{erg\,s^{-1}}) = 47.0$ have been suggested by thermal accretion disc models (Netzer 2019), which primarily cover the "big blue bump" of the quasar SED (Shields 1978). Another method using the $1\,\mu\mathrm{m} - 8\,\mathrm{keV}$ integrated SED is more consistent with Richards et al. (2006), suggesting $k_{\mathrm{BC}} = 4.75$ for $\log(L_{3000}/\mathrm{erg\,s^{-1}}) = 47.0$ (Runnoe et al. 2012). Significant differences in black hole mass or continuum luminosity between samples can have a second-order effect on the bolometric luminosity and hence the derived Eddington ratio by nature of the luminosity-dependent bolometric correction.

If it is unlikely that a significant population of massive quiescent black holes exists at these redshifts, then the observed mass function approximates the intrinsic mass distribution. This picture is supported by high-redshift cosmological hydrodynamical simulations (e.g. Li et al. 2007; Sijacki et al. 2009; Bhowmick et al. 2022) which find that accretion-driven growth becomes highly efficient by $z \sim 6$ and the most massive black holes are also accreting close to the Eddington limit. This is in contrast to lower-redshift ($z < 4$) observations (e.g. Barger et al. 2005; Vestergaard & Osmer 2009; Kelly et al. 2010; Willott et al. 2010a) and simulations (e.g. Di Matteo

et al. 2008; Sijacki et al. 2015; Volonteri et al. 2016), which find clear signatures of "cosmic downsizing" where the brightest AGN shift to lower black hole masses and the overall energy density production of AGN drops rapidly with decreasing redshift. One possibility to explain this occurrence is the preferential mass starvation of the most massive black holes at low redshift. However, the often poorly-constrained low-Eddington regime is not expected to play a role in this $z \sim 5$ study.

The general prevailing picture that emerges is that quasar activity follows two distinct phases across cosmic history (Small & Blandford 1992): a sustained active period of Eddington-limited accretion from the plentiful gas supply in high-redshift galaxies, followed by decreased activity or intermittent sub-Eddington accretion as feedback mechanisms clear out the surrounding gas and massive black holes are preferentially starved. The quasar population at $z \sim 5$ is experiencing exponential build-up towards the peak quasar epoch (Schmidt et al. 1995), as supported by the high mean (median) Eddington ratio in XQz5, which is 0.59 (0.58) (Lai et al. 2024), where all quasars in the sample are actively accreting with $\lambda > 0.19$. The underlying Eddington ratio distribution function as shown in Figure 4.2 is consistent with a log-normal function,

$$\rho_\lambda = \frac{1}{\sqrt{2\pi}\sigma_\lambda} \exp\left\{\left(-\frac{\log\lambda - \langle\log\lambda\rangle}{2\sigma_\lambda^2}\right)\right\}, \qquad (4.5)$$

where $\langle\log\lambda\rangle$ is the mean Eddington ratio, and σ_λ is the log standard deviation. Our Eddington ratio distribution is plotted with H23 at $z \sim 4$ and E-XQR-30+ at $z \sim 6$, where each distribution is represented with a mean log-normal model and uncertainty reflected by the shaded region. We note that the three datasets are derived from surveys reaching different depths. Therefore, their Eddington ratio distribution functions are not directly comparable. Furthermore, the E-XQR-30+ Eddington ratio distribution is not adjusted for incompleteness, because this dataset was compiled from inhomogeneous samples such that its selection function is not well-defined. The effect of a flux-dependent selection limit, if applied, is likely to broaden the $z \sim 6$ distribution and lower the mean Eddington ratio.

Although there are multiple other functional forms that can be adopted for the Eddington ratio distribution, such as the Schecter function, a log-normal function is well-matched to the low Eddington turnover in these distributions (e.g. Kollmeier et al. 2006; Willott et al. 2010a; Shen & Kelly 2012; Shen et al. 2019a; Farina et al. 2022). However, it's possible that flux-limited detection can emulate the turnover and underestimate the low Eddington population in the intrinsic distribution (e.g. Schulze et al. 2015; Li et al. 2023a). The best fit to our distribution of 72 XQz5+

Table 4.2:   Binned Eddington ratio distribution function for XQz5+ at $z \sim 5$ estimated by the $1/V_{\mathrm{max}}$ approach.

$\log L_{\mathrm{bol}}/L_{\mathrm{Edd}}$	N_{QSO}	$\Phi(L_{\mathrm{bol}}/L_{\mathrm{Edd}})$ 10^{-9} Mpc^{-3} dex^{-1}
-0.63	5	18.41 ± 17.88
-0.45	12	1.73 ± 0.53
-0.26	24	2.71 ± 0.71
-0.08	17	2.03 ± 0.59
0.10	8	1.13 ± 0.55
0.29	5	0.49 ± 0.25
0.47	1	0.23 ± 0.23

quasars within the parent survey footprint is $\langle \log \lambda \rangle = -0.23 \pm 0.05$, with a width of $\sigma_\lambda = 0.29 \pm 0.04$ dex, which is a similar Eddington ratio distribution to the $z \sim 6$ sample (Mazzucchelli et al. 2023; D'Odorico et al. 2023; Fan et al. 2023), if the bolometric luminosity estimates are also corrected with the same 0.75 anisotropy correction factor.

4.2.3   Continuity equation

The time evolution of an accretion-dominated black hole mass function can be described by the following continuity equation (Shankar et al. 2013; Tucci & Volonteri 2017),

$$\frac{\delta \Phi(M_{\mathrm{BH}}, t)}{\delta t} = -\frac{\delta \left[\langle \dot{M}_{\mathrm{BH}} \rangle \Phi(M_{\mathrm{BH}}, t) \right]}{\delta M_{\mathrm{BH}}}, \tag{4.6}$$

where every black hole grows constantly at the mean accretion rate, $\langle \dot{M}_{\mathrm{BH}} \rangle$. In practice, this picture is complicated by the duty cycle, which is the fraction of black holes in the active state, and merger events, which redistribute mass. To develop a more complete picture, we relate the Eddington ratio to the mass accretion rate by the radiative efficiency, $\epsilon \in (0, 1]$,

$$\dot{M}_{\mathrm{BH}} = \frac{(1 - \epsilon)\lambda}{\epsilon} \frac{L_{\mathrm{Edd}}}{c^2}, \tag{4.7}$$

which simplifies to an exponential mass growth with an e-folding time of $450\lambda^{-1}\epsilon(1 - \epsilon)^{-1}$ Myr (Salpeter 1964). In a more general picture, the mean mass accretion rate can be written with the expectation value for Eddington ratio, which is

$$\langle \dot{M}_{\mathrm{BH}} \rangle = \int d \log \lambda P(\lambda | M_{\mathrm{BH}}, z) \lambda U(M_{\mathrm{BH}}, z) \frac{M_{\mathrm{BH}}}{450 \, \mathrm{Myr}} \frac{(1 - \epsilon)}{\epsilon}, \tag{4.8}$$
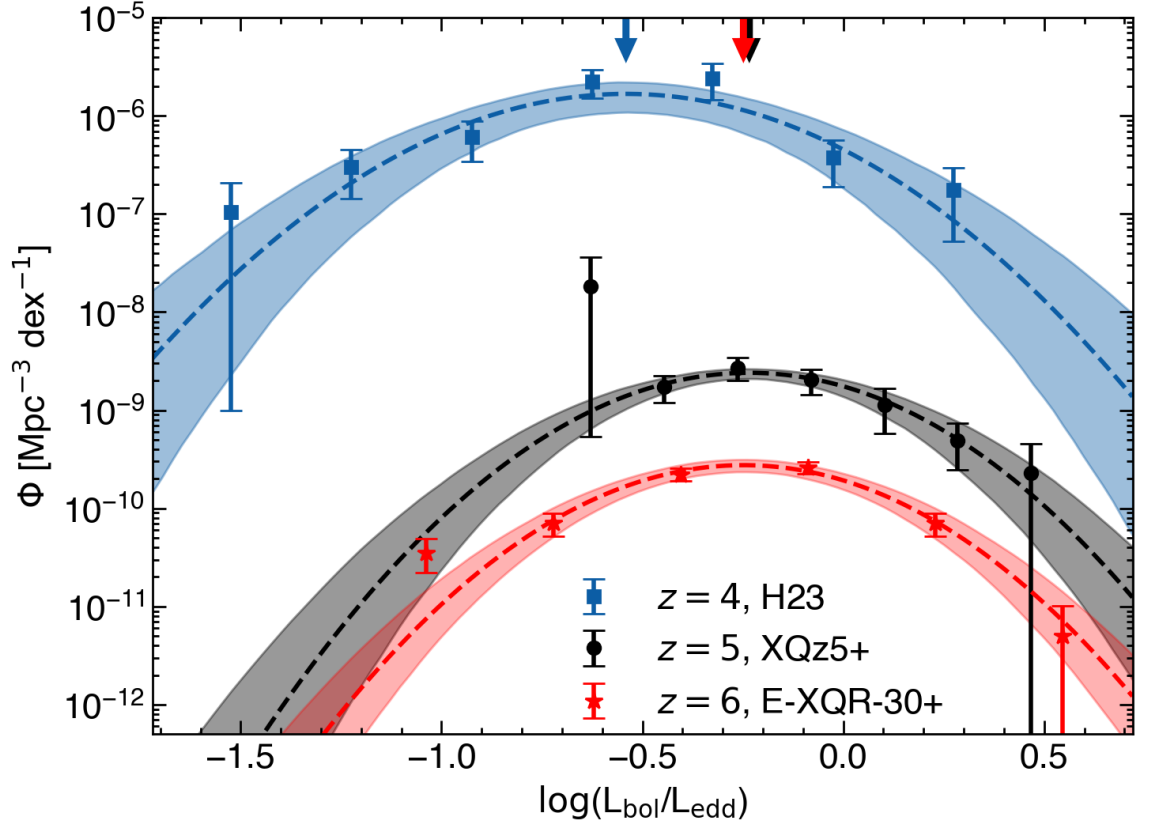
Figure 4.2: Eddington ratio distribution functions of XQz5+ (black circles) alongside H23 (blue squares) at $z \sim 4$ and E-XQR-30+ (red stars) at $z \sim 6$. Mass function model lines share the same colour as the points. The three datasets are derived from surveys which reach different depths. As such, their Eddington ratio distribution functions are not directly comparable. Furthermore, the E-XQR-30+ distribution function is not corrected for completeness. The Eddington ratio distribution of XQz5+ is best fit with a log-normal function, with a mean of $\langle \log \lambda \rangle = -0.23$ and the width of 0.29 dex. The mean value, indicated with the arrows on the top of the plot, is constrained to $\log(L_{bol}/L_{Edd}) = -0.54 \pm 0.06$ for H23, -0.23 ± 0.05 for XQz5+, and -0.25 ± 0.04 for E-XQR-30+.

where $P(\lambda|M_{\mathrm{BH}}, z)$ is the normalised Eddington ratio probability distribution and $U(M_{\mathrm{BH}}, z) \in [0, 1]$ is the duty cycle. In this study, our approach is to observationally estimate the effective e-folding time under the assumption of time invariance of the radiative efficiency and Eddington ratio distribution over the observed period as well as constant duty cycle U. We define a dimensionless growth rate scale factor,

$$k_{\mathrm{ef}} \equiv \frac{450\,\mathrm{Myr}}{t_{\mathrm{ef}}} = \frac{\langle \lambda \rangle U(1 - \epsilon)}{\epsilon}\,, \tag{4.9}$$

which behaves as a joint constraint on the unknown parameters (ϵ, U), for an underlying Eddington ratio distribution, $P(\lambda|M_{\mathrm{BH}}, z)$.

Standard thin accretion disc models predict that the radiative efficiency is a non-linear, but monotonic function of black hole spin. In the local universe, the fiducial value for the radiative efficiency based on the Sołtan argument (Soltan 1982) applied to the local black hole mass density is $\epsilon = 0.1$ (Yu & Tremaine 2002), which corresponds to a black hole spin of $a \sim 0.7$. For individual quasars, observational constraints on the radiative efficiency can be obtained with X-ray reflection measurements or thermal continuum modelling (see review by Reynolds 2019). Estimates obtained from inhomogeneous quasar samples at higher redshifts are not significantly different from the local fiducial value (e.g. Capellupo et al. 2015; Vasudevan et al. 2016; Trakhtenbrot et al. 2017; Reynolds 2021, and references therein), which may be expected as massive black holes are expected to be spun up by prolonged periods of coherent accretion (Dotti et al. 2013; Volonteri et al. 2013; Dubois et al. 2014; Trakhtenbrot 2014; Capellupo et al. 2015; Ananna et al. 2020). However, radiatively inefficient accretion from uncorrelated flows (King et al. 2005, 2008) may be a mechanism by which the most extreme mass black holes could be produced at high redshift (King & Pringle 2006; Zubovas & King 2021). Constraints on the black hole spin for the highest mass quasars can be obtained by the proxy of the radiative efficiency.

Observational constraints on quasar lifetimes and duty cycle based on clustering suggest that luminous high-redshift (up to $z \sim 4-5$) quasars are biased towards rare massive haloes (Shen et al. 2007; White et al. 2008). Subsequent modeling efforts predict that the duty cycle must therefore be high, with $U \sim 0.5$ at $z \sim 4.5$ to $U \sim 0.9$ at $z \sim 6$ (Shankar et al. 2010), which is also supported by clustering simulations (DeGraf & Sijacki 2017). A high duty cycle implies that most of the massive black hole population in the mass function is reflected in observations. However, these results are at odds with measurements from the sizes of quasar proximity zones (e.g. Fan et al. 2006; Eilers et al. 2017, 2018; Khrykin et al. 2019; Eilers et al.

2020; Morey et al. 2021; Khrykin et al. 2021; Satyavolu et al. 2023b), which often measure lifetimes shorter than 10^7 yrs and sometimes $< 10^5$ yrs even at $z \sim 6$. One possible explanation for the discrepancy is that quasar light curves are described by a flickering model (Ciotti & Ostriker 2001; Novak et al. 2011; Oppenheimer & Schaye 2013; Schawinski et al. 2015; Davies et al. 2020; Satyavolu et al. 2023a) instead of a standard light bulb. Proximity zone studies probe timescales of the most recent emission episode, which can be orders of magnitude shorter than the overall active fraction in a flickering model. Another possibility is that quasars spend a considerable amount of time growing in an obscured phase in their evolution (e.g. Hopkins et al. 2005), which implies a significant fraction of obscured quasars at high redshift (Davies et al. 2019; Ni et al. 2020; Satyavolu et al. 2023a), at a much higher ratio than observations at lower redshifts (e.g. Lawrence & Elvis 2010; Assef et al. 2015). Thus, the black hole mass function derived in this study would only reflect the active and unobscured subset of the underlying black hole population.

While black hole mergers do not alter the total mass in the population, they can still modify the shape of the mass function through redistribution. This can potentially affect the inferred evolution from the continuity equation if mergers play a critical role in growing the highest mass quasars over the probed redshift range. Theoretical and simulation-based works generally suggest that black hole mergers may play an important role at early times ($z \gtrsim 9$) to provide an early boost to black hole masses (Valiante et al. 2016; Bhowmick et al. 2022) and at late times ($z \lesssim 2$) when galaxies are comparatively gas-starved (Shankar et al. 2013; Dubois et al. 2014; Kulier et al. 2015). However, the majority of the assembled black hole mass can be attributed to secular processes (Martin et al. 2018). We also note that there are numerous studies in this space with a diversity of assembly histories capable of producing the high black hole masses observed at $z \sim 6$ (Li et al. 2007; Sijacki et al. 2009; Costa et al. 2014; Feng et al. 2014; Smidt et al. 2018; Valentini et al. 2021; Zhu et al. 2022a), where the differences originate from the adopted accretion and feedback models. This highlights how continued work in this area will require improved observational constraints on high redshift supermassive black holes.

4.3 Results and Discussion

We apply the model described in Section 4.2 to the XQz5+ data using the maximum likelihood approach and compare the result to a $z \sim 4$ mass function (He et al. 2023). The observed evolution between these samples suggests an effective e-folding time for accretion-dominated growth based on the continuity equation. We compare this
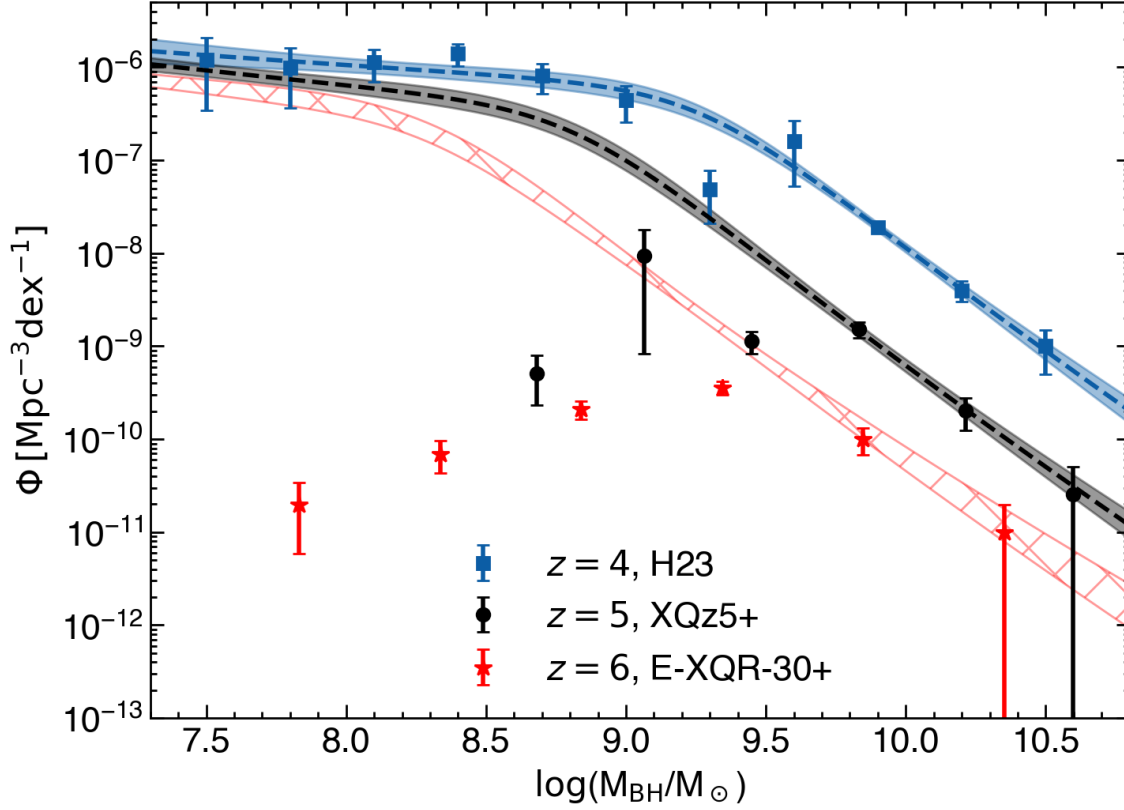
Figure 4.3: Black hole mass functions of XQz5+ (black circles) with H23 (blue squares) at $z \sim 4$ and E-XQR-30+ (red stars) at $z \sim 6$. The binned values are estimated with the $1/V_{max}$ method, but the E-XQR-30+ mass function is not corrected for completeness. We plot the double power-law mass function models and the hatched model is the prediction for $z \sim 6$ assuming a constant growth of $k_{ef} = 1.62$, estimated between $z = 5 - 4$, and extrapolated onto $z \sim 6$ from $z \sim 5$.

value to what we measure internally within our sample through the integrated mass density and we construct a mock universe simulation from the derived model mass functions to estimate Monte Carlo uncertainties. Finally, we discuss the implications of the measured mass evolution on the duty cycle and the radiative efficiency. We also derive the expected mass function at $z \sim 6$ and compare with results from the literature.

4.3.1   XQz5 mass function and evolution

In this section, we first discuss the XQz5+ $z \sim 5$ binned black hole mass function. We then discuss two methods by which the dimensionless growth rate, k_{ef} in Equation 4.9, is estimated, either between redshifts $z = 5 - 4$ or within $z \sim 5$. We compare the results and use a mock universe simulation to estimate the Monte Carlo uncertainties.

Table 4.3:   Binned black hole mass function for XQz5+ at $z \sim 5$ estimated by the $1/V_{\mathrm{max}}$ approach.

$\log M_{\mathrm{BH}}/M_\odot$	$\mathrm{N_{QSO}}$	$\Phi(M_{\mathrm{BH}})$ 10^{-9} Mpc^{-3} dex^{-1}
8.68	4	0.51 ± 0.28
9.06	9	9.37 ± 8.54
9.45	18	1.13 ± 0.30
9.83	33	1.52 ± 0.30
10.21	7	0.20 ± 0.08
10.60	1	0.03 ± 0.03

Growth between $z = 5 - 4$

The binned mass function of XQz5+, measured with the $1/V_{\mathrm{max}}$ method described in Equation 4.3, clearly shows an artificial turnover at $\log\left(\mathrm{M_{BH}/M_\odot}\right) \lesssim 9.5$ due to the sample incompleteness. In order to constrain the low-mass end, we refer to H23, which has constrained the mass function at $z \sim 4$ down to $\log\left(\mathrm{M_{BH}/M_\odot}\right) \sim 7.5$. We first fit their binned black hole mass function for their combined sample using the double power-law model in Equation 4.4 and the optimised parameters are presented in Table 4.4 with associated uncertainties. The $z \sim 4$ model is then transformed to $z \sim 5$ with the continuity equation until the model is optimised to the XQz5+ mass function at $\log\left(\mathrm{M_{BH}/M_\odot}\right) \gtrsim 9.5$. After this, the double power-law is fit to the three most massive XQz5+ bins with the low-mass end constrained by the transformed $z \sim 4$ data. To ensure that we do not bias the high-mass model, we do not use the highest mass bins of the H23 mass function in the model at $z \sim 5$. The optimised mass function parameters are presented in Table 4.4 with associated uncertainties.

Both the H23 $z \sim 4$ and XQz5+ $z \sim 5$ binned mass function with their respective models are presented in Figure 4.3. Although the slope of the $z \sim 5$ model mass function is steeper on the low-mass regime in comparison to the $z \sim 4$ model, the difference is not statistically significant. The turnover mass, M_{BH}^*, has translated horizontally and the normalisation of the mass function also increases with cosmic time. The evolution between the $z \sim 5$ and $z \sim 4$ mass functions implies an effective growth scale factor of $k_{\mathrm{ef}} = 1.62 \pm 0.01$, which is fit to the highest mass data with the lowest uncertainties in H23. The k_{ef} error term does not include uncertainties in the mass functions, their completeness corrections, or cosmic variance, which are the dominant sources of uncertainty. We model this systematic error from mock universe simulations in Section 4.3.1.

Table 4.4: Optimised fit parameters for the black hole mass function double power-law model in Equation 4.4. We fit the model to datasets spanning different redshift ranges. The bolded parameters represent the $z \sim 5$ mass function maximum likelihood fit from this study.

Redshift	Dataset	$\Phi(M^*_{\mathrm{BH}})$ 10^{-7} Mpc^{-3} dex^{-1}	M^*_{BH} $10^x M_\odot$	α	β
$3.50 < z < 4.25$	He et al. (2023)	6.1 ± 1.7	9.28 ± 0.08	-4.7 ± 2.1	-53.8 ± 3.3
$4.50 < z < 5.30$	**This work**	**3.7 ± 1.1**	**8.83 ± 0.10**	**-6.6 ± 1.7**	**-52.5 ± 3.4**
$5.80 < z < 6.40^*$	D'Odorico et al. (2023); Fan et al. (2023)	3.5 ± 1.1	8.33 ± 0.10	-6.4 ± 1.7	-48.4 ± 3.4

*Fit to mock universe model, with uncertainties adopted from the $z \sim 5$ model.

Growth within $z \sim 5$

We present an alternative method to measure the mass evolution within the XQz5+ sample. We first bin the redshift range from $z = 4.5 - 5.2$ into N_{bin} shells of equivalent comoving volume. The redshift range, covering ~ 200 Myr, is selected from a region with more reliable completeness. In each bin, we measure the completeness-corrected total mass of the N_{BH} most massive black holes. We assume that, in each redshift bin, the selected black holes reflect a random sampling from an underlying population of the most extreme supermassive black holes that is growing together with a mean population rate. We then fit the mass in each bin with the standard accretion exponential growth, finding $k_{\mathrm{ef}} = 2.11 \pm 0.25$, representing the mean and median absolute deviation of fits to all combinations of $N_{\mathrm{bin}} = [6, 12]$ and $N_{\mathrm{BH}} = [6, 16]$. The result is $\Delta k_{\mathrm{ef}} \approx 0.5$ greater the observed growth between the ~ 360 Myr from redshifts $z = 5 - 4$. However, the discrepancy is not statistically significant.

Mock universe model

To test the robustness of the k_{ef} measurements, we simulate mock universes and estimate the Monte Carlo uncertainty. We anchor the simulator's reference mass function to the $z \sim 5$ model. The simulator functions by stepping through thin shells of comoving volume over a defined redshift range. We use the continuity equation to evolve the model mass function to the mean shell redshift for a prescribed k_{ef}, and an integrated number of quasars above a chosen mass threshold are randomly generated within each shell based on the probability distribution. The simulator reliably reproduces the reference $z \sim 5$ mass function with the expected Poissonian noise and predicts its evolution across redshifts.

We use the mock universe simulator to estimate the Monte Carlo uncertainty from measuring the mass evolution within the XQz5+ sample which covers ~ 200 Myr of time, finding a systematic uncertainty of $\sigma_{k_{\mathrm{ef}}} = 0.5 - 0.8$ due to Poisson variance from small number statistics. The value of $\sigma_{k_{\mathrm{ef}}}$ is sensitive to the width of the redshift

range under consideration, where performing a measurement across a ~ 700 Myr width results in $\sigma_{k_{\mathrm{ef}}} \sim 0.2$. The uncertainty is also dependent on the number of quasars counted in each bin, but does not change significantly with the number of bins, implying $\sigma_{k_{\mathrm{ef}}} \propto (\sqrt{N_{\mathrm{BH}}}\Delta T)^{-1}$.

Furthermore, we determine the expected Monte Carlo uncertainty from measuring k_{ef} between a mass function derived at $z \sim 5$ and $z \sim 4$, finding a median absolute deviation of $\sigma_{k_{\mathrm{ef}}} \sim 0.06$. Deriving the mass evolution factor between the XQz5+ and H23 dataset, each covering ~ 240 and ~ 360 Myr respectively with ~ 90 Myr in between, is less sensitive to cosmic variance than using the XQz5+ sample on its own.

The experiments performed with the mock universe simulator produce estimates of the uncertainty in the black hole mass growth measured between $z = 5-4$ and within $z \sim 5$ due to cosmic variance. Whichever the method, the uncertainty derived from the mock universe experiments is dominant over the measurement error and we find that this additional systematic uncertainty is most sensitive to the redshift coverage of the sample. We use the results of these experiments to describe the statistical significance of our k_{ef} measurements.

4.3.2 Effective cosmic mass growth

The dimensionless growth factor, defined in Equation 4.9, is measured to be $k_{\mathrm{ef}} = 1.62 \pm 0.01$ from the evolution between the $z \sim 5$ to $z \sim 4$ mass functions or $k_{\mathrm{ef}} = 2.11 \pm 0.25$ from the mass evolution within the XQz5+ sample using the integrated mass of the N_{BH} most massive in a range of redshift bins. The expected Monte Carlo uncertainty derived from the mock universe experiment is $\sigma_{k_{\mathrm{ef}}} > 0.5$ for the mass evolution within XQz5+ and $\sigma_{k_{\mathrm{ef}}} \sim 0.06$ for the change in the mass function between the $z \sim 5$ to $z \sim 4$ quasar samples. There is no evidence of a change in black hole mass growth rate within the $z \sim 5$ sample and between $z = 5-4$, due to the high uncertainty in the k_{ef} mass evolution within XQz5+.

Based on these results, we present a surface plot in Figure 4.4, adopting a $k_{\mathrm{ef}} = 1.62$ prescription. The plot shows joint constraints on the duty cycle and radiative efficiency for an estimated mean Eddington ratio in the underlying population. Contours of constant radiative efficiency are labelled and plotted as dashed lines. We overplot the expected value, $\langle \lambda \rangle$, of the log-normal Eddington ratio model for XQz5+, marking the mean and standard error with dotted lines. The expectation value is well-constrained to $\langle \log \lambda \rangle = -0.23 \pm 0.05$ or equivalently, $\langle \lambda \rangle = 0.59^{+0.09}_{-0.07}$.

Based on the results in Figure 4.4 where $k_{\mathrm{ef}} = 1.62$, the growth between $z = 5 - 4$ mass functions suggests that the underlying population of black holes could have mean radiative efficiencies of $\epsilon < 0.34$, depending on the duty cycle. Mean radiative efficiencies of $\epsilon > 0.34$ are excluded at the 3σ level, based on the Eddington ratio distribution of the $z \sim 5$ dataset. However, because ϵ is a slow function of the dimensionless black hole spin, a_*, only the highest spin black holes are excluded by $\epsilon < 0.34$. The results are also consistent with the fiducial $\epsilon = 0.10$ efficiency for a duty cycle of $U \sim 0.31$. Alternatively, if the average spin is biased towards low values ($0 \lesssim |a_*| \lesssim 0.3$) expected for chaotic accretion (e.g. King et al. 2008; Berti & Volonteri 2008), then the duty cycle would be in the range $U = 0.17 - 0.21$.

If the high-redshift massive black hole population duty cycle is as low as $U \sim 0.1$, suggested by the standard light bulb model in proximity zone studies (e.g. Khrykin et al. 2021), then the observed growth would require the accretion radiation feedback to be inefficient ($\epsilon \sim 0.03$), which implies that the accretion disc and the black hole spin are counter-aligned. This scenario is plausible if the massive black hole population primarily grows through short episodes of uncorrelated flows (King & Pringle 2006), which prevents the black hole from spinning up (e.g. King et al. 2005; Lodato & Pringle 2006). Spin misalignment, expected from infalling material that is insensitive to the spin direction of the inner accretion disc, could also result in severely warped structures in the accretion disc (e.g. Chatterjee et al. 2020), which can obscure the broad-line region (Lawrence & Elvis 2010). This is also consistent with the prediction of a significant population of obscured quasars at high redshift (e.g. Davies et al. 2019), which we discuss further in Section 4.3.3. Low radiative efficiencies can also be the result of photon trapping in supercritically accreting thick discs (e.g. Ohsuga et al. 2002; Wyithe & Loeb 2012).

At high duty cycles, the measured growth is also consistent with a population of quasars that have been spun up by coherent accretion flows over long episodes. High duty cycles are consistent with clustering studies (e.g. Shen et al. 2007; White et al. 2008), but the constraints on the inferred lifetimes are weak owing to uncertainties in models of quasar-hosting dark matter haloes (e.g. Shen et al. 2009; Cen & Safarzadeh 2015). Additional clarity on the high-redshift quasar duty cycle will enable firmer conclusions on the implied black hole spin, based on the observed mass evolution.

4.3.3   Comparison to $z \sim 6$

We show the $z \sim 6$ mass function measured from the E-XQR-30+ database in Figure 4.3, without applying completeness corrections. For comparison, we evolve
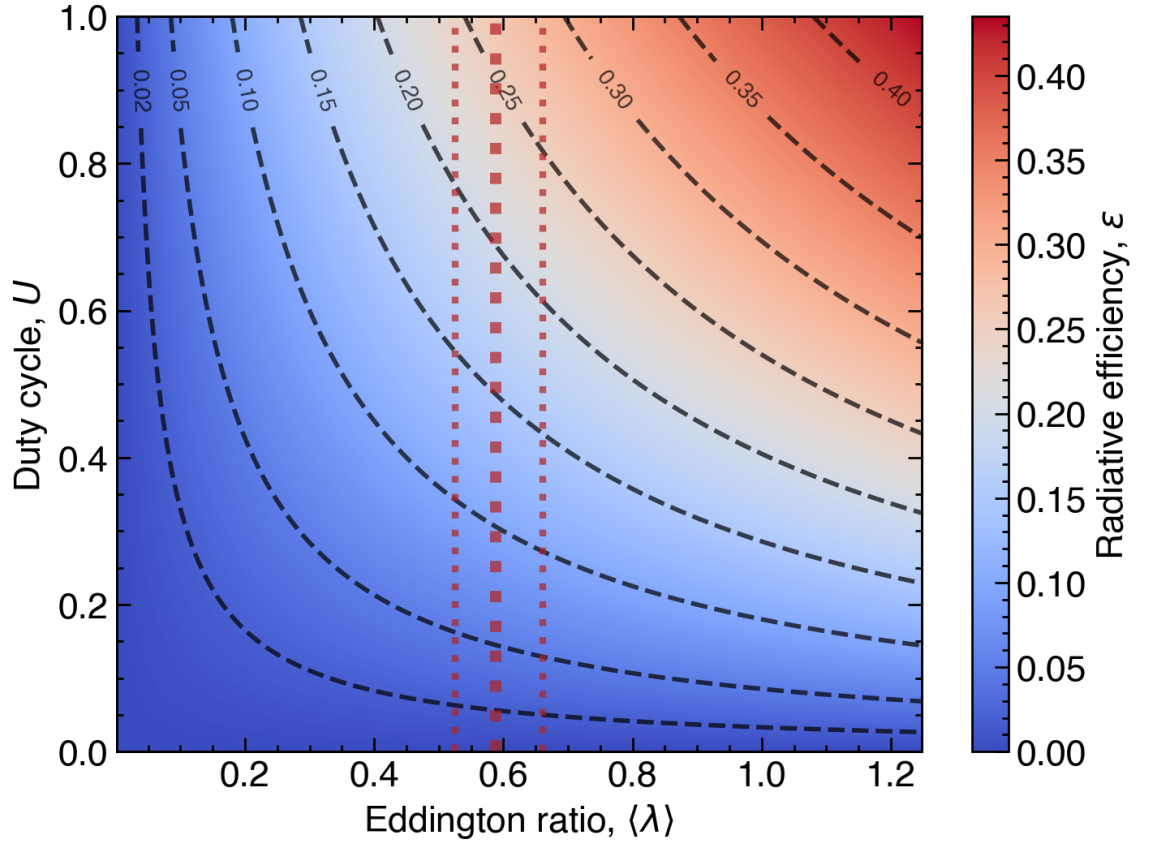
Figure 4.4: Surface plot showing the relationship between the Eddington ratio, duty cycle, and radiative efficiency satisfying Equation 4.9 for $k_{\mathrm{ef}} = 1.62$. We overplot dashed radiative efficiency contours and the uncertainty on the expected value of the XQz5+ Eddington ratio log-normal model as the solid line, which is described by a mean and width of $\langle \log \lambda \rangle = -0.23 \pm 0.05$ dex, shown as vertical dotted lines.
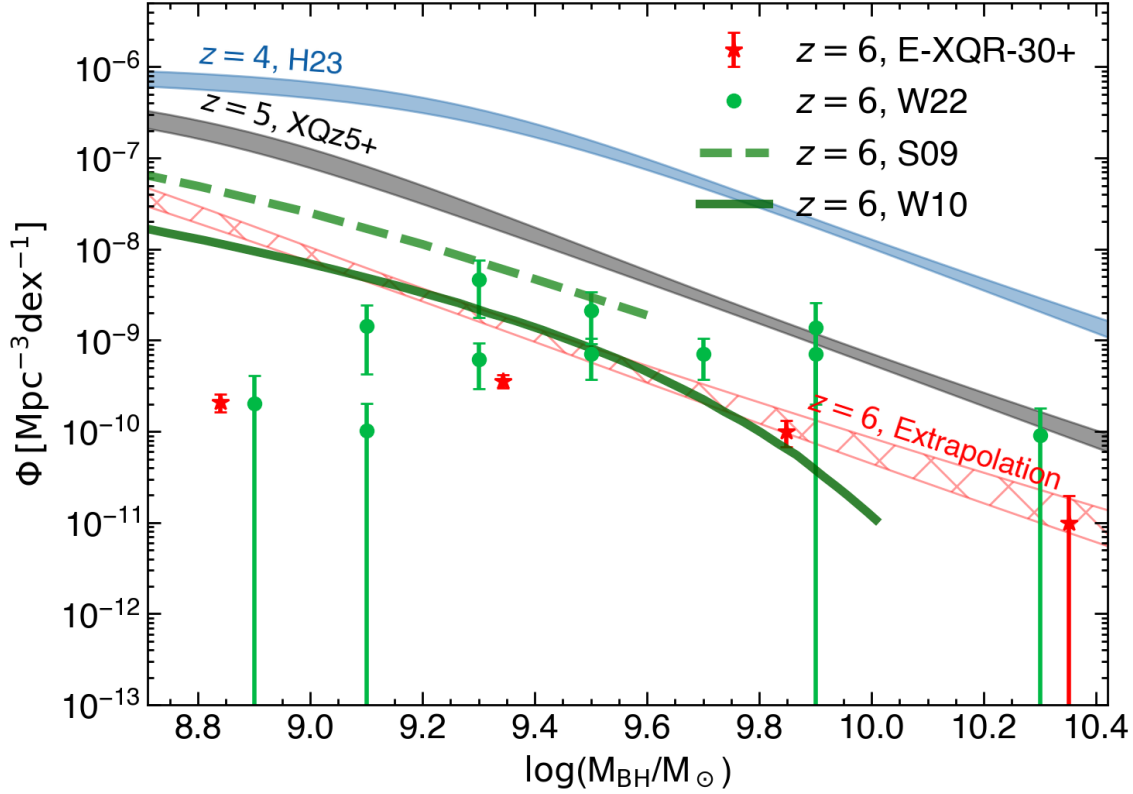
Figure 4.5: Literature estimates of the $z \sim 6$ active black hole mass function compared to the mass function models from Table 4.4 at redshifts $z = 6 - 4$, with the same identifying characteristics as in Figure 4.3. The active black hole mass functions of Willott et al. (2010a) (green solid line), Shankar et al. (2009) (green dashed line), Wu et al. (2022) (green points), and E-XQR-30+ (red stars) are shown. In some of the Wu et al. (2022) mass bins, there are two spatial density estimates, because they consider two quasar samples, each with their own completeness function. We have not corrected E-XQR-30+ for completeness due to heterogeneity in its sample construction.

the $z \sim 5$ mass function model with the dimensionless growth factor $k_{\text{ef}} = 1.62 \pm 0.06$ derived between $z = 5 - 4$ and plot the predicted $z \sim 6$ model with the hatched region. Optimised fit parameters are presented in Table 4.4 and we report parameter uncertainties adopted from the $z \sim 5$ model.

We remark that despite the absence of a completeness correction, the two highest mass binned points of E-XQR-30+ are consistent with the model expectation. Taken at face value, this result would imply that E-XQR-30+ is highly complete $(\Omega(L, z)f_{\text{obs}} > 0.5)$ at the high mass end and it disfavours scenarios where the black holes evolve more rapidly between $z = 6 - 5$ than $z = 5 - 4$. This observation is at odds with the general expectation that black holes in the early Universe need to evolve quickly to reach their observed masses and are decelerating in their growth as seen in the cosmic downsizing phenomenon (e.g. Barger et al. 2005).

Other studies of quasar demographics at $z \sim 6$ (Shankar et al. 2009; Willott et al. 2010a; Wu et al. 2022) generally predict higher quasar abundances than measured from the uncorrected E-XQR-30+. The mass function from the Shankar et al. (2009) study was the result of models fit to the local black hole mass function, the X-ray background, and the luminosity functions at a variety of redshifts up to $z \sim 6$. The black hole masses are translated to luminosities by assuming a constant Eddington ratio of $\lambda = 0.4$ and radiative efficiency of $\epsilon = 0.065$, while the duty cycle $U(z = 6, \log M_{\text{BH}} = 9.5) = 0.5$ is a function of mass and redshift. They have also adopted a correction for the obscured fraction, which is sensitive to AGN luminosity (e.g. Lawrence 1991; Willott et al. 2000; Ueda et al. 2003; Hasinger 2008; Merloni et al. 2014; Ueda et al. 2014), and they used the luminosity-dependent observable fraction, parameterised with a power-law by Hopkins et al. (2007). The Shankar et al. (2009) active black hole mass function can be obtained by applying the inverse of the obscuration correction. In the Shankar et al. (2009) reference model, the duty cycle is relatively flat for high mass $(\log(M_{\text{BH}}/M_\odot) > 9.0)$ black holes, falling from $U(6, 9.5) = 0.5$ to $U(5, 9.5) = 0.2$ and subsequently $U(3, 9.5) = 0.07$. Under this model, much of the mass assembly would already have occurred at even higher redshifts in order for the results to match the local black hole mass function. Thus, in light of the strong duty cycle evolution and difference in radiative efficiency, it is not surprising that the spatial densities in the Shankar et al. (2009) mass function is higher at all masses than our extrapolated mass function.

A separate analysis from Willott et al. (2010a) assumes $\epsilon = 0.09$, a distribution of Eddington ratios centred at $\lambda = 0.6$ with a dispersion of 0.3 dex, and a uniform duty cycle distribution between $U = 0.5 - 1.0$. This model is fit to the Willott et al. (2010b) $z \sim 6$ luminosity function based on 40 quasars. In the Willott et al. (2010b)

study, the additional correction factor for obscured quasars was also included, which raises the space density of both the luminosity function and the black hole mass function. Compared to the Shankar et al. (2009) mass function, the Willott et al. (2010a) black hole mass function was determined to be considerably lower by a factor of ~ 3. By transforming the Willott et al. (2010a) obscuration-corrected mass function into the expected active black hole mass function, we find a result that is consistent with the $z \sim 6$ mass function extrapolated from the evolution between $z = 5 - 4$, except for the high-mass regime where their mass function is steeper.

The Wu et al. (2022) mass function utilised a sample of 29 quasars with mostly Mg II-based virial black hole mass estimates and just over 100 quasars with M_{1450} estimates from a fixed power-law continuum extrapolation. The quasars with black hole mass estimates are split into two samples (see Jiang et al. 2016), hence there can be two estimates for the spatial density in the same mass bin. At high masses, the Wu et al. (2022) binned spatial density is more consistent with the $z \sim 5$ spatial density than with other $z \sim 6$ mass functions. We estimate a mass growth factor of $k_{\rm ef} = 1.5 - 1.8$ between the Wu et al. (2022) $z \sim 6$ and the H23 $z \sim 4$ binned mass functions, depending on the sample under consideration. Although the result is consistent with the $z = 5 - 4$ growth rate, the Wu et al. (2022) completeness corrections are highly uncertain (L. Jiang, priv. comm.).

We plot the discussed literature active black hole mass functions in comparison to the model mass functions from Table 4.4 in Figure 4.5 and we reproduce the binned mass function measured from E-XQR-30+. The mass functions from Shankar et al. (2009) and Willott et al. (2010a) have been corrected to the active black hole mass function by removing the duty cycle and obscuration fraction corrections. The hatched $z \sim 6$ model is extrapolated from the evolution between $z = 5 - 4$. E-XQR-30+ is a much larger heterogeneously constructed sample of quasars with Mg II-based black hole mass estimates and it serves as a sensible lower-bound for the $z \sim 6$ quasar space density. At the high mass end, we observe that the Wu et al. (2022) $z \sim 6$ spatial densities are of similar magnitude as our XQz5+ $z \sim 5$ sample while the Shankar et al. (2009) mass function lies above our $z \sim 6$ extrapolated model for all masses. In the following sections, we list and discuss several limitations in our study that can affect the measured growth rate, the extrapolation to $z \sim 6$, and explanations for discrepancies between mass functions from different studies.

Overestimated completeness?

It is possible that the high flux completeness, $\Omega(L, z)$, of our parent sample at $z \sim 5$ does not translate directly to a high completeness in black hole mass as previously assumed. This would be the case if there exists a significant fraction of obscured, quiescent, or low-Eddington quasars with massive black holes. If the active fraction also evolves over the redshift range of $z = 6 - 4$, then the differential correction across mass functions at different redshifts would also capture this time-dependence, limiting the ability to interpret the observed growth in terms of accretion properties. There are indications that the obscured fraction is more significant at higher redshifts than at lower redshifts (e.g. Davies et al. 2019; Vijarnwannaluk et al. 2022), which would cause the mass functions to diverge. Clustering studies suggest that changes to the obscuration fraction may be secondary to the redshift evolution in the duty cycle (Porciani et al. 2004; Porciani & Norberg 2006; Shen et al. 2007), which describes a general decline in quasar activity over the age of the universe across all masses. The high space density in the massive black hole population observed at $z \sim 4$ (He et al. 2023) and the consistency in the mass function slope in the $z = 6 - 4$ redshift range suggest that the most massive black holes have yet to turn off and move to lower luminosities, as described by cosmic downsizing (e.g. Barger et al. 2005; Vestergaard & Osmer 2009; Kelly et al. 2010). More work is needed to understand the population of obscured quasars and the quasar duty cycle at high redshift.

Overestimated black hole masses?

Overestimated black hole masses can have a significant effect on the black hole mass function. Black hole masses can be overestimated in a systematic fashion when measurements of the most massive black holes are the result of the long tail of the virial black hole mass estimate error function or when mass estimates are derived from different emission-lines with separate calibrations. We first remark that the H23 $z \sim 4$ black hole masses are derived from the broad C IV emission-line, whereas the $z \sim (5, 6)$ samples use the Mg II line. The C IV line is more likely to be affected by non-virial motions (e.g. Proga et al. 2000; Shen & Liu 2012; Saturni et al. 2018), which motivated the development of new calibrations with correction factors for the C IV blueshift (Coatman et al. 2016, 2017). H23 investigated an alternative mass calibration (Park et al. 2017), which sought to compensate for the peculiarities of C IV. This led to a much tighter black hole mass distribution centred at lower masses, which would imply a steeper bright-end slope and lower-mass turnover in the $z \sim 4$ mass function. Our analysis would then have overestimated the growth in the most massive black holes between $z = 5 - 4$, consistent with slow evolution

between $z = 6 - 5$. However, H23 ultimately disfavoured this alternative scenario on account of the lack of high-mass calibrations sources and the abandonment of a virial-like dependence on the line width.

Black hole masses estimated from single-epoch virial mass estimates depend on a high-luminosity extrapolation of the radius-luminosity relationship from reverberation mapping experiments (McLure & Dunlop 2004; Shen et al. 2011). Reverberation mapping campaigns focused on high-redshift and high-luminosity quasars are expensive due to the large broad-line region sizes and cosmological time dilation, which necessitates long-term monitoring programmes. Recent results on high-luminosity quasars (e.g. Lira et al. 2018; Hoormann et al. 2019; Grier et al. 2019; Kaspi et al. 2021) suggest a shallower radius-luminosity than measured in McLure & Dunlop (2004), which is more consistent with the photoionisation expectation of $R \propto L^{0.5}$. Black hole masses that are over-sensitive to the observed luminosity could obfuscate the underlying mass growth rates of the population, artificially boosting the apparent mass evolution when there is luminosity evolution.

Next, we observe that the two highest mass bins of the $z \sim 6$ mass function from Wu et al. (2022), which appear to deviate from the mass function of Willott et al. (2010a), contain only 5 quasars, including J0100+2802 ($z = 6.3$), which is the sole occupant of the highest mass bin. The derived spatial densities are then boosted by large correction factors. The black hole mass of J0100+2802 adopted in Wu et al. (2022) is arguably mildly overestimated based on new James Webb Space Telescope spectra (Eilers et al. 2023). Furthermore, nothing else in the E-XQR-30+ database, which includes quasars over a much larger sky area, has a luminosity comparable to J0100+2802, which is more luminous by a factor of ten over the second most luminous quasar. This makes J0100+2802 a one-of-a-kind outlier. It is also notable that, while the redshift coverage of Wu et al. (2022) extends to $z = 6.42$, the space between $6.31 < z < 6.42$ is void of any quasars and two of the three quasars at $z > 6.3$ are among the four most massive quasars in the entire sample to the extent that excluding quasars at the under-complete $z > 6.3$ space has a dramatic effect on the mass function in the highest mass bins. By excluding quasars at $z > 6.3$, the Wu et al. (2022) binned mass function at $\log(M_{\rm BH}/M_\odot) > 9.2$ becomes consistent within 1σ with the $z \sim 6$ extrapolated model.

Another way that the black hole masses can be overestimated is if they represent the tail end of the virial black hole mass error function. Because of the precipitous decline in abundance in the high mass regime, lower-mass black holes are more likely to be scattered high by a symmetric error function. However, our quasars are selected by luminosity and not black hole mass, which is proportional to mass by $M_{\rm BH} \propto L^b$

in Equation 4.2, where $b = 0.5$ under standard photoionisation calculations and $b = 0.62$ in the Shen et al. (2011) calibration. This has a weaker effect on the black hole mass than the measured full-width at half maximum, to which the black hole mass is correlated by $M_{\rm BH} \propto {\rm FWHM}^2$, based on the virial theorem. Because the scatter in FWHM is not systematically biased by our luminosity selection, any mass bias resulting from a fixed virial mass estimate error distribution would cancel out in a differential growth analysis between redshifts.

Slower growth between $z = 6 - 5$?

The $1/V_{\rm max}$ binned mass function measured with the E-XQR-30+ database disfavours scenarios where the mass growth between $z = 6 - 5$ is more rapid than between $z = 5 - 4$. Instead, the completeness corrected $z \sim 6$ active black hole mass functions (Shankar et al. 2009; Willott et al. 2010a; Wu et al. 2022) suggest that the evolution from $z = 6 - 5$ could be even more gradual, which is counter to the general expectation that black holes in the early Universe need to evolve quickly to match observed masses at high-redshift. In principle, the slow growth of massive black holes from $z = 6 - 5$ can be caused by cosmic downsizing, where the highest mass black holes are experiencing preferential mass starvation and turning off, but it is inconsistent with the more rapid growth seen between $z = 5 - 4$, unless the black hole masses in H23 are overestimated by uncorrected C IV virial estimates.

The evolution of the quasar luminosity function is potentially enhanced between $z = 6.0 - 5.5$ compared to $z = 5.5 - 5.0$ (Kashikawa et al. 2015; Giallongo et al. 2019; Grazian et al. 2020; Santos et al. 2021). However, a constant evolution in the quasar luminosity function across the end of reionisation epoch between $z = 6 - 5$ is not excluded. Based on the comparison with literature $z \sim 6$ mass functions and the mass function extrapolated from the measured growth between $z = 5 - 4$, our analysis indicates that the mean rate of change in the black hole mass function between $z = 6 - 5$ is consistent with $z = 5 - 4$, implying no change in the mass growth rate across $z = 6 - 4$.

Additional remarks

New luminosity function analyses at high redshift focusing on bright quasars (Onken et al. 2022a; Grazian et al. 2022) updated previous determinations (e.g. Yang et al. 2016; McGreer et al. 2018; Niida et al. 2020) with an increased space density of bright quasars. This result was prefaced by surveys of the ultraluminous quasar population (e.g. Schindler et al. 2017, 2019a; Boutsia et al. 2020; Cristiani et al. 2023) which showed that previous surveys had underestimated their completeness

corrections by $\sim 30\%$ (Schindler et al. 2019b; Boutsia et al. 2021). In the black hole mass function context, Wu et al. (2022) attributed their high-mass divergence from Willott et al. (2010a) to their inclusion of an error model, which implies that the virial black hole masses of quasars within their highest mass bins are possibly overestimated. However, applying an upper redshift threshold of $z = 6.3$ to Wu et al. (2022), as discussed in Section 4.3.3, corrects their mass function to within 1σ of our model extrapolation from the observed $z = 5 - 4$ k_{ef} growth. We expect that discrepancies between mass functions derived from heterogeneous methods to be an unavoidable consequence of the multitude of correction factors, broad scatter from uncertainties in the black hole mass and luminosity determinations, as well as cosmic variance. This highlights the importance of wide-area surveys of high completeness, as well as the need for improving the accuracy of black hole mass measurement techniques.

4.3.4   Black hole initial mass function

Although there are a few supermassive ($> 10^{10}\,M_\odot$) black holes in XQz5+, this dataset does not produce the most stringent constraints on black hole seeds due to their relatively low redshift compared to billion solar mass black holes observed at $z > 7$ (e.g. Mortlock et al. 2011; Bañados et al. 2018; Wang et al. 2018; Yang et al. 2019a, 2020). More recently, the James Webb Space Telescope enabled the search of quasars to push into higher redshifts (e.g. Larson et al. 2023), leading to the highest redshift quasar ($z \sim 10$) discovery thus far, revealed by its X-ray emission as seen by the Chandra X-ray Observatory (Bogdán et al. 2023). Its mass was inferred to be $10^7 - 10^8\,M_\odot$, comparable to the stellar mass of its host, which would require heavy seeds of $10^4 - 10^5\,M_\odot$ even with constant accretion at the Eddington limit.

Using the $z \sim 5$ black hole mass function model derived in this study, we trace the evolution of the mass function back to $z = 20$ ($\sim 175\,\mathrm{Myr}$ post Big Bang), which is an accessible redshift for the future Laser Interferometer Space Antenna (Amaro-Seoane et al. 2017). We derive the hypothetical initial mass function at $z = 20$ that would be consistent with the observed $z \sim 5$ mass function for effective growth $k_{\mathrm{ef}} = 1 - 9$, where $k_{\mathrm{ef}} = 9$ is the growth rate of a black hole that is growing without stopping at the Eddington limit with the fiducial radiative efficiency of $\epsilon = 0.1$. Figure 4.6 presents the $z = 20$ initial mass functions with proposed seeding mechanisms and their associated seed masses: Pop III remnants ($< 10^3\,M_\odot$), runaway mergers ($10^3 - 10^4\,M_\odot$), and supermassive star collapse ($10^4 - 10^6\,M_\odot$) (Inayoshi et al. 2020). Black holes would need to grow at $k_{\mathrm{ef}} > 5.0$ since their formation at $z = 20$ in order for the observed mass function to be consistent with the maximum mass of heavy
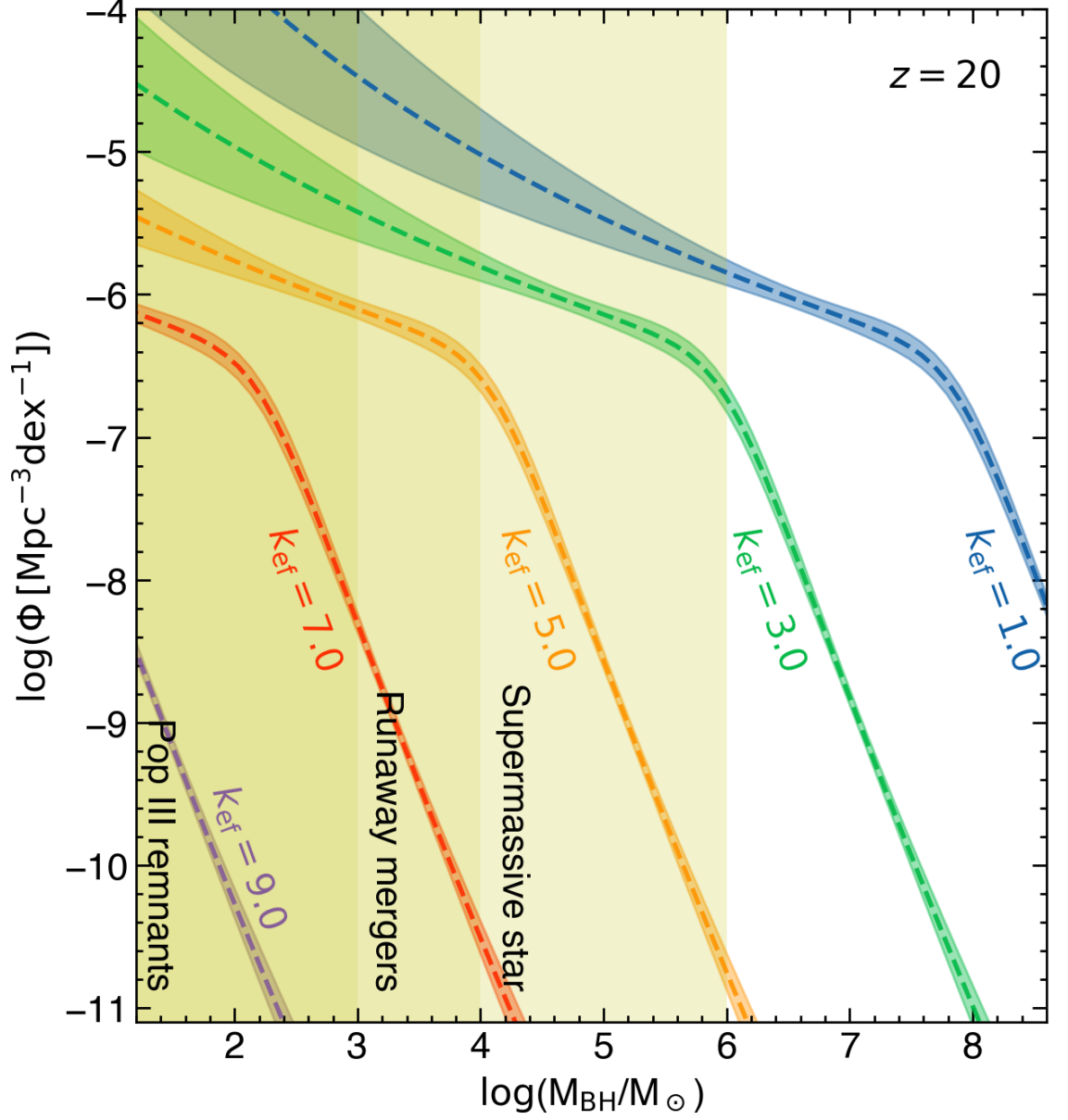
Figure 4.6: Black hole mass functions evolved to $z = 20$ through the continuity equation based on the reference mass function model at $z \sim 5$ and effective dimensionless growth parameters, $k_{\mathrm{ef}} = 1-9$. Overplotted are three proposed seeding mechanisms for the most massive high-redshift black holes and their seed mass range: Pop III remnants ($< 10^3\ M_\odot$), runaway mergers ($10^3 - 10^4\ M_\odot$), and supermassive star collapse ($10^4 - 10^6\ M_\odot$) (see review from Inayoshi et al. 2020). A $z = 20$ reference redshift for the initial black hole mass function corresponds to ~ 175 Myr after the Big Bang.

seeds. Even the most massive black holes of XQz5+ are consistent with Pop III remnants if allowing for perpetual Eddington limited growth at the fiducial radiative efficiency of $\epsilon = 0.1$. Unlike supermassive black holes at redshifts $z > 6$, the lower redshift black holes are not as strongly limited by the available cosmic time and thus there are multiple channels of mass assembly that are consistent with the observed spatial and mass densities.

In Figure 4.7, we estimate the redshift at which a $10^4\,M_\odot$ black hole would need to be born by to produce a black hole with $10^{10}\,M_\odot$ by $z = 5$, given a particular growth rate, k_{ef}. We choose $10^4\,M_\odot$ as the fiducial seed mass because it is the interface between two of the heavy seed mechanisms: supermassive star collapse and runaway merger from a dense stellar cluster. We have set an upper limit to the birth redshift at $z = 30$, which corresponds to ~ 100 Myr age for the universe. The results show that $10^4\,M_\odot$ seeds could not produce the observed ten billion solar mass black holes by $z = 5$ unless the mean growth rate exceeds $k_{\mathrm{ef}} = 6.2$. As shown in Figure 4.8, the joint constraints on the radiative efficiency, Eddington ratio, and duty cycle from a growth rate of $k_{\mathrm{ef}} > 6$ would exclude $\epsilon > 0.14$ for Eddington limited accretion.

In Figure 4.7, black holes with masses $\log\left(M_{\mathrm{BH}}/M_\odot\right) > 9.5$ at $z \sim 5$ are excluded by the upper redshift limit $z_{\mathrm{max}} = 30$ when $k_{\mathrm{ef}} = 5$ and the seed mass is $10^4\,M_\odot$. The majority of XQz5+ black holes are more massive than $\log\left(M_{\mathrm{BH}}/M_\odot\right) = 9.5$, which provides evidence that the rate of growth by accretion in the early universe is likely to be a factor of ~ 3.5 higher than observed between $z = 5 - 4$. If the seed mass is within the range of $10^{5-6}\,M_\odot$ instead, indicative of a direct collapse heavy black hole seed, then growth rates ~ 3 times that of $z = 5 - 4$ is sufficient to explain the $z \sim 5$ mass function with $z_{\mathrm{birth}} = 30$ as shown in Figure 4.6. Otherwise, if faster evolution is not occurring at higher redshifts, a growth factor of $k_{\mathrm{ef}} = 1.62$ extrapolated to $z = 30$ would require seeds of $\sim 10^{8.4}\,M_\odot$ to produce $10^{10}\,M_\odot$ black holes by $z = 5$.

4.4   Summary and Conclusion

In this study, we analyse the black hole mass function at $z \sim 5$ and compare to mass functions at $z \sim 4$ and $z \sim 6$. We measure the evolution in the mass function between $z = 5 - 4$ using the continuity equation and present joint constraints on the duty cycle, radiative efficiency, and mean Eddington ratio. Finally, we discuss the implications of our study on the population of black hole seeds in the early universe. The main results of this study are summarised:
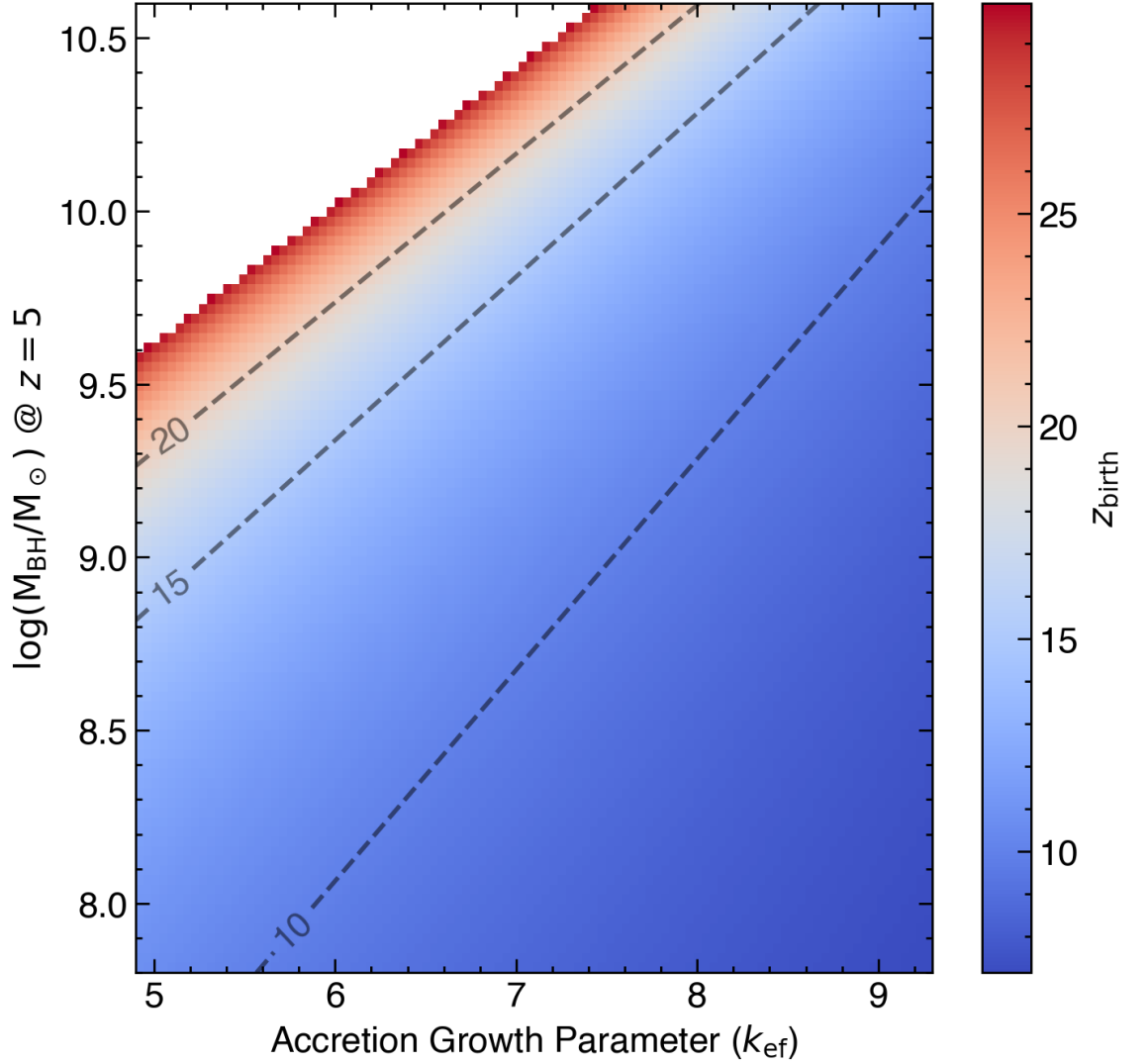
Figure 4.7: Redshift of $10^4 \, M_\odot$ black hole seed birth required to accrete a black hole of a specific mass by redshift $z = 5$ for a variety of accretion growth rates. The white exclusion region is set by an upper redshift limit of $z = 30$, which corresponds to an age of ~ 100 Myr. The ten billion solar mass black holes observed in XQz5+ are only consistent with $10^4 \, M_\odot$ black hole seeds if the accretion growth rate is ~ 3.5 times the observed growth between $z = 5 - 4$ mass functions.
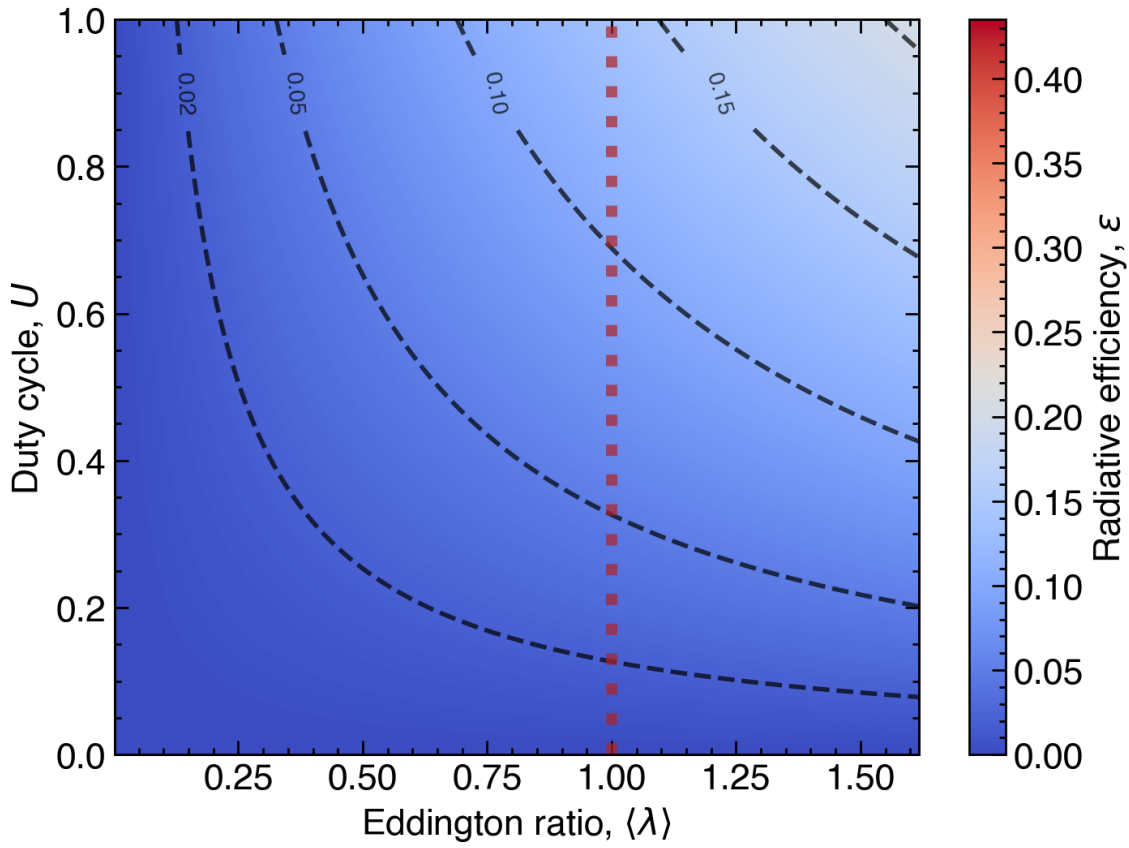
Figure 4.8: Surface plot showing the relationship between the Eddington ratio, duty cycle, and radiative efficiency satisfying Equation 4.9 for $k_{\mathrm{ef}} = 6.2$. We overplot dashed radiative efficiency contours and highlight $\langle\lambda\rangle = 1.0$ with the vertical dashed line.

- Our sample, collated from Trakhtenbrot et al. (2011); López et al. (2016); Lai et al. (2024) and collectively referred to as XQz5+, is composed of 72 of the most luminous quasars with spectroscopic follow-up observations over the redshift range $4.5 < z < 5.3$. The black hole masses of the quasars in the sample are measured using the single-epoch virial mass estimate based on the Mg II broad emission-line in their respective studies. We describe the standard $1/V_{\mathrm{max}}$ method used to derive population distribution functions and present our two-dimensional completeness correction grid over redshift and luminosity. Our sample occupies a highly complete parameter space, enabling further demographic analysis.

- We present the Eddington ratio distribution function for XQz5+ and show that it is consistent with a log-normal function centered around $\langle \log \lambda \rangle = -0.23 \pm 0.05$, with the dispersion $\sigma_\lambda = 0.29 \pm 0.04$ dex. In comparison to other observed Eddington ratio distributions at lower (He et al. 2023) and higher (D'Odorico et al. 2023) redshifts, the distribution of XQz5+ is centered on a higher value, but the dispersion is comparable.

- The mass function of XQz5+ is consistent with a power-law on the high-mass regime with an artificial turnover at $\log(M_{\mathrm{BH}}/M_\odot) \lesssim 9.5$ caused by incompleteness. We model the mass function with a double power-law model using the low-mass constraints of He et al. (2023) evolved from $z \sim 4$ to $z \sim 5$. The growth from XQz5+ to the He et al. (2023) mass function implies an accretion growth factor of $k_{\mathrm{ef}} = 1.62 \pm 0.06$, where the systematic uncertainty caused by cosmic variance is the dominant source of error.

- We also estimate the growth observed in black holes within the central ~ 200 Myr of the XQz5+ sample, where the completeness is more reliable, finding $k_{\mathrm{ef}} = 2.11 \pm 0.25$ with $0.5 - 0.8$ dex in systematic uncertainty due to cosmic variance. This result is consistent with the growth measured between $z = 5-4$, but due to the large uncertainties, it acts as weak corroborating evidence at best. Improving this measurement requires measuring black hole masses for a larger sample of quasars over a wider area of the sky or improving the survey flux limit. Additionally, an enhanced understanding of the obscured quasar fraction across the relevant redshift and luminosity ranges would further solidify our result. We explore the predicted $z \sim 6$ mass function based on extrapolating from the measured mass evolution, and compare it to literature estimates of the $z \sim 6$ mass function.

- If described by accretion-dominated growth, the evolution of the mass function measured between $z = 5-4$ provides joint constraints on the radiative

efficiency, Eddington ratio, and duty cycle. The Eddington ratio distribution of XQz5+ excludes radiative efficiencies of $\epsilon > 0.34$ by 3σ, because a high radiative efficiency at the observed Eddington ratios would grow too slowly to reproduce the observed mass function evolution.

- We estimate the black hole initial mass function by evolving the measured mass function to $z = 20$ with a variety of growth parameters, finding that the mean mass evolution in the early universe would need to be a factor of $\gtrsim 3-4$ times the rate measured between $z \sim 5-4$ to be consistent with the maximum heavy seed masses from exotic black hole formation mechanisms. This imposes more stringent constraints on the Eddington ratio, radiative efficiency, and duty cycle, which would exclude $\epsilon > 0.14$ at $z > 5$ unless supercritical growth is achieved and maintained over extended durations.

Future constraints on quasar demographics at higher redshift will depend on the results from new facilities such as the James Webb Space Telescope, which will enable black hole mass measurements from the Hβ emission-line between redshifts $5 < z < 10$. The first homogeneous samples at such high redshifts will illuminate the circumstances that gave rise to the accelerated growth required for prospective supermassive black holes to reach their observable masses by $z \lesssim 7$. The future Laser Interferometer Space Antenna has the capability for direct detections of black hole mergers with total participating masses of $\sim 10^4 - 10^7$ beyond redshifts of $z \sim 20$, probing the activity of newly-born massive seeds before they lose the memory of their birth.

Acknowledgements

Data Availability

The data underlying this article will be shared on reasonable request to the corresponding author.

Chemical abundance of $z \sim 6$ quasar broad-line regions in the XQR-30 sample

Context

This chapter is published as "Lai, S., Bian, F., Onken, C. A., Wolf, C., Mazzucchelli, C., Bañados, E., Bischetti, M., Bosman, S. E. I., Becker, G., Cupani, G., D'Odorico, V., Eilers, A.-C., Fan, X., Farina, E. P., Onoue, M., Schindler, J.-T., Walter, F., Wang, F., Yang, J., & Zhu, Y. (2022), *Chemical abundance of $z \sim 6$ quasar broad-line regions in the XQR-30 sample*, MNRAS, 513, 1801."

Preamble

Detailed spectral modelling of quasar spectra can be used to describe chemical abundances in the emitting clouds. The quasar broad-line region (BLR), photoionised by the quasar accretion disc emission, produces broad emission-lines observable in quasar spectra. Using spectral decomposition methods developed in Chapters 2/3, we match observed line ratios with photoionisation models and present constraints on the chemical abundances in quasar BLRs at high redshift ($z \sim 6$). Metallicity diagnostics applied to quasars with different emission profiles suggest metallicities up to ~ 10 times super-solar at high-redshifts, inspiring exotic early chemical enrichment scenarios. In this chapter, we show that metallicity estimates can be complicated by emission from spatial regions with a diversity of physical conditions, as indicated by evidence of outflowing components. When considering quasars without these components, BLR chemical abundances are only $2 - 3\times$ super-solar.

Abstract

The elemental abundances in the broad-line regions of high-redshift quasars trace the chemical evolution in the nuclear regions of massive galaxies in the early universe. In this work, we study metallicity-sensitive broad emission-line flux ratios in rest-frame UV spectra of 25 high-redshift ($5.8 < z < 7.5$) quasars observed with the VLT/X-shooter and Gemini/GNIRS instruments, ranging over $\log(M_{BH}/M_\odot) = 8.4 - 9.8$ in black hole mass and $\log(L_{bol}/\mathrm{erg\,s^{-1}}) = 46.7 - 47.7$ in bolometric luminosity. We fit individual spectra and composites generated by binning across quasar properties: bolometric luminosity, black hole mass, and blueshift of the C IV line, finding no redshift evolution in the emission-line ratios by comparing our high-redshift quasars to lower-redshift ($2.0 < z < 5.0$) results presented in the literature. Using `Cloudy`-based locally optimally-emitting cloud photoionisation model relations between metallicity and emission-line flux ratios, we find the observable properties of the broad emission lines to be consistent with emission from gas clouds with metallicity that are at least 2-4 times solar. Our high-redshift measurements also confirm that the blueshift of the C IV emission line is correlated with its equivalent width, which influences line ratios normalised against C IV. When accounting for the C IV blueshift, we find that the rest-frame UV emission-line flux ratios do not correlate appreciably with the black hole mass or bolometric luminosity.

5.1   Introduction

The broad-line region (BLR) of quasars contains dense ($n_H \approx 10^{9-14}$ cm^{-3}) and high-temperature (T $\sim 10^4$ K) gas (e.g. Peterson 2006), which is in close proximity to the supermassive black hole and photoionised by radiation from the accretion disk. Emission lines originating from the BLR can be used as virial estimators of the black hole mass (e.g Vestergaard 2002; McLure & Dunlop 2004; Greene & Ho 2005; Shen et al. 2008; Onken & Kollmeier 2008; Vestergaard & Osmer 2009), as well as to infer chemical abundances of the gas around black holes (e.g. Hamann & Ferland 1992, 1999; Hamann et al. 2002; Dietrich et al. 2003; Nagao et al. 2006; Matsuoka et al. 2011; Wang et al. 2012; Shin et al. 2017; Xu et al. 2018; Wang et al. 2022). The tight correlation between the supermassive black hole (SMBH) mass and the galactic bulge mass (the $M_{BH} - M_{bulge}$ relation; Magorrian et al. 1998; Marconi & Hunt 2003; Häring & Rix 2004; Greene et al. 2010) as well as the velocity dispersion of the galactic bulge (the $M_{BH} - \sigma$ relation; Ferrarese & Merritt 2000; Gebhardt et al. 2000; Tremaine et al. 2002; Salviander & Shields 2013) suggests that host galaxies and their central SMBH co-evolve over cosmic time. High-redshift quasars

provide an opportunity to understand the formation and evolution of the earliest galaxies and their supermassive black holes. The galaxy stellar mass - gas phase metallicity relationship (MZR) (e.g. Maiolino et al. 2008; Davé et al. 2017; Curti et al. 2020; Maiolino & Mannucci 2019; Sanders et al. 2021) combined with the M_{BH}/M_{host} ratio (e.g. Targett et al. 2012) and a relationship between the quasar BLR metallicity with black hole mass (Z_{BLR} - M_{BH}) can be used to link the mass or metallicity of the central black hole to metallicity in the host galaxy, enabling an investigation of their co-evolution in the young (< 1 Gyr) universe (e.g. Hamann & Ferland 1993).

The study of quasar BLR metallicity is strongly motivated by the relationship between quasar activity, host galaxy evolution, and star formation episodes (e.g. Hamann & Ferland 1999). Elemental abundances in the BLR are indicative of the chemical evolution in galactic nuclear material. Early investigations of BLR metallicity using highly ionised ions of C, N, and O among others, indicated solar or super-solar metallicity with high associated uncertainties (e.g. Baldwin & Netzer 1978; Shields 1976). Given the degeneracies involved with fitting these broad emission features, high signal-to-noise ratio (SNR) spectra or stacking spectra into high SNR composites is needed to accurately fit these lines. Considerable progress has been made since then, pushing towards higher redshift (e.g. Pentericci et al. 2002) and investigating chemical enrichment history. Photoionisation models suggest that rest-frame UV line flux ratios, such as (Si IV+O IV)/C IV and N V/C IV, can be used to infer metallicity in the BLR (Hamann et al. 2002; Nagao et al. 2006). These high-ionisation lines are associated to a region closer to the nuclear engine of the black hole than low-ionisation lines as indicated by reverberation mapping experiments (Collin-Souffrin et al. 1986; Collin-Souffrin & Lasota 1988; Clavel et al. 1991; Korista et al. 1995; Williams et al. 2020). Studies utilizing these metallicity-sensitive lines found that quasar metallicity correlates with luminosity (e.g. Hamann & Ferland 1993; Dietrich et al. 2003; Nagao et al. 2006; Xu et al. 2018), and outflow strength or velocity (e.g. Wang et al. 2012; Shin et al. 2017; Temple et al. 2021b). Additional studies found that metallicity correlates with black hole mass (e.g Matsuoka et al. 2011; Xu et al. 2018; Wang et al. 2022), possibly pointing to a more fundamental relationship between black hole mass and the metallicity of its BLR.

Simultaneously, there is no evidence to suggest that the same line ratios evolve with redshift (e.g. Pentericci et al. 2002; Juarez et al. 2009; Xu et al. 2018) up to redshifts as high as $z = 7.64$ (Onoue et al. 2020; Yang et al. 2021). Such studies consistently estimate metallicities several times the solar value $Z \sim 5Z_{\odot}$, up to $Z > 10Z_{\odot}$ in some quasars (e.g. Juarez et al. 2009). High redshift quasars with super-solar

metallicities suggest rapid chemical enrichment scenarios. Under this paradigm, the nuclei of the most massive galaxies in the early universe were enriched rapidly from the host galaxy's interstellar medium within $\sim 500\,\mathrm{Myr}$ from the formation of the first stars. From then on, observations suggest that the metallicity of the quasar BLR did not change appreciably for a significant span of cosmic time.

It has also been suggested that the diversity of high-ionisation emission line ratios measured across a wide range of black hole masses and luminosities can be attributed, in whole or in part, to gas emission from at least two distinct regions of differing densities, illuminated by different ionizing radiation (Sameshima et al. 2017; Temple et al. 2021b). This model does not necessarily require the metallicity in the BLR to vary across the quasar population in order to account for the observed differences in emission line properties. These studies indicate that inferences on quasar chemical enrichment history utilizing emission-line flux ratios have to account for variations in the physical conditions of the emitting gas.

In this paper, we study spectra of 25 high-redshift ($z > 5.8$) quasars taken with ESO's VLT/X-shooter and Gemini-N/GNIRS. The bulk of our sample consists of high-resolution and high SNR spectra from the ESO-VLT X-shooter Large Program XQR-30 (P.I. V. D'Odorico). We fit and investigate flux ratios of metallicity-sensitive lines (primarily N V/C IV and (Si IV+O IV)/C IV) using individual quasar spectra and composites binned by black hole mass, bolometric luminosity, and blueshift of the C IV line to determine whether these parameters are correlated with metallicity in the BLR. This paper follows closely other studies at lower redshift (e.g. Nagao et al. 2006; Xu et al. 2018; Shin et al. 2019) and high redshift studies based on smaller samples (e.g. Jiang et al. 2007; Juarez et al. 2009; De Rosa et al. 2014; Tang et al. 2019; Onoue et al. 2020; Wang et al. 2022), many of which report measurements of the same metallicity indicators we use. Compared to a recent study of 33 $z \sim 6$ quasars observed with Gemini-N/GNIRS (Wang et al. 2022), our sample contains higher SNR and spectral resolution spectra from X-shooter. Additionally, we consider the effects of BLR outflow on the metallicity-sensitive flux ratios, where the outflow is measured by the blueshift of the C IV emission line (e.g. Sulentic et al. 2000; Baskin & Laor 2005; Vietri et al. 2018).

The content of this paper is organized as follows: in Section 5.2, we describe the properties of our high-redshift quasar sample, data reduction, spectrum processing, and the methodology for generating composites. In Section 5.3, we describe our approach to fitting metallicity-sensitive emission lines and the conversion from line ratios to metallicities in the BLR. We present the results for our high redshift sample in Section 5.4, and in Section 5.5, we discuss and contextualize the results, present-

ing correlations found between the properties of the high redshift quasars and the metallicity of their BLRs. We summarize and conclude in Section 5.6. Throughout the study, we adopt flat ΛCDM cosmology with $H_0 = 70$ km s^{-1} Mpc^{-1} and $(\Omega_{\mathrm{m}}, \Omega_{\Lambda}) = (0.3, 0.7)$. All referenced wavelengths of emission lines are measured in vacuum.

5.2 Quasar Sample and Composites

5.2.1 Sample Selection

The bulk of the sample originates from quasars in the ESO-VLT X-shooter Large Program XQR-30 (P.I. V. D'Odorico, program number 1103.A-0817)[1]. The XQR-30 program targets 30 southern hemisphere bright QSOs at $5.8 < z < 6.6$ to study the universe in its infancy. These quasars have virially estimated BH masses of $(0.8 - 6.0) \times 10^9 \, \mathrm{M_\odot}$ (Mazzucchelli et al. in prep.). At lower BH masses, $0.2 - 1.0 \times 10^9 \, \mathrm{M_\odot}$, we include 1 quasar spectrum from Shen et al. (2019b) and 9 spectra from Yang et al. (2021), all of them taken with Gemini/N GNIRS. From these other samples, we only considered spectra covering quasar properties outside the range of XQR-30 quasars with SNR > 5 per resolution element near rest-frame 1600Å and 2800Å, which are in the proximity of the emission lines of interest. Their redshifts span a similar range from $z = 6.0$ to $z = 6.8$ with one quasar at $z = 7.54$ (i.e. Onoue et al. 2020). All redshifts are measured from the peak of the best fit models to the Mg II emission line, where we use the complete reconstructed line profile in case of multi-component fits. We provide some details of the Mg II fits in Section 5.3.1 and we leave the complete discussion for Mazzucchelli et al. in prep.

Of the 30 quasars in XQR-30, 14 are classified as quasars with broad absorption-lines (BAL) and 16 are considered non-BAL (Bischetti et al. 2023). We exclude quasars with BAL features as they introduce additional uncertainty in the measurement of line flux. From the XQR-30 non-BAL sample, we reject J1535+1943 by visual inspection due to its dust-reddened continuum in the wavelength regions of interest (Yang et al. 2021). Such a continuum is not well-modeled by the continuum fitting method we describe in Section 5.3.1 and it would affect the continuum fit if included in composites. Combined with 10 spectra from Gemini GNIRS, a total of 25 high-redshift quasar spectra are included in this study. Figure 5.1 and Table 5.1 show the distribution of the quasar sample and physical properties.

---

[1]Collaboration website: https://xqr30.inaf.it/
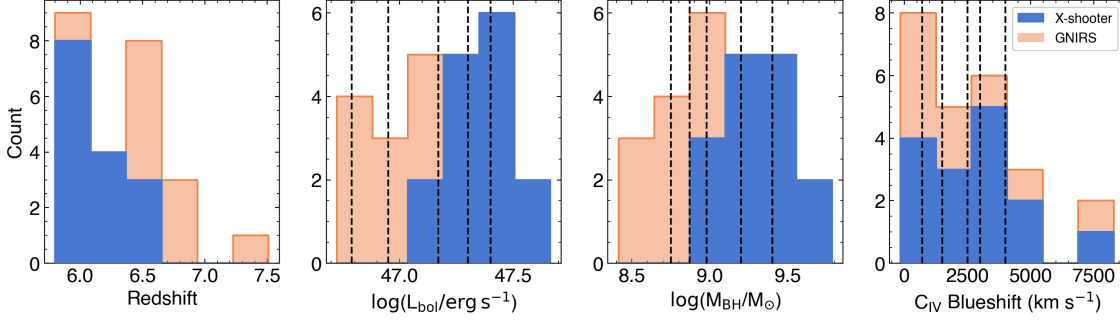
Figure 5.1: Stacked distribution of quasar properties in our sample from left to right: redshift, quasar bolometric luminosity, black hole mass, C IV blueshift. The properties of the XQR-30 sample, observed with ESO's X-shooter, are highlighted in blue while the GNIRS spectra are presented in orange. The inner bin edges of composites by quasar bolometric luminosity, black hole mass, and C IV blueshift are delineated by black dashed lines.

5.2.2   Data Reduction and Post-Processing

The data reduction procedure for GNIRS spectra is described in full in the source papers: Shen et al. (2019b) and Yang et al. (2021). Shen et al. (2019b) used a combination of the `PyRAF`-based `XDGNIRS` (Mason et al. 2015) and the IDL-based `XIDL` package while Yang et al. (2021) used the Python-based spectroscopic data reduction pipeline `PypeIt` (Prochaska et al. 2020a).

XQR-30 data are reduced with an improved version of the flexible custom IDL-based pipeline used with data from the XQ-100 legacy survey (López et al. 2016; Becker et al. 2019). The overall strategy is based on techniques described in Kelson (2003) with optimal sky subtraction, telluric absorption correction, optimal extraction, and direct combination of exposures. The pipeline is described in additional detail in Becker et al. (2012) and it has also been used in other studies based on XQR-30 data (e.g. Zhu et al. 2021). X-shooter data are obtained using three arms with the following wavelength ranges: UVB (300-559.5 nm), VIS (559.5-1024 nm), and NIR (1024-2480 nm). We extract data from only the VIS and NIR arms because there is no light in the UVB for our sources.

In the 50 km s^{-1} rebinned quasar spectra from the XQR-30 sample, the mean SNR per pixel measured in the range 1400-1600Å in the rest frame, is $\sim$ 30 with a minimum of 24 and maximum of 38, while the mean SNR per pixel for the GNIRS sample is $\sim$ 13, ranging between 6 and 30. Median pixel widths are 0.25Å for the rebinned XQR-30 spectra and 0.43Å for GNIRS spectra between rest-frame 1400-1600Å. The XQR-30 SNR reported here can be different from those of other studies based on XQR-30 data because of differences in binning strategies and wavelength

region over which the SNR is measured.

After data reduction, each spectrum undergoes a common post-processing procedure described as follows:

1. For every reduced spectrum in our quasar sample prior to creating composite spectra, the data are restricted to relatively high SNR. The per-pixel SNR floor is 1 for GNIRS spectra and 5 for XQR-30 spectra. Data restricted by the SNR floor are omitted from further processing and fitting.

2. We then apply a sigma-clip mask with a box width of 30 pixels, and a 3-σ threshold to remove narrow absorption features and noise above 3-σ. These absorption features are not desired when fitting the intrinsic flux and profile of the broad emission lines. For the noisier and lower resolution GNIRS spectra, the sigma-clip mask has a minimal effect on the resulting spectra.

3. As the spectra are observed with different instruments and exhibit a diversity of redshifts, we standardize the rest-frame wavelength domain for all of the spectra, facilitating the stacking of composites later. Every spectrum is resampled using a flux-conserving algorithm into a common wavelength domain with 1 Å bins in the rest-frame. The resampling calculation and error propagation are described in detail in Carnall (2017). The number of pixels per 1 Å bin in the raw spectra is wavelength-dependent, ranging from 1-3 pixels per bin for GNIRS spectra and 2-8 for X-shooter spectra.

To test the robustness of our measurements, we vary the details of the post-processing procedure, Among the many variations, we perform the sigma-clipping before resampling rather than after, apply an upper error threshold to restrict the maximum allowable error, and in one instance, we do not perform resampling on individual quasar spectra. In each case, we find that the majority of measurements are consistent within their uncertainties and the overall correlations and conclusions we draw from our measurements are unaffected. This gives us confidence in our results.

5.2.3 Black Hole Mass Estimate

The black hole mass of each quasar is based on single-epoch virial mass estimates. We source the black hole masses from Shen et al. (2019b), Yang et al. (2021), and Mazzucchelli et al. in prep. which span $\log\left(M_{BH}/M_\odot\right) = 8.4 - 9.8$ over the entire quasar sample. To determine the masses, these studies use the rest-frame UV Mg II broad emission line and the Mg II-based virial estimator, described generally by the

following,

$$\left(\frac{M_{\mathrm{BH,vir}}}{M_\odot}\right) = 10^{\mathrm{a}} \left[\frac{\lambda L_\lambda}{10^{44}\,\mathrm{erg\,s^{-1}}}\right]^b \left[\frac{\mathrm{FWHM(Mg\,II)}}{1000\,\mathrm{km\,s^{-1}}}\right]^2 , \qquad (5.1)$$

where λL_λ is the monochromatic luminosity of the continuum at rest frame 3000 Å, and (a,b) are empirically calibrated against reverberation mapping experiments to the values (6.86, 0.5) in Vestergaard & Osmer (2009) and (0.74, 0.62) in Shen et al. (2011). The masses of quasars in the XQR-30 and Yang et al. (2021) samples are estimated using the Vestergaard & Osmer (2009) calibration. The mass of the one quasar we've included from Shen et al. (2019b) is reported with the Shen et al. (2011) calibration, but we have re-calibrated the mass with Vestergaard & Osmer (2009), resulting in a 0.1 dex difference. The continuum luminosity is estimated by fitting a power-law continuum and Fe II emission around the Mg II line, as described in Section 5.3.1 and the Fe II template (i.e. Vestergaard & Wilkes 2001) is consistent between the different studies. The absolute fluxing of the XQR-30 spectra is based on calibrations against observed near-infrared photometry and is described in full in Mazzucchelli et al. in prep. The Mg II full-width at half maximum (FWHM) is determined with single or multi-component Gaussian fits to the broad emission line and the peak of the total line profile is used to calibrate the systemic redshift of the quasar spectrum. Typical systematic errors from the virial mass estimator for the Mg II line can be up to 0.55 dex (Shen et al. 2008; Vestergaard & Osmer 2009). Bolometric luminosities are measured from the flux-calibrated spectrum using the continuum luminosity at 3000Å and adopting a bolometric correction of 5.15 (Shen et al. 2011) throughout our entire sample.

The virial mass estimate is routinely applied to quasars (e.g. McLure & Dunlop 2002; Shen & Liu 2012) and aside from the Mg II line, Hβ and C IV emission lines have been used. Virial mass estimates using the Hβ emission line is not feasible for high redshift quasar studies prior to the James Webb Space Telescope, but the Mg II line width is correlated with Hβ and can be used as its substitution in single-epoch virial black hole mass estimates (e.g. Salviander et al. 2007; Shen et al. 2008; Wang et al. 2009; Shen & Liu 2012). Compared to the C IV emission line, the advantage of the Mg II line is that it is less affected by non-virial components of the black hole emission, such as the radiatively-driven BLR wind (e.g. Saturni et al. 2018). The difference between the C IV and Mg II virial mass estimates is correlated with the C IV blueshift (Shen & Liu 2012; Coatman et al. 2017).

5.2.4 C IV Blueshift Measurement

The C IV emission line is of particular interest in assessing BLR outflow strength which has also been linked to metallicity (e.g. Wang et al. 2012; Shin et al. 2017). This high-ionisation line can exhibit significant blueshifts (e.g. Gaskell 1982; Wilkes 1984; Marziani et al. 1996; Vanden Berk et al. 2001; Baskin & Laor 2005; Sulentic et al. 2007) and asymmetric velocity profiles (e.g. Sulentic et al. 2000; Baskin & Laor 2005), structure that is often interpreted as arising from a disk wind or outflow (e.g. Sulentic et al. 2007; Vietri et al. 2018). The blueshift of C IV is therefore an indication of the balance of emission between the outflowing ionised gas and the emission at a systematic redshift, which we call the "wind" and "core" component respectively (adopting the terminology of Temple et al. 2021b). At high redshifts (z > 5.8), the mean and median C IV-Mg II velocity shifts are greater than for luminosity-matched quasars at lower redshifts, although this may potentially be biased by increased torus opacity and orientation-driven selection effects (Meyer et al. 2019; Schindler et al. 2020; Yang et al. 2021). In this study, we define our estimate of the C IV blueshift as

$$\frac{\text{C IV blueshift}}{\text{km s}^{-1}} \equiv c \times (1549.48\text{Å} - \lambda_{\text{med}})/1549.48\text{Å}\,, \tag{5.2}$$

where c is the speed of light and λ_{med} is the median wavelength bisecting the total continuum-subtracted C IV emission line flux. The wavelength 1549.48Å is the average of the C IV $\lambda\lambda1548.19, 1550.77$ doublet. This definition is the same as in Temple et al. (2021b), but their redshift is defined using a variety of low-ionization emission lines, some of which are known to exhibit velocity shifts relative to Mg II. In this study, we define our redshift using only the Mg II line. Due to the 1 Å wavelength resolution, we prescribe a minimum precision of ~ 200 km s^{-1} for the C IV blueshift, evaluated as an error of ±1Å at the average wavelength of the C IV doublet. The overall uncertainty of the C IV blueshift is combined with the uncertainty from the measured redshift.

The C IV blueshift is also known to be anti-correlated with the line's equivalent width (EW; Leighly & Moore 2004; Richards et al. 2011; Vietri et al. 2018; Rankine et al. 2020; Schindler et al. 2020; Temple et al. 2021b), a relationship which is reproduced for our high-redshift quasar sample in Figure 5.2. This correlation may be driven by orientation, properties of BLR winds, or the Baldwin effect linking properties of high-ionisation lines like C IV with the quasar luminosity (Baldwin 1977). The results show highly blueshifted C IV lines are weak, while stronger lines are less blueshifted and more symmetric.

We note that a velocity shift relative to C II] of 5510^{+240}_{-110} km s^{-1} was measured for

J1342+0928 (Bañados et al. 2018; Onoue et al. 2020) and Schindler et al. (2020) also measured velocity shifts relative to Mg II for several XQR-30 quasars in our sample. However, due to differences in the definition of C IV blueshift[2], choice of Fe II template, and sometimes the referenced line to estimate the redshift, we have re-measured the blueshifts for most quasars in our sample. However, the C IV blueshift could not be reliably determined for one individual quasar: J2338+2143, which, despite the minimum SNR requirement, has an overall SNR too poor to obtain a reliable fit.

5.2.5   Composite Spectra

The primary objective of this work is to measure flux ratios of metallicity-sensitive lines binning by quasar properties, such as bolometric luminosity, black hole mass, and C IV blueshift, to determine whether these parameters are correlated with metallicity in the BLR. Although most of the spectra have sufficient SNR to proceed with the emission-line fitting independently, the weak and blended emission lines of some SNR/pixel ≤ 8 spectra in this sample could not be fit convincingly. By stacking the spectra, we are able to obtain higher SNR. Another reason to stack the spectra is to average out peculiarities of individual quasars in each bin in order to construct better comparisons to the photoionisation models referenced in Section 5.3.2. As we are interested in the average spectral properties within a binned parameter space rather than the specific individual properties, we use equivalent weighting of spectra within each composite regardless of the SNR of input spectra so that the output is not biased in favor of any contributing quasar observed with high SNR. We construct 6 bins from each of the 3 quasar properties (black hole mass, bolometric luminosity, and C IV blueshift), with a similar number of contributing quasar spectra in each bin. We also avoid extending the width of each bin too wide. Therefore, the average number of quasar spectra in each bin is 4, and all composites are created from 3-6 input spectra.

The dynamic range of quasar bolometric luminosity in this sample is $\log\left(\mathrm{L_{bol}/erg\,s^{-1}}\right) = 46.7 - 47.7$. We split the sample into 6 luminosity bins with the following edges: 46.72, 46.79, 46.95, 47.17, 47.30, 47.40, 47.70, and a composite is created from each bin. The first three bins include all 10 GNIRS spectra and the final three bins are composed of exclusively X-shooter spectra. The total BH mass

---

[2]It is also possible to define the C IV blueshift by the maximum of the C IV line profile or the blueshift and asymmetry index (BAI) defined as the flux blueward of 1549.48Å. Although we don't use these definition in this study, we have checked that these alternatives have little effect on the relative C IV blueshifts between quasars. The relationship found in Figure 5.2 and the correlations found in this study hold are unaffected.
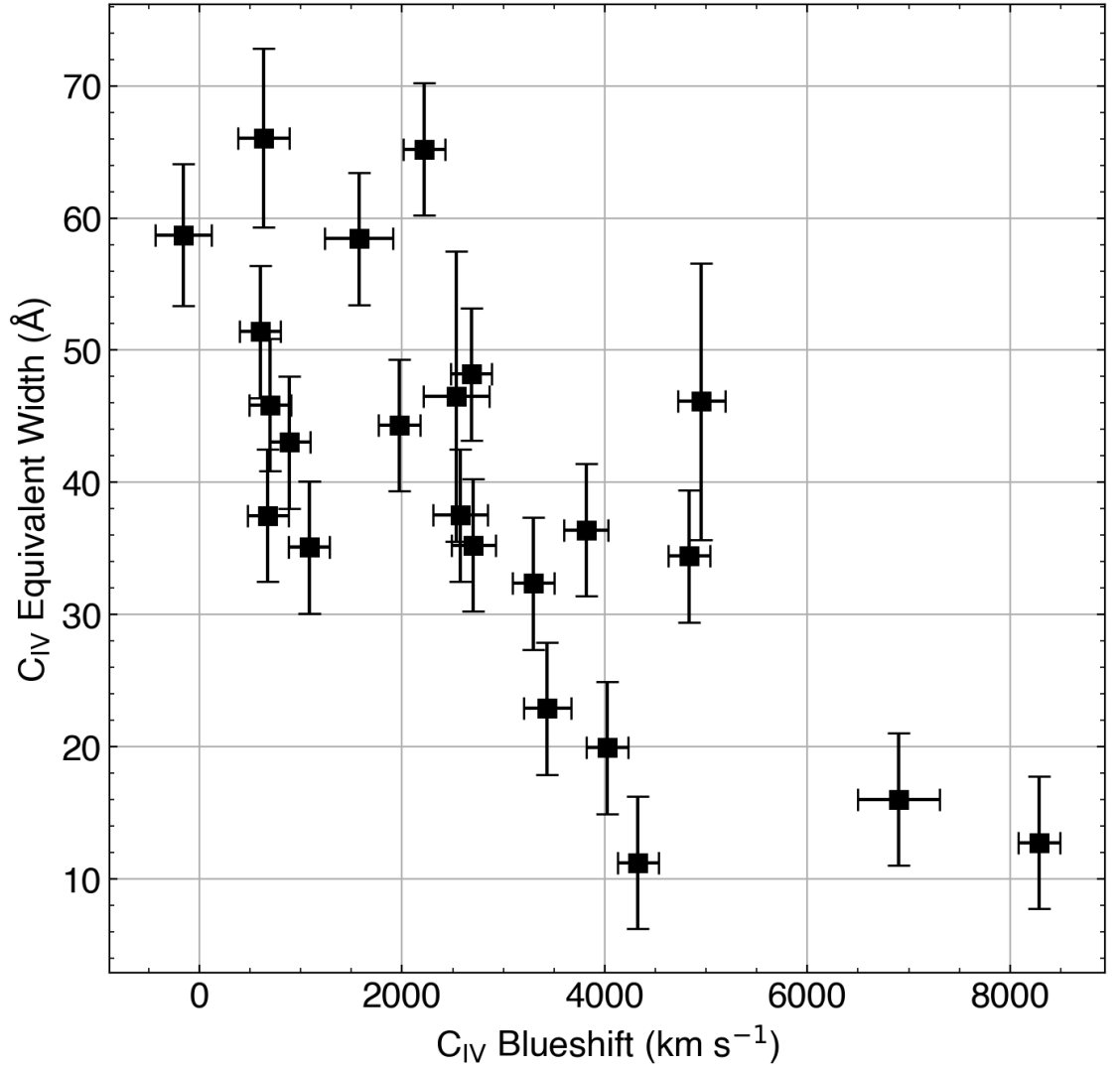
Figure 5.2: C IV equivalent width as a function of C IV blueshift. There is a moderate anti-correlation between these two quantities, implying that weaker C IV lines are more strongly blueshifted and stronger lines are less blueshifted. The outlier with high EW and blueshift is J1216+4519. Its SNR is low ($\sim$ 7 per pixel) which is reflected by the large error in EW.

range reflected in our high-redshift quasar spectra is $\log\left(M_{BH}/M_\odot\right) = 8.4 - 9.8$. Again, we form 6 mass bins with the following edges: 8.40, 8.75, 8.87, 8.98, 9.20, 9.40, 9.80, and create a composite spectrum from each bin. We also arrange and stack all individual quasars in the sample into 6 C IV blueshift bins, with the following bin edges: -200, 680, 1500, 2500, 3000, 4000, 5000 km s^{-1}. Figure 5.1 shows the bin edges of each composite delineated by black dashed lines.

Prior to stacking, we apply an upper error threshold equal to 2 times the minimum error within box widths of 50 pixels to restrict data to where the error is reasonable. The error threshold clips wavelength bins with unusually high error and high flux that were not masked by the general post-processing procedure. The resulting spectra contains the most stable and robustly measured elements. Without the upper error threshold, the propagation of error from a small number of component spectra can create unstable composites, leading to greater uncertainty in the final flux measurements. Every spectrum is then normalised across the rest-frame 1430Å$\sim$1450Å wavelength range and the arithmetic mean of each stack is taken to generate the composite. We also take the median or geometric mean (e.g. Vanden Berk et al. 2001) of the stack and find that it does not significantly influence the result. Furthermore, we generate composites after subtracting a power-law continuum, fitted as described in Section 5.3.1, and find that the resulting measured broad emission-line fluxes are not significantly discrepant either. In all cases, the resulting line ratio measurements regardless of taking the composite arithmetic mean, geometric mean, median, or after subtracting the continuum agree to within 2.0 σ, with $\sim 75\%$ of measurements within 1.0 σ.

The uncertainty in each resolution element is composed of the error in every contributing spectrum added in quadrature, but we also estimate the systematic error in each composite by generating all of the possible composites that can be obtained if any one contributing quasar spectrum is excluded. The standard deviation in each 1Å pixel from all such simulated composites is treated as the systematic error, added in quadrature to the uncertainty propagated from each contributing spectrum. This systematic error is an additional source of error which raises the uncertainty floor of the combined spectrum and reduces the relative uncertainty between each resolution element, affecting the weighting of each pixel in a least-squares fitting routine. After combining all sources of uncertainty, the resulting SNR per pixel of the composites measured between rest-frame 1400-1600Å is 20–100. We show a composite constructed from all 25 quasars in our sample in Figure 5.3.

Three individual quasar spectra are treated differently for our composites. PSOJ007+04, PSOJ025-11, and J1212+0505 are affected by proximate damped Ly α
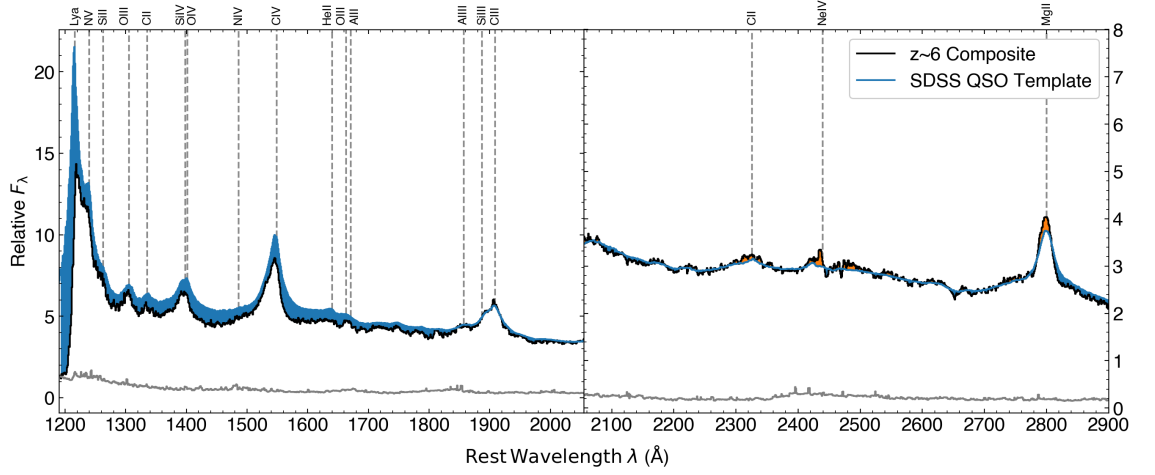
Figure 5.3: Composite created from all 25 high-redshift quasars in our sample compared against the SDSS quasar template comprised of 2200 spectra described in Vanden Berk et al. (2001). The composite is split into two sections with independent y-axis scaling to better visualise the various spectral emission features, which are denoted with the grey dashed lines. The composite and SDSS template are normalised together at 2200-2250Å, and the grey spectrum is the error spectrum of the composite. The blue and small patches of orange shaded regions indicate when the template or the composite is in excess respectively. Our high-redshift composite has a noticeably flatter continuum slope and significant Ly α absorption compared to the lower redshift SDSS sample, but the profiles and relative integrated fluxes of emission features other than Ly α are comparable.

absorption (pDLA) systems (Farina et al. 2019; Bañados et al. 2019), which causes a significant fraction of its Ly α emission to be absorbed at the systemic redshift. We fit the emission lines of pDLA affected quasars individually, and mask their emission blueward of the N v centroid from contributing to composites.

5.3 Line Fitting and Metallicity Measurement

5.3.1 Emission-line Fitting

In this work, we study a large number of rest-frame UV emission lines: Ly α, N v, Si II, Si IV, O IV, N IV], C IV, He II, O III], Al II, Al III, Si III, C III], and Mg II. The measurement of emission-line fluxes can be tricky due to adjoining and heavily blended lines, such as N v λ1240Å with Ly α λ1216Å or Al III λ1857Å, Si III λ1887Å, and C III] λ1909Å. Furthermore, the strong Fe II emission biases the underlying continuum level measurement. Despite these challenges, there are two widely employed methods for fitting quasar emission-lines (Nagao et al. 2006). One method measures the emission-line flux by integrating above a well-defined independent local

continuum model (e.g. Vanden Berk et al. 2001) and the other method endeavors to fit emission lines using one or more appropriate functions, such as Gaussians or Lorentzians (e.g. Zheng et al. 1997). Both of these methods have shortcomings in measuring accurate emission-line fluxes. Defining an appropriate local continuum level below an emission-line is challenging and is sensitive to where the baseline is anchored. The additional uncertainty propagates into the resulting metallicity estimates. Regarding the function fitting approach, a single Gaussian or Lorentzian profile is insufficient for broad emission-lines with asymmetric velocity profiles (e.g. Corbin 1997; Vanden Berk et al. 2001; Baskin & Laor 2005). The approach utilising multiple Gaussian functions can obtain smooth realisations of the line profile, but the decomposition is not unique and a large number of free parameters is required. Modified functions such as a skewed Gaussian (defined in Appendix C.1) or asymmetric Lorentzian depend on fewer parameters and are arguably more physically relevant (e.g. Mallery et al. 2012). With multiple reasonable approaches, there is a concern that the resulting line flux can be method-dependent. In this work, we use various appropriate functions to fit emission lines and we compare the several different methods against similar fits from existing literature in Appendix C.1.

We follow the general procedure from Xu et al. (2018) and define the following two line-free windows in rest-frame to fit the continuum: $1445\text{Å}-1455\text{Å}$, $1973\text{Å}-1983\text{Å}$. In specific circumstances, we identify two additional windows ($1320\text{Å}-1325\text{Å}$, and $1370\text{Å}-1380\text{Å}$) to further constrain the continuum shape or we extend the blue-end of the first line-free window to 1432Å in the case of a blueshifted C IV line. The continuum is fit with a power-law function normalised to rest-frame 3000 Å,

$$F_{\mathrm{pl}}(\lambda) = F_{\mathrm{pl},0} \left(\frac{\lambda}{3000\text{Å}} \right)^{\gamma} , \qquad (5.3)$$

where $F_{\mathrm{pl},0}$ and γ represent the normalization and power-law slope respectively. We also consider the contribution of the Fe II pseudo-continuum spectrum using the empirical template from Vestergaard & Wilkes (2001) to cover the wavelength range from 1200 Å to 3500 Å. We convolve the template with a Gaussian broadening kernel to better fit the variety of features from the Fe II pseudo-continuum seen across spectra in our sample,

$$F_{\mathrm{Fe}}(\lambda) = \zeta_0 \, F_{\mathrm{template}}|_{\lambda(1+\delta)} \circledast G(\lambda, \sigma) , \qquad (5.4)$$

where the free parameters of the Fe II flux contribution include a flux scaling factor ζ_0, the FWHM of the broadening kernel σ, and a small wavelength shift δ. The contribution from the iron continuum is more relevant at wavelengths close to the

Mg II $\lambda 2799$Å line and is important in obtaining the virial mass estimate. Combined, the power-law and the Fe II template are fit to the data in the line-free windows and form the underlying continuum baseline.

Emission lines are fit with the following double power-law method adopted from Nagao et al. (2006), Matsuoka et al. (2011), and Xu et al. (2018),

$$F_{\mathrm{em}}(\lambda) = \begin{cases} F_0 \times \left(\frac{\lambda}{\lambda_0}\right)^{-\alpha} & \lambda > \lambda_0 \\ F_0 \times \left(\frac{\lambda}{\lambda_0}\right)^{+\beta} & \lambda < \lambda_0 \end{cases} \tag{5.5}$$

where the two power-law indices (α and β) are used to fit the red and blue sides of the emission-line profile. The peak intensity, F_0, controls the height of the emission line and the peak wavelength, λ_0, defines the location of the peak.

Emission lines with different degrees of ionisation often show systematically varied velocity profiles (e.g. Gaskell 1982; Baskin & Laor 2005). Thus, we categorise emission lines into two distinct systems: high-ionisation lines (HILs) and low-ionisation lines (LILs). The HILs include N V, O IV, N IV], C IV, and He II while the LILs include Si II, Si IV, O III], Al II, Al III, Si III, and C III] (Collin-Souffrin & Lasota 1988). The boundary separating the two main groups is an ionisation potential of 40 eV. We assume that the emission-line profiles of lines in the same category are coupled to the same line-emitting gas clouds of the BLR, sharing a common value for the α and β power indices. Because we did not correct for the suppression of Ly α from the intergalactic medium, the redder α index of the Ly α line is coupled with the HILs, while the bluer β index is left unconstrained (Nagao et al. 2006; Xu et al. 2018). [3]

Our adopted piece-wise power-law function fit to emission lines has been compared to the double-Gaussian and modified Lorentzian methods, achieving better fits with fewer or equal number of free parameters (Nagao et al. 2006). In cases when the piece-wise function does not produce a reasonable fit to the shape of the spectral feature, such as significantly blueshifted lines, we fit a skewed Gaussian function, where both the skew and FWHM of the Gaussian are coupled between LILs and HILs. Unlike the default piece-wise strategy, Ly α is completely decoupled from the HIL group when fitting skewed Gaussians. We choose to fit a single skewed Gaussian because it has the same number of free parameters as the piece-wise power-law fit. Changing the fitting strategy is also motivated by the reduction in the minimum chi-square value even when the fits produce similar emission-line flux ratios. A more

---

[3] Although the Ly α line doesn't directly factor into the line ratios we measure or the metallicities we determine, its flux and line profile does affect the measured flux of the N V line.

complete description of the comparison between these two fitting methods and the definition of the skewed Gaussian are provided in Appendix C.1.

When LILs and HILs are not coupled, some local continuum methods can produce emission-line profiles with very different widths and skewness (Vanden Berk et al. 2001). We assume, as several similar other studies do (e.g. Nagao et al. 2006; Matsuoka et al. 2011; Xu et al. 2018), that emission lines with similar ionising potentials originate from similar line-emitting regions in the BLR. The coupling of power indices in Equation 5.5 provides a crucial constraint in ensuring that the kinematics of line-emitting clouds are preserved within the LIL and HIL groups. Furthermore, without the coupling of HILs, the decomposition of the Ly α and N V emission profile is not unique. The coupling of the N V profile and the red wing of Ly α to HILs provides a way to obtain a unique solution that disentangles their line profiles and fluxes.

The emission lines Ly α $\lambda1216$, N V $\lambda1240$, Si II $\lambda1263$, Si IV $\lambda1398$, O IV $\lambda1402$, N IV] $\lambda1486$, C IV $\lambda1549$, He II $\lambda1640$, O III] $\lambda1663$, Al II $\lambda1671$, Al III $\lambda1857$, Si III $\lambda1887$, and C III] $\lambda1909$ are all fit simultaneously. The line-fitting regions generally are 1214–1290, 1360–1430, 1450–1700, and 1800–1970Å with some flexibility depending on the width and kinematics of the spectral features. Each line is allowed an independent ±25Å shift in central wavelength, λ_0, with respect to the rest-frame vacuum wavelength. Whether we used the piece-wise power-law or skewed Gaussian approach, a single emission-line is fit with only four parameters. Figure 5.4 shows an example fit to ATLASJ029-36 which was observed with VLT/X-shooter. In this example, all of the lines from Ly α at 1216 Å to C III] at 1909 Å have been fit simultaneously, with coupled LILs and HILs.

We fit the C IV emission line to estimate the blueshift according to Equation 5.2. When C IV blueshifts < 4000 km s^{-1}, we adopt the piecewise power-law fit and at higher blueshifts, we use the skewed Gaussian function. We find both methods produce consistent results at lower C IV blueshifts as shown in the comparison described in Appendix C.1.

We also fit the Mg II line independently with one skewed Gaussian or two symmetric Gaussians, using the following line-free windows: 1770–1810, 2060–2340, 2600–2740, 2840–3100Å to measure the continuum. The continuum is measured independently for the Mg II line fit because the contribution from the Fe II emission is much more significant at these longer wavelengths. Although the fit parameters are not always consistent between the two wavelength ranges, we find the power-law to be an adequate local approximation of the accretion disk emission. We use the Mg II FWHM, Equation 5.1, and calibration from Vestergaard & Osmer (2009) to determine the
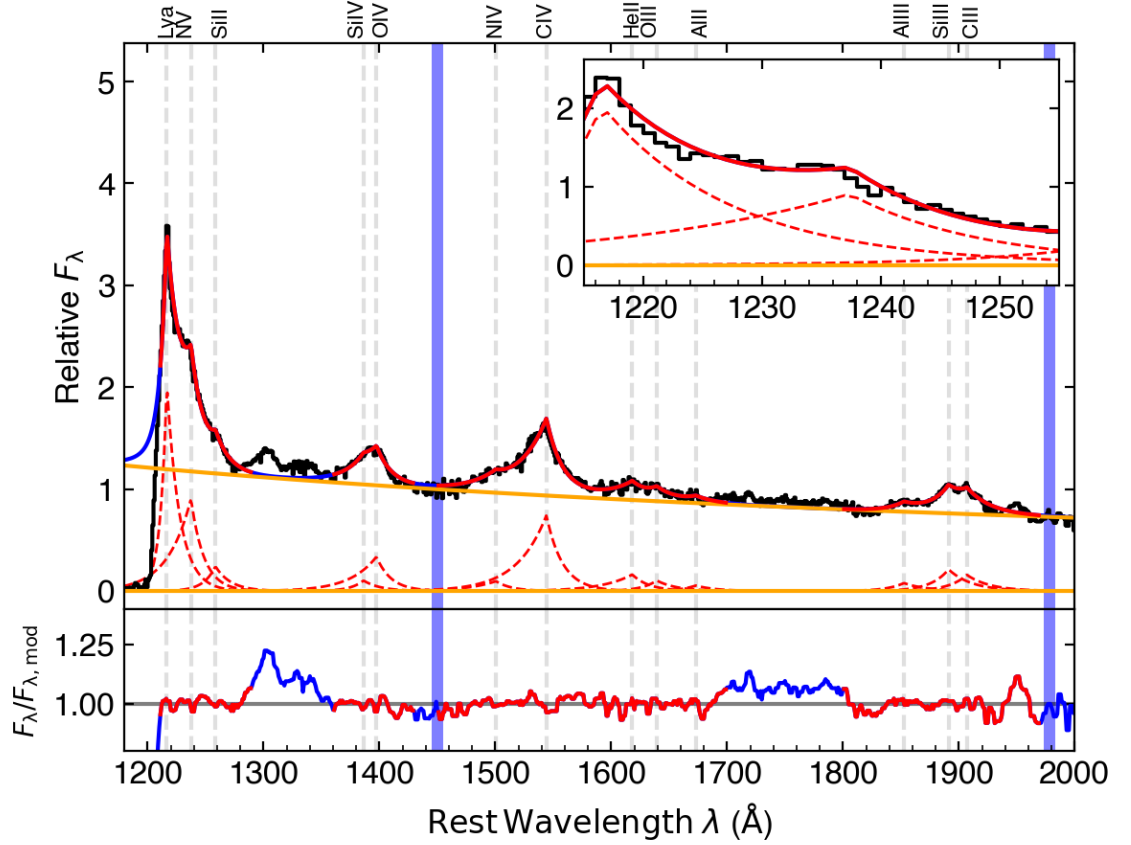
Figure 5.4: Example fit to ATLASJ029-36 observed using VLT/X-shooter with a mean SNR per 1Å pixel of 27.35 between 1400-1600Å. The top plot shows the spectrum after the post-processing techniques and the bottom plot shows the residuals. The inset plot provides a closer look at the line profiles of Ly α and N v. The vertical blue bars indicate the continuum fitting windows, which are fit by the power-law continuum denoted by the orange line. The red lines indicate the emission line fits as well as the extent of the individual line-fitting windows. All fitted emission lines are labeled and their individual line profiles are shown.
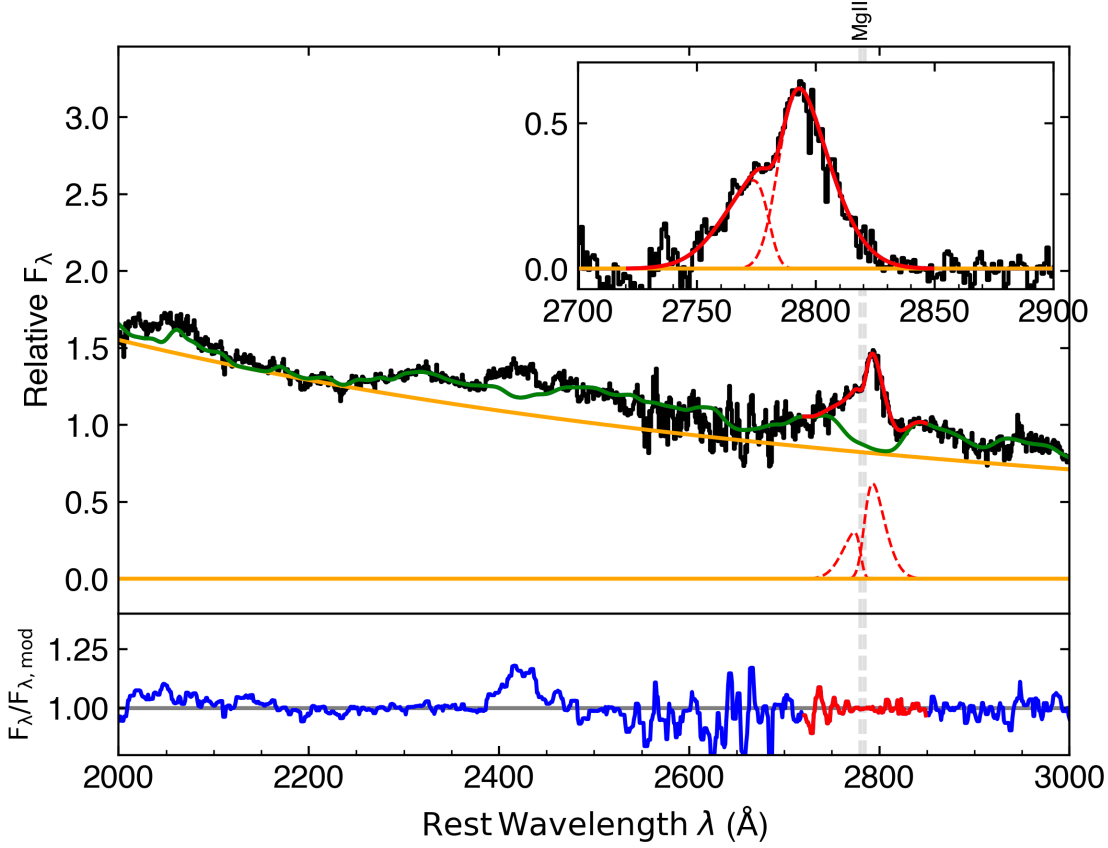
Figure 5.5: Example two-Gaussian fit to the Mg II emission line of PSOJ217-16, observed using VLT/X-shooter. The top plot shows the spectrum after the post-processing techniques and the bottom plot shows the residuals. The inset plot provides a closer look at the Mg II line profile after continuum subtraction. The orange line is the power-law and the green line is full baseline continuum with the Fe II template. The red line marks the fit to the emission line and the extent of the fitting windows. These fits are presented in greater detail in Mazzucchelli et al. in prep.

black hole mass and find good agreement with Mazzucchelli et al. in prep. We calibrate the spectrum against the observed quasar AB magnitude in the J bandpass, where flux from the spectrum integrated over the filter transmission profile is scaled appropriately to the observed value. The peak flux wavelength of the total Mg II line profile is used to determine the redshift and its error. Figure 5.5 shows an example of a multiple Gaussian fit to the Mg II emission line along with the combined power-law and Fe II continuum.

For the line flux error estimation, we adopt a Monte-Carlo approach used in similar studies of high-redshift quasar spectra (e.g. Shen et al. 2019b; Yang et al. 2020; Wang et al. 2021). We create 50 mock spectra for each individual spectrum and stacked composite, where the flux at each pixel is resampled from a symmetric distribution

with a standard deviation equivalent to the pixel spectral error. We assume the spectrum noise to follow a Gaussian distribution in this case. The same fitting procedure is applied to every mock spectrum generated in this way and we filter out outlier fits by sigma-clipping the line flux measurements using a 3-σ threshold. The final line flux of each metallicity-sensitive line is the median of all remaining fits and the final uncertainty is its standard deviation.

Using other empirical templates of the Fe II emission (e.g. Tsuzuki et al. 2006; Bruhweiler & Verner 2008; Mejía-Restrepo et al. 2016) can result in a maximum discrepancy of 20% in the Mg II FWHM, and 0.2% in the estimated redshift. Although this can modify the significance of the black hole mass correlation presented in Section 5.4, it has no effect on the metallicity estimates or the conclusions of this study, which depends primarily on the C IV profile.

Figure 5.1 presents the distribution of redshift, bolometric luminosity, black hole mass, and C IV blueshift in our sample. The completed sample covers redshifts $z = 5.8 - 7.5$, spanning a range in bolometric luminosity $\log{(\mathrm{L_{bol}/erg\,s^{-1}})} = 46.7 - 47.7$ and a range in black hole mass $\log{(\mathrm{M_{BH}/M_\odot})} = 8.4 - 9.8$. Quasars with luminosities $\log{(\mathrm{L_{bol}/erg\,s^{-1}})} \leq 47.0$ and black hole masses $\log{(\mathrm{M_{BH}/M_\odot})} \leq 8.9$ are all observed with GNIRS. We measure C IV blueshifts spanning over 5000 km s^{-1} in our sample, from values consistent with no detectable blueshift to the most extreme outflow-dominated spectrum in PSOJ065-25. None of the targets exhibit a significantly redshifted C IV emission line. We list all of the measured quasar properties in Table 5.1.

5.3.2 Line Ratios and Metallicity

In order to interpret the results of the fitting, it is useful to compare the measured high-ionisation line ratios against predictions from photoionisation models. It's well-known that single-zone photoionisation models are unable to fully reproduce the observed emission from the BLR, because the gas clouds span a wide range of densities and degrees of ionisation (e.g. Davidson 1977; Collin-Souffrin & Lasota 1988). Multi-zone models incorporate emission from gas with a wide range of physical properties and are shown to be consistent with observation (e.g. Rees et al. 1989; Hamann et al. 1998).

The flux ratio-metallicity relation is sensitive to the density of line-emitting clouds, spectral energy distribution (SED) of the ionizing continuum, and microturbulence, but under the locally optimally-emitting cloud model (LOC; Baldwin et al. 1995), the net emission spectrum can be reproduced by integrating across a wide range of physical conditions. Therefore, the characteristics of the observable spectrum

originate from an amalgamation of emitters, where each emission line is formed in a region that is optimally suited to emit the targeted line. This model consistently reproduces properties of both low and high-ionisation emission lines observed in quasar spectra (e.g. Korista & Goad 2000; Hamann et al. 2002; Nagao et al. 2006).

We primarily utilise two broad emission-line flux ratios ($N\,V/C\,IV$, $(Si\,IV+O\,IV)/C\,IV$) because the relevant lines are easier to detect and more commonly studied in the existing literature. However, we also present results for additional line ratios $((O\,III]+Al\,II)/C\,IV$, $Al\,III/C\,IV$, $Si\,III/C\,IV$, $C\,III]/C\,IV)$. The emission from these other lines are substantially more difficult to measure and can only be detected in a robust manner in high SNR spectra, such as our XQR-30 sample of high-redshift quasars. We convert all of the line ratios into metallicity estimates using relations derived from `Cloudy` photoionisation simulations described in Hamann et al. (2002) and Nagao et al. (2006). Both models utilise the LOC model (Ferland et al. 1998). Nagao et al. (2006) predicts line flux ratios for all listed line ratios with two models for the ionizing continuum: one with a strong UV thermal bump matching results from Scott et al. (2004) and one with a weak UV thermal bump similar to Hubble Space Telescope quasar templates (Zheng et al. 1997; Telfer et al. 2002). These two SEDs are thought to be extreme and opposite cases for the actual ionising continuum (Nagao et al. 2006), which gives us the full range of possible inferred metallicities. Hamann et al. (2002) predicts line flux ratios of only $N\,V/C\,IV$ for three mock incident spectra: that of Mathews & Ferland (1987); a single hard power-law with index $\alpha = -1.0$ ($f_\nu \propto \nu^\alpha$); and a segmented power-law with indices $\alpha = [-0.9, -1.6, -0.6]$ for 0.25Å to 12Å, 12Å to 912Å, and 912Å to 1 μm respectively. The segmented power-law continuum approximates data gathered from observations (e.g. Laor et al. 1997). For Hamann et al. (2002), the Mathews & Ferland (1987) incident spectrum predicts the highest metallicities for the same line ratio and the $\alpha = -1.0$ spectrum produces the lowest. The spread in metallicities predicted for the same line ratio is incorporated into our uncertainties. For $N\,V/C\,IV$ the results from both publications are largely consistent with minor differences arising from the SED of the ionizing continuum, integration ranges of gas density (n_H) or ionizing flux (Φ_H), cloud column density, and the version of `Cloudy` used.

Line ratios which imply metallicities over 10 $Z_\odot$ extend beyond the parameter space probed by Hamann et al. (2002) or Nagao et al. (2006). This occurs when the measured line ratio exceeds 0.84 for $N\,V/C\,IV$ or 0.45 for $(Si\,IV+O\,IV)/C\,IV$. For the other line ratios, this occurs at (0.39, 0.16, 0.36, 0.57) for $((O\,III]+Al\,II)/C\,IV$, $Al\,III/C\,IV$, $Si\,III/C\,IV$, $C\,III]/C\,IV)$. In order to investigate inferred metallicities for

higher line ratios, we assume that the observed line flux ratio-metallicity relationship maintains a linear trend in log-space and linearly extrapolate beyond the parameter space probed by the simulations. Super-solar metallicites over 10 $Z_\odot$ have not been calibrated against `Cloudy` simulations.

We consider all of the photonisation calculations with different ionizing SEDs in our metallicity estimate. The effect of the ionizing continuum SED is responsible for up to a factor of two difference in the resulting metallicity predictions from N v/C iv. For N v/C iv, the uncertainty from the metallicity calibration based on the various photoionisation models is dominant over the observational uncertainty. (Si iv+O iv)/C iv is a more robust metallicity indicator than N v/C iv because it is not as sensitive to differences in the ionizing continuum or assumed weighting functions (e.g. Nagao et al. 2006; Matsuoka et al. 2011; Maiolino & Mannucci 2019), and it is not affected by bias propagating from a poor fit to the highly absorbed Ly α emission line. However, in this study, we offer no discussion on the discrepancy between the metallicity indicators. Instead, we present the inferred metallicities separately and use the spread of results from different assumed ionizing SEDs as the uncertainty of each individual measurement. A comparison between inferred metallicities from N v/C iv and (Si iv+O iv)/C iv is provided in the online supplementary material.

5.4   Results

We present all quasars and their measured properties in Table 5.1. In addition to fitting the composites described in Section 5.2.5, the emission-lines of nearly all of the quasar spectra can be fit individually. We fit the N v/C iv line ratio for 16 of the 25 individual quasars, wherever the N v emission can be separated from the Ly α emission. We show the N v/C iv and (Si iv+O iv)/C iv line ratio results for individual fits in Table 5.1 and provide 6 example fits to individual quasar spectra in online supplementary material, covering the lowest and highest quasar bolometric luminosity, black hole mass, and C iv blueshift. Also available are figure sets which show sample fits to bolometric luminosity composites, black hole mass composites, and C iv blueshift composites. We provide all line fluxes measured from our composites normalised against C iv in Tables C.1, C.2, and C.3.

We present the measured line ratios of all individual and composite fits of bolometric luminosity and black hole mass in Figure 5.6. For comparison, we show SDSS low-redshift composites reported in Xu et al. (2018) and high-redshift ($z \sim 6$) quasars observed with GNIRS from Wang et al. (2022). Square symbols indicate measure-

Table 5.1:   Properties of the quasars and spectra included in this study and their measured emission line flux ratios. The redshift is determined from the Mg II line with an uncertainty floor of 0.001. The C IV blueshift is measured using the median wavelength of the C IV fit and the mean SNR is measured in the rest-frame wavelength range 1400-1600Å. We prescribe a minimum error of the C IV blueshift equivalent to $\sim$200 km s^{-1}, based on the 1Å resolution of the resampled grid. All quasars listed above the horizontal divider are observed with GNIRS and all quasars listed below the divider are observed with X-shooter. The last column indicates our source for the black hole mass and bolometric luminosity. The bolometric correction used to measure the luminosity, single-epoch virial mass calibration, and Fe II template used to measure Mg II are all consistent throughout the sample.

Name	R.A. (J2000)	Decl. (J2000)	Mg II Redshift	C IV Blueshift (km s^{-1})	SNR	N V/C IV	(Si IV+O IV)/C IV	M_{BH}/L_{bol} Ref
J0024+3913	00:24:29.77	39:13:19.00	6.620 ± 0.004	635 ± 255	9.45	0.77 ± 0.15	0.27 ± 0.06	1
J0829+4117	08:29:31.97	41:17:40.40	6.773 ± 0.007	1574 ± 336	16.33	0.49 ± 0.09	0.12 ± 0.05	1
J0837+4929	08:37:37.84	49:29:00.40	6.702 ± 0.001	600 ± 204	30.91	1.49 ± 0.08	0.66 ± 0.10	1
J0910+1656	09:10:13.63	16:56:29.80	6.719 ± 0.005	−159 ± 279	9.42	0.50 ± 0.08	0.19 ± 0.09	1
J0921+0007	09:21:20.56	00:07:22.90	6.565 ± 0.001	678 ± 204	9.66	0.49 ± 0.13	0.16 ± 0.05	1
J1216+4519	12:16:27.58	45:19:10.70	6.648 ± 0.003	4955 ± 232	7.63	—	0.50 ± 0.33	1
J1342+0928	13:42:08.10	09:28:38.60	7.510 ± 0.010	6900 ± 405	24.79	—	0.78 ± 0.28	1
J2102-1458	21:02:19.22	−14:58:54.00	6.652 ± 0.003	3433 ± 232	11.47	1.82 ± 0.44	0.57 ± 0.23	1
P333+26	22:15:56.63	26:06:29.40	6.027 ± 0.006	2534 ± 325	5.73	0.80 ± 0.47	0.27 ± 0.19	2
J2338+2143	23:38:07.03	21:43:58.20	6.565 ± 0.009	—	7.07	—	—	1
PSOJ007+04	00:28:06.56	04:57:25.64	6.001 ± 0.002	3816 ± 218	24.58	—	0.45 ± 0.20	3
PSOJ025-11	01:40:57.03	−11:40:59.48	5.816 ± 0.004	2575 ± 266	26.54	—	0.70 ± 0.13	3
PSOJ029-29	01:58:04.14	−29:05:19.25	5.976 ± 0.001	3295 ± 205	27.39	1.14 ± 0.13	0.64 ± 0.15	3
ATLASJ029-36	01:59:57.97	−36:33:56.60	6.020 ± 0.002	2705 ± 217	27.35	1.07 ± 0.11	0.49 ± 0.13	3
VDESJ0224-4711	02:24:26.54	−47:11:29.40	6.528 ± 0.001	2217 ± 204	28.68	0.79 ± 0.04	0.34 ± 0.11	3
PSOJ060+24	04:02:12.69	24:51:24.42	6.170 ± 0.001	1082 ± 204	30.73	0.76 ± 0.05	0.10 ± 0.05	3
PSOJ065-26	04:21:38.05	−26:57:15.60	6.188 ± 0.001	8288 ± 204	36.57	—	0.78 ± 0.65	3
PSOJ108+08	07:13:46.31	08:55:32.65	5.945 ± 0.001	4832 ± 205	37.27	—	0.78 ± 0.27	3
PSOJ158-14	10:34:46.50	−14:25:15.58	6.068 ± 0.001	2683 ± 204	31.67	0.81 ± 0.07	0.28 ± 0.09	3
J1212+0505	12:12:26.98	05:05:33.49	6.439 ± 0.001	4329 ± 204	31.27	—	0.93 ± 0.37	3
PSOJ217-16	14:28:21.39	−16:02:43.30	6.150 ± 0.001	4023 ± 204	34.57	—	0.30 ± 0.13	3
PSOJ242-12	16:09:45.53	−12:58:54.11	5.830 ± 0.001	891 ± 205	15.55	0.87 ± 0.11	0.34 ± 0.22	3
PSOJ308-27	20:33:55.91	−27:38:54.60	5.799 ± 0.001	1971 ± 205	33.18	0.98 ± 0.06	0.95 ± 0.10	3
PSOJ323+12	21:32:33.19	12:17:55.26	6.586 ± 0.001	697 ± 204	31.34	0.73 ± 0.05	0.36 ± 0.08	3
PSOJ359-06	23:56:32.45	−06:22:59.26	6.172 ± 0.001	1082 ± 204	35.36	0.96 ± 0.13	0.11 ± 0.04	3

[1] Yang et al. (2021) [2] Shen et al. (2019b) [3] Mazzucchelli et al. in prep.

ments from fits of composites while circular points indicate fits of individual spectra. Our data, indicated in blue and black, have the highest SNR and spectral resolution of the data represented in the figure. Measurements of both metallicity-sensitive line ratios show a large scatter between individual quasar fits even when controlling for quasar luminosity or black hole mass. Particularly at a bolometric luminosity range of $\log(L_{\rm bol}/{\rm erg\,s^{-1}}) = 47.30 - 47.35$, we see over a factor of 8 difference between the individual quasar measured with the highest and lowest (Si IV+O IV)/C IV line ratio, as seen in Figure 5.7. The composites suppress the high variance that we observe in the individual measurements, which can be attributed to varied C IV blueshifts. The associated uncertainty of the bolometric luminosity and black hole mass for each composite is determined by the mean and standard deviation of the input spectra. We note that in Xu et al. (2018), the black hole masses are estimated using the C IV emission line which can be biased by its blueshift.

The line flux ratio measurements of our high-redshift quasar sample are essentially indistinguishable from the lower-redshift results of comparable luminosity and black hole mass sourced from Xu et al. (2018). Therefore, we do not observe appreciable evolution with redshift. However, our high-redshift sample does not show a statistically appreciable correlation between observed line ratios and the bolometric luminosity, as evidenced in previous work (Hamann & Ferland 1993; Dietrich et al. 2003; Nagao et al. 2006; Xu et al. 2018). This may be because this sample covers a restricted luminosity range compared to the lower redshift sample. Deeper observations of quasars with high redshift and lower luminosity (e.g. Matsuoka et al. 2016) are needed to verify any trend in emission-line ratio with quasar bolometric luminosity. On the other hand, we recover the positive correlation between (Si IV+O IV)/C IV and the estimated black-hole mass as shown in Figure 5.6. The measurements of individual quasars exhibit large scatter for very similar quasar properties. We present the line ratio dependence on the C IV blueshift in the following section to explain this variance.

5.4.1   C IV Blueshift and Line Flux Ratios

Figure 5.8 plots emission line flux ratios against the C IV blueshift along with the estimated black hole mass as a third axis, represented by the blue-green color scale. The C IV blueshift and uncertainty of the composite spectra is obtained from the mean and standard deviation of the input spectra. We prescribe an uncertainty floor of the C IV blueshift equivalent to 200 km s^{-1} based on the 1 Å wavelength grid, but the total uncertainty for measurements of individual quasars is composed also of the redshift error added in quadrature. On average, the C IV blueshift error
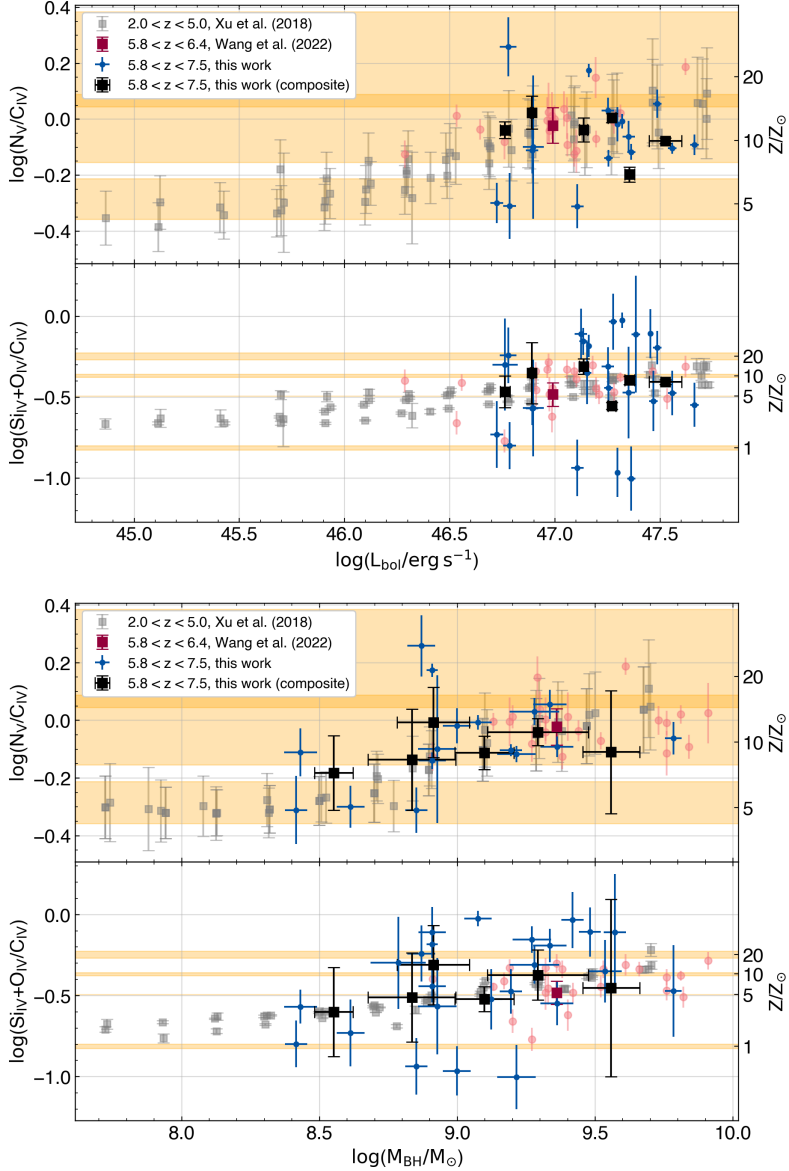
Figure 5.6: $N\,V/C\,IV$ and $(Si\,IV+O\,IV)/C\,IV$ flux ratios as a function of the quasar bolometric luminosity (left) and virially estimated black hole mass (right). The low-redshift sample $(2.0 < z < 5.0)$ indicated in grey is from Xu et al. (2018) while another higher-redshift comparison sample indicated in red is sourced from Wang et al. (2022). Our sample is presented in blue and black. Square points with capped error bars indicate composites while circular points indicate individual fits. Not all individual quasars involved in the composites are plotted. The single red square denotes the composite from Wang et al. (2022). The black hole masses in this study and in Wang et al. (2022) are estimated with single-epoch virial estimates using the $Mg\,II$ emission line, while the Xu et al. (2018) study uses the $C\,IV$ emission line. The orange shaded space indicates a range of line ratios which are consistent with the metallicity indicated in the secondary axis based on photoionisation calculations with different ionizing SEDs. The overlapping region in the $N\,V/C\,IV$ plot indicates a range of line ratios which is consistent with both $Z = 10\,Z_{\odot}$ and $Z = 20\,Z_{\odot}$ (e.g. Hamann et al. 2002; Nagao et al. 2006). Metallicity values larger than $10\,Z_{\odot}$ are extrapolated.
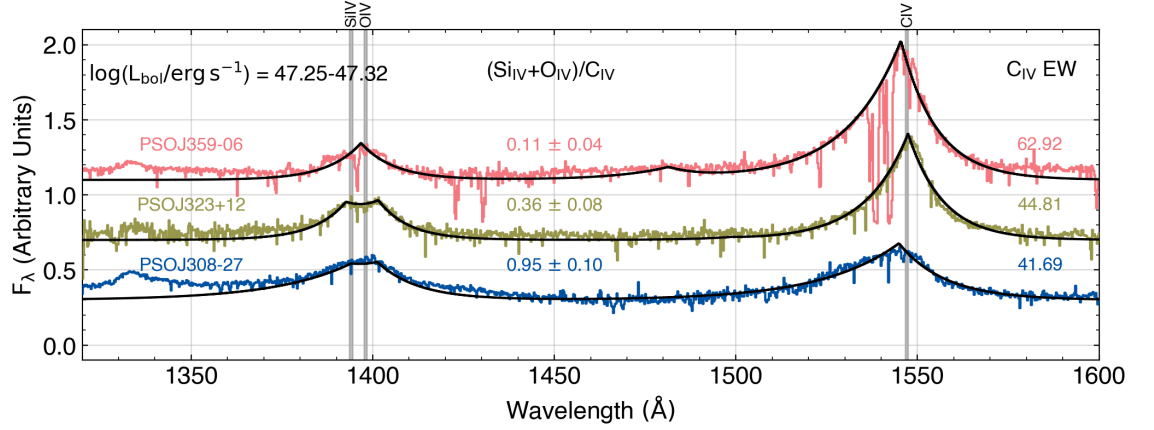
Figure 5.7: Example spectra of three quasars in the sample (PSOJ242-12, PSOJ308-27, and PSOJ359-06) which exhibit similar bolometric luminosities. The raw spectrum is shown in this plot, but many of the significant absorption features (e.g. in PSOJ359-06) are masked by the post-processing procedure. Overall line fits are shown in black. A large scatter in the (Si IV+O IV)/C IV emission line flux ratio is observed between quasar spectra with significantly different C IV equivalent width, which is inversely correlated with the C IV blueshift.

is 230 km s^{-1}. Measurements of the N V emission line becomes more challenging to deblend from the Ly α flux at high blueshifts, especially for individual lower SNR spectra, thus the high C IV blueshift parameter space for N V/C IV is only sparsely explored.

The results from Figures 5.7 and 5.8 demonstrate that the measured emission line ratios are strongly correlated with the C IV blueshift. Controlling for the C IV spectral shape in Figure 5.8, the relationship between the two emission line ratios with black hole mass is no longer clear. The C IV lines of the highest mass quasars are typically more blueshifted, but the most massive quasars do not necessarily have the highest line ratios among other quasars with similar blueshifts. It could also be seen that quasars with moderate ($\sim$1000 km s^{-1}) C IV blueshifts can have a very large scatter in observable line ratios whereas quasars with higher blueshifts consistently possess some of the highest line ratios observed in our sample. At high C IV blueshifts, the lower flux of the C IV line, as evidenced by its correlation with narrower EWs shown in Figure 5.2, drives the C IV-normalised flux ratio measurements higher. The responses of the N V, Si IV, and O IV equivalent widths are not proportionate to that of the C IV line as the C IV blueshift rises. We see similar trends on other metallicity-sensitive line ratios that depend on the C IV flux as shown in Appendix Figure C2.

Figure 5.9 presents the correlations found in our sample between the C IV blueshift with the virially estimated black hole mass, quasar bolometric luminosity, and Ed-

dington ratio. The C IV blueshift is not significantly correlated with the quasar bolo-
metric luminosity, but there is a moderate relationship between the C IV blueshift
with the Eddington ratio and estimated black hole mass, with the magnitude of
Spearman correlation coefficients greater than 0.4 and at least 5% significance. We
show in Figure 5.10 the residuals calculated by subtracting the correlation found
between composites of C IV blueshift and the (Si IV+O IV)/C IV line ratio from the
measured line ratios of individual quasars. The results show that higher mass and
more luminous quasars are not more likely to lie above this relationship, indicat-
ing no strong correlation with black hole mass or luminosity when controlling for
blueshift (also see Temple et al. 2021b). The stronger and more significant cor-
relation between line ratios and the C IV blueshift could be attributed to the fact
that the C IV blueshift is a more direct observable compared to the black hole mass
or luminosity, which are estimated using calibrations with large associated uncer-
tainties. When not controlled, the C IV blueshift can bias other correlations found
between quasar properties and the metallicity in the BLR, such as the apparent
mass correlation in Figure 5.6. It's important to note that the C IV blueshift and
quasar properties are not independent for our sample. This suggests that studies
measuring metallicity-sensitive line flux ratios dependent on the C IV flux should
consider the C IV spectral shape before interpreting the diversity of emission-line
ratios as an indication of evolution in the BLR metallicity.

5.4.2   Inferred Metallicity in the Quasar BLR

Using models derived from the photoionisation code `Cloudy`, we convert the mea-
sured N V/C IV and (Si IV+O IV)/C IV line ratios into metallicity estimates in the
BLR. Figures 5.6 and 5.8 show the range of line ratios consistent with 5, 10, and 20
$Z_\odot$ for N V/C IV and 1, 5, 10, and 20 $Z_\odot$ for (Si IV+O IV)/C IV. The minimum and
maximum bounds of each metallicity estimate are determined by the variations on
the assumed ionizing SED used in `Cloudy` photoionisation LOC models presented in
Hamann et al. (2002) and Nagao et al. (2006). The central tick is determined by the
median of all relevant models. Larger variations in metallicity can be seen for the
N V/C IV line ratio, indicating that (Si IV+O IV)/C IV is less dependent on the shape
of the ionizing flux SED (e.g. Nagao et al. 2006; Matsuoka et al. 2011; Maiolino &
Mannucci 2019). The overlapping region in the N V/C IV plot shows a range in the
line ratio which is consistent with both $Z = 10\,Z_\odot$ and $Z = 20\,Z_\odot$ depending on the
referenced photoionisation model, implying a factor of two uncertainty. The results
for the other line ratios ((O III]+Al II)/C IV, Al III/C IV, Si III/C IV, and C III]/C IV)
plotted against quasar bolometric luminosity, estimated black hole mass, and C IV
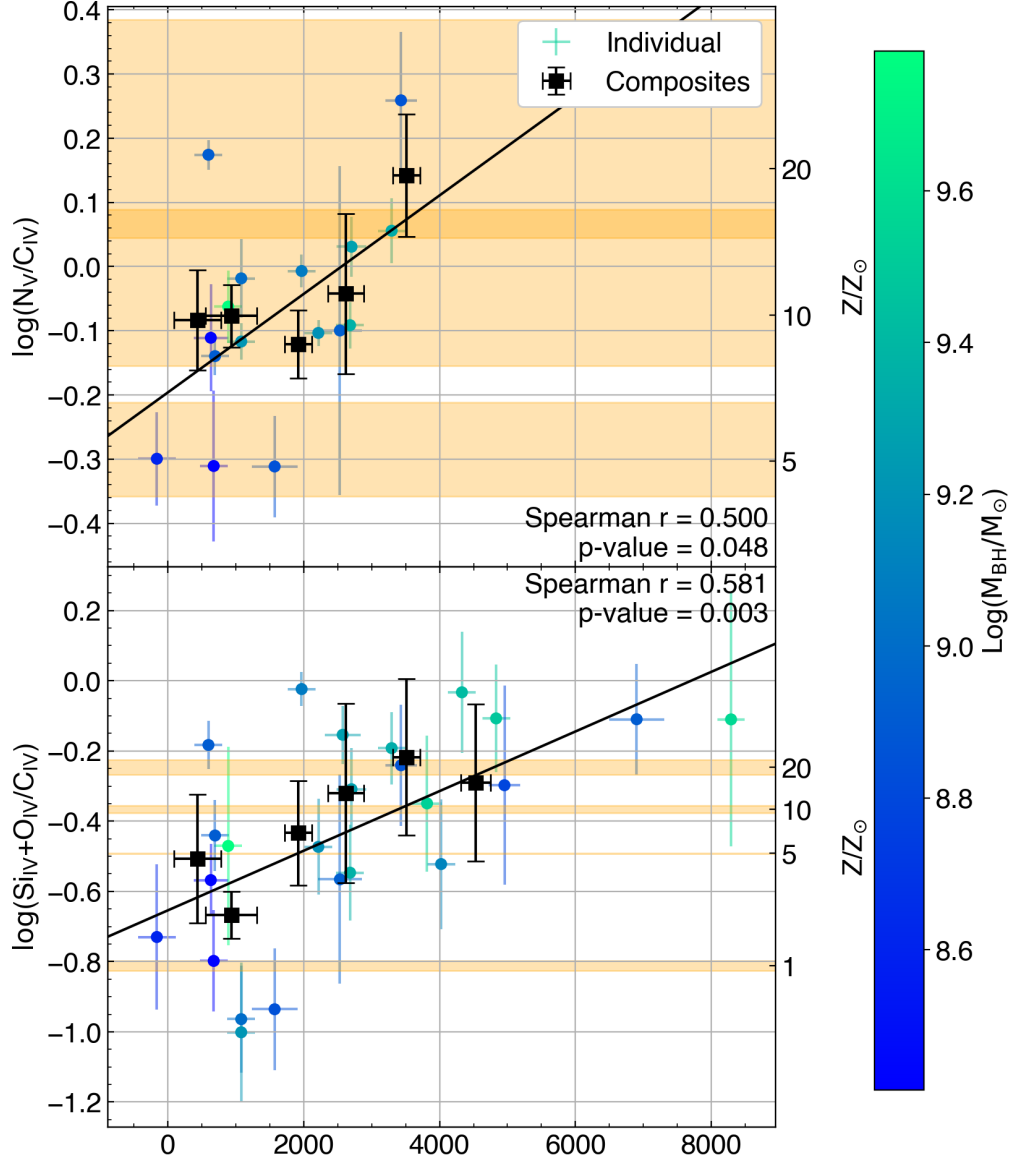
Figure 5.8: N V/C IV and (Si IV+O IV)/C IV flux ratios as a function of the C IV blueshift of quasars in the sample. Blueshift composites are presented in black while individual fits are mapped onto a blue-green gradient scaled to the black hole mass. The minimum C IV blueshift error is 200 km s^{-1} based on the 1Å wavelength bins, but the contribution from the systemic redshift error is added in quadrature for an average total of 230 km s^{-1} uncertainty. The Spearman correlation coefficients and p-values are derived from the fits to individual quasars. The orange shaded space indicates a range of line ratios which are consistent with the metallicity indicated in the secondary axis based on photoionisation calculations with different ionizing SEDs. The overlapping region in the N V/C IV plot indicates a sub-space of parameters which is consistent with both $Z = 10\,Z_{\odot}$ and $Z = 20\,Z_{\odot}$. The line ratio correlation with the C IV blueshift is more significant than the correlation with black hole mass or bolometric luminosity.
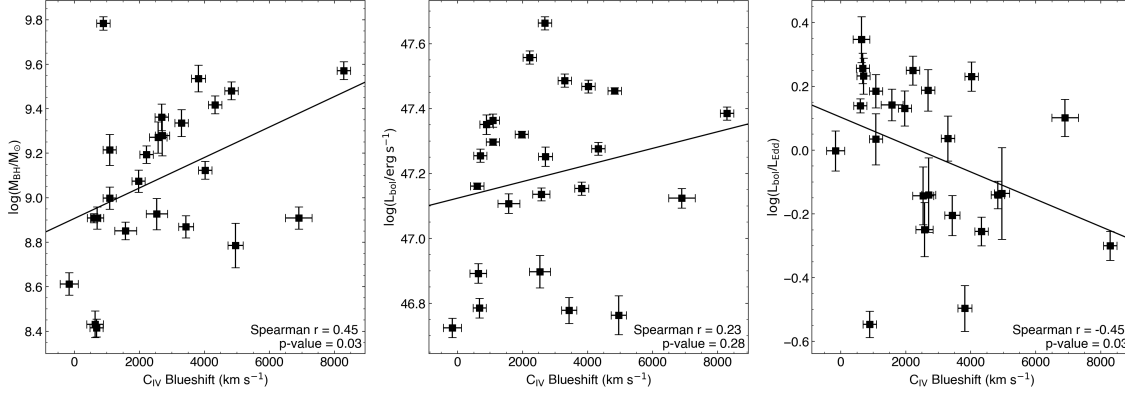
Figure 5.9: The quasar black hole mass (left), bolometric luminosity (middle), and Eddington ratio (right) are plotted against the measured C IV blueshift for our sample. The least-squares linear fits are shown along with the Spearman r-coefficients and their significance. There is a moderate, but significant, correlation between the quasar outflow indicator, i.e. the C IV blueshift, and the black hole mass. The correlation between the C IV blueshift with the Eddington ratio is weaker and less significant, while no significant correlation was found with the bolometric luminosity.

blueshift are presented in Figure C2 in the Appendix. Generally, these other line ratios predict metallicities similar to (Si IV+O IV)/C IV.

Spectra with high C IV blueshift are dominated by emission from an outflowing BLR wind, which is correlated with high X/C IV line flux ratios. Photoionisation models suggest that the wind emission originates from higher density gas clouds closer in to the accretion disk, illuminated by high ionising fluxes, while the core emission is composed of emission from clouds with a broad range of physical properties, as in the LOC model (Temple et al. 2021b). We therefore consider the metallicity results from spectra where the C IV blueshift < 1500 km s^{-1}, minimizing the contribution from the wind emission. The two composites satisfying this requirement yield (N V/C IV, (Si IV+O IV)/C IV) line ratios of (0.83 ± 0.15, 0.31 ± 0.13) and (0.84 ± 0.09, 0.22 ± 0.03) for C IV blueshifts from -200–680 and 680–1500 km s^{-1} respectively. We do not consider the other line ratios in this discussion as they are substantially more difficult to measure. The N V/C IV line ratio typically predicts higher metallicities with greater corresponding uncertainty than the (Si IV+O IV)/C IV line ratio. Figure 5.8 also plots the line ratios for each C IV blueshift composite and the inferred metallicity in the secondary axis. Using the aforementioned reference photoionisation models, the measured N V/C IV line ratio is consistent with being produced by gas clouds with $Z_{-200-680} = 9.77\pm2.35$ $Z_\odot$ and $Z_{680-1500} = 9.96\pm2.42$ $Z_\odot$ for the two lowest C IV blueshift composites. For (Si IV+O IV)/C IV, it is $Z_{-200-680} = 4.61 \pm 0.01$ $Z_\odot$ and $Z_{680-1500} = 2.01 \pm 0.01$ $Z_\odot$. Both metallicity indicators individually suggest super-solar metallicities with high significance ($\gtrsim 4$-σ). The absolute measured metallicity
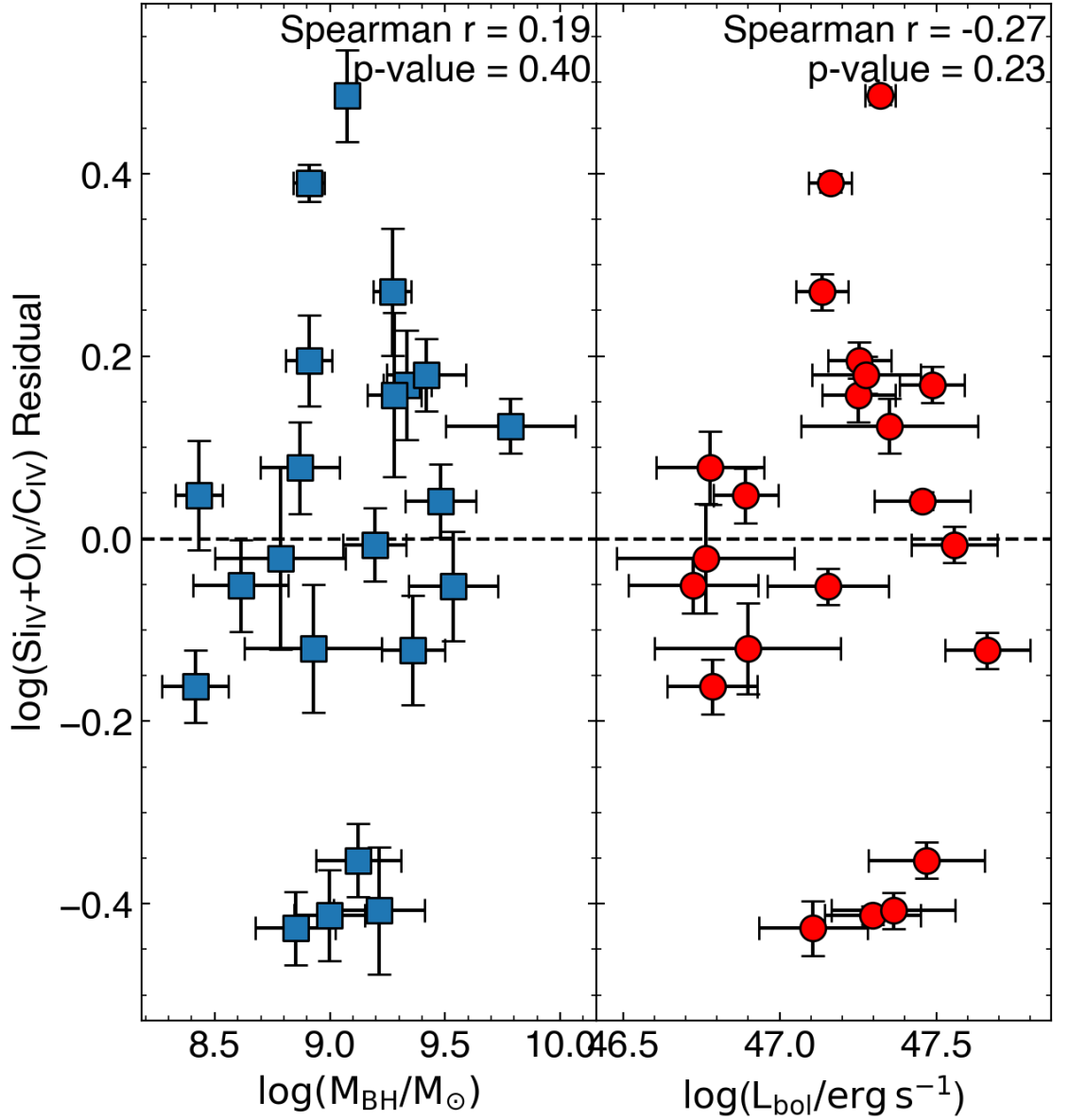
Figure 5.10: (Si IV+O IV)/C IV residual as a function of black hole mass (left) and bolometric luminosity (right). The residual is measured by subtracting the correlation found between composites of C IV blueshift and the (Si IV+O IV)/C IV line ratio from the measured line ratios of individual quasars. The scatter is large around zero with no apparent systematic deviation with black hole mass or bolometric luminosity. This shows that higher mass or more luminous quasars are not more likely to exhibit higher line ratios than their smaller or fainter counterparts. However, we caution the reader when interpreting this relationship, because the C IV blueshift and quasar properties are not independent.

differs by a factor of 2-4 between the indicators although the (Si IV+O IV)/C IV line provides more robust results and is less affected by the model chosen for the ionising flux. Using the (Si IV+O IV)/C IV line ratio, we can see that the metallicity in the quasar BLR at $z \sim 6$ is at least 2-4 times super-solar. Inferred metallicities from spectra observed with high C IV blueshifts range from $Z_{>1500} = 8\ Z_\odot$ to as high as $Z_{>3000} = 20\ Z_\odot$.

5.5   Discussion

Previous studies of chemical abundances in the BLR have suggested metallicities that are several times solar across a wide range of redshifts ($2.0 < z < 7.5$) (e.g. Hamann & Ferland 1992; Dietrich et al. 2003; Juarez et al. 2009; Xu et al. 2018; Onoue et al. 2020), consistent with some galactic chemical evolution models (Tinsley 1980; Arimoto & Yoshii 1987; Hamann & Ferland 1993, 1999). Complementary probes targeting quasar narrow absorption features also suggest super-solar (Z > 2 $Z_\odot$) metallicites (e.g. Hamann & Ferland 1999; D'Odorico et al. 2004; Jiang et al. 2018; Maiolino & Mannucci 2019). The lack of apparent redshift evolution up to $z \sim 6$ stands in contrast to studies of metallicity in star-forming galaxies and Lyman-break galaxies up to $z \sim 3.5$, which show evolution in the mass-metallicity relationship and an overall decrease in metallicity with redshift (e.g. Maiolino et al. 2008; Mannucci et al. 2009). It's possible to infer the host galaxy metallicity using the mass of the central black hole using the tight (0.1 dex) galaxy stellar mass - gas phase metallicity relationship (MZR) (e.g. Maiolino et al. 2008; Davé et al. 2017; Curti et al. 2020; Maiolino & Mannucci 2019; Sanders et al. 2021) combined with the M_{BH}/M_{host} ratios (e.g. Targett et al. 2012). The results from comparisons between quasar BLR and host galaxy metallicities at redshifts $2.25 < z < 5.25$ suggest that the BLR is enriched in excess of the inferred metallicities of the host galaxies, which are approximately solar (Xu et al. 2018). This discrepancy has been attributed to the black hole mass-metallicity relationship and selection effects, where only the most massive and enriched high-redshift quasars are selectively observed in a magnitude-limited survey (e.g. Juarez et al. 2009; Maiolino & Mannucci 2019). However, Xu et al. (2018), Wang et al. (2022), and this work study samples with comparable quasar properties as shown in Figure 5.6. The Xu et al. (2018) composites include hundreds of SDSS DR12 quasar spectra in the redshift range $2.25 < z < 5.25$, whereas Wang et al. (2022) utilises a higher-redshift sample with 33 $z \sim 6$ quasars. These quasars occupy a similar black hole mass and luminosity range, and show very similar line ratios within the scatter of the data, suggesting that a selection bias is not sufficient to explain the apparent lack of redshift evolution.

Additionally, we note that the C IV blueshift, a signature of quasar outflows, is a significant factor correlated with the measured C IV flux (see Figure 5.2). According to a study of 34 low-redshift quasars spanning nearly 3 dex in black hole mass and bolometric luminosity, outflow indicators are not correlated with black hole mass and only marginally correlated with luminosity and Eddington ratio (Shin et al. 2017). Although our study covers a smaller range of quasar parameters, our results in Figure 5.9 show a moderate, but significant, correlation between the C IV blueshift and the black hole mass. There is also a similar negative correlation between the C IV blueshift and the Eddington ratio, and no significant correlation with quasar bolometric luminosity. There are several methodical differences between the measurements in our study and those in Shin et al. (2017). We measure black hole virial masses based on Mg II instead of Hβ, and calculate systemic redshifts from the Mg II line rather than from a combination of low-ionisation narrow lines (Si II, O II], O I], Hβ). We also use different outflow indicators: our C IV blueshift is defined in Equation 5.2, in contrast to the "velocity shift index" (VSI) and "blueshift and asymmetry index" (BAI) defined in Equations 2 and 3 of Shin et al. (2017). According to our result, a correlation between the black hole mass or bolometric luminosity with the C IV blueshift implies that the C IV flux is anti-correlated with the C IV blueshift by extension (see Figure 5.2). As the C IV blueshift is found to be correlated with the metallicity-sensitive rest-frame UV line ratios and quasar properties, this has the potential to bias correlations between metallicity and black hole mass or luminosity. The relationship between the C IV blueshift and these line ratios can be explained by increased gas opacity with metallicity, leading to larger absorption and increased acceleration (e.g. Wang et al. 2012). However, the extreme metallicities ($\sim 20\,\mathrm{Z}_\odot$) seen in the most blueshifted high redshift ($z > 6.0$) quasars in our sample suggest that while the relationship between the C IV blueshift and the line ratio is real, the comparison to the simple photoionisation models is no longer appropriate as emission from the BLR outflow dominates the observed spectrum. The dynamics, density, and geometry of the BLR wind is not the same as for symmetric core emission (Temple et al. 2021b). An alternative explanation is that the C IV blueshift relationship with the rest-frame UV line ratios is driven primarily by the weakening of the symmetric C IV core emission and enhanced emission toward the line-of-sight from quasar orientation (e.g. Yong et al. 2020). Further studies on quasar properties and their emission-line flux ratios will need to account for indications of quasar outflows or avoid using emission lines that are strongly affected by BLR outflow.

It has also been suggested that the observed diversity of line ratios (N V/C IV and (Si IV+O IV)/C IV among others) can be attributed to the variation of density of

the emitting gas and the incident ionizing flux instead of metallicity. Temple et al. (2021b) proposes a model with two kinematically distinct regions, the core and the wind, that can reproduce the range of observed broad emission-line flux ratios under solar metallicities, as long as the spatial density distribution of the emitting gas clouds is adjusted accordingly. Such multiple zone photoionisation models have been used to great effect in reproducing quasar and AGN spectra (e.g. Rees et al. 1989; Peterson 1993; Baldwin et al. 1996; Hamann et al. 1998; Korista & Goad 2000). The locally optimally emitting cloud (LOC) model, proposed in Baldwin et al. (1995), is a natural extension of multi-zone models. The advantage of the LOC model is that the total line emission is composed of an integration over the density (n_H) and ionizing flux (Φ_H) parameter space assuming certain empirically motivated distribution functions (Nagao et al. 2006), thereby bypassing the need for specific knowledge of either n_H or Φ_H. The properties of the emission lines are then dominated by the emitters that are optimally suited to emit the targeted line (Baldwin et al. 1995). It is well-documented that the line ratios depend sensitively on n_H and Φ_H (e.g. Hamann et al. 2002; Nagao et al. 2006; Temple et al. 2021b), but the LOC results represent the average properties of diverse quasar samples. We note that the high-density wind component ($n_H \approx 10^{13-14}$ cm^{-3}, $\Phi_H \approx 10^{22-24}$ cm^{-2} s^{-1}) and the range of typically assumed BLR properties ($n_H \approx 10^{9-12}$ cm^{-3}, $\Phi_H \approx 10^{18-21}$ cm^{-2} s^{-1}) suggested in Temple et al. (2021b) are parameter ranges which are also covered by the LOC photoionisation models used in this study ($n_H \approx 10^{7-14}$ cm^{-3}, $\Phi_H \approx 10^{17-24}$ cm^{-2} s^{-1}) (Hamann et al. 2002; Nagao et al. 2006). However, if the assumed cloud distribution functions used in photoionisation models are inaccurate, the absolute metallicity inferred from line ratios is subject to change. For example, photoionisation models using emission from clumpy disk winds can produce spectra resembling that of quasars (Dannen et al. 2020; Matthews et al. 2020), showing that there are viable alternatives to the LOC models we have referenced for the conversions between line ratio and metallicity.

The results from Temple et al. (2021b) further motivated us to use a quasar outflow indicator, the C IV blueshift, as a control to limit the effect of the BLR wind. Even for composites of low C IV blueshift where the assumed contribution to the overall emission from the wind is low, we observe in Figure 5.8 that the average emission-line properties are comparable to emission from gas clouds with metallicity several times solar (e.g. $Z_{-200-680} = 4.61 \pm 0.01$ $Z_\odot$ using (Si IV+O IV)/C IV) under the LOC model.

The super-solar metallicities in the quasar BLR inferred from low C IV blueshift composites imply rapid enrichment scenarios that are not unrealistic under normal

galactic chemical evolution scenarios in the cores of massive galaxies (e.g. Gnedin & Ostriker 1997; Dietrich et al. 2003). The BLR is a small nuclear region of the galaxy (<1 pc) with higher densities entailing shorter dynamical timescales (e.g. Gnedin & Ostriker 1997; Cen & Ostriker 1999; Kauffmann & Haehnelt 2000; Granato et al. 2004). The total mass of the BLR is on the order of $10^4 \, M_\odot$ (Baldwin et al. 2003), and it can be enriched rapidly to super-solar metallicities within 10^8 yrs by a single supernova explosion every 10^4 yrs (Juarez et al. 2009). Under some multi-zone chemical evolution models, massive star formation in the galactic central regions and subsequent metal enrichment via supernovae can predict super-solar metallicities (up to 10 $Z_\odot$) within 0.5 - 0.8 Gyrs (e.g. Hamann & Ferland 1993; Friaca & Terlevich 1998; Romano et al. 2002). This rapid enrichment scenario means that the properties of the BLRs do not necessarily trace the chemical properties of their host galaxies (e.g. Suganuma et al. 2006; Matsuoka et al. 2018a). This is supported by studies presenting estimates of metallicity in the quasar narrow-line region (NLR) which represent a region over 1000 pc in size (e.g. Bennert et al. 2006). The metallicity in the NLR was found to be 2-3 times lower than the BLR, following similar MZR trends as star-forming galaxies (e.g. Dors et al. 2019). However, in addition to high-metallicity BLRs, there is now mounting evidence that entire host galaxies can be highly enriched to solar values in early cosmic time as evidenced by measurements of C, N, and O ions (e.g. Walter et al. 2003; Venemans et al. 2017; Novak et al. 2019; Pensabene et al. 2021).

More exotic enrichment scenarios such as enhanced supernova rates in central star clusters (e.g. Artymowicz et al. 1993; Shields 1996), star formation inside quasar accretion disks (e.g. Collin & Zahn 1999; Goodman & Tan 2004; Toyouchi et al. 2022), or nucleosynthesis without stars (e.g. Chakrabarti & Mukhopadhyay 1999; Hu & Peng 2008; Datta & Mukhopadhyay 2019) are also capable of producing highly enriched BLRs in a short time. However, we do not consider these to be strictly necessary to explain the metallicities in the $z \sim 6$ redshift quasars inferred from observations in this study. Pushing metallicity estimates to even higher redshifts $z > 8$ when the universe is only 0.6 Gyr old would place more stringent constraints on the metal enrichment timescales from the era of re-ionisation of the universe, where such rapid enrichment scenarios could be required to produce super-solar metallicities (e.g. Friaca & Terlevich 1998).

5.6   Conclusions

In this study, we examined a sample of 25 high-redshift ($z > 5.8$) quasars, 15 of which were observed with X-shooter during the XQR-30 programme and 10 of which were observed with Gemini North's GNIRS sourced from Shen et al. (2019b) and Yang et al. (2021). The sample from XQR-30 contains the highest-quality spectra covering the rest-frame UV emission lines observed in quasars in this redshift range. The bolometric luminosity of the quasars in this sample covers $\log\left(L_{\mathrm{bol}}/\mathrm{erg\,s^{-1}}\right) = 46.7 - 47.7$ assuming a bolometric correction factor of 5.15 from the continuum luminosity at 3000Å. The black hole mass range in the sample is $(0.2-6.0)\times10^9\,\mathrm{M_\odot}$, measured with single-epoch virial mass estimates utilizing the FWHM of the Mg II emission line. We measured the blueshift of the C IV line in most of the quasars in this sample and created composites by quasar luminosity, black hole mass, and C IV blueshift. We then measured broad rest-frame UV emission-line flux ratios in individual quasar spectra and all composites. The main results are as follows:

- Due to the relationship between the C IV blueshift and its equivalent width, the metallicity-sensitive broad emission-line ratios correlate with the C IV blueshift, which is an indicator of the projected BLR outflow velocity. If not accounted for, this correlation biases studies of quasar metallicity and its relationship with black hole mass and luminosity. The correlation between the metallicity-sensitive emission line flux ratios and the C IV blueshift is stronger and more significant than for the quasar bolometric luminosity or black hole mass.

- Comparing against `Cloudy`-based photoionisation models, the metallicity inferred from line ratios of the high-redshift ($z \sim 6$) quasars in this study is several (at least 2–4) times super-solar, consistent with studies of much larger samples at lower redshifts and similar studies at comparable redshifts. We also find no strong evidence of redshift evolution in the BLR metallicity, indicating that the BLR is already highly enriched at $z \sim 6$. The metallicity-sensitive emission-line flux ratios are sensitive to the density n_{H} of gas clouds and the incident ionizing flux Φ_{H}, but we use locally optimally-emitting cloud photoionisation models to draw conclusions based on the average properties of diverse samples of quasars. Our low C IV blueshift composites are good probes of metallicity at this redshift as they minimise the effects of the BLR wind.

- The lack of redshift evolution in the BLR metallicity is contrary to studies of metallicity in star-forming and Lyman-break galaxies, which show a significant redshift dependence. Furthermore, estimates of host galaxy properties based

on black hole mass suggest metallicities that are approximately solar. We find that selection effects are not sufficient to explain the apparent lack of redshift evolution and the discrepancy between the BLR metallicity and host galaxy metallicity. However, given the small scale of the BLR, rapid enrichment scenarios make it a poor tracer of host galaxy metallicity.

- The super-solar metallicity inferred for BLRs at $z \sim 6$ provides stringent constraints on the timescales of star formation and metal enrichment in the vicinity of some of the earliest supermassive black holes. Rapid metal enrichment scenarios of the BLR are not unrealistic under normal galactic chemical evolution models and more exotic explanations, such as nucleosynthesis or star formation inside the accretion disk, are not strictly necessary.

Intrinsic absorption lines could, in principle, provide more straightforward estimates of the BLR metallicity (e.g. Hamann & Ferland 1999; D'Odorico et al. 2004; Maiolino & Mannucci 2019). In the past, such studies were not possible due to low SNR of quasar spectra at $z \sim 6$, but the high-quality data of XQR-30 enables this type of investigation, which will be explored in a future study. More precise metallicity diagnostics would solidify and refine these results, especially for individual quasars.

Acknowledgements

Data Availability

The data underlying this article will be shared on reasonable request to the corresponding author.

Characterising SMSS J2157–3602, the most luminous known quasar, with accretion disc models

Context

This chapter is published as "Lai, S., Wolf, C., Onken, C. A., & Bian, F. (2023), *Characterising SMSS J2157-3602, the most luminous known quasar, with accretion disc models*, MNRAS, 521, 3682."

Preamble

Quasar demographics studies, particularly of the black hole mass function, are limited by the number of quasars with high-quality spectroscopic follow-up observations, because the determination of black hole masses from reverberation mapping or single-epoch virial mass calibrations, as in Chapters 2/3, is observationally expensive. In this chapter, we develop and explore a black hole characterisation method based on the accretion disc continuum that has the potential to constrain black hole properties without spectroscopic data. We fit the observed continuum shape with theoretical thermal accretion disc models in order to estimate the black hole mass, showing that the measured mass is consistent with virial estimates for SMSS J2157–3602, even when accretion disc models are fit to broadband photometry. This work produces an independent and complementary method for constraining black hole properties, with significant potential to extend the method further with more detailed theoretical modelling. However, additional studies are needed to compare the results from accretion disc modelling with more popular existing methods.

Abstract

We develop an accretion disc (AD) fitting method, utilising thin and slim disc models and Bayesian inference with the Markov-Chain Monte-Carlo approach, testing it on the most luminous known quasar, SMSS J215728.21-360215.1, at redshift $z = 4.692$. With a spectral energy distribution constructed from near-infrared spectra and broadband photometry, the AD models find a black hole mass of $\log(M_{\mathrm{AD}}/M_\odot) = 10.31^{+0.17}_{-0.14}$ with an anisotropy-corrected bolometric luminosity of $\log\left(L_{\mathrm{bol}}/\mathrm{erg\,s^{-1}}\right) = 47.87 \pm 0.10$, and derive an Eddington ratio of $0.29^{+0.11}_{-0.10}$ as well as a radiative efficiency of $0.09^{+0.05}_{-0.03}$. Using the near-infrared spectra, we estimate the single-epoch virial black hole mass estimate to be $\log(M_{\mathrm{SE}}/M_\odot) = 10.33 \pm 0.08$, with a monochromatic luminosity at 3000Å of $\log\left(L(3000\text{Å})/\mathrm{erg\,s^{-1}}\right) = 47.66 \pm 0.01$. As an independent approach, AD fitting has the potential to complement the single-epoch virial mass method in obtaining stronger constraints on properties of massive quasar black holes across a wide range of redshifts.

6.1   Introduction

Active galactic nuclei (AGNs) with black holes weighing up to 10 billion solar masses have been discovered in the early Universe, less than a billion years after the Big Bang (Ghisellini et al. 2015; Wu et al. 2015). These luminous high-redshift quasars (QSOs) hosting massive black holes present significant challenges to theoretical models of supermassive black hole growth. Discovering and characterising luminous QSOs allows us to better understand the massive seeds and super-Eddington accretion scenarios necessary for the black holes to reach the observed masses (Bromm & Loeb 2003; Pacucci et al. 2015; Amarantidis et al. 2019; Zubovas & King 2021). Furthermore, luminous QSOs at high-redshift are also useful for mapping our Universe's cosmic reionisation history (e.g. Bañados et al. 2018; Davies et al. 2018).

As QSOs are powered by rapid accretion onto supermassive black holes (SMBHs), the thermal emission from an accretion disc typically peaks in the rest-frame ultraviolet (UV) and lends a degree of homogeneity to samples of QSO spectra. Complete samples of QSOs, however, have a tail towards redder UV-optical colours, usually attributed to dust obscuration (e.g. Webster et al. 1995; Richards et al. 2003; Glikman et al. 2007; Klindt et al. 2019; Fawcett et al. 2022). But also, accretion discs of more massive black holes are colder and thus their intrinsic spectra peak at longer wavelengths (Laor & Davis 2011). This is because the innermost stable orbits of discs scale with the black hole mass M_{BH}, while the thin accretion disc radius for a given temperature scales with $\sim M_{\mathrm{BH}}^{2/3}$ at fixed Eddington ratio. The most extreme

SMBHs in QSOs might thus appear red in the rest-frame UV due to a large BH mass instead of dust. Disentangling the effects of BH masses and dust on QSO colours then relies on observing the disc over a sufficiently broad wavelength range.

A number of different methods have been employed in recent years to estimate black hole masses (M_{BH}) including: reverberation mapping (e.g. Blandford & McKee 1982; Peterson 1993; Netzer & Peterson 1997; Wandel et al. 1999; Kaspi et al. 2000; Peterson et al. 2004), velocity-delay maps (Grier et al. 2013; De Rosa et al. 2018), gravitational micro-lensing (e.g. Irwin et al. 1989; Sluse et al. 2011; Guerras et al. 2013), polarization of broad emission-lines (e.g. Savić et al. 2018, 2021; Capetti et al. 2021; Popović et al. 2022), single-epoch virial estimates (e.g. Vestergaard 2002; McLure & Jarvis 2002; McLure & Dunlop 2004; Greene & Ho 2005; Vestergaard & Peterson 2006), accretion disc fitting (e.g. Malkan 1983; Wandel & Petrosian 1988; Sun & Malkan 1989; Laor 1990; Rokaki et al. 1992; Tripp et al. 1994; Calderone et al. 2013; Capellupo et al. 2015; Campitiello et al. 2018; Mejía-Restrepo et al. 2018; Cheng et al. 2019), dynamical estimates (e.g. Davies et al. 2006; Onken et al. 2007; Hicks & Malkan 2008; Greene et al. 2010; Raimundo et al. 2019), and gravitational redshift of the Fe III line (Mediavilla et al. 2018, 2019). These methods are widely applied based on the features of the system being studied and the availability of data on various observables. In particular, the single-epoch virial mass estimate is frequently used on large samples across a wide range of redshifts (e.g. Shen et al. 2011). It is also the most common method applied for QSOs found at the highest redshifts (e.g. Wu et al. 2015; Mazzucchelli et al. 2017; Reed et al. 2019; Wang et al. 2022) due to the relative ease of obtaining single-epoch spectra compared to spatially or temporally resolved observations.

In this study, we characterise SMSS J215728.21$-$360215.1 (hearafter J2157–3602), the most luminous known quasar, with a spectroscopically measured redshift of $z = 4.692$ (Wolf et al. 2018a; Onken et al. 2020). Using both survey photometry and spectra, we construct a spectral energy distribution (SED) from the rest-frame infrared to ultraviolet. We describe further developments to the accretion disc fitting technique by Bayesian inference of black hole mass with the Markov-Chain Monte-Carlo sampling approach and compare our measurements against the single-epoch virial method. Constraining the peak of the accretion disc emission proves to be effective at measuring the black hole mass (Campitiello et al. 2018). For the peak accretion disc emission to be located at wavelengths longer than $\mathrm{Ly}\,\alpha$, the black hole needs to be sufficiently high mass. Our results show that AD fitting is a viable independent method for characterising the highest mass QSO black holes, which can be applied even in the absence of spectra, making it suitable for large samples. This

creates an opportunity to obtain more stringent constraints on black hole properties and their growth rates, particularly for high-redshift QSOs where other techniques are impractical.

The content of this paper is organised as follows: in Section 6.2, we describe the photometric and spectroscopic data obtained for J2157–3602. In Section 6.3, we present the two complementary methods we use in this study to characterise black hole mass. In Section 6.4, we discuss measurements of the black hole mass and bolometric luminosity, in addition to estimates of the Eddington ratio and radiative efficiency. We conclude with Section 6.5. Throughout the paper, we adopt a flat ΛCDM cosmology with $H_0 = 70$ km s^{-1} Mpc^{-1} and $(\Omega_{\mathrm{m}}, \Omega_{\Lambda}) = (0.3, 0.7)$. All referenced emission-line wavelengths are measured in vacuum.

6.2   Spectral Energy Distribution

We use spectroscopic observations and publicly available survey photometry to construct the SED of J2157–3602.

6.2.1   Photometric Data

We crossmatch J2157–3602, positioned at RA = 329.36762° and Dec = -36.03756° (J2000), with AllWISE (Wright et al. 2010; Cutri et al. 2013), the VISTA Hemisphere Survey (VHS; McMahon et al. 2013) DR6, Two Micron All-Sky Survey (2MASS; Skrutskie et al. 2006), SkyMapper Southern Survey (SMSS; Onken et al. 2019) DR3, and NOIRLab Source Catalog (NSC; Nidever et al. 2021) DR2 to collect photometry from the infrared to optical passbands. The W1 and W2 magnitudes from CatWISE2020 (Marocco et al. 2021) are not appreciably different from that of AllWISE. Properties of J2157–3602, including its photometry, can be found in the discovery paper (Wolf et al. 2018a). We also obtain the transmission profile of all broadband filters using the SVO Filter Profile Service (Rodrigo & Solano 2020).

6.2.2   Spectroscopic Data

Comprehensive details of the spectroscopic observation and data description are presented in Onken et al. (2020). Briefly, observations were obtained from two medium resolution and wide-band spectrographs: the Near-Infrared Echellette Spectrometer (NIRES) instrument (Wilson et al. 2004b) at Keck Observatory and the X-shooter instrument (Vernet et al. 2011) at the Very Large Telescope. The full observed

wavelength coverage is from 3000 Å to nearly 2.5 μm, although little of the source flux is transmitted shortward of Ly α at an observed wavelength of $\sim$ 6920 Å. The data are reduced using `PypeIt` (Prochaska et al. 2020a) and a stacked spectrum is created by scaling the NIRES spectrum to the X-shooter data in the overlapping wavelength region. The absolute flux calibration of the combined spectrum is based on the VHS DR6 J-band photometry. From the Mg II line, the systemic redshift is measured to be $z = 4.692$ and the median signal-to-noise (SNR) per $\sim$50 km s^{-1} velocity dispersion bin measured between rest-frame $2700-2900$Å is nearly 200.

6.2.3   Galactic Extinction

For Galactic extinction, we use $R_v = 3.1$ and the Schlegel, Finkbeiner & Davis (SFD; Schlegel et al. 1998) extinction map to apply a correction in the observed frame. We also utilise a 14% re-calibration factor $E(B-V) = 0.86 \times E(B-V)_{\mathrm{SFD}}$ (Schlafly & Finkbeiner 2011), which is informed by the Sloan Digital Sky Survey (SDSS; York et al. 2000) data and an analysis of the blue tip of the stellar locus (Schlafly et al. 2010). We find the Galactic extinction to be small for J2157–3602, confirmed by $E(B-V) = 0.013$, and due to its extreme luminosity, we assume no host galaxy extinction. However, we briefly discuss the effect of host galaxy extinction on the M_{BH} measurement in Section 6.4.2.

6.3   Black Hole Characterisation

We discuss two complementary methods for estimating the black hole mass of J2157–3602 from photometric and spectroscopic data.

6.3.1   Single-Epoch Virial Mass

We begin by describing the single-epoch (SE) virial mass method, in order to later examine use of the virial mass estimate to inform the Bayesian priors of the accretion disc fitting. The SE technique is routinely applied to QSO spectra (e.g. Vestergaard 2002; McLure & Jarvis 2002; McLure & Dunlop 2004; Greene & Ho 2005; Vestergaard & Peterson 2006). The dynamics of the line-emitting gas is assumed to be virialised with the gravitational potential of the black hole. The velocity-broadened emission-line profile measures the gas velocity, and the continuum luminosity is used to infer the radius of the broad-line region (BLR) through the radius-luminosity (R-L) relation, which is empirically derived from reverberation mapping experiments (e.g. Kaspi et al. 2000, 2005; Bentz et al. 2006, 2013). While most reverberation

mapping experiments calibrate the R-L relation using the Hβ line, the Mg II line profile is found to correlate with Hβ and can be used as its substitute (e.g. Salviander et al. 2007; Shen et al. 2008; Wang et al. 2009; Shen & Liu 2012). This is convenient for the J2157–3602 spectrum where the Hβ line is redshifted out of the X-shooter NIR coverage into wavelengths that are more difficult to observe from the ground. Single-epoch virial mass estimates take on the following form,

$$\left(\frac{M_{\mathrm{SE}}}{M_\odot}\right) = 10^{\mathrm{a}} \left[\frac{\lambda L_\lambda}{10^{44}\,\mathrm{erg\,s^{-1}}}\right]^{b} \left[\frac{\mathrm{FWHM_{line}}}{1000\,\mathrm{km\,s^{-1}}}\right]^{c}, \tag{6.1}$$

where λL_λ is the monochromatic luminosity at a particular wavelength or an emission line luminosity and FWHM is the full-width half-maximum of a broad emission line. In this study, we use the Shen et al. (2011) Mg II calibration with exponents (a, b, c) calibrated to the values (6.74, 0.62, 2.0), based on a high-luminosity local AGN subsample. The differences between sets of calibrations, such as those from Vestergaard & Osmer (2009), are approximately 0.1 dex, but the overall statistical uncertainties of the SE virial mass estimate can be up to 0.5 dex, due to QSO variability and the propagated uncertainties from reverberation mapping masses (e.g. Krolik 2001; Woo et al. 2010; Steinhardt & Elvis 2010; Shen 2013; Kozłowski 2017; Dalla Bontà et al. 2020). In this study, we present the SE virial mass estimates with their measurement uncertainties, but acknowledge that the 0.5 dex statistical uncertainty is often the dominant error.

Spectral fitting

For the SE mass estimate, we fit the stacked spectrum from Keck/NIRES and VLT/X-shooter. One of the primary difficulties in obtaining the pure velocity-broadened profile of Mg II is the treatment of the broad Fe II emission, which forms a pseudo-continuum in QSO rest-frame UV and optical spectra. Following after similar studies of QSO spectra (e.g. Wang et al. 2009), we model the underlying continuum with three components: a power-law, Balmer continuum, and blended Fe II flux. Our power-law is normalised to 3000Å while the Balmer continuum is modeled as a Planck blackbody with a uniform electron temperature T_{e} attenuated by an optical depth τ_λ (e.g. Grandi 1982; Dietrich et al. 2002; Wang et al. 2009; Kovačević et al. 2014). Both parameters, along with the overall normalisation, are free parameters of the continuum fit. The Balmer continuum is often not well constrained independently of the power-law and Fe II continuum, so we do not suggest a physical interpretation of the temperature and optical depth.

The Mg II line profile is sensitive to the underlying Fe II emission features. Adopting

only one Fe II model can induce a bias in the resulting FWHM (e.g. Schindler et al. 2020), so we consider a variety of empirical and semi-empirical Fe II templates. Our Vestergaard & Wilkes (2001, VW01) template is spliced with Salviander et al. (2007), which extrapolates under the Mg II line from the rest-frame $2200-3090$Å; it is the same version of VW01 used in other spectral fitting codes such as `PyQSOFit` (Guo et al. 2018). We also use the Tsuzuki et al. (2006, T06), Bruhweiler & Verner (2008, BV08), and Mejía-Restrepo et al. (2016, M16) templates.

The full pseudo-continuum is uniquely defined by eight free parameters. All components of the continuum are simultaneously fit to selected windows in close proximity to the Mg II line: $2200-2740$Å, $2840-3300$Å, and $3500-3650$Å in the rest-frame. The emission-line is fit to the continuum-subtracted spectrum between the rest-frame wavelengths $2710-2930$Å, which overlaps with the continuum windows in order to force the Mg II flux contribution to converge to zero at the wings. Similar results (within 0.5σ) are obtained without the overlap. The broad line is fit with a maximum of three Gaussian components, each with an independent wavelength shift of up to ±30Å. Although the decomposition of the Mg II line is not necessarily unique, we obtain the FWHM from the total line profile, which is less sensitive to the particulars of the decomposition.

6.3.2 Accretion Disc Fitting

The QSO accretion disc emission can be modeled by a superposition of blackbodies with a wide range of effective temperatures, where the spatial temperature profile is derived from the disc emissivity under classical accretion disc theory (Shakura & Sunyaev 1973; Novikov & Thorne 1973). Under the standard framework of assuming large optical thickness, gas radiates isotropically as a blackbody with a local effective temperature, and flux is integrated across the whole disc surface down to the innermost edge. For a set of black hole properties, its mass and spin, alongside an observed inclination angle and accretion rate or disc luminosity, one can produce predicted SEDs of the observed thermal emission by ray-tracing null geodesics from an observer placed at infinity to the vicinity of the black hole. The steady-state accretion disc structure is solved by semi-analytical or numerical models. The accretion disc fitting method (hereafter AD fitting) can be used to recover black hole properties from observed spectra (e.g. Kawaguchi et al. 2004). Specifically, we use AD fitting to estimate the black hole mass, M_{AD}, where the uncertainty of the measurement originates from a space of degenerate solutions due to the unknown black hole spin and orientation.

Spectral hardening

Realistic accretion disc emission is more complex than a superposition of blackbodies at various temperatures, motivating the addition of a colour correction (hardening) factor, $f_{\mathrm{col}} \geq 1$, to capture the combined effects of Compton scattering, absorption opacity, optical depth, and plasma density structure (e.g. Shimura & Takahara 1993; Ebisawa et al. 1993; Shimura & Takahara 1995). In practice, f_{col} approximates the departure of a more realistic disc from a multitemperature blackbody model. The black hole mass, M_{AD}, is degenerate with the colour correction, following the relation $M_{\mathrm{AD}} \propto f_{\mathrm{col}}^2$ (Ebisawa et al. 1993; Shimura & Takahara 1995) for a Keplerian thin disc with all other intrinsic properties being equal (Li et al. 2005, Eq. 16-17). Thus, any black hole mass measurements from AD fitting will depend sensitively on the hardening factor.

The value of f_{col} is most sensitive to the accretion disc's maximum effective temperature T_{max} (Davis et al. 2005; Done et al. 2012; Davis & El-Abd 2019), where f_{col} converges toward unity for $T_{\mathrm{max}} \leq 3 \times 10^4 \, \mathrm{K}$ (Davis & Laor 2011). At sufficiently low temperatures, helium is largely in a neutral state and the enhanced neutral hydrogen fraction increases absorption opacity, supporting the complete thermalisation of the accretion disc while minimising scattering and Comptonisation effects from free electrons. The maximum effective accretion disc temperature is proportional to accretion rate as $\dot{M}^{1/4}$ and to black hole mass as $M_{\mathrm{BH}}^{-1/2}$ (Laor & Davis 2011). This suggests that the f_{col} correction is high for low-mass black holes accreting at super-Eddington rates, where electron scattering is dominant. In contrast, for supermassive black holes, such as J2157–3602, where $\log(M_{\mathrm{BH}}/M_{\odot}) > 8$ and Comptonisation has little effect (Hubeny et al. 2001), the totality of the accretion disc radiation is likely dominated by thermal emission.

In contrast to the typical value of $f_{\mathrm{col}} = 1.7$, which was developed for X-ray binaries (XRBs) (Shimura & Takahara 1995), similar studies of AGN with supermassive black holes adopt $f_{\mathrm{col}} = 1$ (Vasudevan & Fabian 2007, 2009; Done et al. 2012; Calderone et al. 2013; Campitiello et al. 2018; Mejía-Restrepo et al. 2018; Cheng et al. 2019). However, we caution that some models predict an increased hardening factor with black hole mass (e.g. Davis & El-Abd 2019). Other approaches and theoretical integrated spectra of AGN accretion discs around supermassive BHs predict that the hardening factor should be close to unity (Hubeny et al. 2000, 2001; Czerny et al. 2011). Empirically, if the hardening factor was significant, AD fitting studies that assume a value of unity should find their measurements of M_{BH} to be systematically underestimated compared to independent measurements, but significant overestimation is sometimes observed instead (e.g. Calderone et al. 2013;

Campitiello et al. 2020). In this study, we assume $f_{col} = 1$ to remain consistent with similar AD fitting approaches developed for AGN with supermassive BHs.

We consider both geometrically thin (`kerrbb`; Li et al. 2005) and slim (`slimbh`; Sadowski 2011; Straub et al. 2011) accretion disc emission models, where the pre-calculated spectral tables are accessed through `XSPEC` 12.12.0 (Arnaud 1996), packaged as part of `Sherpa` (Freeman et al. 2001), the modeling and fitting suite of Chandra Interactive Analysis of Observations (CIAO) v4.14. Both models are ray-traced numerical solutions to steady-state accretion disc models with general relativistic effects and they have been found to be consistent with synthetic spectra created from numerical general relativistic radiative magnetohydrodynamic simulations of puffy discs (Wielgus et al. 2022). To tackle the inherent degeneracies in the problem, we use Markov-Chain Monte-Carlo techniques to infer the black hole mass from its posterior probability distribution.

Thin disc

The `kerrbb` model is an optically thick and geometrically thin numerical Keplerian accretion disc model originally designed for black hole X-ray binary spectra (Li et al. 2005). Ray-tracing is used to calculate the spectrum, under the assumption that emission from every point in the accretion disc is locally blackbody-like. A limitation is that the `kerrbb` model assumes a perfectly flat disc with no vertical thickness, flaring, or warping (Li et al. 2005). Nevertheless, Campitiello et al. (2018), hereafter C18, used `kerrbb` to develop analytic expressions approximating the black hole mass M_{BH} and accretion rate $\dot{M}$ from fitting the QSO SED, finding that M_{AD} can be constrained by the peak of the accretion disc spectrum, ν_p, and the peak luminosity, $\nu_p L_{\nu_p}$. However, even for a fixed inclination θ_{inc}, the peak frequency and luminosity are degenerate with M, $\dot{M}$, and a, such that any accretion disc SED can be reproduced by a carefully selected family of solutions. The parameter space covered by the degenerate solutions can be minimised by making reasonable assumptions about the spin and inclination (C18). Despite the degeneracies involved, we discuss how we derive the maximum likelihood black hole mass in Section 6.3.2.

Comparisons of reverberation mapping and SE virial mass estimates showed that the analytical approximations of C18 can measure M_{AD} to a precision of 0.45 dex (Campitiello et al. 2020, hereafter C20). They further showed that the `kerrbb`-based mass estimates are systematically larger (up to 0.4 dex depending on black hole mass and spin) than masses estimated through SE methods for their sample, which spans $\log(M_{BH}/M_\odot) = 7.5 - 9.5$.

In our application of `kerrbb`, we toggle on the effects of self-irradiation, whereby

radiation can be gravitationally deflected, illuminating another part of the accretion disc, and include limb-darkening effects. We also set the torque at the inner boundary of the accretion disc to zero, following the standard theory of accretion discs. The effect of a nonzero torque enhances the disc power by boosting returning radiation, particularly at higher energies. However, nearly indistinguishable spectra can be created by adjusting the effective mass accretion rate even for very high torques (Li et al. 2005). We show in Section 6.4.2 an alternative $M_{\rm AD}$ estimate if the disc power from torque is comparable to the disc emission.

Slim disc

The thin disc approximation breaks down for Eddington ratios ≥ 0.3 (e.g. Laor & Netzer 1989), motivating the relaxation of the thin disc assumption. The XSPEC spectral model, slimbh, is a fully relativistic, optically thick slim disc accretion model with numerical ray-tracing originally designed to fit the X-ray continuum of black hole X-ray binaries (Sadowski 2011; Straub et al. 2011). In contrast to standard thin disc models, slimbh relaxes the imposed Keplerian angular momentum condition and accounts for advective cooling (Sadowski 2011). Campitiello et al. (2019) derived analogous analytical approximations showing that, as with the thin disc model, the black hole mass can be constrained by the peak flux and wavelength of the accretion disc SED. However, in the slimbh model, the mass accretion rate $\dot{M}$ is replaced with the disc luminosity $L_{\rm disc}$ parameterised in terms of the Eddington ratio $\lambda_{\rm Edd}$, which introduces a black hole mass dependence. Additionally, the vertical structure is only evaluated up to the Eddington limit. In the low Eddington regime, slimbh spectra converges towards the geometrically thin kerrbb spectra, making it a more general model, except that zero torque is enforced at the inner boundary of the accretion disc. Another constraint is that slimbh is restricted to positive black hole spins only, whereas kerrbb is also calculated for negative spins.

In our application of slimbh, we toggle on the effects of limb darkening and the heightened surface profile, such that ray-tracing can be performed from the disc photosphere rather than from the equatorial plane. We assume a constant $f_{\rm col} = 1$ and do not utilise BHSPEC disc atmosphere models (Davis et al. 2005). We also set the α-viscosity parameter to 0.01. In Section 6.4.2, we discuss how the $M_{\rm AD}$ estimate is not sensitive to the α-viscosity parameter. We present sample slim disc spectra created using slimbh for various black hole masses, disc luminosities, inclinations, and spins in Figure 6.1.
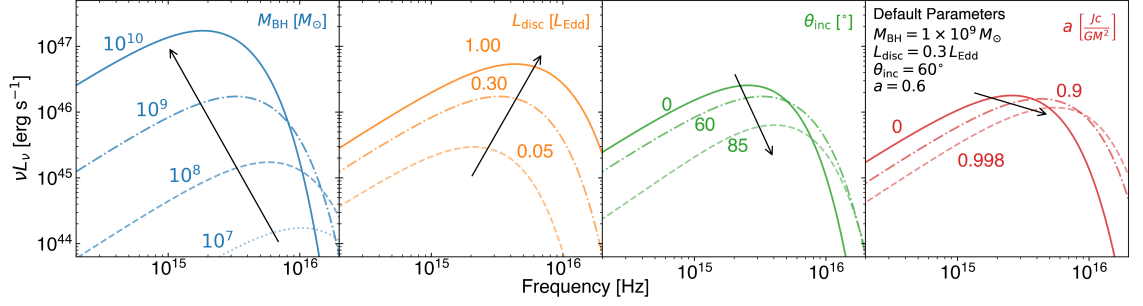
Figure 6.1: Accretion disc spectra created from `slimbh` slim disc models, with each panel varying one of the four parameters: (from left to right) black hole mass, disc luminosity, inclination, and spin. The default parameters are listed in black within the rightmost panel and all SEDs are labelled with the modified value corresponding to the parameter on the top-right of each panel. The black arrows indicate the direction that the SEDs evolve towards as the parameter increases for this test case.

Accretion disc SED

We consider three datasets for fitting the AD models: synthetic photometry created from the stacked spectra, survey photometry, and modified photometry with QSO template subtraction. In all cases, we apply the Galactic extinction correction from Section 6.2.3. We fit accretion disc emission in a region bounded by rest-frame 1 μm and 1600Å, due to the increasing hot dust contribution at the red end and the intergalactic medium Ly α absorption at the blue end. Because of the wide wavelength coverage of each of the photometric data and broad C IV visible in the spectrum, characteristic of a high-ionisation broad absorption line (HiBAL) QSO, we leave a sizable buffer between the blue threshold and the Ly α forest. Very broad photometry, such as those from *Gaia*, are ill-suited to the accretion disc fitting approach because they can hide many details of the underlying spectral shape that are crucial to obtaining a good fit.

1. Synthetic Photometry (SynPhot)

   The presence of broad emission lines, the Balmer continuum, and Fe II flux implies that a significant fraction of the structure observable in spectra is not required for fitting the underlying continuum emission. Instead of fitting the spectrum directly, we create synthetic photometric data points with a flat transmission profile for contiguous sections of accretion disc emission that are free of emission-line contribution. The emission-line-free windows are created by masking all broad lines and identifying regions of the Gaussian-broadened Bruhweiler & Verner (2008, BV08) Fe II template that fall below a flux threshold, which we set to 70% of the median template flux. Both the Gaussian broadening of the Fe II template and the width of the broad line mask are

scaled to a velocity dispersion value, which we set to 4500 km s^{-1}. The size of the mask is three times the velocity dispersion. We found that our results are not sensitive to reasonable values chosen for the Fe II template flux threshold and width of the Gaussian broadening kernel. This procedure creates synthetic photometry from the stacked spectrum, which we use in place of the photometry from the same wavelength region.

For the red end of the SED outside of the wavelength coverage of the stacked spectrum, we scale the Selsing X-shooter template (Selsing et al. 2016) to match the flux of J2157–3602 photometry, where each photometric bandpass is treated independently. The cutouts of the Selsing template, each with the width of one bandpass, are used to create synthetic photometry using the same method as above. In this way, we replace the W1 and W2 photometric points, avoiding flux contribution from bright emission lines, such as Hα. Because each photometric point is treated independently, differences in the global continuum slope between our target and the Selsing template are minimised. We test this by creating variations of the synthetic photometry for deviations in the Selsing template continuum slope, parameterised by an F_λ power-law slope of $\alpha = -1.70$ (Selsing et al. 2016). We test variations of $1\,\sigma_\alpha$, where we take $\sigma_\alpha = 0.6$ from the Rakshit et al. (2020) catalogue, and find median flux variations of $5-7\%$ in the synthetic photometry We find the flux variations to have no significant effect on our measurements as described in Section 6.4.2.

2. Photometry-Only

   For comparison to the synthetic photometry, we present results obtained from fitting only the survey photometry in Section 6.4.2.

3. Template-Corrected Photometry

   In a further modification to the photometry-only models, we apply the same approach as for the long-wavelength data of the SynPhot model and scale the Selsing template to the observed photometry and use its continuum model to correct for flux contribution from emission lines.

These two alternative datasets to the synthetic photometry demonstrate how the black hole mass estimate from AD fitting is affected if spectroscopic data is unavailable.

Markov-Chain Monte-Carlo

The free parameters in AD fitting are the black hole mass M_{BH}, luminosity, spin a, and observer's inclination θ_{inc} with respect to the symmetry axis of the accretion

disc (equivalent to the spin axis), where the luminosity is parameterised in terms of the mass accretion rate $\dot{M}$ for `kerrbb` and the Eddington ratio for `slimbh`. The inclination angle corresponds to $\theta_{\mathrm{inc}} = 0°$ when viewed face-on and $\theta_{\mathrm{inc}} = 90°$ when viewed edge-on. These parameters are inescapably degenerate in the absence of independent constraints. We utilise Bayesian Markov-Chain Monte-Carlo (MCMC) methods, as implemented in the Python `emcee` module (Foreman-Mackey et al. 2013), to probe the multi-dimensional parameter space and obtain a posterior distribution of M_{BH}.

We adopt an uninformative, flat prior probability distribution for all free parameters, except for the black hole mass. There, we investigate three probability distributions: a flat prior, a SE virial mass prior, and a black hole mass function prior. The SE virial mass prior is a Gaussian distribution centred around the SE mass estimate with a width set to a statistical uncertainty of 0.5 dex. The black hole mass function prior is based on a double power-law parameterisation of the QSO luminosity function (Onken et al. 2022a), which is transformed from 145nm absolute magnitude to black hole mass through the Runnoe et al. (2012) bolometric correction and an assumed fixed mean Eddington ratio. For mean Eddington ratios > 0.1, such as 0.25 (Kollmeier et al. 2006) or 0.6 (Trakhtenbrot et al. 2011), the slope of the mass function on the bright-end, which determines the relative likelihood between black hole masses, is constant across the range of black hole masses being considered and the exact Eddington ratio assumed is inconsequential. We use double power-law parameters derived from Onken et al. (2022a) with faint-end constraints from Niida et al. (2020) and the redshift evolution of the normalisation from Fan et al. (2001) for the sample with a median redshift of $z = 4.83$. The location of the knee in the mass function for fixed mean Eddington ratios of 0.25 and 0.6 are $\log(M_{\mathrm{BH}}/M_{\odot}) = 9.28$ and 8.90, respectively. For bright QSOs similar to J2157–3602, the slope of the mass function is a conservative prior which disfavours spuriously high black hole masses.

In Section 6.4.2, we discuss the effect of the prior on our black hole mass measurement. The black hole spin parameter is allowed to explore the space of all positive spins, $0 < a < 0.998$, and we exclude edge-on cases for the inclination, requiring $\theta_{\mathrm{inc}} < 65°$, which is our assumed opening angle of the obscuring torus. We consider edge-on orientations to be intrinsically less likely given the extreme luminosity of J2157–3602. We also check the convergence of our model using `ChainConsumer` (Hinton 2016) and confirm that our M_{BH} posterior is independent of the initial parameters. The final M_{AD} estimates are taken from the maximum likelihood of the posterior distribution, with uncertainties determined by the 68% iso-likelihood line.

If a parameter could not be constrained this way such as when the distribution is strongly skewed towards one end of the allowed parameter space, then the median of the distribution is used instead, with uncertainties determined by the 16th and 84th percentiles.

6.4   Results and Discussion

In this section, we present the results of both methods for determining M_{BH} from the combined photometric and spectroscopic data. We compare these methods against each other and to previous results obtained for the black hole of J2157–3602 (Onken et al. 2020). We discuss bolometric corrections to the observed luminosity at 3000Å with anisotropy correction and use these quantities to further derive the QSO Eddington ratio and radiative efficiency. Finally, we discuss the potential of the AD fitting method.

6.4.1   Black Hole Mass from SE Virial Method

Previous estimates of the black hole in J2157–3602 based on a similar analysis of the Mg II line found $\log(M_{\mathrm{SE}}/M_\odot)_{\mathrm{Mg\,II}} = 10.53 \pm 0.08$ (Onken et al. 2020), using the Shen et al. (2011) calibration. This value, however, depends on the FWHM measured above a continuum defined with the VW01 template, which can result in systematically overestimated FWHMs compared to other Fe II templates (Schindler et al. 2020).

Figure 6.2 presents fits to the Mg II emission feature of J2157–3602 with various Fe II templates. Each template is broadened by a Gaussian kernel with a dispersion between 3300–5100 km s^{-1} depending on the template and the Mg II FWHM is measured in the range 4200–5150 km s^{-1}.

We consider two sources of uncertainty in the measurement: the statistical uncertainty from the choice of Fe II template and the measurement uncertainty. We estimate the statistical uncertainty by independently fitting the emission feature with each of the four Fe II templates and measuring variance in the resulting FWHMs. To minimise bias towards any particular template, the mean from the four fits is used as the final estimate of the FWHM. We also consider an additional measurement uncertainty which is estimated from fitting 100 synthetic spectra, where the flux at each wavelength bin is resampled according to a Gaussian distribution with a standard deviation equivalent to the flux uncertainty. The variance in the resulting fits is added to the final uncertainty of the FWHM. Because of the high SNR of the

spectra, the statistical uncertainty from the Fe II templates is over $5\times$ the measurement uncertainty, but the final error in M_{SE} remains significantly below the overall statistical error of the virial mass estimator.

From the Galactic extinction-corrected and stacked spectrum, we remeasure the FWHM to be 4550 ± 400 km s^{-1} with fits to the Mg II feature, relative to 5720 ± 570 km s^{-1} from Onken et al. (2020). The monochromatic luminosity at 3000Å measured from the power-law continuum is $\log(L(3000\text{Å})/\mathrm{erg\,s}^{-1}) = 47.66 \pm 0.01$. Therefore, the adjusted black hole mass calculated from the SE virial mass estimate is $\log(M_{\mathrm{SE}}/M_\odot)_{\mathrm{Mg\,II}} = 10.33 \pm 0.08$, which is 0.2 dex less massive than the estimate by Onken et al. (2020).

6.4.2 Black Hole Mass from AD Fitting Method

We present the results from the AD fitting method in Table 6.1 for three choices of the prior probability distribution: a flat uninformative prior, a distribution based on the SE virial mass estimate, and another based on the QSO mass function. We also present fits to three datasets: the synthetic photometry (SynPhot), template-subtracted photometry (Template), and photometry-only (Photometry). Descriptions of these three datasets can be found in Section 6.3.2.

In Figure 6.3, we present a corner plot for the parameter chain from the `slimbh` model fits to synthetic photometry using the SE virial mass estimate with 0.5 dex width as the prior, which is our default model for future discussions, unless otherwise stated. A black hole mass estimate of $\log(M_{\mathrm{AD}}/M_\odot) = 10.31^{+0.17}_{-0.14}$ is measured from the M_{BH} posterior, which has a log-normal shape and a slightly extended high-mass tail. It's clear that neither the black hole spin a nor inclination θ_{inc} are well-constrained by the data, but lower spin and face-on orientation solutions are preferred. Notably, while the slim disc model solutions are clearly skewed towards face-on orientations which we consider intrinsically more probable, the thin disc inclination posteriors are more biased towards edge-on. This further supports that, for extremely luminous QSOs such as J2157–3602, the slim disc model is a more realistic representation of the accretion disc spectra. The convergence between the emergent spectra of the two models suggest that the thin disc model is a good approximation for black holes with low Eddington ratios. To test the sensitivity of our result to the synthetic photometry, we consider variations to the data created by changing the Fe II template, the Fe II flux threshold, or the power-law continuum slope applied to the Selsing template, and find no appreciable effect on the resulting black hole mass estimate.

From fitting the photometry alone, we find a $0.05-0.10$ dex greater M_{AD} com-
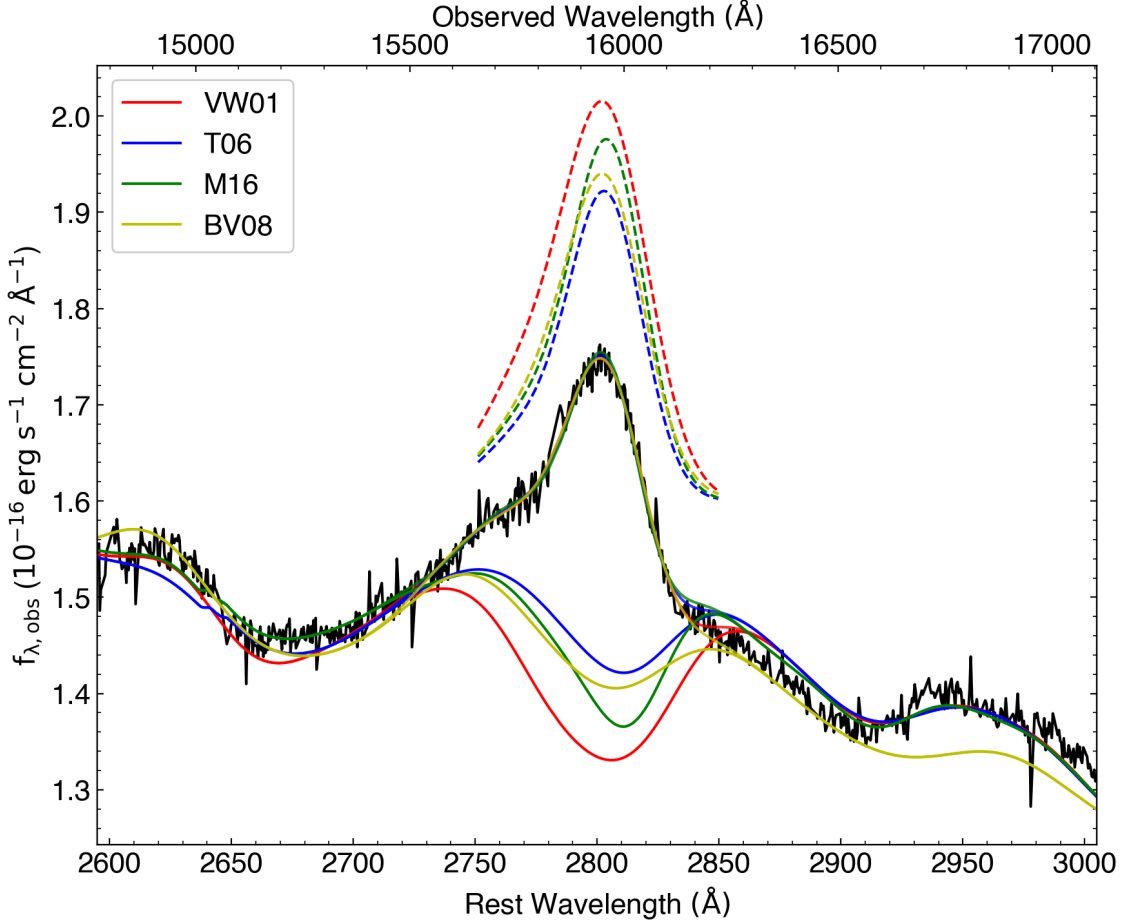
Figure 6.2: Fits of the Mg II emission feature of J2157–3602 with the combined pseudo-continuum from the power-law, Balmer, and Fe II components. The fits differ from one another by the applied Fe II template (see legend). The resulting continuum for each template is plotted in solid lines and the fitted line profile in dashed lines, while the data is shown in black. The BV08 template is not well-matched to features on the red end of the Mg II line. Individual emission line fits are offset to 1.6×10^{-16} erg s^{-1} cm^{-2} Å^{-1} and the FWHM between fits with different Fe II models range from 4200 to 5150 km s^{-1}. The Mg II FWHM mean and standard deviation are 4550 ± 400 km s^{-1}.

pared to synthetic photometry, because the additional flux from broad emission-lines boosts the perceived luminosity of accretion disc models. The results from the template-corrected photometry are intermediate between that of the observed photometry and synthetic photometry, with a small but consistent correction of $\Delta M_{\rm AD} \sim 0.05$ dex over results from synthetic photometry. However, depending on the properties of an individual QSO with respect to the template, this adjustment may be sufficient to offset the higher mass bias from photometry. The `kerrbb` thin disc model estimates are also systematically greater than `slimbh` slim disc models, suggesting that the thin disc assumption may be partially responsible for an overestimation of $M_{\rm AD}$ in C20, although the difference shown for this target is minimal. It remains to be seen whether the discrepancy is greater at lower black hole masses as was the case in C20.

Between prior probability distributions, the SE virial mass estimate with its 0.5 dex uncertainty is not a strong prior, producing results similar to the uninformative prior. In contrast, the steep high-mass end of the QSO mass function favours $M_{\rm AD}$ estimates over 0.10 dex lower. Measurements presented in Table 6.1 imply that the rms uncertainty of $M_{\rm AD}$ from an unconstrained spin and inclinations below 65° is less than 0.2 dex. Relaxing the inclination angle limitation or enforcing a more stringent inclination constraint produces black hole mass estimates within 0.6σ, which implies that our result is not sensitive to the assumed opening angle.

Despite the indications of the spin posterior distribution, one might expect that the spin of the J2157–3602 black hole is fairly high due to its inferred history of prolonged, ordered accretion, in order for it to have grown to its observed mass in roughly 1 Gyr (e.g. Volonteri et al. 2005; Barausse 2012; Walton et al. 2013). If we used a prior of $a > 0.6$, the $M_{\rm AD}$ estimate would be consistent with the unconstrained case, at $\log(M_{\rm AD}/M_\odot) = 10.39^{+0.19}_{-0.10}$. Independent constraints on degenerate parameters, such as an estimate of spin from the Fe-Kα broad lines in the X-ray (e.g. Reynolds & Fabian 2008; Reynolds 2021), have the potential to improve the black hole mass estimates from AD fitting. However, as estimated in the later Section 6.4.4, the radiative efficiency is fairly low, implying lower spins ($a \lesssim 0.5$) in concordance with the MCMC result and that the growth history of J2157–3602 may have involved periods of chaotic accretion, suppressing its spin and radiative efficiency, while maintaining high mass accretion rates (Zubovas & King 2021). In this study, we remain agnostic about the spin distribution, preferring to keep the spin prior uniform across the entire positive spin parameter space, which produces a conservative estimate of the precision by which the black hole mass can be measured.

For the results of the thin disc `kerrbb` model, if the disc power from the torque at the inner boundary of the accretion disc were assumed to be comparable to the disc emission, then the resulting mass estimate using synthetic photometry with the SE prior would be $\log(M_{AD}/M_\odot) = 10.61^{+0.15}_{-0.21}$, which is 0.18 dex higher than with zero torque. As the `kerrbb` mass estimates are already higher than the virial and `slimbh` masses, including the effect of a nonzero torque further exacerbates the disparity. We also consider an alternative slim disc `slimbh` model with the α-viscosity parameter set to 0.1 instead of 0.01, which is a high estimate for AGN accretion discs (e.g. Starling et al. 2004). The mass estimate with the higher α-viscosity is $\log(M_{AD}/M_\odot) = 10.31^{+0.16}_{-0.15}$, virtually indistinguishable from the original estimate. This is expected as the viscosity parameter has little effect on the emergent spectrum aside from boosting the spectrum to higher energies through electron scattering (Kawaguchi 2003). However, as discussed previously, Compton effects are unlikely to be significant in the regime of supermassive black holes accreting at sub-Eddington rates. To test this assumption, we utilise our Bayesian MCMC AD fitting method with the slim disc model to constrain the hardening factor, finding $f_{col} = 1.00^{+0.25}_{-0.00}$ from the posterior distribution. Therefore, the hardening factor is consistent with unity as we have assumed.

When the limb darkening effect is disabled, we find $\log(M_{AD}/M_\odot) = 10.33^{+0.15}_{-0.12}$ using the `slimbh` model with the SE prior. The black hole mass estimate is marginally increased and the mass posterior distribution is slightly narrower. However, the difference between the mass estimates with and without limb darkening depends on the shape of the inclination posterior. For J2157–3602, we find face-on solutions are generally favoured by the slim disc model and the thin disc model favours inclinations closer to edge-on. In this scenario, the `kerrbb` mass estimates experience a marginal decrease when limb darkening is disabled and the `slimbh` mass estimates increase slightly.

Dust extinction

The average QSO with HiBAL features typically exhibits some reddening due to host galaxy dust (e.g. Brotherton et al. 2001; Reichard et al. 2003). The dust extinction inferred from QSOs at $z < 2.2$ is consistent with the SMC extinction curve (Richards et al. 2003; Hopkins et al. 2004). At higher redshifts, the extinction curve has a tendency to flatten at $\lambda \leq 2000\text{Å}$, indicating a different dust production mechanism or a different physical mechanism by which dust is processed into the ISM (Gallerani et al. 2010), although an SMC extinction law is still consistent with the data in most cases (e.g. Krawczyk et al. 2015).
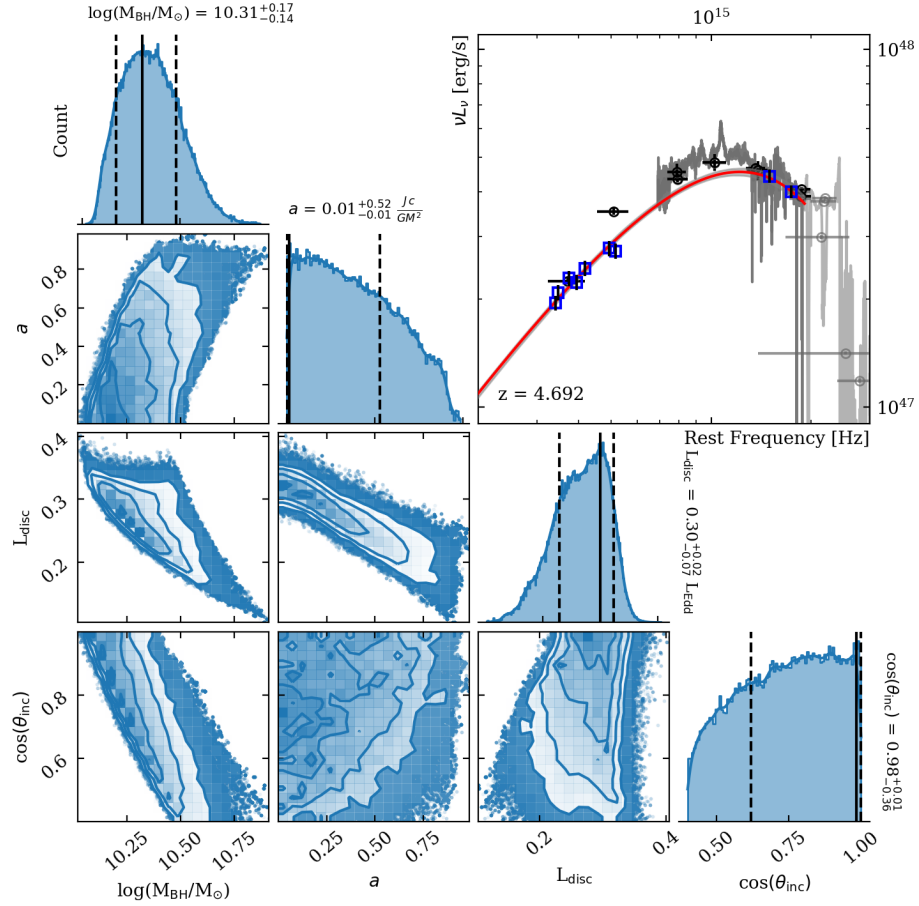
Figure 6.3: Corner plot for the accretion disc fit to J2157–3602 synthetic photometry using the `slimbh` model. The frequency is presented in the rest-frame. The SE virial mass estimate is used as a prior probability distribution on the black hole mass. The final estimate of each parameter is determined by the maximum likelihood of the posterior distribution, with uncertainties determined by the 68% iso-likelihood line. The top-right panel shows the stacked spectrum in dark grey, the synthetic photometry in blue square points, photometry in black, and masked data in light grey. The red model is the highest likelihood model and the one-sigma spread from a random sample of posterior models is similar in width to the red model line. Neither black hole spin a or inclination $\theta_{\rm inc}$ are constrained by the data, but the black hole mass is estimated to be $\log(M_{\rm AD}/M_\odot) = 10.31^{+0.17}_{-0.14}$.

Table 6.1: Black hole masses, $\log\left(M_{BH}/M_\odot\right)$, measured by the AD fitting method for thin and slim accretion disc models and three different prior probability distributions. The three sets of measurements are distinguished by the dataset to which the AD model is fit. "SynPhot" refers to the synthetic photometry created from spectroscopic data, "Template" refers to the photometric data scaled to the continuum model of an average QSO template (Selsing et al. 2016), and "Photometry" refers to the photometry-only data. The Galactic extinction correction is applied to all datasets. Our default AD fitting model, marked in bold font and referenced throughout this paper, is the `slimbh` model fit to synthetic photometry using the Single-Epoch prior.

Model (Data) / Prior	Flat	Single-Epoch	Mass Function
`kerrbb` (SynPhot)	$10.44^{+0.11}_{-0.25}$	$10.43^{+0.12}_{-0.21}$	$10.29^{+0.17}_{-0.15}$
`slimbh` (SynPhot)	$10.32^{+0.17}_{-0.15}$	$\mathbf{10.31^{+0.17}_{-0.14}}$	$10.21^{+0.18}_{-0.10}$
`kerrbb` (Template)	$10.49^{+0.12}_{-0.24}$	$10.47^{+0.12}_{-0.22}$	$10.31^{+0.20}_{-0.13}$
`slimbh` (Template)	$10.37^{+0.17}_{-0.17}$	$10.35^{+0.17}_{-0.15}$	$10.27^{+0.16}_{-0.13}$
`kerrbb` (Photometry)	$10.51^{+0.13}_{-0.23}$	$10.51^{+0.10}_{-0.24}$	$10.35^{+0.19}_{-0.14}$
`slimbh` (Photometry)	$10.39^{+0.18}_{-0.16}$	$10.36^{+0.20}_{-0.14}$	$10.27^{+0.19}_{-0.11}$

In order to quantify the effects of host galaxy dust attenuation, we assume the empirically inferred mean extinction curve from Gallerani et al. (2010) with an SMC-like $R_V = 2.7$ (Bouchet et al. 1985) The mean reddening measured for QSOs with HiBAL features is $\Delta E_{B-V} \sim 0.02$ relative to an ensemble average QSO composite, which is itself reddened by $\Delta E_{B-V} \sim 0.004$ compared to a non-BAL composite (Reichard et al. 2003). However, individual measurements show a wide distribution, with a sizable fraction (30–40%) of HiBALs less reddened than a similar sample of non-BALs (Reichard et al. 2003). Thus, we do not refer to the mean case to infer host galaxy reddening for an individual target, especially not for a target as extreme as J2157–3602. However, to test how significant dust reddening would affect our measurements, we choose $E_{B-V} = 0.08$, which is fairly substantial dust extinction for a QSO (Krawczyk et al. 2015). This value was also chosen to keep the disc luminosity sub-Eddington and constrained by the slim disc model.

An AD fit to the de-reddened synthetic photometry results in a black hole mass estimate of $\log(M_{AD}/M_\odot) = 10.15^{+0.14}_{-0.19}$, which is $\Delta \log(M_{AD}/M_\odot) = -0.16$ for $E_{B-V} = 0.08$. Increasing the host galaxy extinction has two competing effects on the AD fit: the true luminosity of the continuum rises and the intrinsic continuum becomes bluer. The former favours higher black hole masses, while the latter implies higher accretion disc temperatures, which favours lower black hole masses. Overall, the influence from a bluer continuum is stronger, resulting in an AD model with a less massive black hole, but higher luminosity and Eddington ratio.

The SE virial black hole mass estimate with host galaxy extinction would be in-

creased by the boosted 3000Å monochromatic luminosity, which implies a larger BLR radius. Assuming the measured FWHM does not change appreciably, the extinction law implies

$$d\log(M_{\rm SE}/M_\odot)/d(\Delta E_{\rm B-V}) = 0.248\, R_V\, (A_{3000Å}/A_V)\ , \qquad (6.2)$$

where $(A_{3000Å}/A_V)$ is evaluated from the mean extinction curve and the extinction of the object is measured relative to the mean extinction of the SE calibration sample, meaning $\Delta E_{\rm B-V} = E_{\rm B-V,obj} - E_{\rm B-V,cal}$. Using the Gallerani et al. (2010) curve with $(A_{3000Å}/A_V) = 1.86$, we find $d\log(M_{\rm SE}/M_\odot)_{\rm SE}/d(\Delta E_{\rm B-V}) = +1.2$. Thus, increasing host galaxy extinction causes our two independent $M_{\rm BH}$ measurement methods to diverge, which implies our source is likely to be minimally extinguished. In further discussions, we use the $M_{\rm BH}$ estimates without host galaxy extinction, specifically $\log(M_{\rm AD}/M_\odot) = 10.31^{+0.17}_{-0.14}$ from the default slim AD fitting model.

6.4.3 Bolometric Luminosity

Using the myriad of accretion disc models from the MCMC posterior, we integrate all of the resulting SEDs with an anisotropy correction to derive a bolometric luminosity of $\log(L_{\rm bol}/{\rm erg\,s^{-1}}) = 47.87 \pm 0.10$, implying a bolometric correction factor of $k_{3000Å} \sim 1.62$, following $L_{\rm bol} = k_\lambda L(\lambda)$. This differs from empirically derived bolometric correction factors, such as $k_{3000Å} \sim 5.15$ (Richards et al. 2003), $k_{3000Å} \sim 3.33$ (Runnoe et al. 2012), $k_{3000Å} \sim 3.2$ (Trakhtenbrot & Netzer 2012), and $k_{3000Å} \sim 1.84$ (Netzer 2019), from which we estimate $\log(L_{\rm bol}/{\rm erg\,s^{-1}}) = 48.17 \pm 0.16$ using all four correction factors. We provide a detailed description of the bolometric luminosity measurement in Appendix D.1, and compare it with commonly used empirical bolometric corrections. We also derive and present mean flux anisotropy corrections for samples of QSOs in Appendix D.1.3.

6.4.4 Eddington Ratio and Radiative Efficiency

The Eddington ratio, ϵ, is calculated by the ratio of the bolometric luminosity and the Eddington luminosity for a particular black hole mass, $L_{\rm bol} = \epsilon L_{\rm Edd}$, where $L_{\rm Edd} \approx 1.26 \times 10^{38}(M_{\rm BH}/M_\odot)\,{\rm erg\,s^{-1}}$. From the AD mass estimate, $\log(M_{\rm AD}/M_\odot) = 10.31^{+0.17}_{-0.14}$, we measure $\epsilon = 0.29^{+0.11}_{-0.10}$. As discussed in Onken et al. (2020), the relatively low Eddington ratio suggests that the extreme luminosity of J2157–3602 is a consequence of the size of its black hole.

Other studies of radiative efficiency for individual QSOs, defined as η in $L_{\rm bol} = \eta\dot{M}c^2$, are also based on accretion disc models (e.g. Davis & Laor 2011; Trakhtenbrot

2014; Trakhtenbrot et al. 2017). In order to address the degeneracy with inclination, these studies assumed $\cos(\theta_{\mathrm{inc}}) = 0.8$, functionally a Dirac δ-function prior in the MCMC context. In the absence of an independent constraint on the inclination, we use the black hole mass prior determined by the SE virial mass estimate. The `kerrbb` thin disc model with four parameters (M_{BH}, $\dot{M}$, a, θ_{inc}) is considered, because the disc luminosity is parameterised in terms of the mass accretion rate. From the fit to synthetic photometry, we determine the MCMC posterior mass accretion rate to be $\dot{M} = 144^{+84}_{-48}\, M_\odot\,\mathrm{yr}^{-1}$, suggesting that the radiative efficiency is $\eta = 0.09^{+0.05}_{-0.03}$, which is consistent with estimates based on the Sołtan argument (e.g Yu & Tremaine 2002).

6.4.5   Potential of AD Fitting

Recently, the potential for AD fitting to complement other black hole mass measurements, such as the SE virial mass method, has been confirmed by several studies (Calderone et al. 2013; Capellupo et al. 2015; Mejía-Restrepo et al. 2018; Campitiello et al. 2020). Here we find that although neither the black hole spin or observed inclination are constrained by the data, we can obtain approximately log-normal posterior distributions of the black hole mass with widths under 0.2 dex. We are also able to use the model SED to estimate anisotropy-corrected bolometric luminosities within 0.1 dex precision.

As an independent method of estimating black hole masses, the AD fitting method can be used to disentangle cases for which SE virial mass estimates between different broad lines are in disagreement. For instance, the QSO SDSS J102325.31+514251.0, hereafter J1023+5142, is measured to host a black hole of mass $\log(M_{\mathrm{SE}}/M_\odot)_{\mathrm{Mg\,II}} = 10.52 \pm 0.08$ or $\log(M_{\mathrm{SE}}/M_\odot)_{\mathrm{H}\beta} = 9.58 \pm 0.14$, as estimated from the Mg II or Hβ line, respectively (Zuo et al. 2015). We collect photometric data by crossmatching J1023+5142 with AllWISE, 2MASS, and PanSTARRS DR1. We also use the SFD extinction map with the 14% recalibration (Schlafly & Finkbeiner 2011), finding $E(B - V) = 0.013$, coincidentally matching that of J2157–3602. Assuming no host galaxy extinction and by fitting only photometry, we find $\log(M_{\mathrm{AD}}/M_\odot) = 9.55^{+0.20}_{-0.17}$ using the AD fitting method, which strongly disfavours the Mg II-based estimate. As the measured black hole mass scales inversely to extinction, additional host galaxy reddening corrections will not boost the mass estimate to become consistent with $\log(M_{\mathrm{SE}}/M_\odot)_{\mathrm{Mg\,II}}$. A more comprehensive description of the fits to J1023+5142 photometry can be found in Appendix D.2 alongside a discussion of its spectral properties, measured bolometric luminosity, Eddington ratio, and radiative efficiency.

From the Shen et al. (2011) QSO catalogue of 105,783 QSOs, we find 1599 targets

with $\log(M_{\mathrm{SE}}/M_\odot) > 8$ and a difference between the Hβ and Mg II-based virial mass estimate of over 0.5 dex. Applying the same criteria to the Rakshit et al. (2020) catalogue, we find 1122 such QSOs. In a forthcoming study, we will use AD fitting to investigate targets for which the SE mass estimates are discrepant.

We showed in Section 6.4.2 that a host galaxy extinction correction has diverging effects on the SE and AD fitting mass estimate. Hence, they can be used together to constrain the magnitude of the host galaxy extinction. A unique advantage of AD fitting is that it can also be used to constrain the radiative efficiency of individual QSOs, as shown in Section 6.4.4.

Having explored the AD fitting approach extensively on a single target, J2157–3602, we will apply the method to much larger samples in future studies. Samples of luminous QSOs with high-quality spectra, such as XQ-100 (López et al. 2016) and XQR-30 (e.g. Zhu et al. 2021; Lai et al. 2022), will enable us to produce comparisons between AD fitting and the more established SE virial mass estimate, particularly for supermassive ($\log(M_{\mathrm{BH}}/M_\odot) > 8$) black holes at high redshift.

6.5 Conclusions

In this study, the survey photometry and high-quality medium-resolution spectra of the extremely luminous QSO SMSS J215728.21−360215.1 enabled us to compare two complementary methods of estimating black hole masses. The main results are as follows:

- An updated black hole mass of $\log(M_{\mathrm{SE}}/M_\odot)_{\mathrm{Mg\,II}} = 10.33 \pm 0.5$ was obtained from the Mg II line using multiple empirical and semi-empirical templates to constrain the surrounding Fe II emission. This estimate is 0.2 dex lower than an earlier analysis for J2157–3602 (Onken et al. 2020).

- The best performing model from fitting the accretion disc using MCMC suggested a black hole mass of $\log(M_{\mathrm{AD}}/M_\odot) = 10.31^{+0.17}_{-0.14}$, in concordance with the SE estimate.

- We measured the anisotropy-corrected bolometric luminosity to be $\log(L_{\mathrm{bol}}/\mathrm{erg\,s^{-1}}) = 47.87 \pm 0.10$ from the SEDs of the accretion disc models. We also measured the monochromatic luminosity at 3000Å to be $\log(L(3000\text{Å})/\mathrm{erg\,s^{-1}}) = 47.66 \pm 0.01$, from which we inferred $\log(L_{\mathrm{bol}}/\mathrm{erg\,s^{-1}}) = 48.17 \pm 0.16$, using bolometric corrections from Richards et al. (2003), Runnoe et al. (2012), Trakhtenbrot & Netzer (2012), and Netzer (2019). We use the bolometric luminosity measured from the accretion disc SED to further derive the Eddington ratio and radiative efficiency.

- The Eddington ratio was calculated to be $\epsilon = 0.29^{+0.11}_{-0.10}$, based on the AD model estimates of the BH mass and bolometric luminosity.

- We also estimated the radiative efficiency to be $\eta = 0.09^{+0.05}_{-0.03}$, measured from the thin disc mass accretion rate posterior distribution.

We demonstrated the utility of fitting accretion disc models in characterising basic properties of high-mass black holes in QSOs. As an independent estimate of black hole mass, this method can be used to complement the SE virial mass estimate, especially at high redshift where other methods are not as easily accessible. The key findings of the AD fitting method are the following:

- Both black hole mass M_{BH} and the anisotropy-corrected bolometric luminosity L_{bol} can be constrained without prior knowledge of the black hole spin or the observed inclination angle. The uncertainties of these measurements are 0.2 dex and 0.1 dex on the mass and luminosity, respectively. Independent constraints on either spin or inclination would improve measurement precision.

- Quantities such as the Eddington ratio and radiative efficiency can be derived from comparing observed properties of the black hole to its intrinsic properties, parameterised as part of the disc models.

- It is possible to obtain a reasonable estimate of black hole mass with only broadband photometric data. The offset is found to be 0.1 dex for the target examined in this study, but spectroscopic data can further refine these results.

- Host galaxy dust extinction has diverging effects on single-epoch and AD fitting mass estimates. There is potential to exploit this idea to constrain host galaxy extinction for luminous QSOs and the shape of the extinction curve.

We plan future studies to investigate a larger sample of luminous QSOs with high-quality spectra, comparing black hole mass estimates between measurements of broad emission-line profiles and the large-scale accretion disc continuum emission.

Acknowledgements

Data Availability

The data underlying this article will be shared on reasonable request to the corresponding author.

Applications of Accretion Disc Fitting

Context

Sections of this chapter are published in "Wolf, C., Lai, S., Onken, C. A., Amrutha, A., Bian, F., Hon, W. J., Tisserand, P., & Webster, R. (2024), *The accretion of a solar mass per day by a 17-billion solar mass black hole*, Nature Astronomy, accepted" and "Tang, J.-J., Wolf, C., Tonry, J., Lai, S., Yong, S. Y., & Steyn, Z. (2023), *Probing quasar viewing angle with the variability structure function*, MNRAS, 523, 4441", which are studies to which I have made significant contributions as a co-author.

In Wolf et al. (accepted), I led the quantitative analysis to characterise SMSS J052915.80–435152.0, evidently the fastest growing black hole currently known. This involves data processing, spectral decomposition, and fitting the observed spectral energy distribution with accretion disc models. This work allowed us to estimate the black hole mass, luminosity, and accretion rate of SMSS J052915.80–435152.0. In Tang et al. (2023b), I provided the relation describing the luminosity dependence on orientation based on accretion disc modelling. This is a critical element in the study, because it is used in conjunction with model orientation diagnostics, such as the Hβ FWHM and C IV velocity shift, to evaluate empirical data from a large sample of quasars.

In this chapter, I present my textual contributions to each of these publications, wrapped in additional text written in traditional thesis style to contextualise the work. Each of these sections, which is reproduced directly from the publication, is preceded by a contribution statement.

Preamble

While the method developed in Chapter 6 was originally developed for independent and complementary black hole mass measurements in the absence of data from more expensive observational techniques, the intersection between theoretical modelling and observation has the potential for numerous other applications. In this chapter, we demonstrate how we have used accretion disc modelling to contribute to studies related to quasar orientation and record-breaking extreme quasars. This highlights how continued developments in the theoretical modelling of quasar accretion discs are necessary for unifying and understanding the diversity of observable active galactic nuclei properties.

7.1 The Fastest Growing Black Hole in the Universe

7.1.1 Introduction

Exceptionally rare intrinsically ultraluminous high-redshift quasars are windows into the most extreme black holes and most well-developed massive galaxies in the early Universe. Their existence challenges theories of black hole formation and evolution as well as the coevolution of black holes and their galaxies. Supermassive black holes seen at the highest redshifts (Bogdán et al. 2023; Pacucci et al. 2023), which have only recently been identified by the James Webb Space Telescope, show that some quasars harbour black holes with masses comparable to the total stellar mass of its host galaxy, in contrast to the mass budget of $\sim 0.1\%$ for the black hole in the local Universe (e.g. Reines & Volonteri 2015). Such overmassive black holes are also potential targets for the VLTI/GRAVITY+ instrument, which is an upgrade to GRAVITY (GRAVITY Collaboration et al. 2017), which can produce well-resolved spatio-kinematic maps of the BLR. Bright quasars are also critical for the Sandage test (Sandage 1962; Martinelli et al. 2012), which will directly measure the expansion of the universe through the shifting redshifts in absorption lines of the Ly α forest in the era of extremely large telescopes. In summary, extremely luminous quasars offer the ideal laboratory for future studies requiring large BLRs and high luminosity for maximum signal strength.

This work discusses a recently identified ultraluminous quasar SMSS J052915.80–

435152.0, which was discovered through optical and mid-infrared colour selection (Onken et al. 2023) and confirmed by using the wide-field spectrograph (Dopita et al. 2007, 2010) on the Australian National University (ANU) 2.3-meter telescope at Siding Spring Observatory. Early indications were that it had comparable or brighter luminosity than the most luminous known quasar at the time, J2157–3602 (Wolf et al. 2018a; Onken et al. 2020; Lai et al. 2023b), and with no clear evidence of gravitational lensing (Onken et al. 2023).

In the following "Methods" section, as part of Wolf et al. (accepted), we describe the spectroscopic observations of J0529–4351 and data processing, as well as efforts to constrain the black hole properties through spectral decomposition and accretion disc modelling. This section begins with a description of the spectroscopic observations of J0529–4351 and its data processing, where another co-author, Christopher A. Onken, and I shared the responsibility for the data reduction, which included a custom telluric correction and photometric calibration. Due to the overlap between intrinsic emission features and atmospheric absorption windows, the spectrum of J0529–4351 was ill-suited for the standard data reduction pipeline. Using the reduced spectrum, I performed the spectral decomposition and emission-line modelling in this study, which informed the black hole mass, luminosity, and accretion rate estimates. Finally, I was responsible for applying the accretion disc modelling to the J0529–4351 spectral energy distribution, which provided an independent constraint on black hole parameters.

The following section is reproduced from Wolf et al. (accepted) without modification, of which the spectral decomposition, luminosity estimation, and continuum fitting sub-sections represent my textual contribution to the study.

7.1.2 Methods

Spectroscopic observations and data processing

The optical/near-IR spectrum of J0529–4351 was obtained with the X-Shooter instrument (Vernet et al. 2011) on ESO's Very Large Telescope (UT3) on 2023, Jan 14. The airmass at the time of observation was 1.06 and the estimated seeing was about 1.5 arcsec. In the UVB, VIS, and NIR arms, the slit widths and total exposure times were: 1.0 arcsec and 500 s; 0.9 arcsec and 400 s; and 0.9 arcsec and 800 s, respectively.

The data were reduced using PypeIt, a Python-based spectroscopic data reduction pipeline (Prochaska et al. 2020a,b).

Because it was not possible to *a priori* know the underlying true shape of the C
IV $\lambda 1549$ emission line beneath the atmospheric A-band absorption, we could not
reliably fit the telluric model to the J0529–4351 VIS spectrum alone. To obtain
an improved correction, we took the telluric model generated from a standard star
observed on the same night and modified it by adopting a power-law intrinsic stellar
spectrum across a broad span of wavelengths unaffected by strong stellar atmo-
spheric lines. Applying this modified model to J0529–4351 yielded a final spectrum
with a smooth C IV $\lambda 1549$ profile containing only narrow absorption lines and no
spurious emission from overcorrected telluric absorption.

The observed spectrum was corrected for slit losses by calibration to external
photometric data, in particular, the quasar's VHS DR6 *J*-band magnitude of
14.812 ± 0.003 mag (Vega). With the VHS calibration anchoring the NIR arm,
the VIS and UVB data were sequentially matched to the spectroscopic flux levels
in the wavelength regions of overlap between the arms. This *J*-band calibration is
consistent (within the photometric errors) with that of the i_{SDSS} X-Shooter acquisi-
tion image, as calibrated by synthetic photometry for a neighbouring, non-variable
star with *Gaia* low-resolution spectroscopy, and the flux scale measured in the *Gaia*
spectrum of J0529–4351 itself.

Spectral decomposition and emission-line fitting

The reduced and telluric-corrected X-Shooter spectrum is then transformed into
the rest-frame using a redshift of $z = 3.962$. We model the broad emission-line
profile of both the C IV $\lambda 1549$ line and Mg II $\lambda 2799$ line using the code `PyQSpecFit`
([Lai 2023b](#)), a python-based spectral modelling package that is designed for rest-
frame UV and optical quasar spectra. We model each line individually, selecting
independent windows in wavelength to constrain the quasar continuum and the
emission-line flux. We mask the narrow absorption features present in our spectrum
by applying a boxcar sigma-clipping routine with a width of 50 pixels and a 3σ
threshold.

For C IV $\lambda 1549$, we constrain the continuum on either side of the feature with a
power-law model over line-free wavelength windows of 1445Å–1455Å and 1973Å–
1983Å. The emission-line model is composed of a maximum of three broad Gaus-
sian components with a minimum full-width at half-maximum (FWHM) of 1000
km s^{-1}. We fit the C IV $\lambda 1549$ profile between 1480Å–1528Å and 1537Å–1565Å,
avoiding the narrow absorption feature between 1528Å–1537Å. We also measure the
monochromatic luminosity at 1450Å using the power-law model of the continuum.
We estimate the errors in the spectral fitting by creating 50 realisations of the spec-

trum after randomly redistributing the flux data according to each point's Gaussian uncertainties. The standard deviation in each of the derived properties of the C IV λ1549 emission-line is adopted as the statistical error.

For Mg II λ2799, the continuum model is composed of a power-law and a template of the UV flux contribution from broad Fe II emission, which is constrained across the wavelength ranges 1973Å–1983Å, 2060Å–2340Å, 2600Å–2740Å, 2840Å–3100Å. The emission-line model for Mg II λ2799 is composed of up to one narrow and three broad Gaussian components, where the narrow and broad distinction is set at a FWHM of 1000 km s^{-1}. We fit the Mg II λ2799 line between 2700Å–2870Å and the monochromatic luminosity as 3000Å is also measured from the continuum power-law model. We derive the uncertainty in each of the line properties by adopting four different templates of the UV Fe II emission (Vestergaard & Wilkes 2001; Tsuzuki et al. 2006; Mejía-Restrepo et al. 2016; Bruhweiler & Verner 2008). As with C IV λ1549, we also resample the spectrum 50 times and measure the standard deviation in the Mg II λ2799 line properties, summing in quadrature with the uncertainty derived from Fe II templates. More information about the `PyQSpecFit` modelling of C IV λ1549 and Mg II λ2799 lines are detailed in a study of the now second-most luminous quasar, SMSS J2157–3602 (Lai et al. 2023b), and also in a study of line properties in the luminous quasar sample of the European Southern Observatory Large Programme XQ-100 (Lai et al. 2023a), which is at a comparable redshift range to J0529–4351.

Luminosity calculations

For calculating monochromatic continuum luminosities, we corrected the spectra for extinction by dust in the Milky Way. We used the estimate of $E(B - V) = 0.041 \pm 0.0027$ from the Schlegel maps (Schlegel et al. 1998) with the correction factor (Schlafly & Finkbeiner 2011) of 0.86 and the extinction law by Fitzpatrick (Fitzpatrick 1999), which yields restframe absorption values of $A_{1450} = 0.074$ mag and $A_{3000} = 0.025$ mag. We then apply bolometric corrections for mean quasar SEDs (Richards et al. 2006) of $k_{1350} = 3.81$ and $k_{3000} = 5.15$ and apply an anisotropy correction factor of 0.75 assuming mean orientation (Runnoe et al. 2012)). The accretion disc continuum fitting described below determines the bolometric luminosity directly from the integrated disc model SEDs and implies a spin- and inclination-dependent anisotropy correction. We then take the average of the luminosity measurements.

Spectral decomposition and continuum fitting

We use a publicly available code (Lai 2023a) to model the shape of the accretion disc continuum to spectral energy distribution models predicted for slim discs with `slimbh` (Sadowski 2011), which is a grid of synthetic spectra from ray-traced numerical solutions of slim accretion disc equations. The free parameters are mass and spin of the black hole as well as accretion rate and disc inclination. A Markov chain Monte Carlo (MCMC) method is used to map out likelihood contours across the 4D parameter space. We collect the Milky Way extinction-corrected spectrum and extend the IR coverage with *WISE* photometry, specifically the CatWISE2020 (Marocco et al. 2021) *W1* and *W2* photometric passbands. We then create synthetic data points to represent the accretion disc flux within selected line-free windows in the observed spectrum. For the *WISE* wavelengths, we adopt the spectrum of the Selsing high-luminosity quasar template (Selsing et al. 2016), scaled independently to the flux of *W1* and *W2* bandpasses, and create synthetic line-free data points in the same fashion. Furthermore, we use the X-Shooter UVB arm to estimate the continuum flux through the Lyα forest and create one more synthetic data point to constrain the continuum. We then use MCMC to infer the Bayesian posterior probability distributions of the intrinsic black hole properties using the set of synthetic data points to represent the flux of the accretion disc continuum.

Further detailed information on the continuum fitting method is presented in an in-depth study of the quasar SMSS J2157–3602 (Lai et al. 2023b). However, unlike this previous study, the static and smooth thermal accretion disc models are unable to fully reproduce the hardening of the continuum in the VIS arm or the flux passing through the Lyα forest.

It has been shown previously that quasars with high C IV $\lambda1549$ blueshift, which are indicative of strong outflows and winds, tend towards a bluer UV continuum to the blue side of $\lambda_{\mathrm{rest}} \approx 200$ nm and a slightly redder continuum on the red side (Temple et al. 2021a), thus producing a spectral break that is missing in the thermal disc models. Therefore, our `slimbh` synthetic spectra utilises the disc atmosphere model, `BHSPEC` (Davis et al. 2005; Davis & Hubeny 2006), to help reproduce the emerging Compton-hardened radiation.

We also attempted to fit the data with alternative models. E.g., we adopt `kerrbb` thin disc models (Li et al. 2005) despite the fact that the slim disc model reproduces the thin disc SED at low Eddington ratios, and find indeed similar results for the mass of the black hole and the luminosity of the disc, although the colour of the UV continuum is not properly reproduced in the absence of Comptonisation considerations. We also examine the option of J0529–4351 being lensed by demagnifying the

spectrum and find that it does not improve the quality of fit.

Host galaxy dust extinction

We assume no dust extinction in the quasar host galaxy given that typical host reddening levels are found to be consistent with $E(B - V) \approx 0.0$ among luminous quasars (Krawczyk et al. 2015), while less than 1% of quasars seem to have $E(B - V) > 0.1$. Also, an object appearing as the brightest object in the Universe has a low probability of being extinguished by notable levels of dust. If dust were present, it would make the continuum redder and the measured luminosity lower. This will lead to the black hole mass being overestimated by the continuum-fitting method and underestimated by the virial single-epoch method. Such a discrepancy is not observed here.

7.1.3 Discussion and Conclusion

The section from Wolf et al. (accepted) is concluded and what follows is an expanded discussion to explore and contextualise the content.

The spectral decomposition of J0529–4351 is presented in Figure 7.1, where the C IV and Mg II emission-lines observed in the rest-frame ultraviolet spectrum of J0529–4351 were fit with the `PyQSpecFit` package (Lai 2023b), which decomposes the observed spectrum into the continuum components and emission-line components. The result was translated into a black hole mass estimate using established virial relations (e.g. Shen et al. 2011; Coatman et al. 2017). We also show the Bayesian posterior distributions from the continuum fitting of J0529–4351 using the `BADFit` package (Lai 2023a) in Figure 7.2, where parameter estimates are based on the peak of the marginalised posterior and the iso-likelihood contour capturing the central 68%. The result of the spectral analysis is summarised in Table 7.1, where the best black hole mass is $\log(M_{\rm BH}/M_\odot) = 10.24 \pm 0.02$ and the best bolometric luminosity estimate is $\log(L_{\rm bol}/{\rm erg\,s}^{-1}) = 48.27 \pm 0.06$. The bolometric luminosity of J0529–4351 implies that it is the brightest and likely the fastest-growing black hole known. The Eddington ratio is close to unity, which translates to a mass accretion rate of ~ 400 solar masses each year.

Exceptional quasars are often hidden in plain sight. In the era of massive quasar searches and machine-learning classification (e.g. Storey-Fisher et al. 2023), quasars such as J0529–4351 can be misclassified as Milky Way stars (Delchambre et al. 2023) due to high apparent brightness. Follow-up of the All-sky Bright Complete Quasar
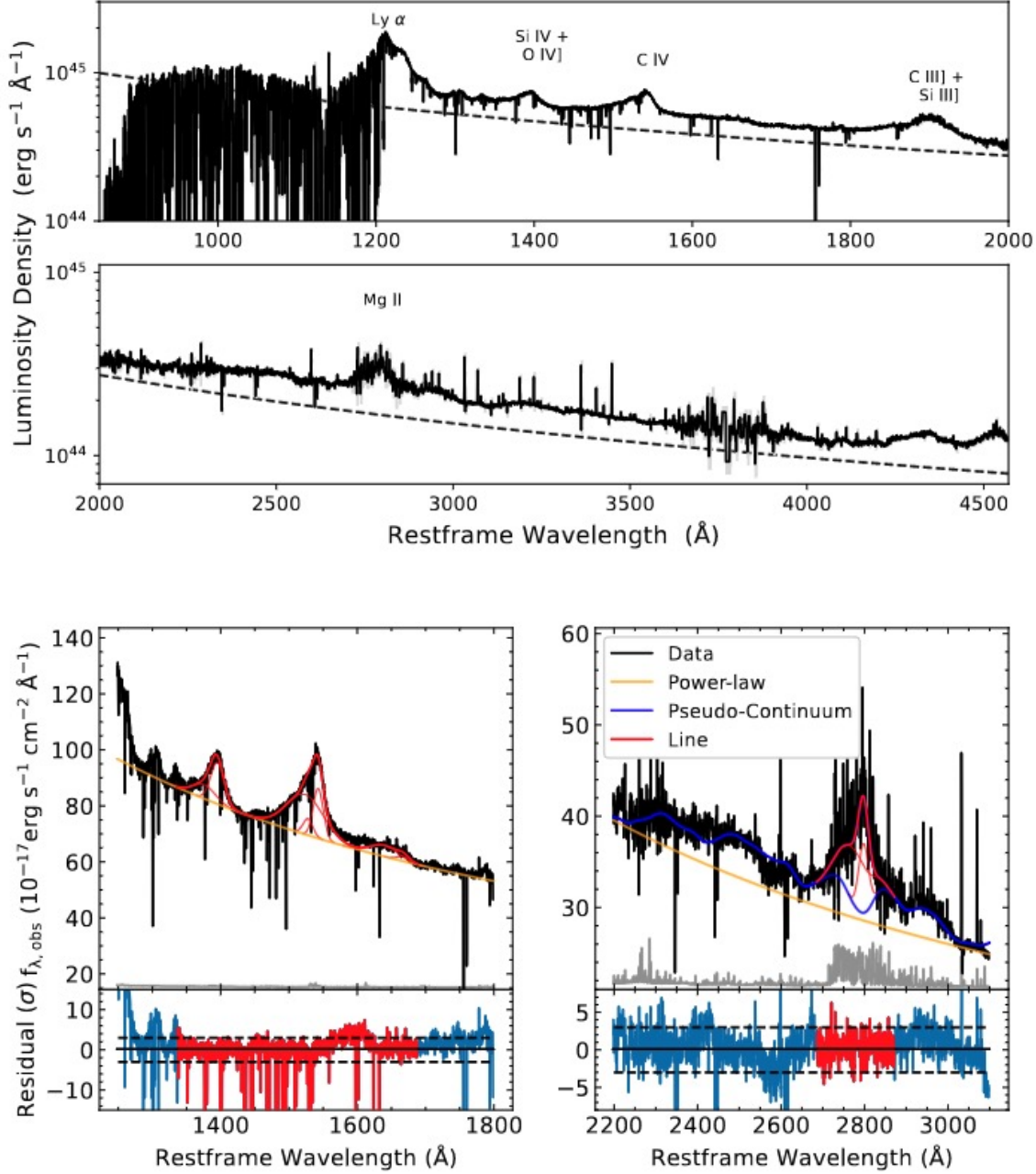
Figure 7.1: The spectrum of SMSS J052915.80–435152.0 is shown in the top and middle panel from the observed wavelength of $0.42 - 2.27\,\mu$m, covering the restframe ultraviolet emission. A power-law with a slope of $\alpha_\lambda = -0.5$ is overplotted as a dotted line for comparison. The bottom two panels show the spectral decomposition of C IV (left) and Mg II (right), with the noise level shown in grey. This figure is reproduced from Wolf et al. (accepted).
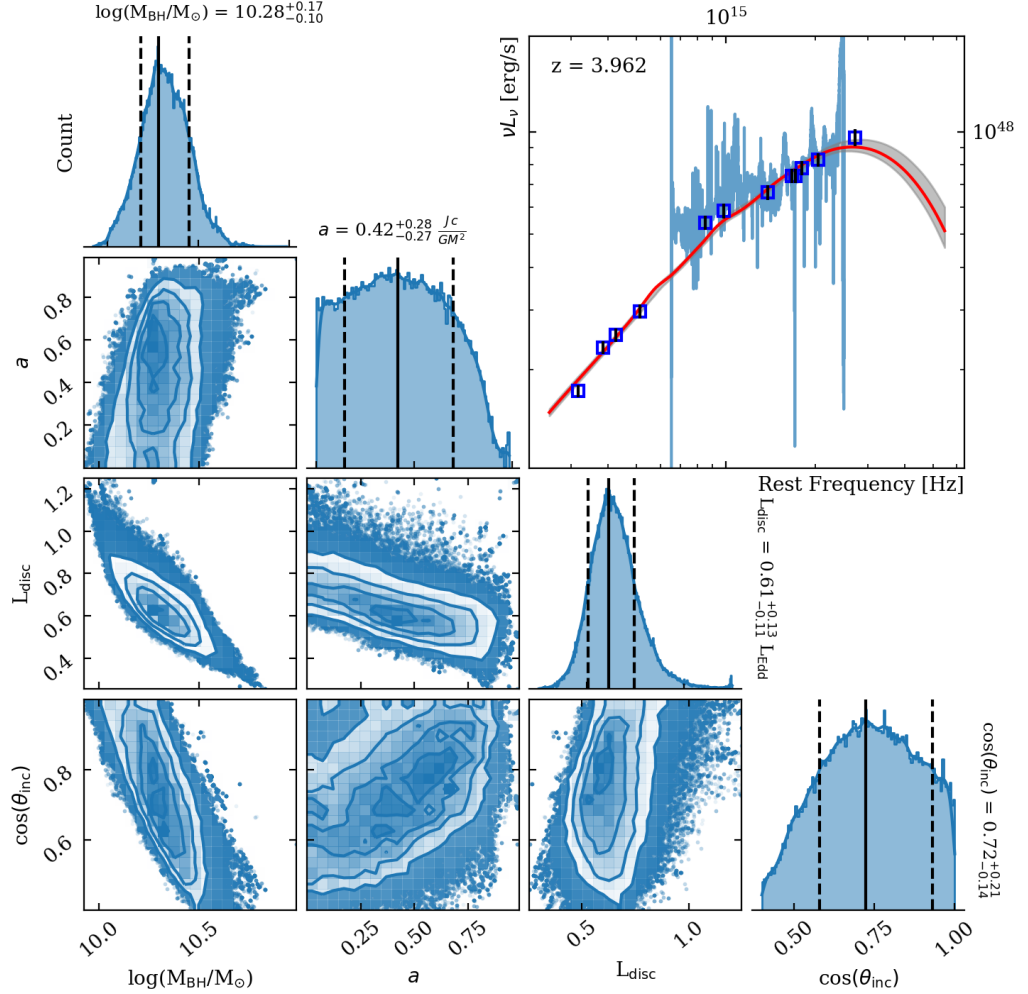
Figure 7.2: Bayesian corner plots and marginalised posteriors showing the continuum fitting of SMSS J052915.80–435152.0 with accretion disc models. Parameter estimates are based on the peak of the marginalised posterior and the central 68% iso-likelihood contours. Black hole spin is denoted by a and the disc luminosity, L_{disc}, is in units of the Eddington luminosity. This figure is reproduced from Wolf et al. (accepted).

Table 7.1: Luminosity, black hole mass and accretion rate for the quasar J052915.80–435152.0: given are best-fit estimates and 68% confidence intervals. Systematic uncertainties for the mass estimates are proposed to be as high as 0.4 dex. This table is reproduced from Wolf et al. (accepted).

Luminosity	$\log L/(\mathrm{erg\ s^{-1}})$
λL_{135}	47.93
λL_{300}	47.76
L_{bol} (from 135 nm)	48.39
L_{bol} (from 300 nm)	48.35
L_{bol} (slim disc model)	48.16
L_{bol} (best estimate)	48.27 ± 0.06
Black hole mass	$\log M/M_\odot$
C IV $\lambda1549$ line (average)	10.24 ± 0.15
Mg II $\lambda2799$ line (average)	10.20 ± 0.08
Continuum fit (slim disc)	$10.28^{+0.17}_{-0.10}$
All methods (best estimate)	10.24 ± 0.02
Mass accretion rate	$\log \dot{M}/(M_\odot\ \mathrm{yr^{-1}})$
for plausible inclination range	2.57 ± 0.06

Survey (AllBRICQS; Onken et al. 2023) which discovered J0529–4351[1] through colour selection and the absence of astrometric motions is now complete at $R_p < 16$. The high completeness and efficiency of the survey suggests that it is unlikely for a quasar of comparable luminosity to be found in the future, except at low Galactic latitudes of $|b| < 10°$, where enhanced dust extinction and crowded fields complicate quasar discovery in that space.

Future observations of J0529–4351 with the Atacama Large Millimetre Array (ALMA) has the potential to probe the mass and kinematics of the host galaxy, revealing clues about how the J0529–4351 supermassive black hole accretes at such a rapid rate, such as possible merger signatures. The upgraded GRAVITY+ interferometric instrument can also probe the spatial and kinematic properties of the quasar BLR directly and the forthcoming Extremely Large Telescope may be able to use bright quasars to observe the expansion of the universe directly through redshift drift. The brightest known quasar, J0529–4351, will play an important role in future studies.

---

[1]Also discovered independently by the QUBRICS Survey (Cristiani et al. 2023).

7.2 Luminosity Inclination Dependence

7.2.1 Introduction

Quasars are intrinsically variable astronomical objects that can exhibit significant fluctuations in brightness and spectral properties over various timescales. This stochastic variability, possibly caused by magneto-rotational instabilities in the disc, can be appropriately described by a damped random walk (e.g. Kelly et al. 2009; MacLeod et al. 2010; Zu et al. 2013) and a variability structure function (e.g. Hughes et al. 1992; Kozłowski 2016), which is a statistical method used to quantify variability properties by measuring the change in brightness as a function of the time lag between different observations. Previous studies have shown that the change in quasar brightness grows as a function of the time delay between two measurements and that there is an anti-correlation between the quasar luminosity and variability amplitude (e.g. Vanden Berk et al. 2004; MacLeod et al. 2010; Morganson et al. 2014; Caplar et al. 2017; Li et al. 2018; Stone et al. 2022).

Using light curves of the ~ 5000 brightest quasars collected from NASA/Asteroid Terrestial-impact Last Alert System (ATLAS; Tonry et al. 2018), the work of Tang et al. (2023a) describes a universality in the quasar variability structure function, suggesting a common variability mechanism which manifests as an intrinsically tight relationship between the variability amplitude, A, and time separation, Δt, expressed in units of the luminosity-dependent thermal timescale, $t_{\rm th} \propto L^{1/2}$, for thin disc accretion[2]. We show this result in Figure 7.3, where the left panel shows the variability structure function as measured from the NASA/ATLAS data and the right panel shows the structure function normalised by the thermal timescale. The slope of the relation, measured from the normalised data in the right panel, is $\gamma_{\rm th} = \log(A/A_0)/\log(\Delta t/t_{\rm th}) = 0.510 \pm 0.002$ from the right panel, which is consistent with $\gamma_{\rm th} = 1/2$ of a random walk stochastic process. We can also observe a short timescale variability amplitude suppression, where the location of the break between the dampened variability and the universal relation is sensitive to the thermal timescale itself.

Individual measurements are dispersed around the mean relation in the universal quasar structure function, which may be indicative of variations in the disc orientation, black hole spin, and host extinction. These would affect the inferred luminosity, and therefore the estimated thermal timescale used to normalise the time separation in the structure function. Variations in the interior structure of the disc and its

---

[2]The orbital timescale may be the more fundamental property, but the two timescales are related by viscosity.
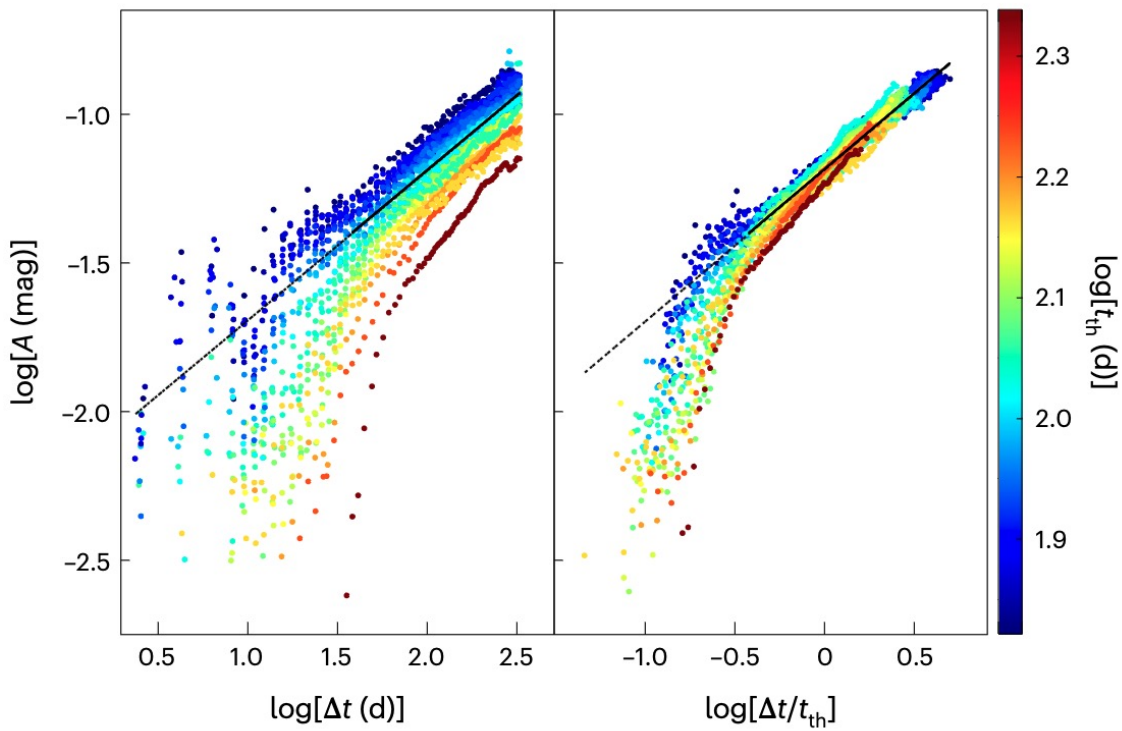
Figure 7.3: Variability amplitude, $\log A$, as a function of the time separation $\log \Delta t$ in days (left) and normalised in units of the thermal timescale, t_{th} (right). The data is also colour-coded in thermal timescale, from blue (short) to red (long). The best-fit for the slope of the relation for the normalised data in the right panel is $\gamma_{\text{th}} = 0.510 \pm 0.002$, which is consistent with the random walk expectation.

temperature profile may also modify the true thermal timescale. One hypothesis, presented in Tang et al. (2023b), is that the offsets of individual quasars from the mean relation are caused by orientation effects, which modify the apparent luminosity, requiring corrections for the anisotropic nature of quasar emission. If confirmed, the offset in a quasar's variability behavior from the universal relation can be used to constrain the observed orientation angle. The orientation of the observer with respect to the accretion disc is a parameter that has significant effects on our perception of a quasar, but the only widely accepted method for constraining the viewing angle is by radio core dominance (Orr & Browne 1982). Thus, a new independent method utilising the variability of an entirely separate region of the electromagnetic spectrum would be invaluable to the understanding of quasars, particularly by enabling tests of the AGN paradigm unified by orientation.

The content in the following "Accretion disc luminosity" section is published in Tang et al. (2023b) and it describes the orientation dependence of the monochromatic luminosity at 3000Å based on accretion disc modelling. I used a geometrically thin, optically thick, steady state accretion disc model with general relativistic and limb darkening effects, called KERRBB (Li et al. 2005). I evaluated the effect of orientation on the monochromatic luminosity at 3000Å. Once renormalised, I found little difference in the luminosity-orientation relation as a function of black hole parameters, such as its mass or spin. As a result, the relative accretion disc luminosity at 3000Å as a function of orientation can be considered a global relation, consistent to within 10% across a large range of supermassive black hole masses. This model is a necessary component in the analysis which aims to probe orientation through variability behavior. We discuss the results of the analysis in Section 7.2.3.

The following section is reproduced from Tang et al. (2023b) without modification and represents my textual contribution to the study.

7.2.2 Accretion disc luminosity

We inspect the relation between inclination angle, i, and luminosity offset by calculating the theoretical accretion disc luminosity using a steady-state, optically thick, and geometrically thin accretion disc model, called KERRBB (Li et al. 2005). We access the pre-calculated spectral tables through XSPEC 12.12.0 (Arnaud 1996), packaged in SHERPA (Freeman et al. 2001), the modelling and fitting suite of Chandra Interactive Analysis of Observations (CIAO) v4.14. The KERRBB spectra are calculated by ray tracing from an inclined observer, assuming that the disc radiates locally as a blackbody. All general relativistic effects such as the Lense-Thirring effect, Doppler boosting, and gravitational redshifting are included.

As a representative example, we consider a model black hole with $\log(M_{BH}/M_\odot) = 9$. We set the Eddington ratio to 0.5, radiative efficiency to 10 per cent, and hardening factor to unity, and prescribe zero torque at the inner edge of the disc. Using pre-calculated spectral tables with limb darkening, we evaluate the monochromatic accretion disc luminosity at 3000 Å for a range of spins and inclinations. We find only a subtle dependence on input black hole model parameters, except at inclinations close to 90°, which are not expected in optically selected samples due to strong extinction from a dusty torus. At this wavelength, we also find no discernible difference in the relative luminosity offsets due to inclination between black hole spins. This remains the case for black hole masses (M_{BH}) up to $\log(M_{AD}/M_\odot) \leq 11$, which encompasses all known black holes with reliable mass measurements. Then, according to the thin-disc model KERRBB, the relative accretion disc luminosity at 3000 Å between inclination angles for type 1 quasars can be considered as a global relation, consistent to within 10 per cent over three orders of magnitude in M_{BH} from $\log(M_{AD}/M_\odot) = 6 - 9$.

In Fig. 7.4, we present the accretion disc luminosity at 3000 Å for a model black hole with the parameters listed above. These curves trace the model flux for all observed i from 0° to 90° and individual curves are separated by the black hole spin parameter. The shapes of the curves, indicating the relative luminosity offset, are virtually indistinguishable between black hole spins. These luminosity curves are used to estimate the expected luminosity offsets $\Delta \log L_{3000}$. Refer to the appendix of Lai et al. (2023b) for a deeper investigation into the bolometric and monochromatic luminosities at various black hole spins and observed inclinations using the thin-disc model.

7.2.3   Discussion and Conclusion

The section from Tang et al. (2023b) is concluded and what follows is an expanded discussion to explore and contextualise the content.

The $\Delta L_{3000} - \theta_{inc}$ relation developed from accretion disc modelling is combined with a $\Delta v(C\,IV - Mg\,II) - \theta_{inc}$ relation from models of the inclined $C\,IV$ outflow (Yong et al. 2017, 2020; Tang et al. 2023b) in order to plot the expected $\Delta L_{3000} - \Delta v(C\,IV - Mg\,II)$ relation from theoretical modelling. The velocity shift, $\Delta v(C\,IV - Mg\,II)$, is directly observable from the spectral profiles of $C\,IV$ and $Mg\,II$, while the luminosity shift ΔL_{3000} is estimated from the variability offset from the mean relation. The variability offset can manifest as a shift in the thermal timescale, which is related to L_{3000} by $t_{th} \propto \sqrt{L_{3000}}$. The theoretical expectation is that more blueshifted $C\,IV$ lines with respect to $Mg\,II$ lines should be biased toward pole-on observation and
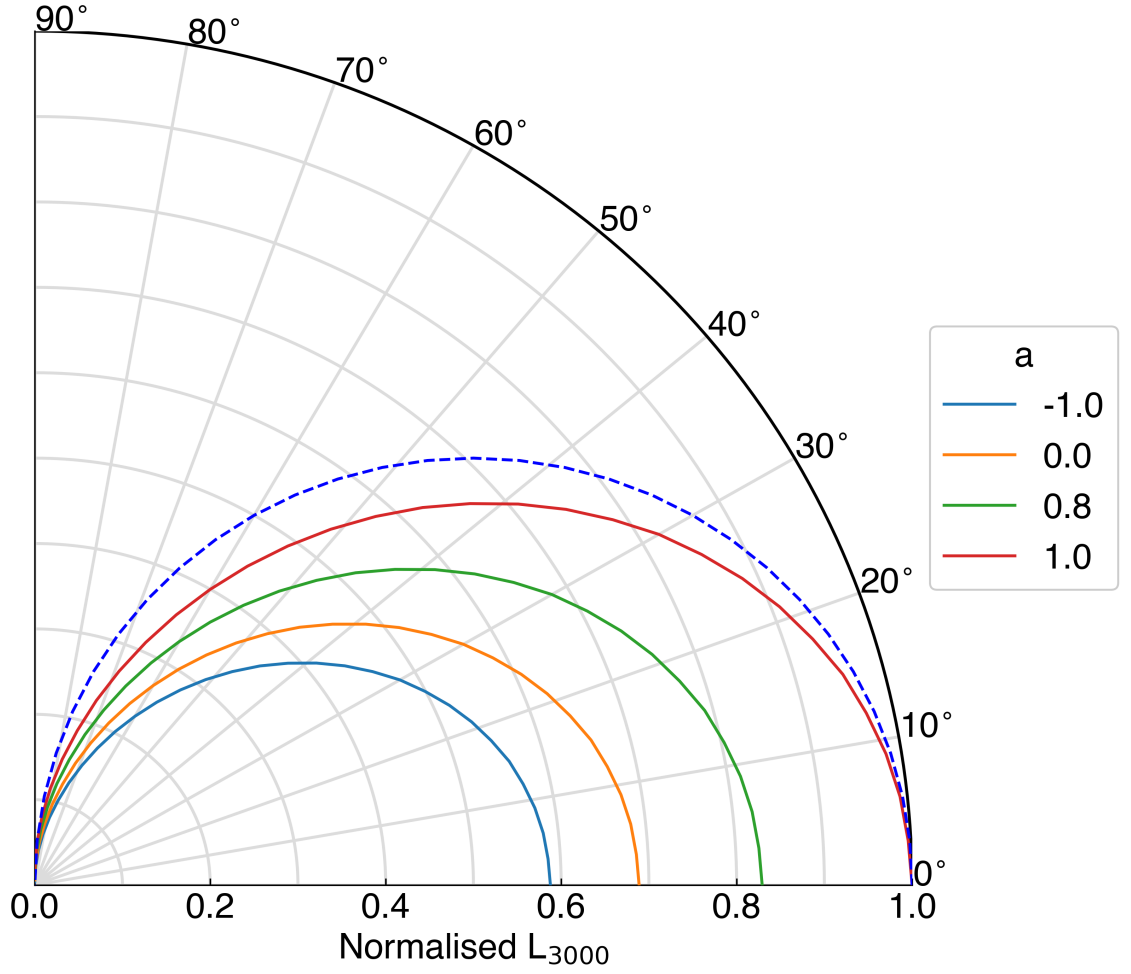
Figure 7.4: Luminosity at 3000 Å normalized to the maximum luminosity for the full range of inclination angles and black hole spins. The dashed blue line represents the classical $\cos i$ luminosity relation. The black hole model parameters are described in Section 7.2.2, but once normalized to a common value at $i = 0$, the shape of all curves is consistent to within 10 per cent, independent of the assumed black hole model.

thus appear overluminous.

A subset of 753 quasars with C IV and Mg II line measurements was constructed from the variability sample of Tang et al. (2023a), which is composed of NASA/ATLAS light curves spanning ~ 6 years of observation with near nightly cadence. The line measurements are taken from Rakshit et al. (2020), where standard quasar spectral decomposition methods were used to measure properties of each line profile. The $\Delta v(C\,\text{IV} - Mg\,\text{II})$ velocity shift is easily measured from the peak wavelengths of each emission line.

Individual and velocity-binned measurements are presented in Figure 7.5, which shows significant scatter in the $\Delta L_{3000} - \Delta v(C\,\text{IV} - Mg\,\text{II})$ relation for individual quasars. However, systematic behavior is observable in the binned measurements, which show highly blueshifted C IV profiles correlate with underluminous quasars, while quasars with mildly blueshifted C IV appear slightly overluminous compared to the quasars with no apparent blueshift. These results, particularly for the points in the highest C IV blueshift bin appear to contradict the relation predicted by theoretical modelling.

Four possible mechanisms were proposed to explain the observed discrepancy: issues with the line diagnostics as orientation indicators, disc luminosity relation with inclination is affected by dust extinction, variability amplitude is dependent on the viewing angle, or high-C IV blueshift quasars are physically distinct from the rest of the quasar population. We discuss each of these four mechanisms.

It's possible that the $\Delta v(C\,\text{IV} - Mg\,\text{II}) - \theta_{\text{inc}}$ relation is manufactured by model assumptions and that $\Delta v(C\,\text{IV} - Mg\,\text{II})$ is an unreliable orientation indicator. This has previously been suggested in comparisons of emission-line properties to radio core dominance (Richards et al. 2011; Runnoe et al. 2014), which find no apparent changes in the shape of the C IV feature with orientation. On the other hand, similar analyses suggest that the Hβ line width is orientation-dependent (e.g. Wills & Browne 1986; Runnoe et al. 2013; Shen & Ho 2014; Marziani et al. 2022) and there is evidence that the Balmer lines are anticorrelated with C IV blueshift (e.g. Coatman et al. 2016; Yong et al. 2020). Thus, despite the theoretical expectation for the $\Delta v(C\,\text{IV} - Mg\,\text{II}) - \theta_{\text{inc}}$ relation in disc-wind models, the reliability of the C IV blueshift as an orientation indicator is yet to be settled.

Offsets in L_{3000} are an inevitability due to the anisotropic accretion disc emission. However, it may not be the case that the $\Delta L_{3000} - \theta_{\text{inc}}$ relation follows the thin disc expectation. An inversion of the $\Delta L_{3000} - \theta_{\text{inc}}$ relation is theoretically possible if dusty outflows extinguish accretion disc radiation with a change in the colour excess of $\Delta E(B - V) \approx 0.25$, which is a significantly elevated extinction compared

to the mean value expected for quasars (Krawczyk et al. 2015). Similarly, the observed variability amplitudes could be affected by the viewing angle if partial dust obscuration changes the observable elements of the accretion disc which may vary at different characteristic timescales. These effects should, in principle, be visible in the accretion disc SED.

Another scenario is that the low C IV blueshift binned quasar measurements are behaving as expected by the $\Delta L_{3000} - \Delta v(C\,\text{IV} - Mg\,\text{II})$ relation, but the two highest blueshift bins reflect quasars with altered accretion disc geometry. Highly blueshifted C IV emission-lines in quasars may reflect quasars accreting close to their Eddington limit (Vietri et al. 2018; Rankine et al. 2020), which are better described by slim discs (Abramowicz et al. 1988; Sadowski 2011) with flatter effective temperature profiles of $T \propto R^{-0.5}$ (e.g. Watarai et al. 2000; Ohsuga et al. 2002). An increase in the thermal timescale of ~ 0.13 dex is sufficient to eliminate the offset seen at the most C IV-blueshifted quasar bins, requiring a temperature profile of $T \propto R^{-0.64}$ as opposed to $T \propto R^{-3/4}$ for thin discs (Tang et al. 2023b). Abrupt changes in the accretion disc temperature profile between accretion disc geometries may be responsible for the observed discrepancy in the expected $\Delta L_{3000} - \Delta v(C\,\text{IV} - Mg\,\text{II})$ relation.

Having discussed several possibilities, we remark that no conclusive picture was offered in Tang et al. (2023b), but it is clear that additional work is required to explore the variability offsets of individual quasars from the mean relation, and on whether there are reliable orientation diagnostics in the rest-frame ultraviolet quasar spectrum.
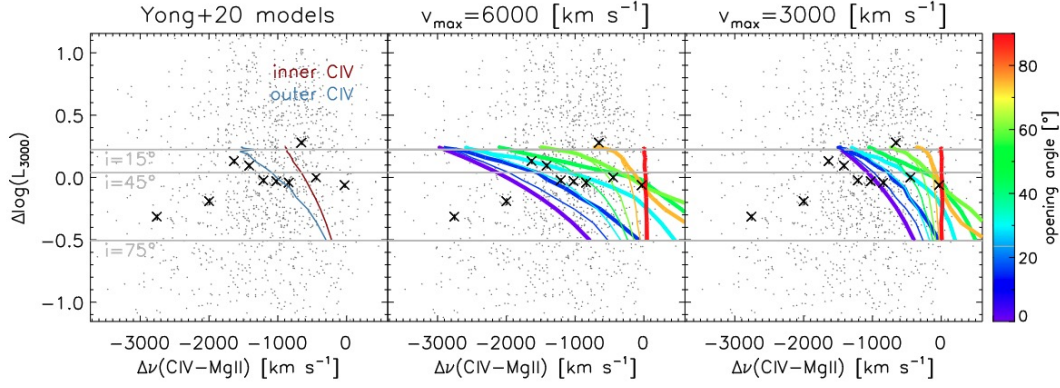
Figure 7.5: Luminosity offset $\Delta \log L_{3000}$ versus $\Delta v(C\,\text{IV} - Mg\,\text{II})$ in the outflow sample. Here, the left-hand panel shows the Yong et al. (2020) model, while the centre and right-hand panels show sets of C IV outflow models with a simple biconical outflow geometry with different terminal outflow velocities, colour-coded by separate opening angle (Tang et al. 2023b) Thin and thick lines show optically thin and thick cases, respectively. This figure is reproduced with permission from Tang et al. (2023b).

Conclusion

In this chapter, I summarise the key results from preceding chapters and discuss potential directions for future work.

8.1 Summary of Thesis

The study of high-redshift ultraluminous and supermassive black holes has benefited immensely from wide-area surveys, such as Sloan Digital Sky Survey (Richards et al. 2006) and Pan-STARRS (Panoramic Survey Telescope & Rapid Response System; Chambers et al. 2016), as well as deeper surveys, such as the Subaru High-z Exploration of Low-Luminosity Quasars (SHELLQs; Matsuoka et al. 2016, 2022). As newer instruments continue to push the quasar redshift limit up to $z \sim 10$ (e.g. Bogdán et al. 2023), higher-efficiency selection techniques improve sample completeness and constraints on quasar spatial densities at lower redshifts (e.g. Yang et al. 2019b; Onken et al. 2022a, 2023). Ever since the discovery of the first $z > 6$ quasars (e.g. Fan et al. 2001), the observed masses of high-redshift black holes have placed stringent constraints on black hole formation and growth mechanisms (e.g. Volonteri et al. 2021). In this thesis, I used established methods and developed independent methods to study characteristics of some of the most ultraluminous known high-redshift quasars. I explored properties of their black holes, broad-line regions, and spectral energy distributions, and I measured black hole cosmic mass assembly, providing valuable insights into the growth of supermassive black holes in the early Universe.

In the first half of the thesis, this was accomplished by collecting spectroscopic follow-up observations on the brightest quasars between $4.5 < z < 5.3$, accompanied by the development of a spectroscopic analysis tool, `PyQSpecFit`, to measure properties of broad emission-lines embedded in the quasar continuum. The high completeness of the parent survey at $z \sim 5$ (e.g. Onken et al. 2022a) was conducive to the measurement of the supermassive black hole mass function and its evolution

compared to literature mass functions at $z \sim 4$ (He et al. 2023) and $z \sim 6$ (Shankar et al. 2009; Willott et al. 2010a; Wu et al. 2022; D'Odorico et al. 2023; Fan et al. 2023). The mass function evolution was used to produce joint constraints on accretion parameters: Eddington ratio, duty cycle, and radiative efficiency. The key question investigated was: what does the evolution of the black hole mass function tell us about the growth of supermassive black holes in the early Universe?

The key results from the first half of the thesis are:

- A high-quality sample of 100 X-shooter spectra of some of the most luminous quasars in the redshift range $3.5 < z < 4.5$ was studied using `PyQSpecFit`. By measuring properties of the broad emission lines, C IV $\lambda1549$Å, Mg II $\lambda2799$Å, and H$\beta\lambda4863$Å, the masses of the black holes were measured to be in the range $\log\left(M_{BH}/M_\odot\right) = 8.6 - 10.3$ with bolometric luminosities of $\log\left(L_{bol}/\mathrm{erg\,s}^{-1}\right) = 46.7 - 48.0$. Just over one-fourth of the sample is accreting at mildly super-Eddington rates.

- Virial estimators rely on an extrapolation of the Hβ reverberation mapping $R - L$ relation, determined for lower-luminosity AGN. In the high-luminosity XQ-100 sample, I find that the black hole mass estimates resulting from C IV, Mg II, and Hβ estimators to remain mutually consistent. Therefore, I find no indication that the relative physical geometry of the three line-emitting regions changes significantly with quasar luminosity.

- I obtained spectroscopic data from my VLT/X-shooter programs 108.22H9.001, 109.23D1.001, and 109.23D1.002, and SOAR/TripleSpec4.1 programs 2021B-0036 and 2022A-389756, to develop a spectral atlas, called XQz5, composed of 83 of the brightest known quasars in the redshift range $4.5 < z < 5.3$ with wide observed-frame spectroscopic wavelength coverage from optical to near-infrared. Compared to an existing large sample at a similar redshift range (Trakhtenbrot et al. 2011), XQz5 contains quasars with 0.6 dex higher median luminosity and 0.4 dex more massive black holes, with masses of $\log\left(M_{BH}/M_\odot\right) = 8.5 - 10.4$ and bolometric luminosities in the range $\log\left(L_{bol}/\mathrm{erg\,s}^{-1}\right) = 47.0 - 48.0$, where 10 quasars accrete at mildly super-Eddington rates. The sample, whose raw/reduced spectra and measured line properties are publicly available, has notable legacy significance and widespread community value due to its high completeness, as it is improbable that a brighter sample of a similar size could be constructed at this redshift range.

- The evolution of the supermassive black hole mass function was measured at $z \sim 5$ using properties of 72 quasars from the XQz5 sample and other

literature samples in the footprint of the parent survey. Between redshifts $z = 5 - 4$, the mass function evolution presents constraints on accretion properties, $k_{\text{ef}} = \langle\lambda\rangle U(1 - \epsilon)/\epsilon = 1.62 \pm 0.06$, where $\langle\lambda\rangle$ is the mean Eddington ratio, U is the duty cycle, and ϵ is the radiative efficiency. The measured growth is inconsistent with high radiative efficiencies of $\epsilon > 0.34$ at 3σ confidence.

- In order for central supermassive black holes to have seeds no larger than $10^{5-6} M_\odot$, aligning with seed masses expected from the direct collapse of supermassive stars, the growth rate of supermassive black holes at higher redshifts must exceed $3\times$ faster than observed between $z = 5 - 4$. Faster growth rates imply that supermassive black holes are formed from accreting black holes with low radiative efficiency, which can be the result of low black hole spin or photon trapping in supercritically accreting thick discs.

In the second half of the thesis, I applied `PyQSpecFit` to measure chemical abundances in the quasar broad-line region and developed `BADFit` to model quasar spectral energy distributions. The study of quasar broad-line region metallicity is strongly motivated by available empirical evidence of relationships between quasar activity, host galaxy evolution, and star formation episodes (e.g. Hamann & Ferland 1999). The observed chemical evolution in the galactic nuclear material at high-redshift provides an opportunity to test and assess models of early galaxy evolution (e.g. Maiolino & Mannucci 2019). Modelling quasar spectral energy distributions with thermal accretion disc emission in order to derive black hole properties is a method that traces back to early studies of 3C 273 (Malkan 1983), but has fallen out of favour due to the widespread availability of spectroscopic data on hundreds of thousands of quasars (e.g. Lyke et al. 2020). I explore accretion disc modelling in the latter half of the thesis and its applications.

The key results from the second half of the thesis are:

- By investigating metallicity-sensitive emission-line flux ratios, including (Si IV+O IV)/C IV and N V/C IV, I found that the elemental abundances in redshift $5.8 < z < 7.5$ quasar broad-line regions to be between $2 - 4\times$ super-solar, which are not unrealistic under normal galactic chemical evolution models due to the small scale of the quasar broad-line region.

- There is a strong anti-correlation between the blueshift of the C IV line and its equivalent width. The C IV blueshift, which is an indicator of projected quasar outflows, can bias chemical abundance diagnostics to high, and likely unphysical, metallicities. This explains how previous studies of chemical abundance in the high-redshift quasar broad-line region inferred enrichment up to $10\times$

super-solar abundances, which required more exotic early chemical enrichment scenarios to explain.

- The rest-frame ultraviolet AGN spectral energy distribution contains a big blue bump, which is a signature of the thermal accretion disc emission. I developed `BADFit`, an accretion disc fitting code which utilises thin and slim disc models and Bayesian inference to characterise black holes based on the observed spectral energy distribution. This independent approach has the potential to complement existing black hole mass characterisation methods.

- Accretion disc modelling was applied to measure properties of two of the most luminous known quasars, SMSS J215728.21–360215 and SMSS J052915.80—435152.0, where I found consistency between the mass estimates obtained by virial diagnostics from velocity-broadened emission-lines and accretion disc modelling.

- I also applied the accretion disc model to estimate the expected quasar emission anisotropy in order to probe the effects of the luminosity anisotropy on the universal variability structure function, which is normalised by the thermal timescale. This study finds that quasars with high C IV blueshift may physically distinct from the rest of the quasar population.

This thesis equips us with the necessary tools of detailed spectroscopic analysis, whose utility was illustrated in studies of black hole and broad-line region properties. In addition, the accretion disc modelling work demonstrates independent techniques that can be applied in concert with more established black hole characterisation methods.

8.2   Future Work

While the research conducted in this thesis has yielded insights into the understanding of high-redshift supermassive black holes and their growth, there are additional research avenues that offer opportunities for further investigation. In this section, I outline potential directions for future research, encompassing both observational and theoretical opportunities, which will deepen our understanding of black holes and their accretion discs during the early epochs of the Universe.

8.2.1   Observations

In recent years, the high-precision Gaia astrometry and optical photometry (Gaia Collaboration et al. 2021) has improved quasar selection purity (Onken et al. 2023),

while the James Webb Space Telescope pushed the quasar redshift frontier up to $z \sim 10$ (Bogdán et al. 2023). The core supermassive black holes of M87 and the Milky Way were also recently imaged using very-long baseline interferometry by the Event Horizon Telescope Collaboration (Event Horizon Telescope Collaboration et al. 2019a, 2022a), while the high spatial resolution of the Atacama Large Millimeter Array (ALMA) can spatially resolve a central black hole's sphere of influence (e.g. Cohn et al. 2021, 2023). It's clear the next epoch of observational quasar studies will be defined by the deployment of newer and more advanced instruments with unprecedented capabilities. Here, I briefly discuss some of the upcoming instruments that have the potential to contribute significantly to this field.

The European Space Agency's wide-angle Euclid space telescope, which launched in July 2023, is expected to provide deep near-infrared photometry to a 5σ depth of 24 AB mag in the Y, J, and H bands for over a third of the sky (Euclid Collaboration et al. 2022), which is beyond the capabilities of ground-based observatories. The deep near-infrared photometry is predicted to yield 100 quasar discoveries between $7.0 < z < 7.5$ and ~ 8 beyond $z = 8.0$ (Euclid Collaboration et al. 2019). Euclid would work well exceptionally well in concert with the ground-based Vera C. Rubin Observatory's Legacy Survey of Space and Time (LSST), which will reach 5σ depths of $25 - 26$ AB mag in the z and y optical bands within a decade (Ivezić et al. 2019). Farther into the future, NASA's Nancy Grace Roman Space Telescope will provide a deep wide-angle infrared view of the Universe (Akeson et al. 2019), which in conjunction with Euclid and LSST, will enable the selection of the earliest ultraluminous quasars. However, spectroscopic characterisation of these targets will require powerful infrared spectrographs such as 30-m class telescopes from the ground or the James Webb Space Telescope.

The ambitious Laser Interferometer Space Antenna (LISA; Amaro-Seoane et al. 2017) will directly observe gravitational waves from energetic events in the universe, such as mergers of massive black holes. In Figure 8.1, I show signal-to-noise contours for the detection of the gravitatational wave signal from black hole mergers plotted as a function of the redshift and binary mass. LISA is designed with the capabilities to detect black hole mergers from $10^5 \, M_\odot$ binaries up to $z = 20$, which will give us the best constraints on the formation and evolution of supermassive black holes. LISA may even be able to probe mergers of binary supermassive star black hole remnants (e.g. Hartwig et al. 2018) or directly detect supermassive star direct collapse (e.g. Shibata et al. 2016). Probing mergers of stellar mass black hole seeds will require the gap between LIGO and LISA detection capabilities to be filled, possibly by the proposed DECi-hertz Interferometer Gravitational wave Observatory (DECIGO;

Sato et al. 2017).

Since 2016, the GRAVITY optical interferometer (GRAVITY Collaboration et al. 2017) has been a remarkable black hole laboratory, whose results include precise orbital determinations of stars near Milky Way's central black hole (e.g. Grould et al. 2017; GRAVITY Collaboration et al. 2018, 2020a) to resolving structure in the immediate vicinity of AGN (GRAVITY Collaboration et al. 2020b). GRAVITY+ is an upgrade to GRAVITY, promising enhanced sensitivity and precision as well as improved sky coverage (Gravity+ Collaboration et al. 2022). These upgrades would uniquely position GRAVITY to provide unprecedented spatial and kinematic detail on broad lines in AGN (Drescher et al. 2022; Gravity Collaboration et al. 2022).

Radio astronomy has already benefited significantly from precursors of the upcoming Square Kilometer Array (SKA; Braun et al. 2019; Weltman et al. 2020), such as MeerKAT (e.g. Santos et al. 2016) and ASKAP (e.g. McConnell et al. 2020). Once completed, the SKA is expected to study a large range of phenomena, including hydrogen mapping at cosmic dawn or relativistic jets spewed from supermassive black holes, at $1-2$ orders of magnitude greater fidelity than existing telescopes. Proposed upgrades to the Event Horizon Telescope array will also form the Next-Generation Event Horizon Telescope (ngEHT; Johnson et al. 2023), which will sharply improve the existing observations of M87 and Milky Way central black holes in order to probe fundamental physics of accretion and jet launching.

At higher energies, NASA's planned Lynx next-generation X-ray Observatory builds upon the success of the Chandra X-ray Observatory (Weisskopf et al. 2000) and is expected to be a transformational upgrade in efficiency, sensitivity, field of view, and spectral resolution (The Lynx Team 2018; Falcone et al. 2019). Lynx will search for extremely faint X-ray sources, signatures of very distant AGN selected from the first generation of supermassive black holes.

8.2.2   Simulations

The Bayesian Markov Chain Monte Carlo `BADFit` tool was successfully used to characterise the black holes in only a handful of ultraluminous quasars, but a more extensive investigation is warranted for larger samples in order to properly compare the accretion disc modelling estimates to more established methods. Comparisons of smaller samples in the literature suggest that there are systematic differences between black hole properties measured by accretion disc modelling and by virial mass estimates (e.g. Calderone et al. 2013; Campitiello et al. 2020), which is potentially related to changes in the virial factor (Mejía-Restrepo et al. 2018). However,
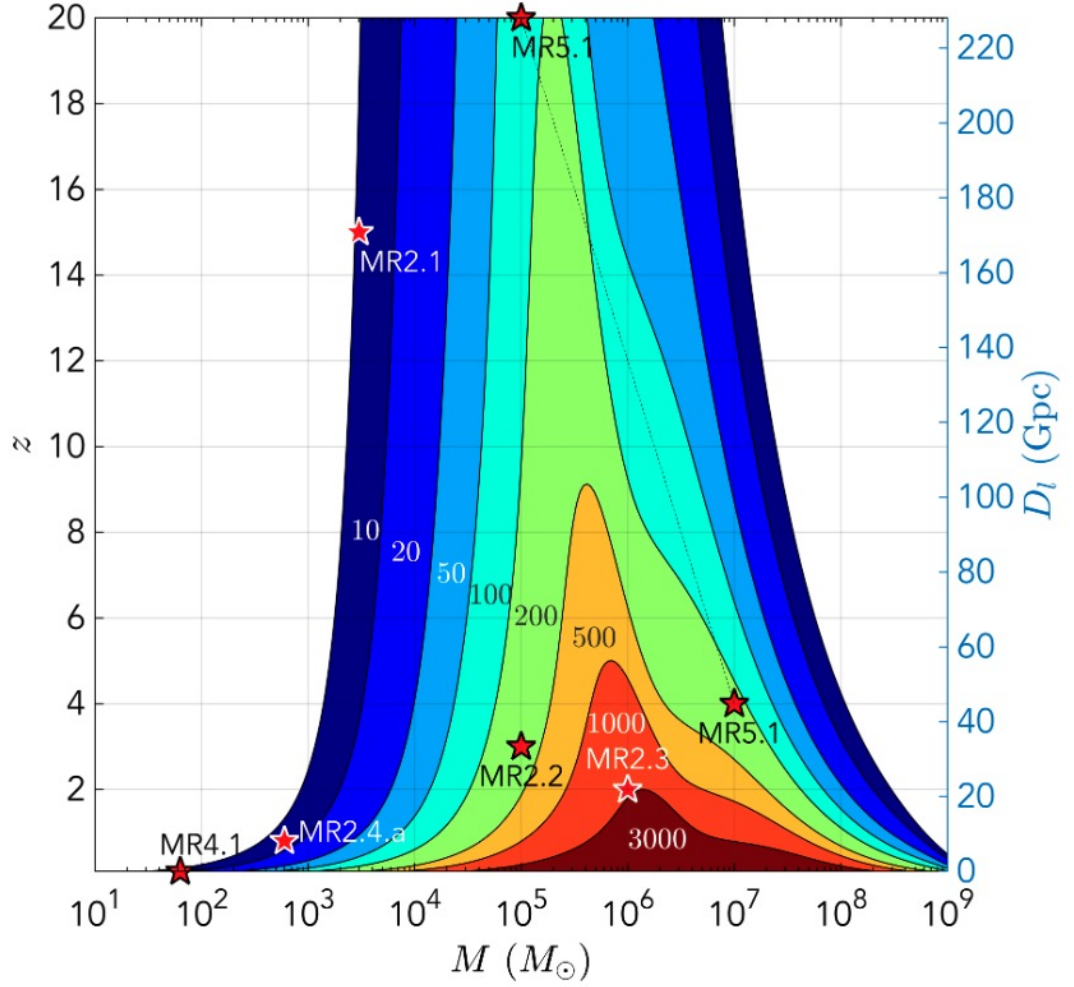
Figure 8.1: Contours of constant signal-to-noise ratio for the detection of the gravitational wave signal from black hole mergers by the Laser Interferometer Space Antenna. The signal-to-noise is illustrated as a function of redshift and source-frame binary mass for binaries with constant mass ratio of $q = 0.2$. Red stars indicate threshold binaries used to define the mission requirements, which includes $10^3 \, M_\odot$ binaries at $z = 15$ (MR2.1) and $10^5 \, M_\odot$ binaries to $z = 20$ (MR5.1). Figure is reproduced from Amaro-Seoane et al. (2017).

there is a lack of homogeneity in how the accretion disc model is fit and how black hole properties have been inferred from the fit. Therefore, the first large sample of quasars with robust spectroscopic measurements and accretion disc modelling results from a publicly available code package would represent a significant development in accretion disc modelling as an independent black hole characterisation method.

The models implemented in `BADFit` are thin (Li et al. 2005) or slim (Sadowski 2011) disc models that are solutions to the set of standard hydrodynamical disc equations. Several physical assumptions have been made to simplify the equations, such as neglecting self-irradiation, magnetic pressure, and torque at the black hole horizon. Furthermore, dissipation and angular momentum transport is controlled by the viscosity prescription, which is constant and assumed to be independent of radius. More modern general-relativistic magnetohydrodynamic (GRMHD) numerical simulations challenge some of these assumptions by showing that, *e.g.,* the disc scale height may be underestimated due to the lack of vertical support from magnetic fields (e.g. Penna et al. 2010), with observable differences potentially as high as $\sim 20\%$ (Noble et al. 2009; Kulkarni et al. 2011). There is the opportunity to expand and improve upon accretion disc models and their synthetic spectra to include the effects of magnetic fields, self-irradiation, Comptonisation, photoionisation, and dissipative processes. Thus, developing a robust pipeline to directly compare synthetic observations of self-consistent GRMHD numerical accretion disc models with observations would be a natural extension of work presented in this thesis.

The standard implementation of GRMHD does not scale well to optically thick luminous accretion flows, due to the enhanced radiative pressure in AGNs compared to the radiatively inefficient regime (Davis & Tchekhovskoy 2020). Traditionally, the bare magnetohydrodynamics equations are agnostic of the characteristic length or density scale, allowing the simulation to be performed for dimensionless code units, which can then be rescaled to a specified mass, up to the supermassive black hole regime. However, this degeneracy is lost with radiation hydrodynamics due to the dependence of opacities and emissivities on temperature and density. Therefore, only a few AGN-specific simulations have been performed (e.g. Jiang et al. 2019a,b), which, among other things, have shown that radiation pressure dominates over the thermal pressure in the disc without resulting in thermal instability and the disc scale height increases with radius significantly (Jiang et al. 2019a). Furthermore, radiative viscosity plays a surprisingly significant role in the overall angular momentum transport, which can sometimes be the dominant mechanism over magneto-rotational instability in luminous accretion flows. Future AGN-specific simulations

would need to focus on larger radii to observe temperature-dependent variations in opacity and longer time evolution to observe variability behaviour.

Bibliography

Abbott, T. M. C., et al. 2021, ApJS, 255, 20 (ADS entry)

Abdo, A. A., et al. 2010, ApJ, 716, 30 (ADS entry)

Abramowicz, M. A., Czerny, B., Lasota, J. P., & Szuszkiewicz, E. 1988, ApJ, 332, 646 (ADS entry)

Abramowicz, M. A., & Fragile, P. C. 2013, Living Reviews in Relativity, 16, 1 (ADS entry)

Akeson, R., et al. 2019, arXiv e-prints, arXiv:1902.05569 (ADS entry)

Akiyama, M., et al. 2018, PASJ, 70, S34 (ADS entry)

Amarantidis, S., et al. 2019, MNRAS, 485, 2694 (ADS entry)

Amaro-Seoane, P., et al. 2017, arXiv e-prints, arXiv:1702.00786 (ADS entry)

Ananna, T. T., et al. 2020, ApJ, 903, 85 (ADS entry)

Anninos, P., Fragile, P. C., & Salmonson, J. D. 2005, ApJ, 635, 723 (ADS entry)

Antonucci, R. 1993, ARA&A, 31, 473 (ADS entry)

Arimoto, N., & Yoshii, Y. 1987, A&A, 173, 23 (ADS entry)

Arnaud, K. A. 1996, in Astronomical Society of the Pacific Conference Series, Vol. 101, Astronomical Data Analysis Software and Systems V, ed. G. H. Jacoby & J. Barnes, 17 (ADS entry)

Artymowicz, P., Lin, D. N. C., & Wampler, E. J. 1993, ApJ, 409, 592 (ADS entry)

Assef, R. J., et al. 2015, ApJ, 804, 27 (ADS entry)

Astropy Collaboration et al. 2013, A&A, 558, A33 (ADS entry)

Avni, Y., & Bahcall, J. N. 1980, ApJ, 235, 694 (ADS entry)

Bañados, E., et al. 2016, ApJS, 227, 11 (ADS entry)

—. 2018, Nature, 553, 473 (ADS entry)

—. 2019, ApJ, 885, 59 (ADS entry)

Balbus, S. A., & Hawley, J. F. 1991, ApJ, 376, 214 (ADS entry)

Baldwin, J., Ferland, G., Korista, K., & Verner, D. 1995, ApJ, 455, L119 (ADS entry)

Baldwin, J. A. 1977, ApJ, 214, 679 (ADS entry)

Baldwin, J. A., Ferland, G. J., Korista, K. T., Hamann, F., & Dietrich, M. 2003, ApJ, 582, 590 (ADS entry)

Baldwin, J. A., & Netzer, H. 1978, ApJ, 226, 1 (ADS entry)

Baldwin, J. A., et al. 1996, ApJ, 461, 664 (ADS entry)

Barausse, E. 2012, MNRAS, 423, 2533 (ADS entry)

Barger, A. J., Cowie, L. L., Mushotzky, R. F., Yang, Y., Wang, W. H., Steffen, A. T., & Capak, P. 2005, AJ, 129, 578 (ADS entry)

Baskin, A., & Laor, A. 2005, MNRAS, 356, 1029 (ADS entry)

Becker, G. D., Bolton, J. S., & Lidz, A. 2015, Publ. Astron. Soc. Australia, 32, e045 (ADS entry)

Becker, G. D., Hewett, P. C., Worseck, G., & Prochaska, J. X. 2013, MNRAS, 430, 2067 (ADS entry)

Becker, G. D., Sargent, W. L. W., Rauch, M., & Carswell, R. F. 2012, ApJ, 744, 91 (ADS entry)

Becker, G. D., et al. 2019, ApJ, 883, 163 (ADS entry)

Bennert, N., Jungwiert, B., Komossa, S., Haas, M., & Chini, R. 2006, A&A, 456, 953 (ADS entry)

Bennert, V. N., et al. 2021, ApJ, 921, 36 (ADS entry)

Bentz, M. C., Peterson, B. M., Pogge, R. W., Vestergaard, M., & Onken, C. A. 2006, ApJ, 644, 133 (ADS entry)

Bentz, M. C., et al. 2009, ApJ, 705, 199 (ADS entry)

—. 2013, ApJ, 767, 149 (ADS entry)

Berg, T. A. M., et al. 2016, MNRAS, 463, 3021 (ADS entry)

Berg, T. A. M., et al. 2019, MNRAS, 488, 4356 (ADS entry)

—. 2021, MNRAS, 502, 4009 (ADS entry)

Berti, E., & Volonteri, M. 2008, ApJ, 684, 822 (ADS entry)

Bhowmick, A. K., et al. 2022, MNRAS, 516, 138 (ADS entry)

Bischetti, M., et al. 2017, A&A, 598, A122 (ADS entry)

—. 2022, Nature, 605, 244 (ADS entry)

—. 2023, ApJ, 952, 44 (ADS entry)

Blandford, R. D., & McKee, C. F. 1982, ApJ, 255, 419 (ADS entry)

Blandford, R. D., & Znajek, R. L. 1977, MNRAS, 179, 433 (ADS entry)

Bogdán, Á., et al. 2023, Nature Astronomy (ADS entry)

Bondi, H. 1952, MNRAS, 112, 195 (ADS entry)

Boroson, T. A., & Green, R. F. 1992, ApJS, 80, 109 (ADS entry)

Bosman, S. E. I., et al. 2022, MNRAS, 514, 55 (ADS entry)

Bouchet, P., Lequeux, J., Maurice, E., Prevot, L., & Prevot-Burnichon, M. L. 1985, A&A, 149, 330 (ADS entry)

Boutsia, K., et al. 2020, ApJS, 250, 26 (ADS entry)

—. 2021, ApJ, 912, 111 (ADS entry)

Boyle, B. J., Shanks, T., Croom, S. M., Smith, R. J., Miller, L., Loaring, N., & Heymans, C. 2000, MNRAS, 317, 1014 (ADS entry)

Braun, R., Bonaldi, A., Bourke, T., Keane, E., & Wagg, J. 2019, arXiv e-prints, arXiv:1912.12699 (ADS entry)

Bromm, V., & Loeb, A. 2003, ApJ, 596, 34 (ADS entry)

Brotherton, M. S., Tran, H. D., Becker, R. H., Gregg, M. D., Laurent-Muehleisen, S. A., & White, R. L. 2001, ApJ, 546, 775 (ADS entry)

Bruhweiler, F., & Verner, E. 2008, ApJ, 675, 83 (ADS entry)

Burke, C. J., et al. 2021, Science, 373, 789 (ADS entry)

Burkert, A., & Tremaine, S. 2010, ApJ, 720, 516 (ADS entry)

Calderone, G., Ghisellini, G., Colpi, M., & Dotti, M. 2013, MNRAS, 431, 210 (ADS entry)

Calderone, G., Nicastro, L., Ghisellini, G., Dotti, M., Sbarrato, T., Shankar, F., & Colpi, M. 2017, MNRAS, 472, 4051 (ADS entry)

Calderone, G., et al. 2019, ApJ, 887, 268 (ADS entry)

Calzetti, D., Kinney, A. L., & Storchi-Bergmann, T. 1994, ApJ, 429, 582 (ADS entry)

Campitiello, S., Celotti, A., Ghisellini, G., & Sbarrato, T. 2019, A&A, 625, A23 (ADS entry)

—. 2020, A&A, 640, A39 (ADS entry)

Campitiello, S., Ghisellini, G., Sbarrato, T., & Calderone, G. 2018, A&A, 612, A59 (ADS entry)

Capellupo, D. M., Netzer, H., Lira, P., Trakhtenbrot, B., & Mejía-Restrepo, J. 2015, MNRAS, 446, 3427 (ADS entry)

—. 2016, MNRAS, 460, 212 (ADS entry)

Capetti, A., Laor, A., Baldi, R. D., Robinson, A., & Marconi, A. 2021, MNRAS, 502, 5086 (ADS entry)

Caplar, N., Lilly, S. J., & Trakhtenbrot, B. 2017, ApJ, 834, 111 (ADS entry)

Cappellari, M. 2017, MNRAS, 466, 798 (ADS entry)

Carnall, A. C. 2017, arXiv e-prints, arXiv:1705.05165 (ADS entry)

Carroll, B. W., & Ostlie, D. A. 1996, An Introduction to Modern Astrophysics (ADS entry)

Cen, R., & Ostriker, J. P. 1999, ApJ, 519, L109 (ADS entry)

Cen, R., & Safarzadeh, M. 2015, ApJ, 798, L38 (ADS entry)

Chakrabarti, S. K., & Mukhopadhyay, B. 1999, A&A, 344, 105 (ADS entry)

Chambers, K. C., et al. 2016, arXiv e-prints, arXiv:1612.05560 (ADS entry)

Chatterjee, K., et al. 2020, MNRAS, 499, 362 (ADS entry)

Chaussidon, E., et al. 2023, ApJ, 944, 107 (ADS entry)

Chen, H., et al. 2022, ApJ, 931, 29 (ADS entry)

Cheng, H., Yuan, W., Liu, H.-Y., Breeveld, A. A., Jin, C., & Liu, B. 2019, MNRAS, 487, 3884 (ADS entry)

Childress, M. J., Vogt, F. P. A., Nielsen, J., & Sharp, R. G. 2014, Ap&SS, 349, 617 (ADS entry)

Ciotti, L., & Ostriker, J. P. 2001, ApJ, 551, 131 (ADS entry)

Cisternas, M., et al. 2011, ApJ, 741, L11 (ADS entry)

Clavel, J., et al. 1991, ApJ, 366, 64 (ADS entry)

Coatman, L., Hewett, P. C., Banerji, M., & Richards, G. T. 2016, MNRAS, 461, 647 (ADS entry)

Coatman, L., Hewett, P. C., Banerji, M., Richards, G. T., Hennawi, J. F., & Prochaska, J. X. 2017, MNRAS, 465, 2120 (ADS entry)

—. 2019, MNRAS, 486, 5335 (ADS entry)

Cohn, J. H., et al. 2021, ApJ, 919, 77 (ADS entry)

—. 2023, ApJ, 958, 186 (ADS entry)

Collin, S., Kawaguchi, T., Peterson, B. M., & Vestergaard, M. 2006, A&A, 456, 75 (ADS entry)

Collin, S., & Zahn, J.-P. 1999, Ap&SS, 265, 501 (ADS entry)

Collin-Souffrin, S., Dumnont, S., Joly, M., & Pequignot, D. 1986, A&A, 166, 27 (ADS entry)

Collin-Souffrin, S., & Lasota, J.-P. 1988, PASP, 100, 1041 (ADS entry)

Cooke, R., Pettini, M., Steidel, C. C., Rudie, G. C., & Nissen, P. E. 2011, MNRAS, 417, 1534 (ADS entry)

Corbin, M. R. 1997, ApJS, 113, 245 (ADS entry)

Costa, T., Sijacki, D., Trenti, M., & Haehnelt, M. G. 2014, MNRAS, 439, 2146 (ADS entry)

Cristiani, S., et al. 2023, MNRAS, 522, 2019 (ADS entry)

Croton, D. J., et al. 2006, MNRAS, 365, 11 (ADS entry)

Curti, M., et al. 2020, MNRAS, 492, 821 (ADS entry)

Curtis, H. D. 1918, Publications of Lick Observatory, 13, 9 (ADS entry)

Cushing, M. C., Vacca, W. D., & Rayner, J. T. 2004, PASP, 116, 362 (ADS entry)

Cutri, R. M., et al. 2013, Explanatory Supplement to the AllWISE Data Release Products, Explanatory Supplement to the AllWISE Data Release Products (ADS entry)

Czerny, B., Hryniewicz, K., Nikołajuk, M., & Sadowski, A. 2011, MNRAS, 415, 2942 (ADS entry)

Dalla Bontà, E., et al. 2020, ApJ, 903, 112 (ADS entry)

Dall'Aglio, A., Wisotzki, L., & Worseck, G. 2008, A&A, 491, 465 (ADS entry)

Dannen, R. C., Proga, D., Waters, T., & Dyda, S. 2020, ApJ, 893, L34 (ADS entry)

Datta, S. R., & Mukhopadhyay, B. 2019, MNRAS, 486, 1641 (ADS entry)

Davé, R., Rafieferantsoa, M. H., Thompson, R. J., & Hopkins, P. F. 2017, MNRAS, 467, 115 (ADS entry)

Davidson, K. 1977, ApJ, 218, 20 (ADS entry)

Davies, F. B., Hennawi, J. F., & Eilers, A.-C. 2019, ApJ, 884, L19 (ADS entry)

—. 2020, MNRAS, 493, 1330 (ADS entry)

Davies, F. B., et al. 2018, ApJ, 864, 142 (ADS entry)

Davies, R. I., et al. 2006, ApJ, 646, 754 (ADS entry)

Davies, R. L., et al. 2023, MNRAS, 521, 289 (ADS entry)

Davis, B. L., Graham, A. W., & Cameron, E. 2019, ApJ, 873, 85 (ADS entry)

Davis, S. W., Blaes, O. M., Hubeny, I., & Turner, N. J. 2005, ApJ, 621, 372 (ADS entry)

Davis, S. W., & El-Abd, S. 2019, ApJ, 874, 23 (ADS entry)

Davis, S. W., & Hubeny, I. 2006, ApJS, 164, 530 (ADS entry)

Davis, S. W., & Laor, A. 2011, ApJ, 728, 98 (ADS entry)

Davis, S. W., & Tchekhovskoy, A. 2020, ARA&A, 58, 407 (ADS entry)

Dayal, P., Rossi, E. M., Shiralilou, B., Piana, O., Choudhury, T. R., & Volonteri, M. 2019, MNRAS, 486, 2336 (ADS entry)

De Rosa, G., Decarli, R., Walter, F., Fan, X., Jiang, L., Kurk, J., Pasquali, A., & Rix, H. W. 2011, ApJ, 739, 56 (ADS entry)

De Rosa, G., et al. 2014, ApJ, 790, 145 (ADS entry)

—. 2018, ApJ, 866, 133 (ADS entry)

DeGraf, C., & Sijacki, D. 2017, MNRAS, 466, 3331 (ADS entry)

Delchambre, L., et al. 2023, A&A, 674, A31 (ADS entry)

Denney, K. D., et al. 2010, ApJ, 721, 715 (ADS entry)

Devecchi, B., & Volonteri, M. 2009, ApJ, 694, 302 (ADS entry)

Dexter, J. 2016, MNRAS, 462, 115 (ADS entry)

Dey, A., et al. 2019, AJ, 157, 168 (ADS entry)

Di Matteo, T., Colberg, J., Springel, V., Hernquist, L., & Sijacki, D. 2008, ApJ, 676, 33 (ADS entry)

Dietrich, M., Appenzeller, I., Vestergaard, M., & Wagner, S. J. 2002, ApJ, 564, 581 (ADS entry)

Dietrich, M., Hamann, F., Shields, J. C., Constantin, A., Heidt, J., Jäger, K., Vestergaard, M., & Wagner, S. J. 2003, ApJ, 589, 722 (ADS entry)

Ding, X., et al. 2020, ApJ, 888, 37 (ADS entry)

D'Odorico, V., Bruscoli, M., Saitta, F., Fontanot, F., Viel, M., Cristiani, S., & Monaco, P. 2008, MNRAS, 389, 1727 (ADS entry)

D'Odorico, V., Cristiani, S., Romano, D., Granato, G. L., & Danese, L. 2004, MN-RAS, 351, 976 (ADS entry)

D'Odorico, V., et al. 2022, MNRAS, 512, 2389 (ADS entry)

—. 2023, MNRAS, 523, 1399 (ADS entry)

Dolence, J. C., Gammie, C. F., Mościbrodzka, M., & Leung, P. K. 2009, ApJS, 184, 387 (ADS entry)

Done, C., Davis, S. W., Jin, C., Blaes, O., & Ward, M. 2012, MNRAS, 420, 1848 (ADS entry)

Dopita, M., Hart, J., McGregor, P., Oates, P., Bloxham, G., & Jones, D. 2007, Ap&SS, 310, 255 (ADS entry)

Dopita, M., et al. 2010, Ap&SS, 327, 245 (ADS entry)

Dors, O. L., Monteiro, A. F., Cardaci, M. V., Hägele, G. F., & Krabbe, A. C. 2019, MNRAS, 486, 5853 (ADS entry)

Dotti, M., Colpi, M., Pallini, S., Perego, A., & Volonteri, M. 2013, ApJ, 762, 68 (ADS entry)

Drescher, A., et al. 2022, in Society of Photo-Optical Instrumentation Engineers (SPIE) Conference Series, Vol. 12183, Optical and Infrared Interferometry and Imaging VIII, ed. A. Mérand, S. Sallum, & J. Sanchez-Bermudez, 121830T (ADS entry)

Dubois, Y., Volonteri, M., & Silk, J. 2014, MNRAS, 440, 1590 (ADS entry)

Dye, S., et al. 2018, MNRAS, 473, 5113 (ADS entry)

Earl, N., et al. 2022, astropy/specutils: V1.7.0 (Link)

Ebisawa, K., Makino, F., Mitsuda, K., Belloni, T., Cowley, A. P., Schmidtke, P. C., & Treves, A. 1993, ApJ, 403, 684 (ADS entry)

Edelson, R., et al. 2015, ApJ, 806, 129 (ADS entry)

Edge, A., Sutherland, W., Kuijken, K., Driver, S., McMahon, R., Eales, S., & Emerson, J. P. 2013, The Messenger, 154, 32 (ADS entry)

Eilers, A.-C., Davies, F. B., Hennawi, J. F., Prochaska, J. X., Lukić, Z., & Mazzucchelli, C. 2017, ApJ, 840, 24 (ADS entry)

Eilers, A.-C., Hennawi, J. F., & Davies, F. B. 2018, ApJ, 867, 30 (ADS entry)

Eilers, A.-C., et al. 2020, ApJ, 900, 37 (ADS entry)

—. 2023, ApJ, 950, 68 (ADS entry)

Elitzur, M. 2008, New Astron. Rev., 52, 274 (ADS entry)

Elvis, M. 2010, in Co-Evolution of Central Black Holes and Galaxies, ed. B. M. Peterson, R. S. Somerville, & T. Storchi-Bergmann, Vol. 267, 55–64 (ADS entry)

Elvis, M., et al. 1994, ApJS, 95, 1 (ADS entry)

Etienne, Z. B., Paschalidis, V., Haas, R., Mösta, P., & Shapiro, S. L. 2015, Classical and Quantum Gravity, 32, 175009 (ADS entry)

Euclid Collaboration et al. 2019, A&A, 631, A85 (ADS entry)

—. 2022, A&A, 662, A112 (ADS entry)

Event Horizon Telescope Collaboration et al. 2019a, ApJ, 875, L1 (ADS entry)

—. 2019b, ApJ, 875, L6 (ADS entry)

—. 2022a, ApJ, 930, L12 (ADS entry)

—. 2022b, ApJ, 930, L16 (ADS entry)

Falcone, A. D., Kraft, R. P., Bautz, M. W., Gaskin, J. A., Mulqueen, J. A., Swartz, D. A., & Lynx Science Technology Definition Team. 2019, Journal of Astronomical Telescopes, Instruments, and Systems, 5, 021019 (ADS entry)

Fan, X., Bañados, E., & Simcoe, R. A. 2023, ARA&A, 61, 373 (ADS entry)

Fan, X., Banados, E., & Simcoe, R. A. 2022, arXiv e-prints, arXiv:2212.06907 (ADS entry)

Fan, X., et al. 2001, AJ, 121, 54 (ADS entry)

—. 2004, AJ, 128, 515 (ADS entry)

—. 2006, AJ, 132, 117 (ADS entry)

Fanaroff, B. L., & Riley, J. M. 1974, MNRAS, 167, 31P (ADS entry)

Farina, E. P., et al. 2019, ApJ, 887, 196 (ADS entry)

—. 2022, ApJ, 941, 106 (ADS entry)

Fath, E. A. 1909, Lick Observatory Bulletin, 149, 71 (ADS entry)

Fawcett, V. A., Alexander, D. M., Rosario, D. J., Klindt, L., Lusso, E., Morabito, L. K., & Calistro Rivera, G. 2022, MNRAS, 513, 1254 (ADS entry)

Feng, Y., Di Matteo, T., Croft, R., & Khandai, N. 2014, MNRAS, 440, 1865 (ADS entry)

Ferland, G. J., Korista, K. T., Verner, D. A., Ferguson, J. W., Kingdon, J. B., & Verner, E. M. 1998, PASP, 110, 761 (ADS entry)

Ferrarese, L. 2002, ApJ, 578, 90 (ADS entry)

Ferrarese, L., & Merritt, D. 2000, ApJ, 539, L9 (ADS entry)

Fitzpatrick, E. L. 1999, PASP, 111, 63 (ADS entry)

Flesch, E. W. 2015, Publ. Astron. Soc. Australia, 32, e010 (ADS entry)

—. 2021, arXiv e-prints, arXiv:2105.12985 (ADS entry)

Flewelling, H. A., et al. 2020, ApJS, 251, 7 (ADS entry)

Fonseca Alvarez, G., et al. 2020, ApJ, 899, 73 (ADS entry)

Foreman-Mackey, D. 2016, The Journal of Open Source Software, 1, 24 (Link)

Foreman-Mackey, D., Hogg, D. W., Lang, D., & Goodman, J. 2013, PASP, 125, 306 (ADS entry)

Francis, P. J., Hewett, P. C., Foltz, C. B., Chaffee, F. H., Weymann, R. J., & Morris, S. L. 1991, ApJ, 373, 465 (ADS entry)

Frank, J., King, A., & Raine, D. J. 2002, Accretion Power in Astrophysics: Third Edition (ADS entry)

Freeman, P., Doe, S., & Siemiginowska, A. 2001, in Society of Photo-Optical Instrumentation Engineers (SPIE) Conference Series, Vol. 4477, Astronomical Data Analysis, ed. J.-L. Starck & F. D. Murtagh, 76–87 (ADS entry)

Freudling, W., Romaniello, M., Bramich, D. M., Ballester, P., Forchi, V., García-Dabló, C. E., Moehler, S., & Neeser, M. J. 2013, A&A, 559, A96 (ADS entry)

Friaca, A. C. S., & Terlevich, R. J. 1998, MNRAS, 298, 399 (ADS entry)

Fromerth, M. J., & Melia, F. 2000, ApJ, 533, 172 (ADS entry)

Furlanetto, S. R., Hernquist, L., & Zaldarriaga, M. 2004, MNRAS, 354, 695 (ADS entry)

Gaia Collaboration et al. 2021, A&A, 649, A1 (ADS entry)

Gallerani, S., Ferrara, A., Fan, X., & Choudhury, T. R. 2008, MNRAS, 386, 359 (ADS entry)

Gallerani, S., et al. 2010, A&A, 523, A85 (ADS entry)

Gammie, C. F. 1999, ApJ, 522, L57 (ADS entry)

Gammie, C. F., McKinney, J. C., & Tóth, G. 2003, ApJ, 589, 444 (ADS entry)

Gaskell, C. M. 1982, ApJ, 263, 79 (ADS entry)

Gebhardt, K., et al. 2000, ApJ, 539, L13 (ADS entry)

Ghez, A. M., Klein, B. L., Morris, M., & Becklin, E. E. 1998, ApJ, 509, 678 (ADS entry)

Ghez, A. M., et al. 2008, ApJ, 689, 1044 (ADS entry)

Ghisellini, G., Tagliaferri, G., Sbarrato, T., & Gehrels, N. 2015, MNRAS, 450, L34 (ADS entry)

Giallongo, E., et al. 2019, ApJ, 884, 19 (ADS entry)

Gibson, R. R., et al. 2009, ApJ, 692, 758 (ADS entry)

Giersz, M., Leigh, N., Hypki, A., Lützgendorf, N., & Askar, A. 2015, MNRAS, 454, 3150 (ADS entry)

Gillessen, S., Eisenhauer, F., Trippe, S., Alexander, T., Genzel, R., Martins, F., & Ott, T. 2009, ApJ, 692, 1075 (ADS entry)

Glikman, E., Helfand, D. J., White, R. L., Becker, R. H., Gregg, M. D., & Lacy, M. 2007, ApJ, 667, 673 (ADS entry)

Gnedin, N. Y., & Ostriker, J. P. 1997, ApJ, 486, 581 (ADS entry)

Goodman, J., & Tan, J. C. 2004, ApJ, 608, 108 (ADS entry)

Granato, G. L., De Zotti, G., Silva, L., Bressan, A., & Danese, L. 2004, ApJ, 600, 580 (ADS entry)

Grandi, S. A. 1982, ApJ, 255, 25 (ADS entry)

GRAVITY Collaboration et al. 2017, A&A, 602, A94 (ADS entry)

—. 2018, A&A, 615, L15 (ADS entry)

Gravity Collaboration et al. 2018, Nature, 563, 657 (ADS entry)

GRAVITY Collaboration et al. 2020a, A&A, 636, L5 (ADS entry)

—. 2020b, A&A, 635, A92 (ADS entry)

Gravity Collaboration et al. 2022, The Messenger, 188, 20 (ADS entry)

Gravity+ Collaboration et al. 2022, The Messenger, 189, 17 (ADS entry)

Grazian, A., et al. 2020, ApJ, 897, 94 (ADS entry)

—. 2022, ApJ, 924, 62 (ADS entry)

Greene, J. E., & Ho, L. C. 2005, ApJ, 630, 122 (ADS entry)

Greene, J. E., et al. 2010, ApJ, 721, 26 (ADS entry)

Greenstein, J. L. 1963, Nature, 197, 1041 (ADS entry)

Greenstein, J. L., & Schmidt, M. 1964, ApJ, 140, 1 (ADS entry)

Greggio, L., & Renzini, A. 1983, A&A, 118, 217 (ADS entry)

Grier, C. J., et al. 2013, ApJ, 764, 47 (ADS entry)

—. 2019, ApJ, 887, 38 (ADS entry)

Grould, M., Vincent, F. H., Paumard, T., & Perrin, G. 2017, A&A, 608, A60 (ADS entry)

Guerras, E., Mediavilla, E., Jimenez-Vicente, J., Kochanek, C. S., Muñoz, J. A., Falco, E., & Motta, V. 2013, ApJ, 764, 160 (ADS entry)

Guo, H., Shen, Y., & Wang, S. 2018, PyQSOFit: Python code to fit the spectrum of quasars, Astrophysics Source Code Library, record ascl:1809.008 (ADS entry)

Guo, H., Sun, M., Liu, X., Wang, T., Kong, M., Wang, S., Sheng, Z., & He, Z. 2019, ApJ, 883, L44 (ADS entry)

Guo, H., et al. 2020, ApJ, 888, 58 (ADS entry)

Haardt, F., & Madau, P. 2012, ApJ, 746, 125 (ADS entry)

Hamann, F., Cohen, R. D., Shields, J. C., Burbidge, E. M., Junkkarinen, V., & Crenshaw, D. M. 1998, ApJ, 496, 761 (ADS entry)

Hamann, F., & Ferland, G. 1992, ApJ, 391, L53 (ADS entry)

—. 1993, ApJ, 418, 11 (ADS entry)

—. 1999, ARA&A, 37, 487 (ADS entry)

Hamann, F., Korista, K. T., Ferland, G. J., Warner, C., & Baldwin, J. 2002, ApJ, 564, 592 (ADS entry)

Hardcastle, M. J., & Croston, J. H. 2020, New Astron. Rev., 88, 101539 (ADS entry)

Häring, N., & Rix, H.-W. 2004, ApJ, 604, L89 (ADS entry)

Harris, G. L. H., & Harris, W. E. 2011, MNRAS, 410, 2347 (ADS entry)

Hartwig, T., Agarwal, B., & Regan, J. A. 2018, MNRAS, 479, L23 (ADS entry)

Hasinger, G. 2008, A&A, 490, 905 (ADS entry)

Hazard, C., Mackey, M. B., & Shimmins, A. J. 1963, Nature, 197, 1037 (ADS entry)

He, W., et al. 2023, arXiv e-prints, arXiv:2311.08922 (ADS entry)

Heckman, T. M. 1980, A&A, 87, 152 (ADS entry)

Hicks, E. K. S., & Malkan, M. A. 2008, ApJS, 174, 31 (ADS entry)

Hinton, S. R. 2016, The Journal of Open Source Software, 1, 00045 (ADS entry)

Ho, L. C. 2008, ARA&A, 46, 475 (ADS entry)

Ho, L. C., & Kim, M. 2014, ApJ, 789, 17 (ADS entry)

Homayouni, Y., et al. 2020, ApJ, 901, 55 (ADS entry)

Hoormann, J. K., et al. 2019, MNRAS, 487, 3650 (ADS entry)

Hopkins, P. F., Hernquist, L., Cox, T. J., Di Matteo, T., Martini, P., Robertson, B., & Springel, V. 2005, ApJ, 630, 705 (ADS entry)

Hopkins, P. F., Richards, G. T., & Hernquist, L. 2007, ApJ, 654, 731 (ADS entry)

Hopkins, P. F., et al. 2004, AJ, 128, 1112 (ADS entry)

Hu, T., & Peng, Q. 2008, ApJ, 681, 96 (ADS entry)

Hubeny, I., Agol, E., Blaes, O., & Krolik, J. H. 2000, ApJ, 533, 710 (ADS entry)

Hubeny, I., Blaes, O., Krolik, J. H., & Agol, E. 2001, ApJ, 559, 680 (ADS entry)

Hughes, P. A., Aller, H. D., & Aller, M. F. 1992, ApJ, 396, 469 (ADS entry)

Hunter, J. D. 2007, Computing in Science and Engineering, 9, 90 (ADS entry)

Inayoshi, K., Haiman, Z., & Ostriker, J. P. 2016, MNRAS, 459, 3738 (ADS entry)

Inayoshi, K., Visbal, E., & Haiman, Z. 2020, ARA&A, 58, 27 (ADS entry)

Iršič, V., et al. 2017, MNRAS, 466, 4332 (ADS entry)

Irwin, M. J., Webster, R. L., Hewett, P. C., Corrigan, R. T., & Jedrzejewski, R. I. 1989, AJ, 98, 1989 (ADS entry)

Israel, W. 1968, Communications in Mathematical Physics, 8, 245 (ADS entry)

Ivezić, Ž., et al. 2019, ApJ, 873, 111 (ADS entry)

Jiang, J., et al. 2018, MNRAS, 477, 3711 (ADS entry)

Jiang, L., Fan, X., Vestergaard, M., Kurk, J. D., Walter, F., Kelly, B. C., & Strauss, M. A. 2007, AJ, 134, 1150 (ADS entry)

Jiang, L., et al. 2009, AJ, 138, 305 (ADS entry)

—. 2014, ApJS, 213, 12 (ADS entry)

—. 2016, ApJ, 833, 222 (ADS entry)

Jiang, Y.-F., Blaes, O., Stone, J. M., & Davis, S. W. 2019a, ApJ, 885, 144 (ADS entry)

Jiang, Y.-F., Stone, J. M., & Davis, S. W. 2019b, ApJ, 880, 67 (ADS entry)

Johnson, M. D., et al. 2023, Galaxies, 11, 61 (ADS entry)

Jones, A., Noll, S., Kausch, W., Szyszka, C., & Kimeswenger, S. 2013, A&A, 560, A91 (ADS entry)

Juarez, Y., Maiolino, R., Mujica, R., Pedani, M., Marinoni, S., Nagao, T., Marconi, A., & Oliva, E. 2009, A&A, 494, L25 (ADS entry)

Kammoun, E. S., et al. 2023, MNRAS, 522, 5217 (ADS entry)

Kashikawa, N., et al. 2015, ApJ, 798, 28 (ADS entry)

Kaspi, S., Brandt, W. N., Maoz, D., Netzer, H., Schneider, D. P., Shemmer, O., & Grier, C. J. 2021, ApJ, 915, 129 (ADS entry)

Kaspi, S., Maoz, D., Netzer, H., Peterson, B. M., Vestergaard, M., & Jannuzi, B. T. 2005, ApJ, 629, 61 (ADS entry)

Kaspi, S., Smith, P. S., Netzer, H., Maoz, D., Jannuzi, B. T., & Giveon, U. 2000, ApJ, 533, 631 (ADS entry)

Kato, N., et al. 2020, PASJ, 72, 84 (ADS entry)

Kauffmann, G., & Haehnelt, M. 2000, MNRAS, 311, 576 (ADS entry)

Kawaguchi, T. 2003, ApJ, 593, 69 (ADS entry)

Kawaguchi, T., Pierens, A., & Huré, J. M. 2004, A&A, 415, 47 (ADS entry)

Kelly, B. C., Bechtold, J., & Siemiginowska, A. 2009, ApJ, 698, 895 (ADS entry)

Kelly, B. C., & Shen, Y. 2013, ApJ, 764, 45 (ADS entry)

Kelly, B. C., Vestergaard, M., Fan, X., Hopkins, P., Hernquist, L., & Siemiginowska, A. 2010, ApJ, 719, 1315 (ADS entry)

Kelson, D. D. 2003, PASP, 115, 688 (ADS entry)

Khrykin, I. S., Hennawi, J. F., & Worseck, G. 2019, MNRAS, 484, 3897 (ADS entry)

Khrykin, I. S., Hennawi, J. F., Worseck, G., & Davies, F. B. 2021, MNRAS, 505, 649 (ADS entry)

Kim, Y., et al. 2020, ApJ, 904, 111 (ADS entry)

King, A. R., Lubow, S. H., Ogilvie, G. I., & Pringle, J. E. 2005, MNRAS, 363, 49 (ADS entry)

King, A. R., & Pringle, J. E. 2006, MNRAS, 373, L90 (ADS entry)

King, A. R., Pringle, J. E., & Hofmann, J. A. 2008, MNRAS, 385, 1621 (ADS entry)

Kinney, A. L., Calzetti, D., Bohlin, R. C., McQuade, K., Storchi-Bergmann, T., & Schmitt, H. R. 1996, ApJ, 467, 38 (ADS entry)

Klindt, L., Alexander, D. M., Rosario, D. J., Lusso, E., & Fotopoulou, S. 2019, MNRAS, 488, 3109 (ADS entry)

Kollmeier, J. A., et al. 2006, ApJ, 648, 128 (ADS entry)

Koratkar, A., & Blaes, O. 1999, PASP, 111, 1 (ADS entry)

Korista, K. T., & Goad, M. R. 2000, ApJ, 536, 284 (ADS entry)

Korista, K. T., et al. 1995, ApJS, 97, 285 (ADS entry)

Kormendy, J., Bender, R., & Cornell, M. E. 2011, Nature, 469, 374 (ADS entry)

Kormendy, J., & Gebhardt, K. 2001, in American Institute of Physics Conference Series, Vol. 586, 20th Texas Symposium on relativistic astrophysics, ed. J. C. Wheeler & H. Martel, 363–381 (ADS entry)

Kormendy, J., & Ho, L. C. 2013, ARA&A, 51, 511 (ADS entry)

Kormendy, J., & Richstone, D. 1995, ARA&A, 33, 581 (ADS entry)

Kovačević, J., Popović, L. Č., & Kollatschny, W. 2014, Advances in Space Research, 54, 1347 (ADS entry)

Kovačević-Dojčinović, J., Marčeta-Mandić, S., & Popović, L. Č. 2017, Frontiers in Astronomy and Space Sciences, 4, 7 (ADS entry)

Kozłowski, S. 2016, ApJ, 826, 118 (ADS entry)

—. 2017, ApJS, 228, 9 (ADS entry)

Krawczyk, C. M., Richards, G. T., Gallagher, S. C., Leighly, K. M., Hewett, P. C., Ross, N. P., & Hall, P. B. 2015, AJ, 149, 203 (ADS entry)

Krolik, J. H. 2001, ApJ, 551, 72 (ADS entry)

Kulier, A., Ostriker, J. P., Natarajan, P., Lackner, C. N., & Cen, R. 2015, ApJ, 799, 178 (ADS entry)

Kulkarni, A. K., et al. 2011, MNRAS, 414, 1183 (ADS entry)

Kurk, J. D., et al. 2007, ApJ, 669, 32 (ADS entry)

Lah, P., Onken, C. A., Norris, R. P., & D'Eugenio, F. 2023, MNRAS, 525, 5291 (ADS entry)

Lai, S. 2023a, samlaihei/BADFit: BADFit v1.0.0 (Link)

—. 2023b, samlaihei/PyQSpecFit: PyQSpecFit v1.0.0 (Link)

Lai, S., Onken, C. A., Wolf, C., Bian, F., Cupani, G., Lopez, S., & D'Odorico, V. 2023a, MNRAS, 526, 3230 (ADS entry)

Lai, S., Onken, C. A., Wolf, C., Bian, F., & Fan, X. 2024, MNRAS, 527, 3912 (ADS entry)

Lai, S., Wolf, C., Onken, C. A., & Bian, F. 2023b, MNRAS(ADS entry)

Lai, S., et al. 2022, MNRAS, 513, 1801 (ADS entry)

Laor, A. 1990, MNRAS, 246, 369 (ADS entry)

Laor, A., & Davis, S. W. 2011, MNRAS, 417, 681 (ADS entry)

Laor, A., Fiore, F., Elvis, M., Wilkes, B. J., & McDowell, J. C. 1997, ApJ, 477, 93 (ADS entry)

Laor, A., & Netzer, H. 1989, MNRAS, 238, 897 (ADS entry)

Larson, R. L., et al. 2023, ApJ, 953, L29 (ADS entry)

Lawrence, A. 1991, MNRAS, 252, 586 (ADS entry)

Lawrence, A., & Elvis, M. 2010, ApJ, 714, 561 (ADS entry)

Lawrence, A., et al. 2007, MNRAS, 379, 1599 (ADS entry)

Leighly, K. M., & Moore, J. R. 2004, ApJ, 611, 107 (ADS entry)

Li, L.-X., Zimmerman, E. R., Narayan, R., & McClintock, J. E. 2005, ApJS, 157, 335 (ADS entry)

Li, W., Inayoshi, K., Onoue, M., & Toyouchi, D. 2023a, ApJ, 950, 85 (ADS entry)

Li, W., et al. 2023b, arXiv e-prints, arXiv:2306.06172 (ADS entry)

Li, Y., Yuan, W., Zhou, H. Y., Komossa, S., Ai, Y. L., Liu, W. J., & Boisvert, J. H. 2015, AJ, 149, 75 (ADS entry)

Li, Y., et al. 2007, ApJ, 665, 187 (ADS entry)

Li, Z., McGreer, I. D., Wu, X.-B., Fan, X., & Yang, Q. 2018, ApJ, 861, 6 (ADS entry)

Lira, P., Arévalo, P., Uttley, P., McHardy, I. M. M., & Videla, L. 2015, MNRAS, 454, 368 (ADS entry)

Lira, P., et al. 2018, ApJ, 865, 56 (ADS entry)

Liu, H., Luo, B., Brandt, W. N., Brotherton, M. S., Gallagher, S. C., Ni, Q., Shemmer, O., & Timlin, J. D., I. 2021, ApJ, 910, 103 (ADS entry)

Lodato, G., & Pringle, J. E. 2006, MNRAS, 368, 1196 (ADS entry)

Loeb, A., & Rasio, F. A. 1994, ApJ, 432, 52 (ADS entry)

Londrillo, P., & Del Zanna, L. 2000, ApJ, 530, 508 (ADS entry)

López, S., et al. 2016, A&A, 594, A91 (ADS entry)

Lupi, A., Haardt, F., Dotti, M., Fiacconi, D., Mayer, L., & Madau, P. 2016, MNRAS, 456, 2993 (ADS entry)

Lyke, B. W., et al. 2020, ApJS, 250, 8 (ADS entry)

MacLeod, C. L., et al. 2010, ApJ, 721, 1014 (ADS entry)

Madau, P., Haardt, F., & Dotti, M. 2014, ApJ, 784, L38 (ADS entry)

Madau, P., & Rees, M. J. 2001, ApJ, 551, L27 (ADS entry)

Magorrian, J., et al. 1998, AJ, 115, 2285 (ADS entry)

Maiolino, R., & Mannucci, F. 2019, A&ARv, 27, 3 (ADS entry)

Maiolino, R., & Rieke, G. H. 1995, ApJ, 454, 95 (ADS entry)

Maiolino, R., et al. 2008, A&A, 488, 463 (ADS entry)

Malik, U., et al. 2023, MNRAS, 520, 2009 (ADS entry)

Malkan, M. A. 1983, ApJ, 268, 582 (ADS entry)

Mallery, R. P., et al. 2012, ApJ, 760, 128 (ADS entry)

Mannucci, F., Basile, F., Poggianti, B. M., Cimatti, A., Daddi, E., Pozzetti, L., & Vanzi, L. 2001, MNRAS, 326, 745 (ADS entry)

Mannucci, F., et al. 2009, MNRAS, 398, 1915 (ADS entry)

Marconi, A., & Hunt, L. K. 2003, ApJ, 589, L21 (ADS entry)

Marconi, A., Risaliti, G., Gilli, R., Hunt, L. K., Maiolino, R., & Salvati, M. 2004, MNRAS, 351, 169 (ADS entry)

Marin, F., et al. 2023, Nature, 619, 41 (ADS entry)

Marocco, F., et al. 2021, ApJS, 253, 8 (ADS entry)

Martin, G., et al. 2018, MNRAS, 476, 2801 (ADS entry)

Martinelli, M., Pandolfi, S., Martins, C. J. A. P., & Vielzeuf, P. E. 2012, Phys. Rev. D, 86, 123001 (ADS entry)

Marziani, P., Sulentic, J. W., Dultzin-Hacyan, D., Calvani, M., & Moles, M. 1996, ApJS, 104, 37 (ADS entry)

Marziani, P., Sulentic, J. W., Plauchu-Frayn, I., & del Olmo, A. 2013, A&A, 555, A89 (ADS entry)

Marziani, P., et al. 2022, Astronomische Nachrichten, 343, e210082 (ADS entry)

Mason, R. E., et al. 2015, ApJS, 217, 13 (ADS entry)

Matejek, M. S., & Simcoe, R. A. 2012, ApJ, 761, 112 (ADS entry)

Mathews, W. G., & Ferland, G. J. 1987, ApJ, 323, 456 (ADS entry)

Matsuoka, K., Nagao, T., Marconi, A., Maiolino, R., Mannucci, F., Cresci, G., Terao, K., & Ikeda, H. 2018a, A&A, 616, L4 (ADS entry)

Matsuoka, K., Nagao, T., Marconi, A., Maiolino, R., & Taniguchi, Y. 2011, A&A, 527, A100 (ADS entry)

Matsuoka, Y., et al. 2016, ApJ, 828, 26 (ADS entry)

—. 2018b, ApJ, 869, 150 (ADS entry)

—. 2022, ApJS, 259, 18 (ADS entry)

—. 2023, ApJ, 949, L42 (ADS entry)

Matthews, J. H., Knigge, C., Higginbottom, N., Long, K. S., Sim, S. A., Mangham, S. W., Parkinson, E. J., & Hewitt, H. A. 2020, MNRAS, 492, 5540 (ADS entry)

Matthews, T. A., & Sandage, A. R. 1963, ApJ, 138, 30 (ADS entry)

Mazzucchelli, C., et al. 2017, ApJ, 849, 91 (ADS entry)

—. 2023, A&A, 676, A71 (ADS entry)

McConnell, D., et al. 2020, Publ. Astron. Soc. Australia, 37, e048 (ADS entry)

McConnell, N. J., & Ma, C.-P. 2013, ApJ, 764, 184 (ADS entry)

McGreer, I. D., Fan, X., Jiang, L., & Cai, Z. 2018, AJ, 155, 131 (ADS entry)

McLure, R. J., & Dunlop, J. S. 2002, MNRAS, 331, 795 (ADS entry)

—. 2004, MNRAS, 352, 1390 (ADS entry)

McLure, R. J., & Jarvis, M. J. 2002, MNRAS, 337, 109 (ADS entry)

McMahon, R. G., Banerji, M., Gonzalez, E., Koposov, S. E., Bejar, V. J., Lodieu, N., Rebolo, R., & VHS Collaboration. 2013, The Messenger, 154, 35 (ADS entry)

McQuinn, M. 2016, ARA&A, 54, 313 (ADS entry)

Mediavilla, E., Jiménez-Vicente, J., Fian, C., Muñoz, J. A., Falco, E., Motta, V., & Guerras, E. 2018, ApJ, 862, 104 (ADS entry)

Mediavilla, E., Jiménez-vicente, J., Mejía-restrepo, J., Motta, V., Falco, E., Muñoz, J. A., Fian, C., & Guerras, E. 2019, ApJ, 880, 96 (ADS entry)

Mejía-Restrepo, J. E., Lira, P., Netzer, H., Trakhtenbrot, B., & Capellupo, D. M. 2018, Nature Astronomy, 2, 63 (ADS entry)

Mejía-Restrepo, J. E., Trakhtenbrot, B., Lira, P., Netzer, H., & Capellupo, D. M. 2016, MNRAS, 460, 187 (ADS entry)

Merloni, A., et al. 2014, MNRAS, 437, 3550 (ADS entry)

Merritt, D., & Ferrarese, L. 2001, MNRAS, 320, L30 (ADS entry)

Meyer, R. A., Bosman, S. E. I., & Ellis, R. S. 2019, MNRAS, 487, 3305 (ADS entry)

Miller, J. S., & Goodrich, R. W. 1990, ApJ, 355, 456 (ADS entry)

Minkowski, R. 1960, ApJ, 132, 908 (ADS entry)

Morey, K. A., Eilers, A.-C., Davies, F. B., Hennawi, J. F., & Simcoe, R. A. 2021, ApJ, 921, 88 (ADS entry)

Morganson, E., et al. 2014, ApJ, 784, 92 (ADS entry)

Mortlock, D. J., Patel, M., Warren, S. J., Hewett, P. C., Venemans, B. P., McMahon, R. G., & Simpson, C. 2012, MNRAS, 419, 390 (ADS entry)

Mortlock, D. J., et al. 2011, Nature, 474, 616 (ADS entry)

Nagao, T., Marconi, A., & Maiolino, R. 2006, A&A, 447, 157 (ADS entry)

Narayan, R., SÄ dowski, A., Penna, R. F., & Kulkarni, A. K. 2012, MNRAS, 426, 3241 (ADS entry)

Narayan, R., Zhu, Y., Psaltis, D., & Sadowski, A. 2016, MNRAS, 457, 608 (ADS entry)

Nemmen, R. S., & Brotherton, M. S. 2010, MNRAS, 408, 1598 (ADS entry)

Netzer, H. 2015, ARA&A, 53, 365 (ADS entry)

—. 2019, MNRAS, 488, 5185 (ADS entry)

Netzer, H., & Davidson, K. 1979, MNRAS, 187, 871 (ADS entry)

Netzer, H., & Peterson, B. M. 1997, in Astrophysics and Space Science Library, Vol. 218, Astronomical Time Series, ed. D. Maoz, A. Sternberg, & E. M. Leibowitz, 85 (ADS entry)

Neugebauer, G., Oke, J. B., Becklin, E. E., & Matthews, K. 1979, ApJ, 230, 79 (ADS entry)

Ni, Y., Di Matteo, T., Gilli, R., Croft, R. A. C., Feng, Y., & Norman, C. 2020, MNRAS, 495, 2135 (ADS entry)

Nidever, D. L., et al. 2021, AJ, 161, 192 (ADS entry)

Niida, M., et al. 2020, ApJ, 904, 89 (ADS entry)

Noble, S. C., Krolik, J. H., & Hawley, J. F. 2009, ApJ, 692, 411 (ADS entry)

Noll, S., Kausch, W., Barden, M., Jones, A. M., Szyszka, C., Kimeswenger, S., & Vinther, J. 2012, A&A, 543, A92 (ADS entry)

Noterdaeme, P., et al. 2012, A&A, 547, L1 (ADS entry)

Novak, G. S., Ostriker, J. P., & Ciotti, L. 2011, ApJ, 737, 26 (ADS entry)

Novak, M., et al. 2019, ApJ, 881, 63 (ADS entry)

Novikov, I. D., & Thorne, K. S. 1973, in Black Holes (Les Astres Occlus), 343–450 (ADS entry)

Ohsuga, K., Mineshige, S., Mori, M., & Umemura, M. 2002, ApJ, 574, 315 (ADS entry)

Oke, J. B. 1963, Nature, 197, 1040 (ADS entry)

Onken, C. A., Bian, F., Fan, X., Wang, F., Wolf, C., & Yang, J. 2020, MNRAS, 496, 2309 (ADS entry)

Onken, C. A., Ferrarese, L., Merritt, D., Peterson, B. M., Pogge, R. W., Vestergaard, M., & Wandel, A. 2004, ApJ, 615, 645 (ADS entry)

Onken, C. A., & Kollmeier, J. A. 2008, ApJ, 689, L13 (ADS entry)

Onken, C. A., Wolf, C., Bian, F., Fan, X., Hon, W. J., Raithel, D., Tisserand, P., & Lai, S. 2022a, MNRAS, 511, 572 (ADS entry)

Onken, C. A., Wolf, C., Hon, W. J., Lai, S., Tisserand, P., & Webster, R. 2023, Publ. Astron. Soc. Australia, 40, e010 (ADS entry)

Onken, C. A., et al. 2007, ApJ, 670, 105 (ADS entry)

—. 2019, Publ. Astron. Soc. Australia, 36, e033 (ADS entry)

—. 2022b, Publ. Astron. Soc. Australia, 39, e037 (ADS entry)

—. in prep.

Onoue, M., et al. 2019, ApJ, 880, 77 (ADS entry)

—. 2020, ApJ, 898, 105 (ADS entry)

Oppenheimer, B. D., & Schaye, J. 2013, MNRAS, 434, 1063 (ADS entry)

Orr, M. J. L., & Browne, I. W. A. 1982, MNRAS, 200, 1067 (ADS entry)

Osterbrock, D. E. 1980, in Ninth Texas Symposium on Relativistic Astrophysics, Vol. 336, 22–38 (ADS entry)

Osterbrock, D. E., & Ferland, G. J. 2006, Astrophysics of gaseous nebulae and active galactic nuclei (ADS entry)

Pacucci, F., Nguyen, B., Carniani, S., Maiolino, R., & Fan, X. 2023, ApJ, 957, L3 (ADS entry)

Pacucci, F., Volonteri, M., & Ferrara, A. 2015, MNRAS, 452, 1922 (ADS entry)

Padovani, P. 2011, MNRAS, 411, 1547 (ADS entry)

—. 2016, A&ARv, 24, 13 (ADS entry)

—. 2017, Nature Astronomy, 1, 0194 (ADS entry)

Page, M. J., & Carrera, F. J. 2000, MNRAS, 311, 433 (ADS entry)

Park, D., Barth, A. J., Ho, L. C., & Laor, A. 2022, ApJS, 258, 38 (ADS entry)

Park, D., Barth, A. J., Woo, J.-H., Malkan, M. A., Treu, T., Bennert, V. N., Assef, R. J., & Pancoast, A. 2017, ApJ, 839, 93 (ADS entry)

Patiño Álvarez, V., Torrealba, J., Chavushyan, V., Cruz González, I., Arshakian, T., León Tavares, J., & Popovic, L. 2016, Frontiers in Astronomy and Space Sciences, 3, 19 (ADS entry)

Peng, C. Y., Impey, C. D., Ho, L. C., Barton, E. J., & Rix, H.-W. 2006, ApJ, 640, 114 (ADS entry)

Penna, R. F., McKinney, J. C., Narayan, R., Tchekhovskoy, A., Shafee, R., & McClintock, J. E. 2010, MNRAS, 408, 752 (ADS entry)

Pensabene, A., et al. 2021, A&A, 652, A66 (ADS entry)

Pentericci, L., et al. 2002, AJ, 123, 2151 (ADS entry)

Perrotta, S., et al. 2016, MNRAS, 462, 3285 (ADS entry)

—. 2018, MNRAS, 481, 105 (ADS entry)

Peterson, B. M. 1993, PASP, 105, 247 (ADS entry)

—. 2006, in Physics of Active Galactic Nuclei at all Scales, ed. D. Alloin, Vol. 693, 77 (ADS entry)

Peterson, B. M. 2010, in Co-Evolution of Central Black Holes and Galaxies, ed. B. M. Peterson, R. S. Somerville, & T. Storchi-Bergmann, Vol. 267, 151–160 (ADS entry)

Peterson, B. M., & Bentz, M. C. 2006, New Astron. Rev., 50, 796 (ADS entry)

Peterson, B. M., & Horne, K. 2004, Astronomische Nachrichten, 325, 248 (ADS entry)

Peterson, B. M., et al. 2004, ApJ, 613, 682 (ADS entry)

Pons, E., & Watson, M. G. 2016, A&A, 594, A72 (ADS entry)

Popović, L. Č., Shablovinskaya, E., & Savić, D. 2022, Astronomische Nachrichten, 343, e210089 (ADS entry)

Porciani, C., Magliocchetti, M., & Norberg, P. 2004, MNRAS, 355, 1010 (ADS entry)

Porciani, C., & Norberg, P. 2006, MNRAS, 371, 1824 (ADS entry)

Portegies Zwart, S. F., Baumgardt, H., Hut, P., Makino, J., & McMillan, S. L. W. 2004, Nature, 428, 724 (ADS entry)

Porth, O., Olivares, H., Mizuno, Y., Younsi, Z., Rezzolla, L., Moscibrodzka, M., Falcke, H., & Kramer, M. 2017, Computational Astrophysics and Cosmology, 4, 1 (ADS entry)

Predehl, P., et al. 2021, A&A, 647, A1 (ADS entry)

Prochaska, J., et al. 2020a, The Journal of Open Source Software, 5, 2308 (ADS entry)

Prochaska, J. X., & Wolfe, A. M. 2009, ApJ, 696, 1543 (ADS entry)

Prochaska, J. X., et al. 2020b, pypeit/PypeIt: Release 1.0.0 (ADS entry)

Proga, D., Stone, J. M., & Kallman, T. R. 2000, ApJ, 543, 686 (ADS entry)

Punturo, M., et al. 2010, Classical and Quantum Gravity, 27, 194002 (ADS entry)

Queiroz, C., et al. 2023, MNRAS, 520, 3476 (ADS entry)

Rafiee, A., & Hall, P. B. 2011, ApJS, 194, 42 (ADS entry)

Raimundo, S. I., Pancoast, A., Vestergaard, M., Goad, M. R., & Barth, A. J. 2019, MNRAS, 489, 1899 (ADS entry)

Rakshit, S., Stalin, C. S., & Kotilainen, J. 2020, ApJS, 249, 17 (ADS entry)

Rankine, A. L., Hewett, P. C., Banerji, M., & Richards, G. T. 2020, MNRAS, 492, 4553 (ADS entry)

Reed, S. L., et al. 2017, MNRAS, 468, 4702 (ADS entry)

—. 2019, MNRAS, 487, 1874 (ADS entry)

Rees, M. J. 1984, ARA&A, 22, 471 (ADS entry)

Rees, M. J., Netzer, H., & Ferland, G. J. 1989, ApJ, 347, 640 (ADS entry)

Regan, J. A., Downes, T. P., Volonteri, M., Beckmann, R., Lupi, A., Trebitsch, M., & Dubois, Y. 2019, MNRAS, 486, 3892 (ADS entry)

Regan, J. A., & Haehnelt, M. G. 2009, MNRAS, 396, 343 (ADS entry)

Reichard, T. A., et al. 2003, AJ, 126, 2594 (ADS entry)

Reines, A. E., & Volonteri, M. 2015, ApJ, 813, 82 (ADS entry)

Reitze, D., et al. 2019, in Bulletin of the American Astronomical Society, Vol. 51, 35 (ADS entry)

Reynolds, C. S. 2014, Space Sci. Rev., 183, 277 (ADS entry)

—. 2019, Nature Astronomy, 3, 41 (ADS entry)

—. 2021, ARA&A, 59, 117 (ADS entry)

Reynolds, C. S., & Fabian, A. C. 2008, ApJ, 675, 1048 (ADS entry)

Richards, G. T., Vanden Berk, D. E., Reichard, T. A., Hall, P. B., Schneider, D. P., SubbaRao, M., Thakar, A. R., & York, D. G. 2002, AJ, 124, 1 (ADS entry)

Richards, G. T., et al. 2003, AJ, 126, 1131 (ADS entry)

—. 2006, ApJS, 166, 470 (ADS entry)

—. 2011, AJ, 141, 167 (ADS entry)

Richstone, D. O., & Schmidt, M. 1980, ApJ, 235, 361 (ADS entry)

Robertson, B. E., Ellis, R. S., Furlanetto, S. R., & Dunlop, J. S. 2015, ApJ, 802, L19 (ADS entry)

Rodrigo, C., & Solano, E. 2020, in XIV.0 Scientific Meeting (virtual) of the Spanish Astronomical Society, 182 (ADS entry)

Rokaki, E., Boisson, C., & Collin-Souffrin, S. 1992, A&A, 253, 57 (ADS entry)

Romano, D., Silva, L., Matteucci, F., & Danese, L. 2002, MNRAS, 334, 444 (ADS entry)

Rose, M., Elvis, M., & Tadhunter, C. N. 2015, MNRAS, 448, 2900 (ADS entry)

Runnoe, J. C., Brotherton, M. S., DiPompeo, M. A., & Shang, Z. 2014, MNRAS, 438, 3263 (ADS entry)

Runnoe, J. C., Brotherton, M. S., & Shang, Z. 2012, MNRAS, 427, 1800 (ADS entry)

Runnoe, J. C., Brotherton, M. S., Shang, Z., Wills, B. J., & DiPompeo, M. A. 2013, MNRAS, 429, 135 (ADS entry)

Sadowski, A. 2011, arXiv e-prints, arXiv:1108.0396 (ADS entry)

Sadowski, A., Narayan, R., Tchekhovskoy, A., & Zhu, Y. 2013, MNRAS, 429, 3533 (ADS entry)

Salpeter, E. E. 1964, ApJ, 140, 796 (ADS entry)

Salviander, S., & Shields, G. A. 2013, ApJ, 764, 80 (ADS entry)

Salviander, S., Shields, G. A., Gebhardt, K., & Bonning, E. W. 2007, ApJ, 662, 131 (ADS entry)

Sameshima, H., Yoshii, Y., & Kawara, K. 2017, ApJ, 834, 203 (ADS entry)

Sánchez-Ramírez, R., et al. 2016, MNRAS, 456, 4488 (ADS entry)

Sandage, A. 1962, ApJ, 136, 319 (ADS entry)

Sanders, R. L., et al. 2021, ApJ, 914, 19 (ADS entry)

Santos, M., et al. 2016, in MeerKAT Science: On the Pathway to the SKA, 32 (ADS entry)

Santos, S., et al. 2021, MNRAS, 505, 1117 (ADS entry)

Sato, S., et al. 2017, in Journal of Physics Conference Series, Vol. 840, Journal of Physics Conference Series, 012010 (ADS entry)

Saturni, F. G., et al. 2018, A&A, 617, A118 (ADS entry)

Satyavolu, S., Kulkarni, G., Keating, L. C., & Haehnelt, M. G. 2023a, MNRAS, 521, 3108 (ADS entry)

Satyavolu, S., et al. 2023b, MNRAS, 522, 4918 (ADS entry)

Savić, D., Goosmann, R., Popović, L. Č., Marin, F., & Afanasiev, V. L. 2018, A&A, 614, A120 (ADS entry)

Savić, D. V., Popović, L. Č., & Shablovinskaya, E. 2021, ApJ, 921, L21 (ADS entry)

Schawinski, K., Koss, M., Berney, S., & Sartori, L. F. 2015, MNRAS, 451, 2517 (ADS entry)

Schindler, J.-T., Fan, X., McGreer, I. D., Yang, Q., Wu, J., Jiang, L., & Green, R. 2017, ApJ, 851, 13 (ADS entry)

Schindler, J.-T., et al. 2019a, ApJS, 243, 5 (ADS entry)

—. 2019b, ApJ, 871, 258 (ADS entry)

—. 2020, ApJ, 905, 51 (ADS entry)

—. 2023, ApJ, 943, 67 (ADS entry)

Schlafly, E. F., & Finkbeiner, D. P. 2011, ApJ, 737, 103 (ADS entry)

Schlafly, E. F., Finkbeiner, D. P., Schlegel, D. J., Jurić, M., Ivezić, Ž., Gibson, R. R., Knapp, G. R., & Weaver, B. A. 2010, ApJ, 725, 1175 (ADS entry)

Schlegel, D. J., Finkbeiner, D. P., & Davis, M. 1998, ApJ, 500, 525 (ADS entry)

Schmidt, G. D., & Miller, J. S. 1980, ApJ, 240, 759 (ADS entry)

Schmidt, M. 1963, Nature, 197, 1040 (ADS entry)

—. 1965, ApJ, 141, 1295 (ADS entry)

—. 1968, ApJ, 151, 393 (ADS entry)

Schmidt, M., Schneider, D. P., & Gunn, J. E. 1995, AJ, 110, 68 (ADS entry)

Schneider, D. P., et al. 2010, AJ, 139, 2360 (ADS entry)

Schulze, A., et al. 2015, MNRAS, 447, 2085 (ADS entry)

Scott, J. E., Kriss, G. A., Brotherton, M., Green, R. F., Hutchings, J., Shull, J. M., & Zheng, W. 2004, ApJ, 615, 135 (ADS entry)

Selsing, J., Fynbo, J. P. U., Christensen, L., & Krogager, J. K. 2016, A&A, 585, A87 (ADS entry)

Seth, A., Agüeros, M., Lee, D., & Basu-Zych, A. 2008, ApJ, 678, 116 (ADS entry)

Sexton, R. O., Matzko, W., Darden, N., Canalizo, G., & Gorjian, V. 2021, MNRAS, 500, 2871 (ADS entry)

Seyfert, C. K. 1943, ApJ, 97, 28 (ADS entry)

Shakura, N. I., & Sunyaev, R. A. 1973, A&A, 24, 337 (ADS entry)

Shang, Z., et al. 2011, ApJS, 196, 2 (ADS entry)

Shankar, F., Crocce, M., Miralda-Escudé, J., Fosalba, P., & Weinberg, D. H. 2010, ApJ, 718, 231 (ADS entry)

Shankar, F., Weinberg, D. H., & Miralda-Escudé, J. 2009, ApJ, 690, 20 (ADS entry)

—. 2013, MNRAS, 428, 421 (ADS entry)

Shen, Y. 2013, Bulletin of the Astronomical Society of India, 41, 61 (ADS entry)

Shen, Y., Greene, J. E., Strauss, M. A., Richards, G. T., & Schneider, D. P. 2008, ApJ, 680, 169 (ADS entry)

Shen, Y., & Ho, L. C. 2014, Nature, 513, 210 (ADS entry)

Shen, Y., & Kelly, B. C. 2012, ApJ, 746, 169 (ADS entry)

Shen, Y., & Liu, X. 2012, ApJ, 753, 125 (ADS entry)

Shen, Y., et al. 2007, AJ, 133, 2222 (ADS entry)

—. 2009, ApJ, 697, 1656 (ADS entry)

—. 2011, ApJS, 194, 45 (ADS entry)

—. 2016, ApJ, 831, 7 (ADS entry)

—. 2019a, ApJ, 873, 35 (ADS entry)

—. 2019b, ApJ, 883, L14 (ADS entry)

Shibata, M., Sekiguchi, Y., Uchida, H., & Umeda, H. 2016, Phys. Rev. D, 94, 021501 (ADS entry)

Shields, G. A. 1976, ApJ, 204, 330 (ADS entry)

—. 1978, Nature, 272, 706 (ADS entry)

—. 1996, ApJ, 461, L9 (ADS entry)

—. 1999, PASP, 111, 661 (ADS entry)

Shimura, T., & Takahara, F. 1993, ApJ, 419, 78 (ADS entry)

—. 1995, ApJ, 445, 780 (ADS entry)

Shin, J., Nagao, T., & Woo, J.-H. 2017, ApJ, 835, 24 (ADS entry)

Shin, J., Nagao, T., Woo, J.-H., & Le, H. A. N. 2019, ApJ, 874, 22 (ADS entry)

Shirakata, H., Kawaguchi, T., Oogi, T., Okamoto, T., & Nagashima, M. 2019, MNRAS, 487, 409 (ADS entry)

Shu, Y., Koposov, S. E., Evans, N. W., Belokurov, V., McMahon, R. G., Auger, M. W., & Lemon, C. A. 2019, MNRAS, 489, 4741 (ADS entry)

Sijacki, D., Springel, V., & Haehnelt, M. G. 2009, MNRAS, 400, 100 (ADS entry)

Sijacki, D., Vogelsberger, M., Genel, S., Springel, V., Torrey, P., Snyder, G. F., Nelson, D., & Hernquist, L. 2015, MNRAS, 452, 575 (ADS entry)

Skrutskie, M. F., et al. 2006, AJ, 131, 1163 (ADS entry)

Slipher, V. M. 1917, Lowell Observatory Bulletin, 3, 59 (ADS entry)

Sluse, D., et al. 2011, A&A, 528, A100 (ADS entry)

Small, T. A., & Blandford, R. D. 1992, MNRAS, 259, 725 (ADS entry)

Smethurst, R. J., et al. 2023, MNRAS(ADS entry)

Smidt, J., Whalen, D. J., Johnson, J. L., Surace, M., & Li, H. 2018, ApJ, 865, 126 (ADS entry)

Soltan, A. 1982, MNRAS, 200, 115 (ADS entry)

Songaila, A., & Cowie, L. L. 2002, AJ, 123, 2183 (ADS entry)

Starling, R. L. C., Siemiginowska, A., Uttley, P., & Soria, R. 2004, MNRAS, 347, 67 (ADS entry)

Steffen, A. T., Strateva, I., Brandt, W. N., Alexander, D. M., Koekemoer, A. M., Lehmer, B. D., Schneider, D. P., & Vignali, C. 2006, AJ, 131, 2826 (ADS entry)

Steinhardt, C. L., & Elvis, M. 2010, MNRAS, 406, L1 (ADS entry)

Stone, J. M., Gardiner, T. A., Teuben, P., Hawley, J. F., & Simon, J. B. 2008, ApJS, 178, 137 (ADS entry)

Stone, Z., et al. 2022, MNRAS, 514, 164 (ADS entry)

Storey-Fisher, K., Hogg, D. W., Rix, H.-W., Eilers, A.-C., Fabbian, G., Blanton, M., & Alonso, D. 2023, arXiv e-prints, arXiv:2306.17749 (ADS entry)

Straub, O., et al. 2011, A&A, 533, A67 (ADS entry)

Suberlak, K. L., Ivezić, Ž., & MacLeod, C. 2021, ApJ, 907, 96 (ADS entry)

Suganuma, M., et al. 2006, ApJ, 639, 46 (ADS entry)

Sulentic, J. W., Bachev, R., Marziani, P., Negrete, C. A., & Dultzin, D. 2007, ApJ, 666, 757 (ADS entry)

Sulentic, J. W., Marziani, P., & Dultzin-Hacyan, D. 2000, ARA&A, 38, 521 (ADS entry)

Sun, W.-H., & Malkan, M. A. 1989, ApJ, 346, 68 (ADS entry)

Tang, J.-J., Wolf, C., & Tonry, J. 2023a, Nature Astronomy, 7, 473 (ADS entry)

Tang, J.-J., Wolf, C., Tonry, J., Lai, S., Yong, S. Y., & Steyn, Z. 2023b, MNRAS, 523, 4441 (ADS entry)

Tang, J.-J., et al. 2019, MNRAS, 484, 2575 (ADS entry)

Targett, T. A., Dunlop, J. S., & McLure, R. J. 2012, MNRAS, 420, 3621 (ADS entry)

Telfer, R. C., Zheng, W., Kriss, G. A., & Davidsen, A. F. 2002, ApJ, 565, 773 (ADS entry)

Temple, M. J., Banerji, M., Hewett, P. C., Rankine, A. L., & Richards, G. T. 2021a, MNRAS, 501, 3061 (ADS entry)

Temple, M. J., Ferland, G. J., Rankine, A. L., Chatzikos, M., & Hewett, P. C. 2021b, MNRAS, 505, 3247 (ADS entry)

Temple, M. J., Hewett, P. C., & Banerji, M. 2021c, MNRAS, 508, 737 (ADS entry)

Terrazas, B. A., et al. 2020, MNRAS, 493, 1888 (ADS entry)

The Lynx Team. 2018, arXiv e-prints, arXiv:1809.09642 (ADS entry)

Thorne, K. S. 1974, ApJ, 191, 507 (ADS entry)

Tinsley, B. M. 1980, Fundamentals Cosmic Phys., 5, 287 (ADS entry)

Tonry, J. L., et al. 2018, PASP, 130, 064505 (ADS entry)

Toyouchi, D., Inayoshi, K., Ishigaki, M. N., & Tominaga, N. 2022, MNRAS, 512, 2573 (ADS entry)

Trakhtenbrot, B. 2014, ApJ, 789, L9 (ADS entry)

Trakhtenbrot, B., & Netzer, H. 2012, MNRAS, 427, 3081 (ADS entry)

Trakhtenbrot, B., Netzer, H., Lira, P., & Shemmer, O. 2011, ApJ, 730, 7 (ADS entry)

Trakhtenbrot, B., Volonteri, M., & Natarajan, P. 2017, ApJ, 836, L1 (ADS entry)

Tremaine, S., et al. 2002, ApJ, 574, 740 (ADS entry)

Tripp, T. M., Bechtold, J., & Green, R. F. 1994, ApJ, 433, 533 (ADS entry)

Tsuzuki, Y., Kawara, K., Yoshii, Y., Oyabu, S., Tanabé, T., & Matsuoka, Y. 2006, ApJ, 650, 57 (ADS entry)

Tucci, M., & Volonteri, M. 2017, A&A, 600, A64 (ADS entry)

Ueda, Y., Akiyama, M., Hasinger, G., Miyaji, T., & Watson, M. G. 2014, ApJ, 786, 104 (ADS entry)

Ueda, Y., Akiyama, M., Ohta, K., & Miyaji, T. 2003, ApJ, 598, 886 (ADS entry)

Urry, C. M., & Padovani, P. 1995, PASP, 107, 803 (ADS entry)

Vacca, W. D., Cushing, M. C., & Rayner, J. T. 2003, PASP, 115, 389 (ADS entry)

Valentini, M., Gallerani, S., & Ferrara, A. 2021, MNRAS, 507, 1 (ADS entry)

Valiante, R., Schneider, R., Volonteri, M., & Omukai, K. 2016, MNRAS, 457, 3356 (ADS entry)

van der Walt, S., Colbert, S. C., & Varoquaux, G. 2011, Computing in Science and Engineering, 13, 22 (ADS entry)

Vanden Berk, D. E., et al. 2001, AJ, 122, 549 (ADS entry)

—. 2004, ApJ, 601, 692 (ADS entry)

Vasudevan, R. V., & Fabian, A. C. 2007, MNRAS, 381, 1235 (ADS entry)

—. 2009, MNRAS, 392, 1124 (ADS entry)

Vasudevan, R. V., Fabian, A. C., Reynolds, C. S., Aird, J., Dauser, T., & Gallo, L. C. 2016, MNRAS, 458, 2012 (ADS entry)

Venemans, B. P., et al. 2017, ApJ, 851, L8 (ADS entry)

Vernet, J., et al. 2011, A&A, 536, A105 (ADS entry)

Vestergaard, M. 2002, ApJ, 571, 733 (ADS entry)

Vestergaard, M., & Osmer, P. S. 2009, ApJ, 699, 800 (ADS entry)

Vestergaard, M., & Peterson, B. M. 2006, ApJ, 641, 689 (ADS entry)

Vestergaard, M., & Wilkes, B. J. 2001, ApJS, 134, 1 (ADS entry)

Vietri, G., et al. 2018, A&A, 617, A81 (ADS entry)

Vijarnwannaluk, B., et al. 2022, ApJ, 941, 97 (ADS entry)

Virtanen, P., et al. 2020, Nature Methods, 17, 261 (ADS entry)

Volonteri, M., & Bellovary, J. 2012, Reports on Progress in Physics, 75, 124901 (ADS entry)

Volonteri, M., Dubois, Y., Pichon, C., & Devriendt, J. 2016, MNRAS, 460, 2979 (ADS entry)

Volonteri, M., Haardt, F., & Madau, P. 2003, ApJ, 582, 559 (ADS entry)

Volonteri, M., Habouzit, M., & Colpi, M. 2021, Nature Reviews Physics, 3, 732 (ADS entry)

Volonteri, M., Madau, P., Quataert, E., & Rees, M. J. 2005, ApJ, 620, 69 (ADS entry)

Volonteri, M., Sikora, M., Lasota, J. P., & Merloni, A. 2013, ApJ, 775, 94 (ADS entry)

Walter, F., et al. 2003, Nature, 424, 406 (ADS entry)

Walton, D. J., Nardini, E., Fabian, A. C., Gallo, L. C., & Reis, R. C. 2013, MNRAS, 428, 2901 (ADS entry)

Wandel, A., Peterson, B. M., & Malkan, M. A. 1999, ApJ, 526, 579 (ADS entry)

Wandel, A., & Petrosian, V. 1988, ApJ, 329, L11 (ADS entry)

Wang, F., et al. 2018, ApJ, 869, L9 (ADS entry)

—. 2019, ApJ, 884, 30 (ADS entry)

—. 2021, ApJ, 907, L1 (ADS entry)

Wang, H., Zhou, H., Yuan, W., & Wang, T. 2012, ApJ, 751, L23 (ADS entry)

Wang, J.-G., et al. 2009, ApJ, 707, 1334 (ADS entry)

Wang, S., et al. 2020, ApJ, 903, 51 (ADS entry)

—. 2022, ApJ, 925, 121 (ADS entry)

Warren, S. J., Hewett, P. C., Irwin, M. J., McMahon, R. G., & Bridgeland, M. T. 1987, Nature, 325, 131 (ADS entry)

Waskom, M. L. 2021, Journal of Open Source Software, 6, 3021 (Link)

Watarai, K.-y., Fukue, J., Takeuchi, M., & Mineshige, S. 2000, PASJ, 52, 133 (ADS entry)

Webster, R. L., Francis, P. J., Petersont, B. A., Drinkwater, M. J., & Masci, F. J. 1995, Nature, 375, 469 (ADS entry)

Weisskopf, M. C., Tananbaum, H. D., Van Speybroeck, L. P., & O'Dell, S. L. 2000, in Society of Photo-Optical Instrumentation Engineers (SPIE) Conference Series, Vol. 4012, X-Ray Optics, Instruments, and Missions III, ed. J. E. Truemper & B. Aschenbach, 2–16 (ADS entry)

Weltman, A., et al. 2020, Publ. Astron. Soc. Australia, 37, e002 (ADS entry)

Wenzl, L., et al. 2021, AJ, 162, 72 (ADS entry)

White, M., Martini, P., & Cohn, J. D. 2008, MNRAS, 390, 1179 (ADS entry)

Wielgus, M., et al. 2022, MNRAS, 514, 780 (ADS entry)

Wilkes, B. J. 1984, MNRAS, 207, 73 (ADS entry)

Williams, P. R., et al. 2020, ApJ, 902, 74 (ADS entry)

Willott, C. J., Rawlings, S., Blundell, K. M., & Lacy, M. 2000, MNRAS, 316, 449 (ADS entry)

Willott, C. J., et al. 2010a, AJ, 140, 546 (ADS entry)

—. 2010b, AJ, 139, 906 (ADS entry)

Wills, B. J., & Browne, I. W. A. 1986, ApJ, 302, 56 (ADS entry)

Wills, B. J., Netzer, H., & Wills, D. 1985, ApJ, 288, 94 (ADS entry)

Wilson, J. C., et al. 2004a, in Society of Photo-Optical Instrumentation Engineers (SPIE) Conference Series, Vol. 5492, Ground-based Instrumentation for Astronomy, ed. A. F. M. Moorwood & M. Iye, 1295–1305 (ADS entry)

Wilson, J. C., et al. 2004b, in Society of Photo-Optical Instrumentation Engineers (SPIE) Conference Series, Vol. 5492, Ground-based Instrumentation for Astronomy, ed. A. F. M. Moorwood & M. Iye, 1295–1305 (ADS entry)

Wise, J. H., Turk, M. J., & Abel, T. 2008, ApJ, 682, 745 (ADS entry)

Wolf, C., Bian, F., Onken, C. A., Schmidt, B. P., Tisserand, P., Alonzi, N., Hon, W. J., & Tonry, J. L. 2018a, Publ. Astron. Soc. Australia, 35, e024 (ADS entry)

Wolf, C., Lai, S., Onken, C. A., Amrutha, N., Bian, F., Hon, W. J., Tisserand, P., & Webster, R. L. accepted, Nature Astronomy

Wolf, C., Meisenheimer, K., Rix, H. W., Borch, A., Dye, S., & Kleinheinrich, M. 2003a, A&A, 401, 73 (ADS entry)

Wolf, C., Wisotzki, L., Borch, A., Dye, S., Kleinheinrich, M., & Meisenheimer, K. 2003b, A&A, 408, 499 (ADS entry)

Wolf, C., et al. 2018b, Publ. Astron. Soc. Australia, 35, e010 (ADS entry)

—. 2020, MNRAS, 491, 1970 (ADS entry)

Wolfe, A. M., Gawiser, E., & Prochaska, J. X. 2005, ARA&A, 43, 861 (ADS entry)

Woo, J.-H., Le, H. A. N., Karouzos, M., Park, D., Park, D., Malkan, M. A., Treu, T., & Bennert, V. N. 2018, ApJ, 859, 138 (ADS entry)

Woo, J.-H., Yoon, Y., Park, S., Park, D., & Kim, S. C. 2015, ApJ, 801, 38 (ADS entry)

Woo, J.-H., et al. 2010, ApJ, 716, 269 (ADS entry)

Woosley, S. E., & Hoffman, R. D. 1992, ApJ, 395, 202 (ADS entry)

Wright, E. L., et al. 2010, AJ, 140, 1868 (ADS entry)

Wu, J., et al. 2022, MNRAS, 517, 2659 (ADS entry)

Wu, Q., & Shen, Y. 2022, ApJS, 263, 42 (ADS entry)

Wu, X.-B., et al. 2015, Nature, 518, 512 (ADS entry)

Wyithe, J. S. B., & Loeb, A. 2012, MNRAS, 425, 2892 (ADS entry)

Xu, F., Bian, F., Shen, Y., Zuo, W., Fan, X., & Zhu, Z. 2018, MNRAS, 480, 345 (ADS entry)

XueGuang, Z., YingFei, Z., PeiZhen, C., BaoHan, W., Yi-Li, L., & HaiChao, Y. 2021, ApJ, 922, 248 (ADS entry)

Yang, J., et al. 2016, ApJ, 829, 33 (ADS entry)

—. 2019a, AJ, 157, 236 (ADS entry)

—. 2019b, ApJ, 871, 199 (ADS entry)

—. 2020, ApJ, 897, L14 (ADS entry)

—. 2021, ApJ, 923, 262 (ADS entry)

—. 2023, ApJS, 269, 27 (ADS entry)

Yao, S., et al. 2019, ApJS, 240, 6 (ADS entry)

Yèche, C., Palanque-Delabrouille, N., Baur, J., & du Mas des Bourboux, H. 2017, J. Cosmology Astropart. Phys., 2017, 047 (ADS entry)

Yi, W.-M., et al. 2014, ApJ, 795, L29 (ADS entry)

Yip, C. W., et al. 2004a, AJ, 128, 585 (ADS entry)

—. 2004b, AJ, 128, 2603 (ADS entry)

Yong, S. Y., Webster, R. L., King, A. L., Bate, N. F., Labrie, K., & O'Dowd, M. J. 2020, MNRAS, 491, 1320 (ADS entry)

Yong, S. Y., Webster, R. L., King, A. L., Bate, N. F., O'Dowd, M. J., & Labrie, K. 2017, Publ. Astron. Soc. Australia, 34, e042 (ADS entry)

Yoon, D., Chatterjee, K., Markoff, S. B., van Eijnatten, D., Younsi, Z., Liska, M., & Tchekhovskoy, A. 2020, MNRAS, 499, 3178 (ADS entry)

York, D. G., et al. 2000, AJ, 120, 1579 (ADS entry)

Yu, L.-M., Bian, W.-H., Wang, C., Zhao, B.-X., & Ge, X. 2019, MNRAS, 488, 1519 (ADS entry)

Yu, Q., & Tremaine, S. 2002, MNRAS, 335, 965 (ADS entry)

Yu, Z., et al. 2023, MNRAS, 522, 4132 (ADS entry)

Zheng, W., Kriss, G. A., Telfer, R. C., Grimes, J. P., & Davidsen, A. F. 1997, ApJ, 475, 469 (ADS entry)

Zhu, Q., Li, Y., Li, Y., Maji, M., Yajima, H., Schneider, R., & Hernquist, L. 2022a, MNRAS, 514, 5583 (ADS entry)

Zhu, Y., et al. 2021, ApJ, 923, 223 (ADS entry)

—. 2022b, ApJ, 932, 76 (ADS entry)

Zu, Y., Kochanek, C. S., Kozłowski, S., & Udalski, A. 2013, ApJ, 765, 106 (ADS entry)

Zubovas, K., & King, A. 2021, MNRAS, 501, 4289 (ADS entry)

Zuo, W., Wu, X.-B., Fan, X., Green, R., Wang, R., & Bian, F. 2015, ApJ, 799, 189 (ADS entry)

Appendix: XQ-100 Black Hole Masses

A.1   Significance of the Balmer Continuum

In Section 2.3.1, we discussed our pseudo-continuum model which includes two components: a power-law and Fe II flux. The Balmer continuum is also often considered as part of a QSO pseudo-continuum model. However, we found that for the sources in our XQ-100 sample, the broad emission-line models are not strongly affected by either the inclusion or exclusion of the Balmer continuum. We refer to similar studies of QSO spectra and use the following model for the Balmer continuum (e.g., Grandi 1982; Dietrich et al. 2002; Wang et al. 2009; Kovačević et al. 2014):

$$F_{\mathrm{Bal}}(\lambda; F_0, T_{\mathrm{e}}, \tau_\lambda) = F_{\mathrm{Bal},0}\, B_\lambda(\lambda, T_{\mathrm{e}})(1 - e^{-\tau_\lambda}); \quad \lambda \leq \lambda_{\mathrm{BE}}, \qquad (A.1)$$

where $F_{\mathrm{Bal},0}$ is the normalisation, $B_\lambda(\lambda, T_{\mathrm{e}})$ is the Planck blackbody with uniform electron temperature T_{e}, and τ_λ is the optical depth. This Balmer continuum is defined at wavelengths shorter than the Balmer edge at rest-frame $\lambda_{\mathrm{BE}} \equiv 3646$ Å. Here, we quantify the difference in our results by including the Balmer continuum in Table A.1, which measures the effect in the resulting Mg II model properties. From the entire sample of 100 QSOs, we quantify the effect in terms of the mean residual and its standard deviation. The change in each line property resulting from pseudocontinuum models with the Balmer continuum is typically no larger than 1%. With reference to the mean uncertainties of the measured emission-line properties in our sample, the inclusion of the Balmer continuum has a statistically insignificant effect on all measured Mg II line properties and there is no observable systematic bias to emission-line models by removing the Balmer continuum from our pseudocontinuum model. However, the absence of the Balmer model can affect the slope of the power-law continuum and amplitude of the Fe II models.

Table A.1: Mean difference and standard deviation in the measured line properties of the Mg II line between including and excluding the Balmer continuum flux contribution. Refer to Table 2.2 for a description of each line property. The monochromatic luminosity at 3000Å, L_{3000}, has units of erg s^{-1} and is represented on a log-scale as with the integrated line luminosity, iLuminosity. For comparison, we show the mean value measured in the XQ-100 sample for each line property and the mean uncertainty.

Mg II Property	Balmer Residual	Sample Mean
FWHM	54 ± 189	3633 ± 237
Sigma	16 ± 146	2821 ± 286
Blueshift	7 ± 45	-240 ± 99
EW	0.2 ± 1.0	30 ± 2
pWavelength	-0.10 ± 0.58	2803 ± 1
iLuminosity	0.00 ± 0.01	44.78 ± 0.04
L_{3000}	0.00 ± 0.01	46.78 ± 0.01

A.2 Black hole mass comparisons

In this section, we discuss outliers between black hole masses determined from different emission-lines and variations in mass measurements between different assumptions for the Fe II model. Among those with a greater than 0.3 dex difference between the Mg II-based single-epoch virial mass estimate and the averaged mass from all measured emission-lines as flagged by the "Mbh_Flag", we focus on two targets with the highest mass discrepancy that are not flagged by any quality flags, PSS J0121+0347 and BR J0714–6455, with $\log{(M_{mean}/M_{Mg II})} = -0.36$ and 0.31, respectively. As another example, we show SDSSJ1202–0054, which was identified as an outlier in Section 2.5.2 due to greater than 0.5 dex difference between the Hβ and C IV-based black hole masses.

In Figure A.1, we present example emission-line models of C IV and Mg II for the "Mbh_Flag" outliers PSS J0121+0347 and BR J0714–6455. In the case of PSS J0121+0347, the C IV line profile is sharply peaked. As seen from the residual on both sides of the peak, the intrinsic line profile is possibly broader than the model suggests, but complexities of the line near its peak could not be adequately modeled by three Gaussian components. The narrowest C IV component has a FWHM of $\sim$540 km s^{-1}. Although some studies argue in favour of narrow-line subtraction for C IV (Baskin & Laor 2005), we do not make this consideration in this study.

For BR J0714–6455, the C IV line profile may be broadened by non-virial components, as evidenced by the strong asymmetry present in both C IV and the Si IV+O IV complex. The relative velocity shift between the two lines is $\Delta v(\text{C IV} - \text{Mg II}) \sim 3300$ km s^{-1}, which is in the top 10% highest relative velocity shifts measured in

our sample. The mean mass discrepancy and its standard deviation for targets with $\Delta v(\text{C\,IV} - \text{Mg\,II}) > 3000$ km s^{-1} is $\log(\text{M}_{\text{C\,IV}}/\text{M}_{\text{Mg\,II}}) = 0.25 \pm 0.14$. At lower velocity shifts, this discrepancy is $\log(\text{M}_{\text{C\,IV}}/\text{M}_{\text{Mg\,II}}) = 0.01 \pm 0.14$, indicating the potential for outflows to preferentially bias the C\,IV line profile and resulting mass measurements relative to other lines.

In Figure A.2, we present example emission-line models of all three broad lines for SDSSJ1202–0054, one of the outliers identified due to the discrepancy between C\,IV and Hβ-based virial mass estimates, $\log(\text{M}_{\text{C\,IV}}/\text{M}_{\text{H}\beta}) \approx -0.8$. Similar to PSS J0121+0347, the C\,IV line model is sharply peaked with FWHM $\sim$1750 km s^{-1} for the narrowest C\,IV component. However, the Hβ line profile is truncated and its broad component is poorly constrained. For this target, the Mg\,II virial mass estimate is intermediate between the Hβ and C\,IV-based estimates.

From Section 2.3, we discussed how properties of the Mg\,II and Hβ emission-line models are sensitive to the choice of Fe\,II template. In this study, our reported line properties are averaged over measurements based on applying spectral decomposition with four different UV and optical Fe\,II templates. However, we note that one should always be careful about systematic effects introduced by the choice of templates, particularly if the template is different from the one used in the virial mass calibration (e.g., Woo et al. 2018; Schindler et al. 2020). For instance, Mg\,II line models obtained using the VW01 template to model the underlying Fe\,II emission has been shown to be biased towards broader line profiles, resulting in higher black hole mass estimates (e.g., Schindler et al. 2020).

In Figure A.3, we compare black hole mass, $\log(\text{M}_{\text{BH}}/\text{M}_\odot)$, measurement pairs between Mg\,II and Hβ-based single-epoch virial estimates. We split the panels by the Fe\,II template, resulting in a 4×4 grid of panels for the four UV templates and four optical templates, described in Section 2.3.1, used to constrain the pseudo-continuum model in the vicinity of each emission-line. We show the mean residual, $\log(\text{M}_{\text{Mg\,II}}/\text{M}_{\text{H}\beta})$, and its standard deviation on the top left corner of each panel. The majority of single-epoch virial mass calibrations are based on Mg\,II and Hβ emission-line models obtained using the original VW01 and BG92 templates (e.g., McLure & Dunlop 2004; Vestergaard & Peterson 2006), so combination of these two templates may be expected to present the tightest relationship. However, it is not apparent in this comparison that those measurements are more consistent than the results from any other pair of templates. Thus in our study, we report the line properties from averaging measurements of resulting line models based on applying spectral decomposition with each Fe\,II template.

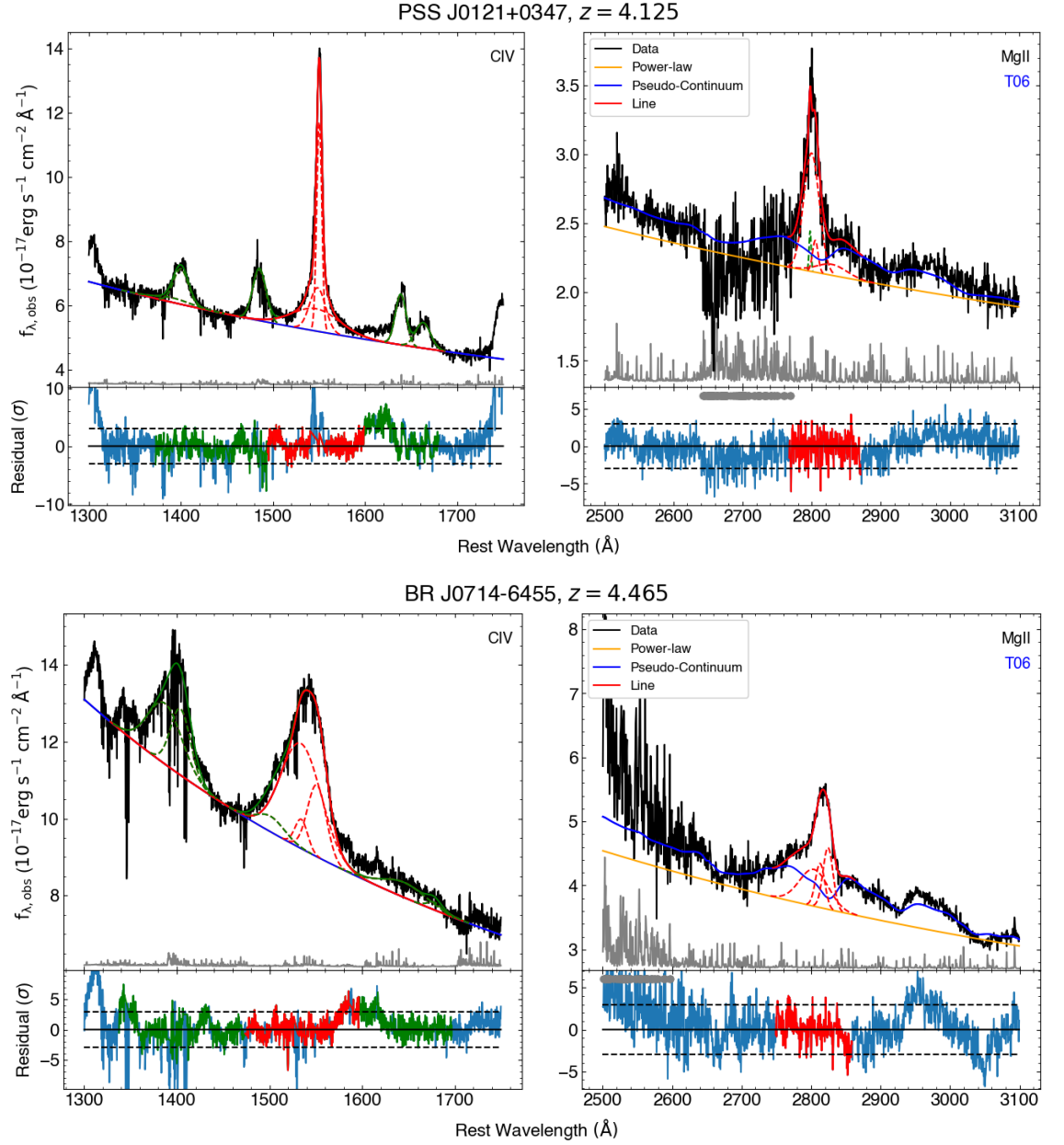In order to examine the black hole mass estimate deviation caused by each individual

Figure A.1: Example models of the C IV and Mg II emission-lines from PSS J0121+0347 and BR J0714–6455, outliers identified by the "Mbh_Flag" which indicates when the Mg II-based virial mass estimate differs from the mean mass estimated from all measured emission-lines by over 0.3 dex. Refer to Figure 2.2 for a description of the plotted elements.
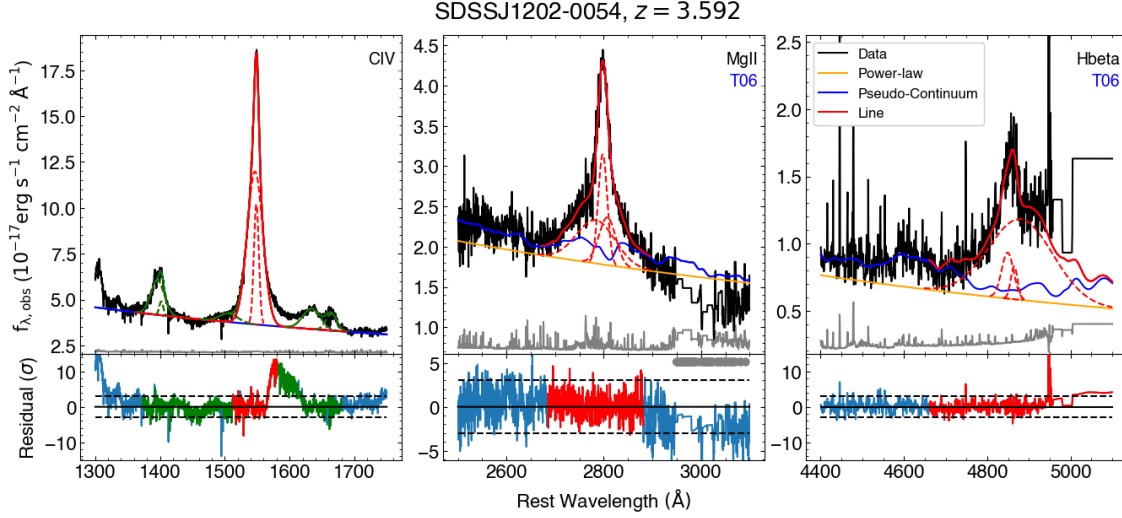
Figure A.2: Example models of the C IV, Mg II, and Hβ emission-lines from SDSSJ1202–0054, an outlier identified by a discrepancy in the C IV and Hβ-based virial mass estimates, $\log\left(M_{C\,IV}/M_{H\beta}\right) \approx -0.8$. Refer to Figure 2.2 for a description of the plotted elements.

Fe II template from the measured average, we present Figures A.4 and A.5, which compare measurements of Hβ and Mg II against their respective mean black hole mass estimates. In each panel, the residual, $\log\left(M_{line}/M_{mean}\right)$, is plotted with its mean shown on the top left along with its standard deviation. From Figure A.4, we observe that all templates of the underlying Fe II emission result in statistically similar black hole mass estimates, albeit with a fairly large scatter in this high-redshift sample due to the lower SNR of the spectrum around Hβ and often truncated line profile. In Figure A.5, we observe the effect seen in Schindler et al. (2020) that the VW01 template tends to result in higher FWHM and overestimated black hole masses compared to other templates. However, at approximately 1σ, we note that the effect is fairly insignificant with respect to the scatter, likely because our VW01 template is a modified version of the original template from Vestergaard & Wilkes (2001), as elaborated upon in Section 2.3.1. With these comparisons, it is reasonable to assume that, at least for black hole mass estimates, all of the Fe II templates tested in this study have similar effects on the resulting line properties and there are minimal observable systematics between them.
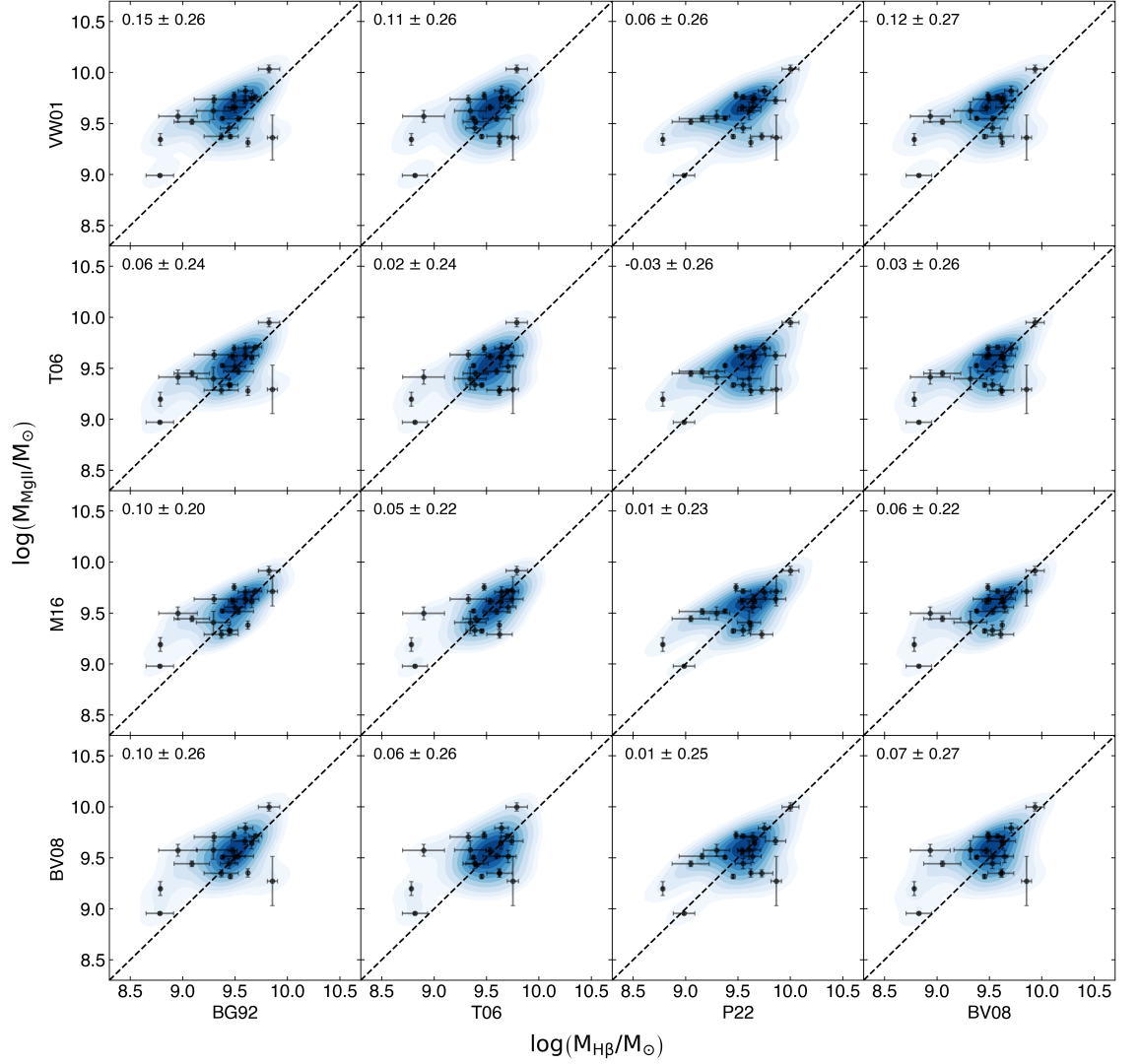
Figure A.3: Black hole mass comparison, $\log\left(M_{BH}/M_\odot\right)$, between different Fe II templates models for both Mg II and Hβ. The top left value displays the mean residual, $\log\left(M_{Mg II}/M_{H\beta}\right)$, and standard deviation between mass measurements. The Fe II templates are labelled along the axes. The blue shaded contours represent the two-dimensional continuous probability density distribution calculated with a kernel density estimator (Waskom 2021). Each subsequent contour level marks density iso-proportions increasing by an additional 10% up to 90% enclosed.
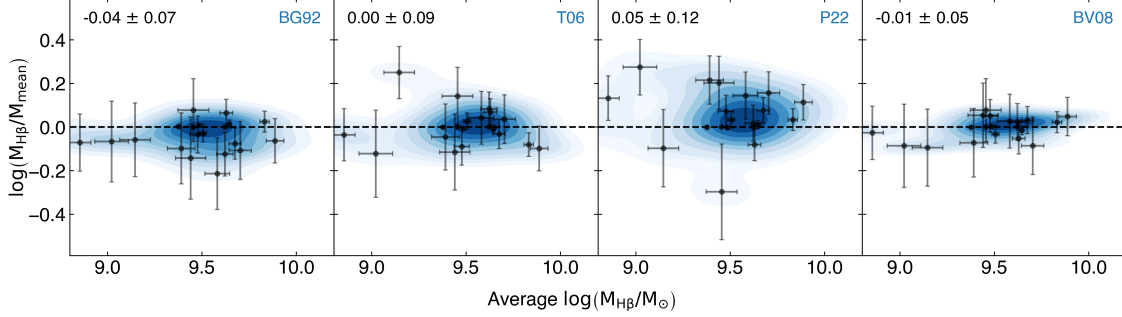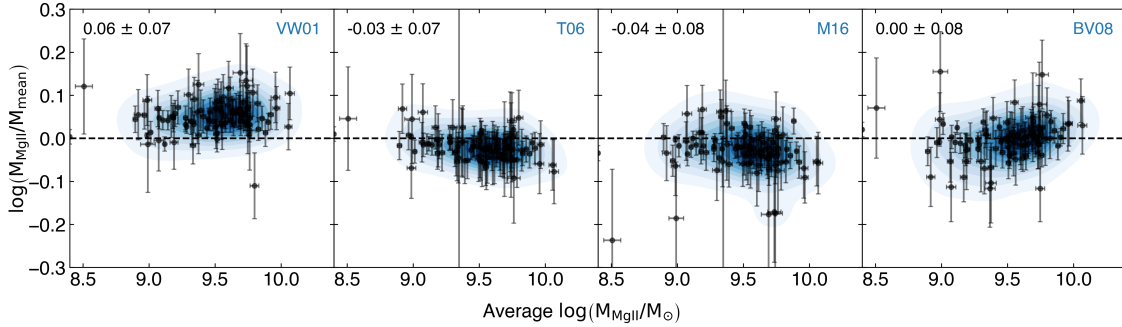
Figure A.4: Black hole mass comparison, $\log(M_{H\beta}/M_{mean})$, between different Fe II templates models for Hβ, compared to the average Hβ-based mass estimate. The top left value displays the mean residual and its standard deviation between mass measurements. The Fe II template is identified in the top-right corner of each panel. The blue shaded contours represent the two-dimensional continuous probability density distribution calculated with a kernel density estimator (Waskom 2021). Each subsequent contour level marks density iso-proportions increasing by an additional 10% up to 90% enclosed.

Figure A.5: Black hole mass comparison, $\log(M_{Mg\,II}/M_{mean})$, between different Fe II templates models for Mg II, compared to the average Mg II-based mass estimate. The top left value displays the mean residual and its standard deviation between mass measurements. The Fe II template is identified in the top-right corner of each panel. The blue shaded contours represent the two-dimensional continuous probability density distribution calculated with a kernel density estimator (Waskom 2021). Each subsequent contour level marks density iso-proportions increasing by an additional 10% up to 90% enclosed.

Appendix: XQz5 Legacy Sample

B.1   Additional Figures

The following Figure B1 presents fits of the pseudo-continuum and Mg II line for all 83 quasars in XQz5. Mg II line models derived using the Tsuzuki et al. (2006) Fe II template are shown, and the remaining diagnostic figures can be located in the GitHub repository. The reported fit parameters include the systematic errors from varying the template. Figure B2 shows the spectrum of SDSS J001115.23+144601.8 at redshift $z = 4.96$ from observed frame $\sim$6000Å–22000Å. The full wavelength coverage of our data extends beyond the plotted region. The underlying spectrum shown in grey is the reduced data which is made available online in the GitHub repository. The coloured spectrum shows the resulting spectrum after the post-processing routine described in Section 3.2.4, which is applied to rest-frame 1050–3600Å. Several prominent broad lines are labeled, and the error spectrum is presented in the bottom of the panel in dark grey. Similar figures are created for all quasars in this sample and are made available in the online repository.
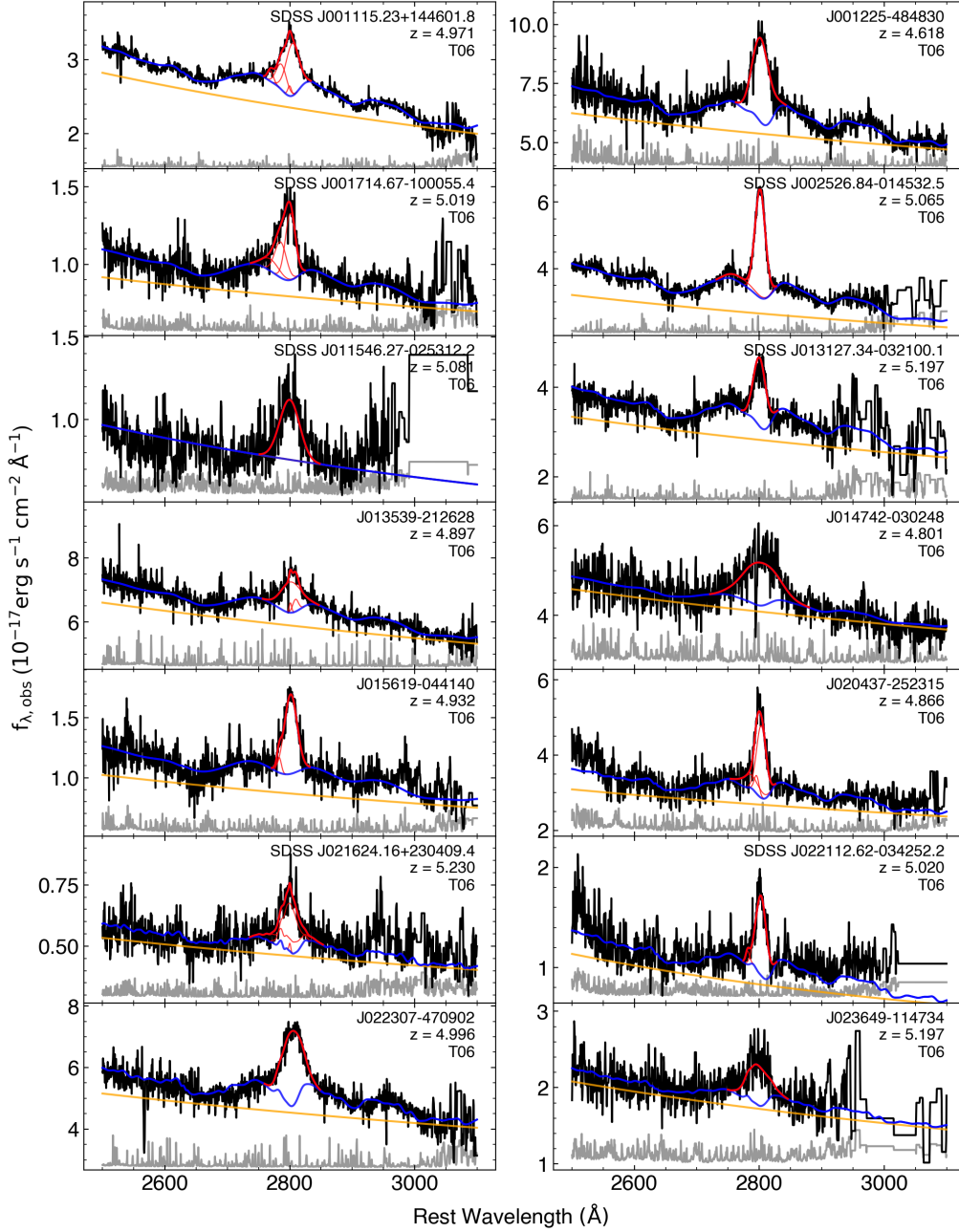
Figure B1: Rest-frame spectra of all ultraluminous quasar sources presented in this study, ordered by increasing right ascension. Within each panel, the data is plotted in black with the best-fit power-law continuum in orange, pseudo-continuum in blue, and Mg II line model in red (with the individual Gaussian components shown as narrower red lines). The error spectrum, presented in grey, is shifted vertically such that the bottom of the panel represents zero flux error. We show an example line model for the Tsuzuki et al. (2006) template with the rest of the line models available as online supplementary material.
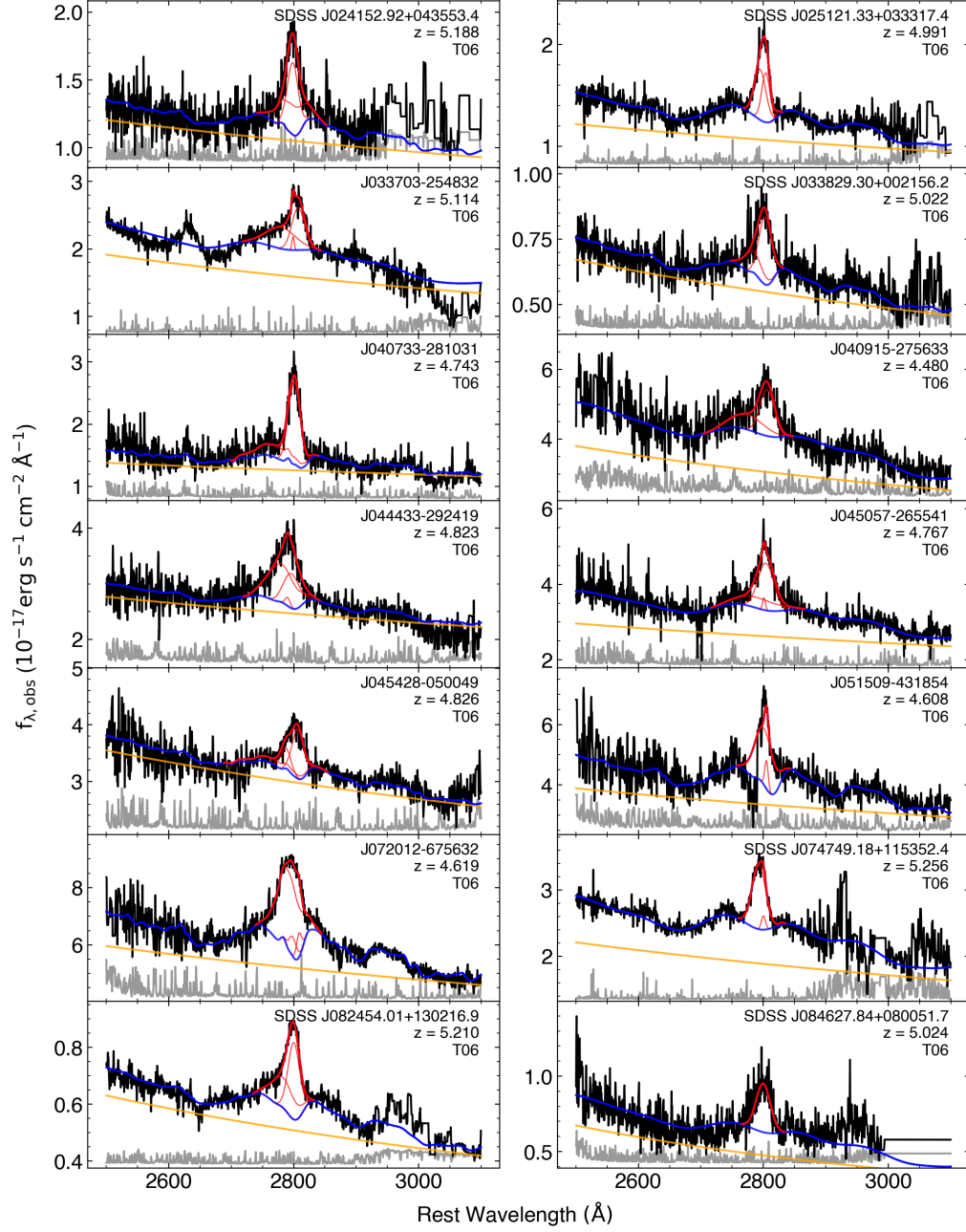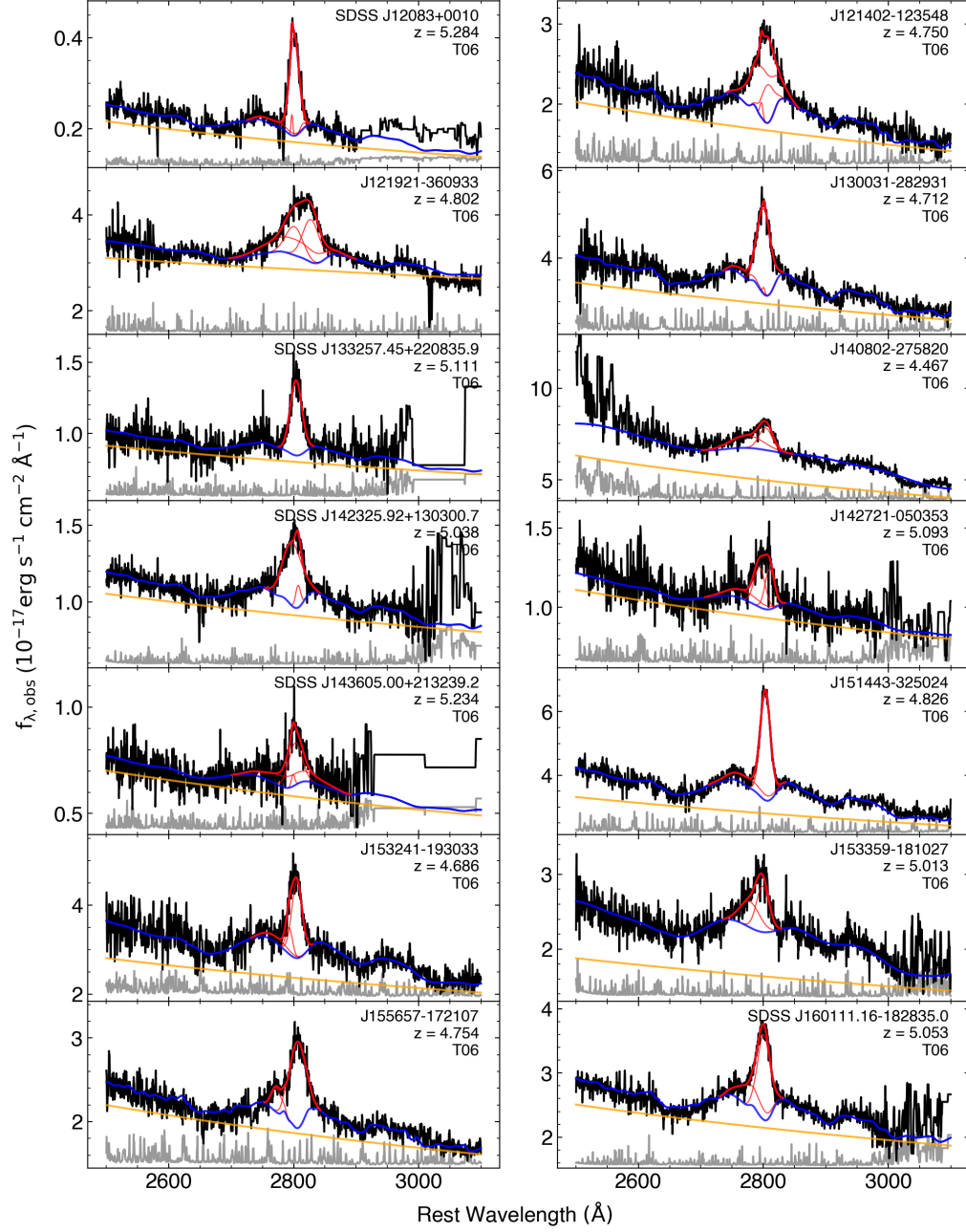
Figure B1: (Continued)
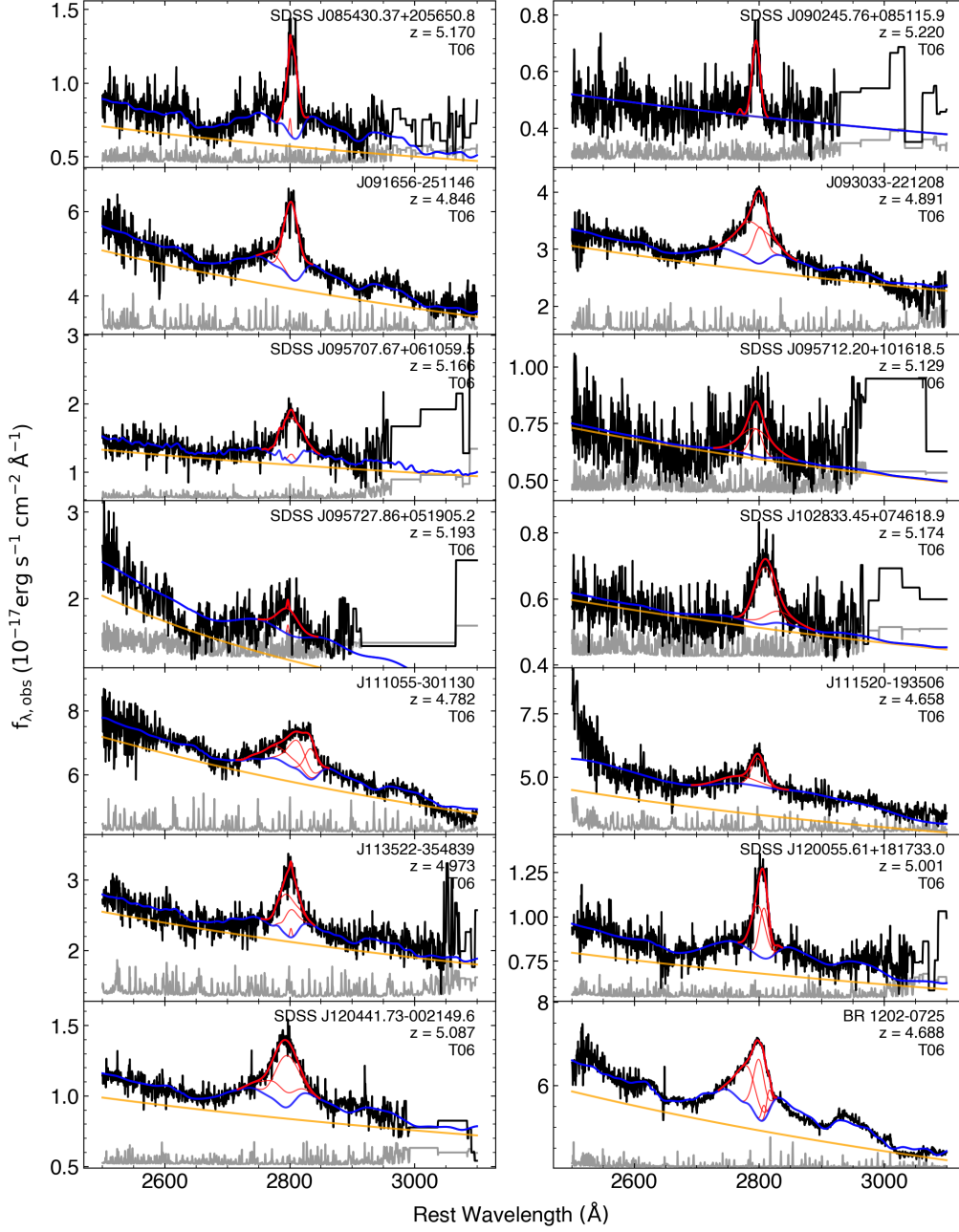
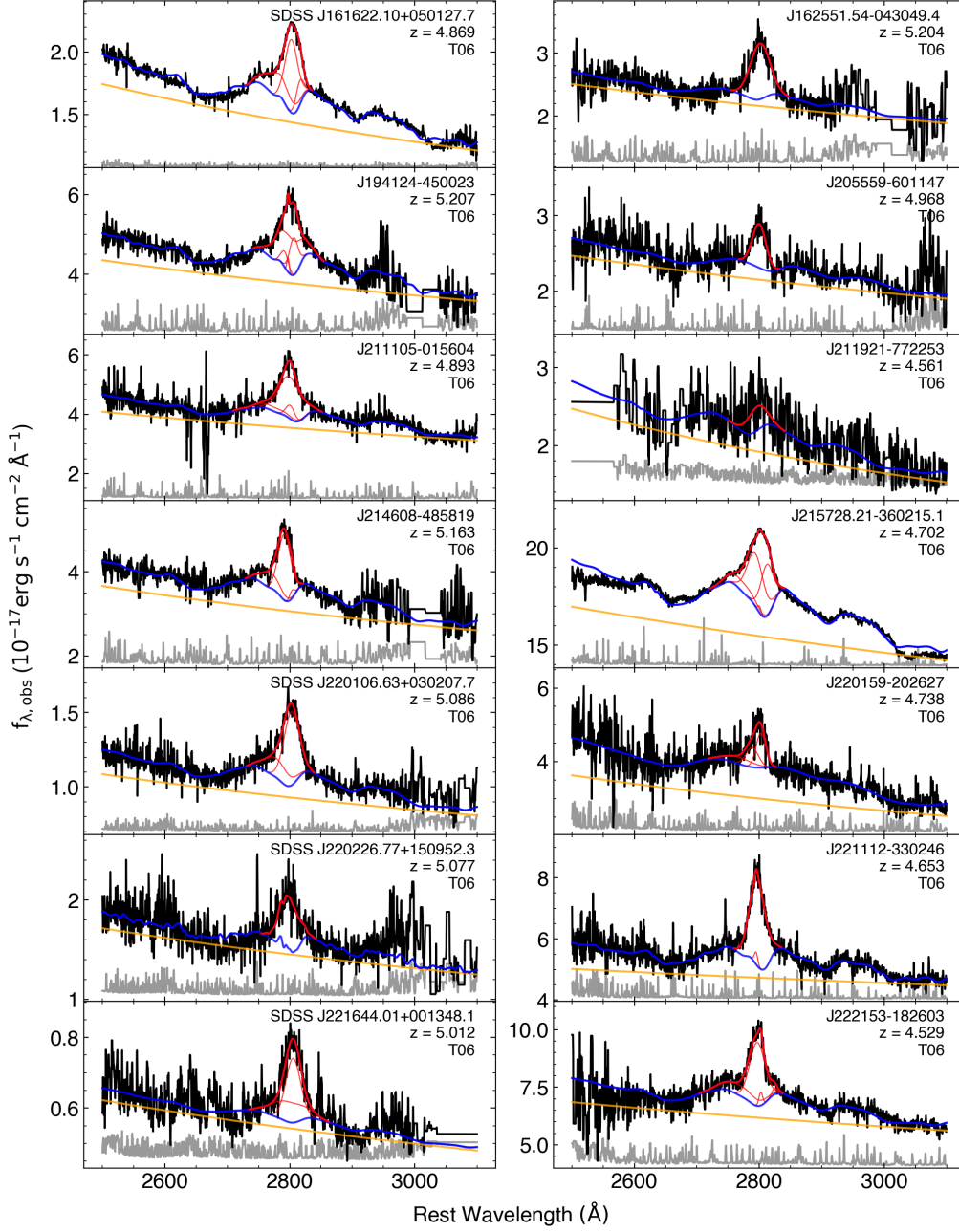Figure B1: (Continued)

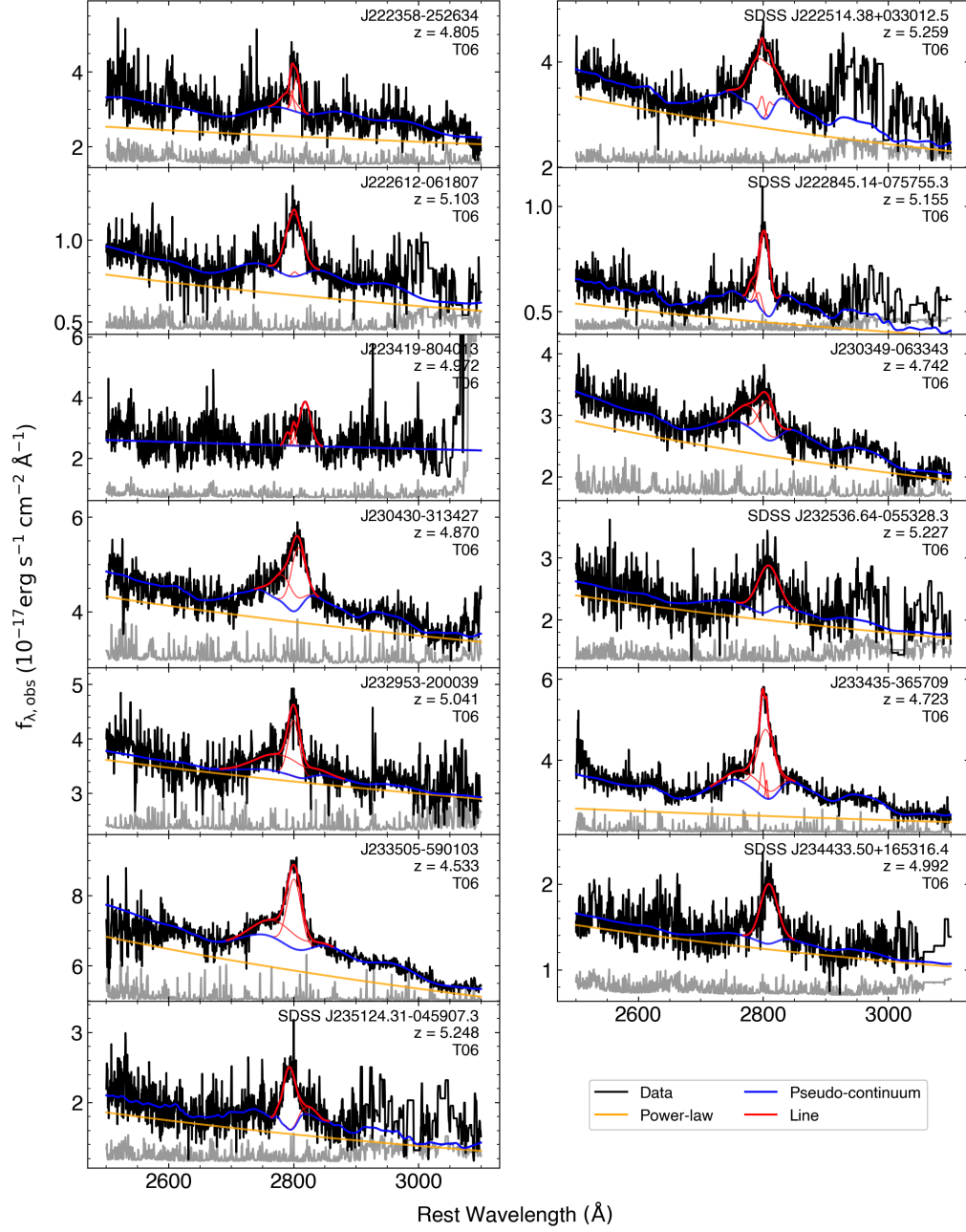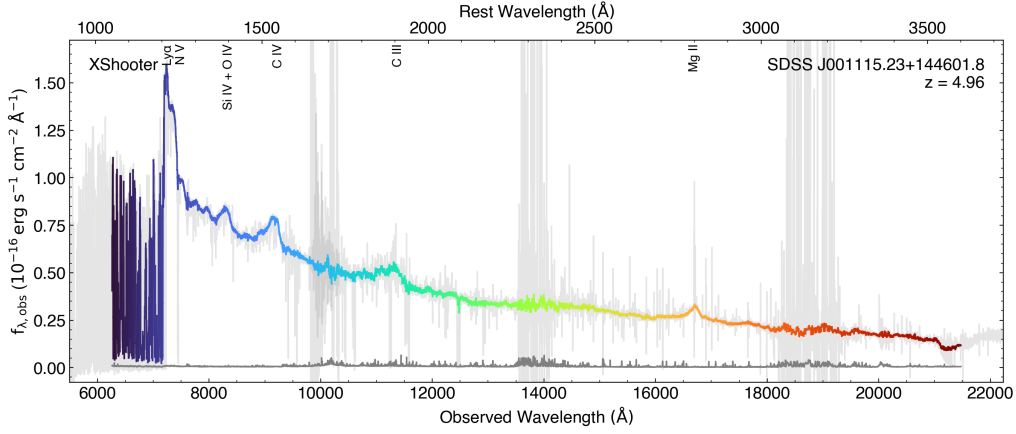Figure B1: (Continued)

Figure B1: (Continued)

Figure B1: (Continued)

Figure B2: Spectrum of SDSS J001115.23+144601.8 at redshift $z = 4.96$ from observed frame $\sim$6000Å–22000Å. The grey data underlying the coloured spectrum show the reduced data that is made available as online supplementary material, while the coloured spectrum shows the resulting data after applying the post-processing steps of Section 3.2.4. The error spectrum is presented in dark grey at the bottom of the panel.

Appendix: XQR-30 Chemical Abundance

C.1 Comparison of emission-line fitting methods

In this study, we use a piece-wise power-law function to fit emission features. This approach to emission-line fitting is different from other widely adopted functions such as multiple Gaussians and modified Lorentzians. Nevertheless, we demonstrate here that the resulting flux ratios are consistent between different emission-line fitting functions. For the comparison, we used the skewed Gaussian distribution because it is an alternative which, like the piece-wise power-law, also fits each emission-line with four free parameters. The probability density function (pdf) of a skewed Gaussian distribution is described by the following formula

$$f(\lambda) = \frac{2}{\omega} F_0 \, \phi\left(\frac{\lambda - \lambda_0}{\omega}\right) \Phi\left(\alpha\left(\frac{\lambda - \lambda_0}{\omega}\right)\right) , \tag{C.1}$$

where $\phi(x)$ is the standard Gaussian pdf,

$$\phi(x) = \frac{1}{\sqrt{2\pi}} e^{-\frac{x^2}{2}} , \tag{C.2}$$

and $\Phi(x)$ is its cumulative distribution function given by,

$$\Phi(x) = \int_{-\infty}^{x} \phi(t) dt , \tag{C.3}$$

and ω controls the scale of the distribution while α determines the skewness. The normalisation, F_0, is proportional to the peak of the emission line at the peak wavelength, λ_0. Analogous to the coupling of power indicies of LIL and HIL lines, we couple the skewness and scale of lines in each category, with the exception of the

parameters of Ly α which can vary independently. The scale of the skewed Gaussian distribution is coupled in velocity space, which preserves the FWHM and kinematic status of line-emitting clouds.

Because of the blended Ly α and N V line profile, and the absence of an analogous approach to coupling the red wing of Ly α to HIL lines with this method, we compare the flux ratio of (Si IV+O IV)/C IV as well as the C IV equivalent width and blueshift. Figure C1 shows a comparison between these quantities, scaled to the maximum value produced by the power-law fitting method. We find no systematic difference with the (Si IV+O IV)/C IV flux ratio, but the C IV equivalent width and blueshift show a slight measurement bias where the piece-wise power-law fit produces larger values ($\sim 1\sigma$) than the skewed Gaussian approach. On average, the scatter in the (Si IV+O IV)/C IV emission-line ratio is 0.7-σ_{SD}, while the scatter in the C IV equivalent width and blueshift are 1.2-σ_{SD} and 1.1-σ_{SD} respectively. In general, the skewed Gaussian approach under-fits the peak of C IV emission lines, especially in the lower C IV blueshift and higher equivalent width regime. This indicates that the skewed Gaussian approach should be used when the C IV emission is more blueshifted, which is the strategy we have adopted in this study.

We also compare our results against a similar study of metallicity at redshift $z \sim 6$ (Wang et al. 2022). Our data overlap consists of 1 quasar (P333+26) out of the 24 considered in this study, for which Wang et al. (2022) does not report measurements for either N V/C IV nor (Si IV+O IV)/C IV. Nevertheless, we obtained 2 of their spectra (J0008-0626 and J1250+3130) from their parent sample, Shen et al. (2019b) which are not used in this study because they are BAL quasars. In Wang et al. (2022), a multiple-Gaussian approach was used for emission-line fitting and each individual quasar spectrum was fit independently. In addition, emission lines were not coupled together into groups of LILs and HILs. Though both spectra were of BAL quasars and despite the different methods used, we find less than 10% difference in N V/C IV and less than 5% difference in (Si IV+O IV)/C IV. These comparisons show that the results and correlations presented in this study can be reproduced with a variety of continuum and line-fitting methods. This gives us confidence that our measurements are robust.

C.2   Additional Tables and Figures

The following section contains additional tables to supplement the main text. Tables C.1, C.2, and C.3 contain information of the line flux ratios from luminosity composites, black hole mass composites, and C IV blueshift composites respectively,
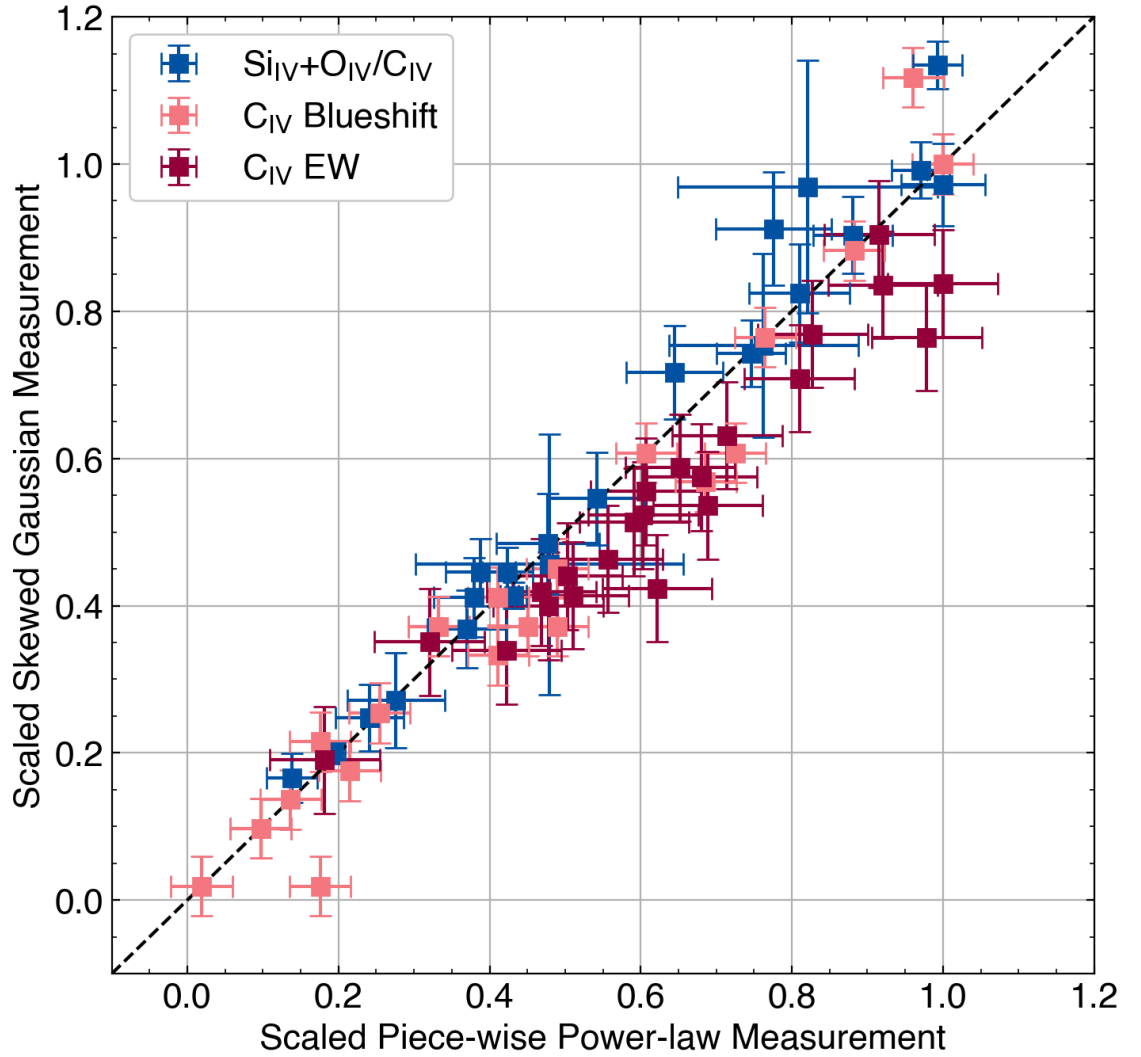
Figure C1: Comparison between measurements obtained with the piece-wise power-law fit and the skewed Gaussian fit. The three quantities plotted are the (Si IV+O IV)/C IV emission-line flux ratio, the C IV blueshift, and the C IV equivalent width. Each of these measurements are scaled to the maximum quantity produced by the piece-wise power-law fitting method. We find no systematic difference with the (Si IV+O IV)/C IV flux ratio, whereas the C IV blueshift and equivalent width show a slight measurement bias where the piece-wise power-law method produces comparatively larger values.

Table C.1: Table of line flux ratios from the bolometric luminosity composites normalised to the flux of the C IV emission line. The uncertainty represents the measurement error of the displayed line, independent of the C IV uncertainty.

Line / $\log\left(L_{bol}/\mathrm{erg\,s^{-1}}\right)$	46.72-46.79	46.79-46.95	46.95-47.17	47.17-47.30	47.30-47.40	47.40-47.70
Ly α	0.62 ± 0.05	0.45 ± 0.08	1.49 ± 0.09	1.86 ± 0.81	1.32 ± 0.07	0.59 ± 0.02
N V	0.91 ± 0.05	1.06 ± 0.12	0.92 ± 0.09	1.01 ± 0.03	0.63 ± 0.04	0.84 ± 0.02
Si II	0.23 ± 0.02	0.48 ± 0.07	0.23 ± 0.02	0.14 ± 0.01	0.07 ± 0.02	0.21 ± 0.01
Si IV	0.07 ± 0.04	0.22 ± 0.13	0.12 ± 0.03	0.28 ± 0.01	0.40 ± 0.02	0.39 ± 0.01
O IV	0.28 ± 0.07	0.23 ± 0.14	0.37 ± 0.04	—	—	—
N IV]	0.09 ± 0.02	—	—	0.04 ± 0.01	—	—
C IV	1.00 ± 0.04	1.00 ± 0.08	1.00 ± 0.02	1.00 ± 0.01	1.00 ± 0.02	1.00 ± 0.01
He II	0.22 ± 0.02	0.24 ± 0.03	0.18 ± 0.01	0.21 ± 0.01	0.18 ± 0.01	0.18 ± 0.00
O III]	—	0.11 ± 0.03	0.00 ± 0.03	0.05 ± 0.04	0.09 ± 0.04	0.06 ± 0.00
Al II	0.16 ± 0.02	0.09 ± 0.03	0.10 ± 0.02	0.06 ± 0.04	0.02 ± 0.04	0.05 ± 0.01
Al III	0.16 ± 0.01	0.12 ± 0.03	0.08 ± 0.01	0.09 ± 0.00	0.09 ± 0.01	0.15 ± 0.00
Si III	0.21 ± 0.01	0.22 ± 0.04	0.12 ± 0.01	0.06 ± 0.02	—	0.18 ± 0.01
C III]	0.29 ± 0.02	0.40 ± 0.03	0.47 ± 0.04	0.53 ± 0.02	0.76 ± 0.03	0.47 ± 0.01

Table C.2: Table of line flux ratios from the black hole mass composites normalised to the flux of the C IV emission line. The uncertainty represents the measurement error of the displayed line, independent of the C IV uncertainty.

Line / $\log(M_{BH}/M_\odot)$	8.40-8.75	8.75-8.87	8.87-8.98	8.98-9.20	9.20-9.40	9.40-9.80
Ly α	1.59 ± 0.26	0.68 ± 0.21	1.58 ± 0.27	1.49 ± 0.21	0.87 ± 0.05	1.10 ± 0.41
N V	0.66 ± 0.17	0.73 ± 0.24	0.98 ± 0.23	0.77 ± 0.10	0.91 ± 0.08	0.78 ± 0.35
Si II	0.36 ± 0.18	0.26 ± 0.16	0.29 ± 0.10	0.15 ± 0.04	0.20 ± 0.04	0.37 ± 0.24
Si IV	0.13 ± 0.13	0.24 ± 0.15	0.25 ± 0.15	0.30 ± 0.05	0.09 ± 0.07	0.35 ± 0.33
O IV	0.12 ± 0.08	0.07 ± 0.11	0.24 ± 0.22	—	0.33 ± 0.13	—
N IV]	0.05 ± 0.05	—	—	—	—	—
C IV	1.00 ± 0.15	1.00 ± 0.23	1.00 ± 0.16	1.00 ± 0.05	1.00 ± 0.07	1.00 ± 0.18
He II	0.10 ± 0.05	0.25 ± 0.08	0.24 ± 0.07	0.17 ± 0.02	0.23 ± 0.03	0.20 ± 0.08
O III]	0.10 ± 0.10	0.03 ± 0.06	0.10 ± 0.07	0.11 ± 0.03	0.09 ± 0.04	0.05 ± 0.07
Al II	0.09 ± 0.11	0.06 ± 0.09	0.03 ± 0.05	0.00 ± 0.02	0.06 ± 0.04	0.15 ± 0.09
Al III	0.12 ± 0.07	0.24 ± 0.09	0.17 ± 0.05	0.11 ± 0.02	0.11 ± 0.02	0.25 ± 0.15
Si III	—	0.17 ± 0.10	0.07 ± 0.10	0.14 ± 0.08	0.21 ± 0.06	0.38 ± 0.31
C III]	0.55 ± 0.20	0.46 ± 0.13	0.60 ± 0.18	0.52 ± 0.12	0.38 ± 0.09	0.51 ± 0.34

each normalised to the flux of the C IV emission line. The error for each line in the tables represents the measurement uncertainty of that line, without propagating the error of the C IV line from the normalisation. Figure C2 presents the line flux ratios of (O III]+Al II)/C IV, Al III/C IV, Si III/C IV, and C III]/C IV as functions of the bolometric luminosity, black hole mass, and C IV blueshift. The online supplementary material includes a comparison between the inferred metallicities using the N V/C IV line ratio and the (Si IV+O IV)/C IV line ratio as well as figure sets which show sample fits of selected individual spectra, bolometric luminosity composites, black hole mass composites, and C IV blueshift composites.
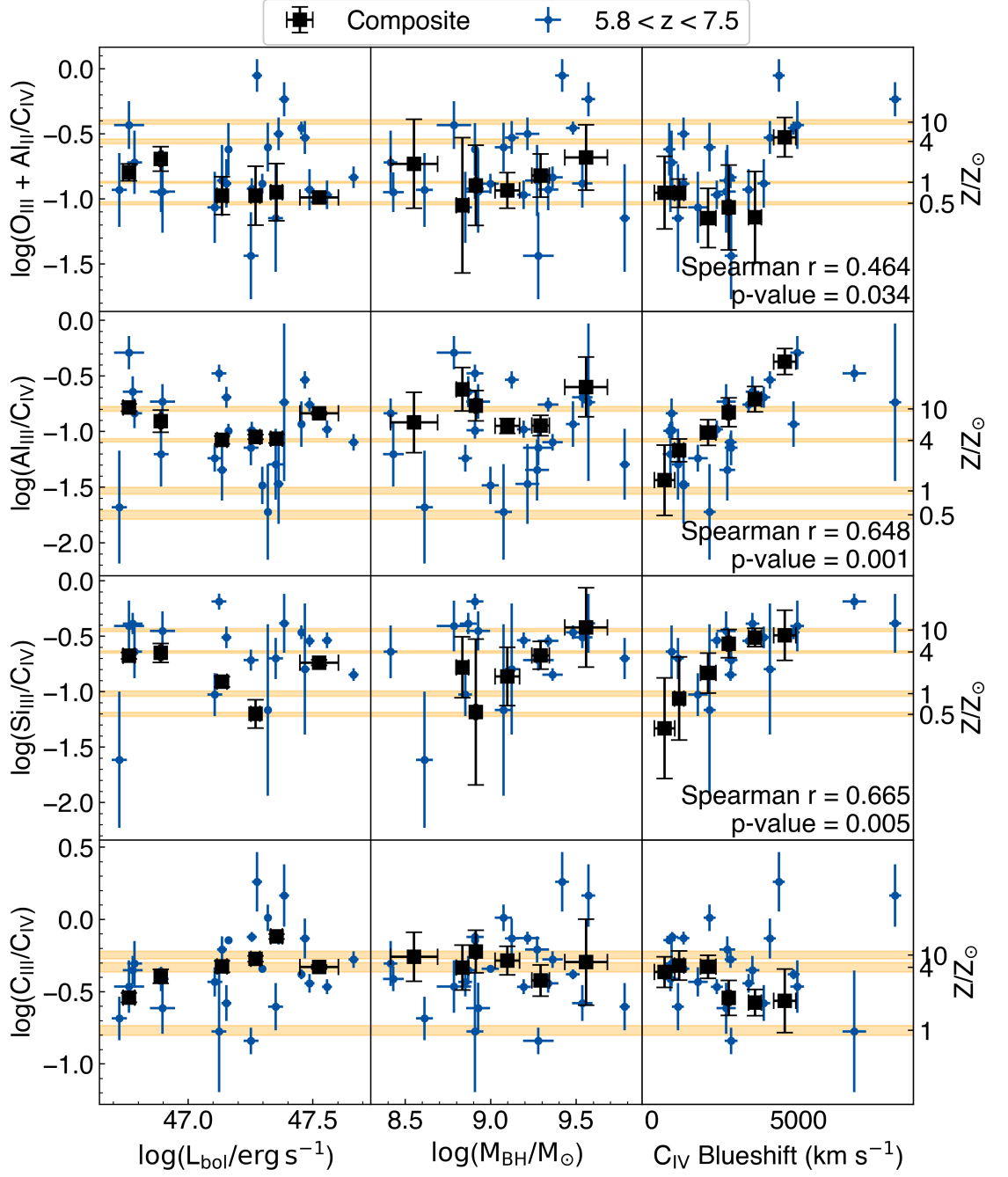
Figure C2: Line flux ratios of (O III]+Al II)/C IV, Al III/C IV, Si III/C IV, and C III]/C IV as functions of the bolometric luminosity, black hole mass, and C IV blueshift of quasars in the sample. Composites are plotted as black squares while individual fits are represented by blue points. The orange shaded space indicates a range of line ratios which are consistent with the metallicity indicated in the secondary axis based solely on varying the assumed ionizing SED in the various photoionisation calculations. We present the Spearman correlation coefficient and p-value for correlations based on fits of individual quasars only if the p-value ≤ 0.1.

Table C.3:   Table of line flux ratios from the C IV blueshift composites normalised to the flux of the C IV emission line. The uncertainty represents the measurement error of the displayed line, independent of the C IV uncertainty.

Line / C IV Blueshift	−200-680 (km s^{-1})	680-1500 (km s^{-1})	1500-2500 (km s^{-1})	2500-3000 (km s^{-1})	3000-4000 (km s^{-1})	4000-5000 (km s^{-1})
Ly α	1.08 ± 0.15	0.80 ± 0.09	0.94 ± 0.12	1.12 ± 0.51	0.49 ± 0.13	—
N v	0.83 ± 0.12	0.84 ± 0.08	0.76 ± 0.08	0.91 ± 0.19	1.39 ± 0.24	—
Si ii	0.22 ± 0.08	0.13 ± 0.02	0.08 ± 0.03	0.18 ± 0.07	0.29 ± 0.08	—
Si iv	0.09 ± 0.09	0.22 ± 0.03	0.21 ± 0.08	0.16 ± 0.16	0.09 ± 0.16	0.35 ± 0.15
O iv	0.22 ± 0.09	—	0.15 ± 0.09	0.32 ± 0.22	0.51 ± 0.25	0.17 ± 0.20
N iv]	0.06 ± 0.05	0.01 ± 0.02	—	—	—	0.15 ± 0.12
C iv	1.00 ± 0.11	1.00 ± 0.06	1.00 ± 0.07	1.00 ± 0.20	1.00 ± 0.13	1.00 ± 0.16
He ii	0.14 ± 0.03	0.19 ± 0.03	0.20 ± 0.03	0.27 ± 0.09	0.23 ± 0.06	0.34 ± 0.09
O iii]	0.11 ± 0.06	0.11 ± 0.03	0.07 ± 0.04	0.02 ± 0.03	0.07 ± 0.05	0.14 ± 0.06
Al ii	—	—	—	0.07 ± 0.05	—	0.16 ± 0.07
Al iii	0.04 ± 0.03	0.07 ± 0.02	0.10 ± 0.03	0.15 ± 0.03	0.20 ± 0.04	0.43 ± 0.09
Si iii	0.05 ± 0.05	0.09 ± 0.07	0.15 ± 0.06	0.27 ± 0.06	0.31 ± 0.04	0.32 ± 0.16
C iii]	0.43 ± 0.09	0.48 ± 0.11	0.47 ± 0.08	0.29 ± 0.06	0.27 ± 0.04	0.27 ± 0.13

Appendix: Accretion Disc Fitting of SMSS J2157–3602

D.1 Bolometric Luminosity

Several bolometric corrections have been proposed to transform monochromatic luminosities into QSO bolometric luminosities. At times, a fixed correction is used, $L_{\text{bol}} = k_\lambda L(\lambda)$, where k_λ is the bolometric correction factor and $L(\lambda)$ represents the monochromatic luminosity, λL_λ at rest wavelength λ. From the power-law continuum model of J2157–3602, we measured $\log{(L(3000\text{Å})/\text{erg s}^{-1})} = 47.66 \pm 0.01$.

D.1.1 Bolometric corrections

Using composite SEDs from 259 SDSS QSOs, Richards et al. (2006) calculated an average bolometric correction factor of $k_{3000\text{Å}} = 5.62 \pm 1.14$, although a fixed median value of $k_{3000\text{Å}} = 5.15$ is more commonly used in practice (e.g. Shen et al. 2011). However, this value likely overestimates the bolometric luminosity for luminous QSOs, motivating a luminosity-dependent correction which flattens to $k_{3000\text{Å}} \sim 3.2$ for $L(3000\text{Å}) > 10^{46}$ erg s^{-1} (Marconi et al. 2004; Trakhtenbrot & Netzer 2012), which is derived from QSO spectral templates.

Another bolometric correction from Runnoe et al. (2012) is derived from the NIR−Xray SED atlas of 63 QSOs (Shang et al. 2011). Using the best-fitting linear correction with non-zero intercepts and the recommended 25% luminosity suppression based on the sample's orientation bias (Nemmen & Brotherton 2010, hereafter N10), the luminosity-dependent bolometric correction for J2157–3602 is then $k_{3000\text{Å}} \sim 3.33$.

A more recent study based on theoretical calculations of optically thick and geometrically thin accretion discs (Netzer 2019) estimated $k_{3000\text{Å}} = 25(L(3000\text{Å})/10^{42}\text{erg s}^{-1})^{-0.2}$, which is approximately $k_{3000\text{Å}} \sim 1.84$ for J2157–3602. This study assumed that accretion through the disc is the only energy production

mechanism and that the accretion rate is sufficiently sub-Eddington for the disc to remain geometrically thin. Furthermore, the X-ray luminosity from a corona heated to temperatures above that of the AD is assumed to be drawn from the same gravitational energy source and does not affect L_{bol}.

The collection of estimated bolometric luminosities with correction factors of (1.84, 3.2, 3.33, 5.15) are $\log\left(L_{\mathrm{bol}}/\mathrm{erg\,s^{-1}}\right) = $ (47.93, 48.17, 48.19, 48.38). The mean bolometric luminosity and the standard deviation is then $\log\left(L_{\mathrm{bol}}/\mathrm{erg\,s^{-1}}\right) = 48.17 \pm 0.16$. This measurement is well-matched to the previous estimate of $\log\left(L_{\mathrm{bol}}/\mathrm{erg\,s^{-1}}\right) \approx 48.2$ (Onken et al. 2020), which was derived with the Runnoe et al. (2012) correction. However, the result from independent bolometric corrections spans 0.45 dex and the individual studies assume a mean SED or that a straightforward luminosity dependence is sufficient to extrapolate the full SED shape for every QSO. We adopt an approach in the following section that is independent of the assumed mean SED shape and sample properties used to calibrate the bolometric corrections.

D.1.2   Integrated SED

The `kerrbb` thin disc and `slimbh` slim disc parameterise disc luminosity in terms of the mass accretion rate and Eddington ratio, respectively. However, while the model parameters describe intrinsic properties of the black hole and its accretion disc, the transformation from the model parameterisation to the observed luminosity is not trivial, due to additional effects considered by general relativistic ray-tracing. The mass accretion rate parameter from `kerrbb` can be converted to luminosity, but the radiative efficiency of the thin disc does not correspond to a standard Keplerian disc (Li et al. 2005), especially if the torque at the inner boundary is non-zero or limb darkening effects are included. For the slim disc, the Eddington luminosity parameterised in the model does not consider general relativistic effects, and thus only roughly corresponds to the total output disc luminosity (Sadowski 2011). Therefore, we circumnavigate these potential issues by integrating the model SED to derive the bolometric luminosity.

Here, we estimate the bolometric luminosity by drawing 1000 random models out of the MCMC posterior distribution from the `kerrbb` thin disc model fits to synthetic photometry and integrating the SED. We use the thin disc model because the mass accretion rate is a fitted parameter, allowing us to constrain the radiative efficiency and correct for anisotropy. The integrated luminosity, defined by

$$L_{\mathrm{iso}} = \int_0^\infty L_\nu d\nu = \int_{-\infty}^\infty \ln(10)\nu L_\nu d\log(\nu)\,, \tag{D.1}$$

is measured to be $\log\left(L_{\mathrm{iso}}/\mathrm{erg\,s}^{-1}\right) = 47.99 \pm 0.01$, where L_{iso} is the luminosity evaluated under the assumption of isotropy. Although a slim disc is arguably a better model of the accretion disc structure, the difference in the integrated luminosity is only $\log\left(L_{\mathrm{thin}}/L_{\mathrm{slim}}\right) = 0.02$. In general, the isotropic-equivalent luminosity, L_{iso}, is evaluated by

$$L_{\mathrm{iso}} = \int_0^{2\pi} \int_0^{\pi} F_{\mathrm{obs}} d_L^2 \sin\theta d\theta d\phi \,,$$
$$= 4\pi d_L^2 F_{\mathrm{obs}} \,, \tag{D.2}$$

where d_L^2 is the luminosity distance and F_{obs} is the observed flux density. The isotropic-equivalent luminosity would only be equivalent to the total bolometric luminosity, integrated over all solid angles, if the emission is isotropic or viewed at an intermediate angle where the isotropy assumption is reasonable. If F_{obs} is a function of the inclination angle, then we would need to determine a correction for the anisotropy. As the spin and orientation of each thin disc model are known, we can calculate an anisotropy correction to the isotropic luminosity, defined as a ratio of the total bolometric radiative efficiency, η_{bol}, to the isotropic-equivalent radiative efficiency, η_{iso}, such that the total bolometric luminosity, L_{bol}, is measured by

$$L_{\mathrm{bol}} = \frac{\eta_{\mathrm{bol}}}{\eta_{\mathrm{iso}}} L_{\mathrm{iso}} = \dot{M}c^2 \int_0^1 \eta(\theta, a) d(\cos\theta) \,, \tag{D.3}$$

where we construct analytical approximations to estimate $\eta(\theta, a)$ defining,

$$\eta(\theta, a) = \sum_{i=0}^{\mathcal{N}_1} \mathcal{F}_i \cos(\theta)^i \,,$$
$$\mathcal{F}_i(a) = \sum_{j=0}^{\mathcal{N}_2} \zeta_j \log^j(1 - a) \,, \tag{D.4}$$

and the ζ_j coefficients are presented in Table D.1, updating the analytical approximation in C18 to include the effects of limb darkening. We caution that our parameterisation differs from that of C18, but we find this model to produce smoother fits. Coefficients have been provided up to $\mathcal{N}_1 = 5$ and $\mathcal{N}_2 = 6$, which are sufficient to estimate $\eta(\theta, a)$ in Equation D.4 to $\sim 0.1\%$ accuracy.

In Figure D1, we compare the observed radiative efficiency and normalised 3000Å monochromatic luminosities with and without limb darkening using the `kerrbb` thin disc model. With limb darkening, the peak observed luminosity is always at face-on orientations, but without limb darkening, the peak luminosity can be at intermediate viewing angles for close to maximally spinning black holes. Over a large range of viewing angles up to 50–60° depending on spin, the models with limb darkening are

brighter than similar models without limb darkening. The relationship between the observed radiative efficiency and the viewing angle depends sensitively on spin, but the response of the monochromatic luminosity to orientation is similar at 3000Å regardless of black hole spin. However, the shape of this curve can be quite different at shorter wavelengths, especially beyond the peak of the SED.

Having derived analytical approximations of $\eta(a,\theta)$, we then define the anisotropy correction, $f(\theta,a)$ and a fractional error, $\Delta L/L$, in the isotropic luminosity as,

$$
\begin{aligned}
f(\theta,a) &= \frac{\eta_{\rm bol}}{\eta_{\rm iso}} = \frac{1}{\eta_{\rm iso}(\theta,a)} \int_0^1 \eta(\theta',a)d(\cos\theta')\,, \\
\frac{\Delta L}{L} &\equiv \frac{L_{\rm iso} - L_{\rm bol}}{L_{\rm bol}} = \frac{1 - f(\theta,a)}{f(\theta,a)}\,,
\end{aligned}
\tag{D.5}
$$

where $\Delta L/L$ estimates the error incurred between the observed and total bolometric luminosity of a QSO if the observed emission is assumed to be isotropic. A fractional error of 0 implies no correction and occurs at intermediate viewing angles, such as $60°$ in the Newtonian case or in specific general relativistic scenarios, $56°$ (Netzer 2019) or $66°$ (N10) depending on the spin of the system.

In Figure D2, we show the fractional error derived from the `kerrbb` thin disc model across inclination angles for the full range of spins from $a = -1$ to $a = 0.998$. We contrast our model with the Newtonian case and the average fractional error from N10. Much of the parameter space is covered by the highest 10% of spins. If all spins are uniformly probable, then the $a = 0.4$ line best represents the average fractional error. It is also well-approximated by a Newtonian model, except for near face-on and edge-on orientation. If only positive spins are considered, then the $a = 0.65$ curve best represents the mean fractional error. These single-spin curves can reproduce the values of their respective mean curves to better than 1% precision. In Appendix D.1.3, we continue the discussion on the anisotropy correction and derive an average correction for QSO samples with any maximum orientation angle, $\theta_{\rm max}$. We create analytical approximations for the correction, $f(\theta_{\rm max},a)$, so that they can be derived for any combination of parameters without evaluating and integrating thin disc model spectra.

For each of the 1000 models drawn from the MCMC posterior, we generate a unique curve from its black hole spin and evaluate its anisotropy correction for its inclination as in Figure D2. After applying each individual correction, we find $\log(L_{\rm bol}/{\rm erg\,s^{-1}}) = 47.87 \pm 0.10$, which implies a bolometric correction factor of $k_{3000\text{Å}} \sim 1.62$. Methodologically, this procedure is similar to Netzer (2019), albeit with the orientation and spin-dependent anisotropy correction instead of a fixed
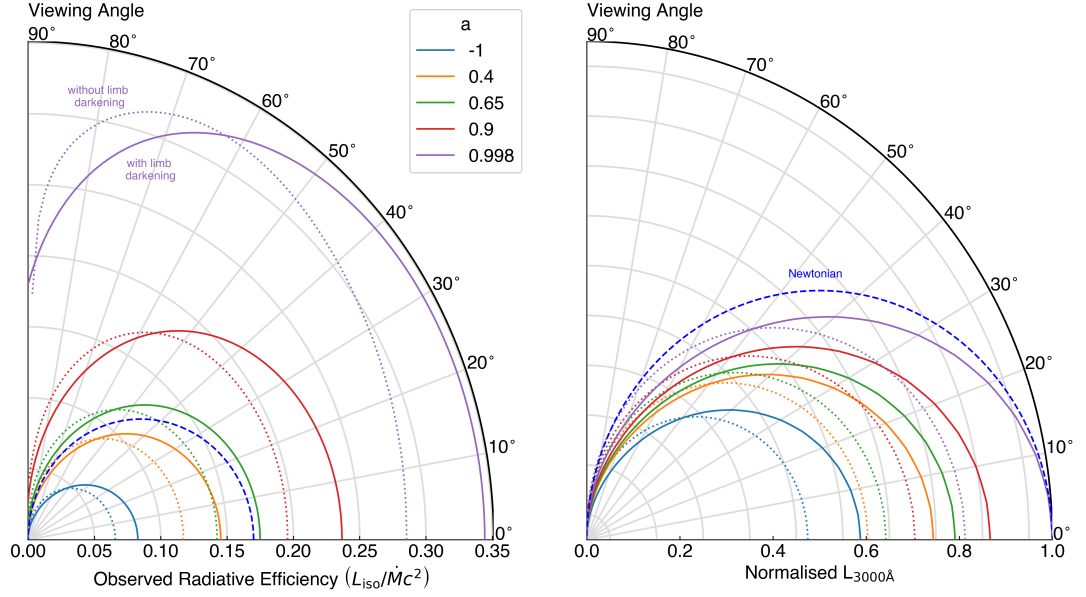
Figure D1: Comparison of the observed radiative efficiency (left) and normalised 3000Å monochromatic luminosities (right) at various viewing angles with and without limb darkening, for selected black hole spins from $a = -1$ to $a = 1$. The solid (dotted) lines show the result with (without) limb darkening and the Newtonian model, which represents $L \propto \cos\theta$, is shown with the blue dashed lines. On the right panel, the monochromatic luminosities are normalised to the brightest model. With the 3000Å monochromatic luminosity, the shape of the curves remains consistent for the full range of black hole spins.

viewing angle assumption of $\sim 56°$, and the estimated luminosity is slightly lower as expected due to the shallower mean viewing angle of $\sim 45°$.

Compared to the empirically derived bolometric corrections from Section D.1.1, the integrated AD SED includes only thermal emission from the accretion disc. Only a small fraction of the total radiative output of QSOs is emitted in the X-rays and this fraction also decreases with the UV luminosity of the AGN (the α_{OX} correlation; e.g. Elvis et al. 1994; Steffen et al. 2006; Vasudevan & Fabian 2007, 2009; Liu et al. 2021). Naturally, we also make the assumption that the thin disc spectra adequately model the observed optical-UV continuum of QSOs. By integrating the locally-blackbody emission, we avoid double-counting reprocessed emission in the infrared or hard X-ray regime. Additionally, we do not depend upon congruence between properties of our target and the mean properties of the samples used to calibrate the bolometric corrections, which can create an order of magnitude difference in the measurement.

Figure D2: Fractional error incurred between the isotropic luminosity and the total bolometric luminosity of a QSO if the observed emission is assumed to be isotropic. The secondary axis (right) shows the isotropic-equivalent luminosity as a fraction of the bolometric luminosity. Our estimates are derived from the `kerrbb` thin disc model and contrasted against N10 and the Newtonian case. The mean fractional error is similar to $a = 0.4$ if all spins are uniformly probable and to $a = 0.65$ if only positive spins are considered.

D.1.3 Anisotropy Correction

In the previous section, we defined an anisotropy correction, $f(\theta, a)$, and its fractional error for any combination of dimensionless black hole spin, a, and inclination, θ_{inc}. The fractional error estimates th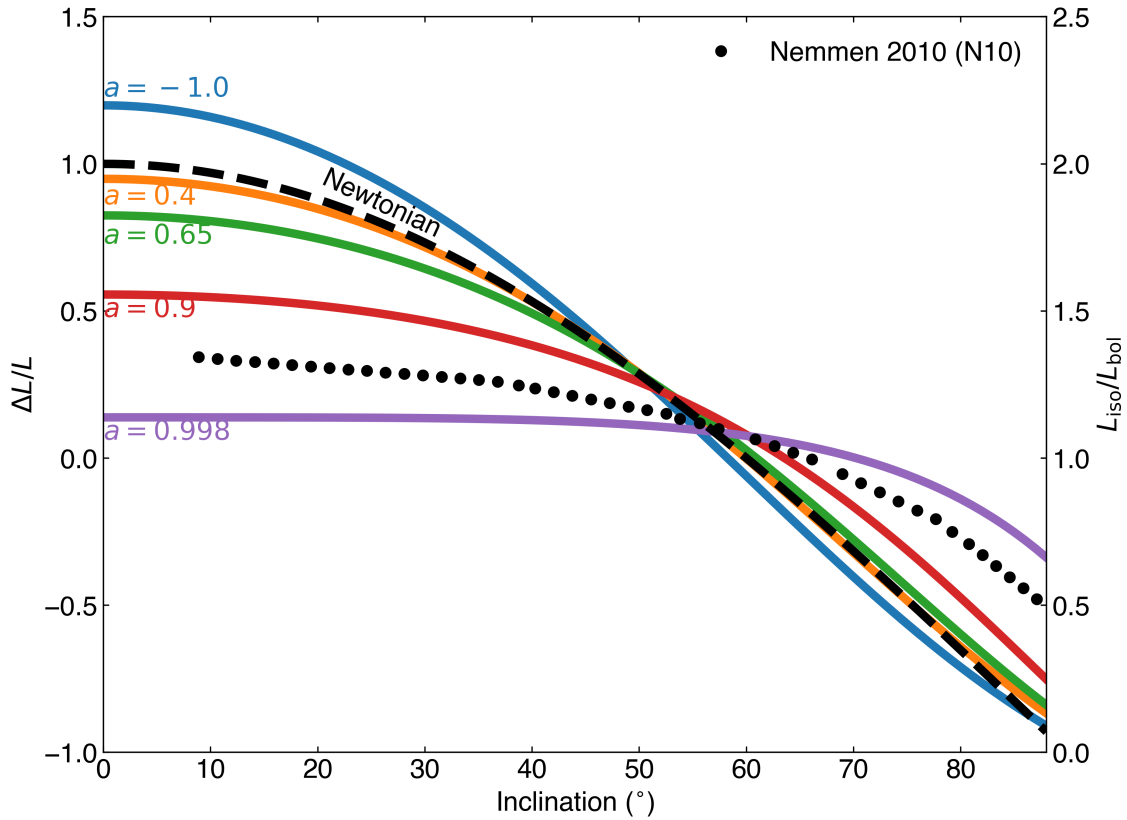e error incurred between the isotropic luminosity and the total bolometric luminosity if the observed emission is assumed to be radiated isotropically. We used the anisotropy correction to estimate the total bolometric luminosity from posterior model SEDs of one QSO with particular spins and observed inclination angles. In this section, we derive the mean anisotropy correction for a sample of QSOs. We first consider the general case of an anisotropy correction that is a function of spin (allowing application to arbitrary spin distributions, e.g., from simulations), then corrections for particular mean spin values.

Under the orientation classification model for Seyfert galaxies and QSOs (Antonucci 1993), there's an assumed opening angle of the obscuring torus, where shallower viewing angles enable the observation of the BLR, rendering it a Type 1. Large samples of Type 1 QSOs, where all orientations shallower than the opening angle, θ_{max}, are equally likely, will need to consider an average anisotropy correction to transform the observed luminosities into the total bolometric luminosities of the AGN sample. We define this correction, $f(\theta_{\mathrm{max}}, a)$, as

$$f(\theta_{\mathrm{max}}, a) = \frac{\int_0^1 \eta(\theta, a) d(\cos\theta)}{1 - \cos(\theta_{\mathrm{max}})} \int_{\cos\theta_{\mathrm{max}}}^1 \eta(\theta, a)^{-1} d(\cos\theta) \, , \tag{D.6}$$

which is a mean anisotropy correction for a particular black hole spin, a, weighted by its probability of being observed at all orientations with $\theta \leq \theta_{\mathrm{max}}$. As before, the radiative efficiency, $\eta(\theta, a)$, is estimated using Equation D.4.

We again derive an analytic expression with the following form to estimate the anisotropy correction without evaluating and integrating thin disc model SEDs,

$$f(\theta_{\mathrm{max}}, a) = C_0(\theta_{\mathrm{max}}) + \sum_{i=1}^{N_1} C_i(\theta_{\mathrm{max}}) \log\left(i - a\right) \, ,$$

$$C_i(\theta_{\mathrm{max}}) = \sum_{j=0}^{N_2} D_j \cos(\theta_{\mathrm{max}})^j \, , \tag{D.7}$$

where we have provided coefficients, C_i and D_j, up to $N_1 = 6$ and $N_2 = 8$ in Table D.2. The provided coefficients are sufficient to estimate $f(\theta_{\mathrm{max}}, a)$ to within 1% error for most combinations of dimensionless spin, a, and maximum inclination, θ_{max}, except for near maximal spin, where the error can be up to 3%.

In Figure D3, we show the mean anisotropy correction for various black hole spins

Table D.1: Coefficients of ζ_j used to solve for $\mathcal{F}_i(a)$ and applied to Equation D.4 to estimate the observed radiative efficiency $\eta(\theta, a)$ for any combination of observed inclination, θ, and black hole spin, a.

	ζ_0	ζ_1	ζ_2	ζ_3	ζ_4	ζ_5	ζ_6
$\mathcal{F}_0$	0.0034	-0.0102	0.0121	0.0091	0.0156	0.0057	0.0006
$\mathcal{F}_1$	0.0760	-0.1092	0.0445	-0.1146	-0.0167	0.0307	0.0076
$\mathcal{F}_2$	0.0698	-0.0942	0.1499	-0.0735	-0.6514	-0.3703	-0.0578
$\mathcal{F}_3$	-0.0192	0.0691	-0.3491	0.9902	1.7997	0.8101	0.1131
$\mathcal{F}_4$	-0.0235	0.0603	0.1863	-1.2190	-1.6659	-0.6792	-0.0894
$\mathcal{F}_5$	0.0106	-0.0397	-0.0237	0.4420	0.5295	0.2039	0.0258

Table D.2: Coefficients of D_j used to solve for $C_i(\theta_{\max})$ and applied to Equation D.7 to estimate the anisotropic correction, $f(\theta_{\max}, a)$, for any sample with black hole spin, a, and maximum inclination angle, $\theta_{\max}$.

	D_0	D_1	D_2	D_3	D_4	D_5	D_6	D_7	D_8
C_0	825839.11	-825654.54	-12727.77	133489.26	-618406.28	1542748.35	-2134722.89	1540498.01	-452008.97
C_1	-145.85	145.92	-0.92	3.70	-11.32	22.76	-27.71	18.39	-5.09
C_2	19815.54	-19601.21	-942.79	-2700.28	27793.58	-86347.80	132556.84	-101623.32	31026.11
C_3	852776.56	-855518.06	-15310.58	350278.39	-1856395.08	4895185.38	-6978921.44	5130863.11	-1524798.56
C_4	19495660.09	-19487281.21	176344.12	-2554055.17	12705285.15	-32688850.21	46008156.13	-33560153.75	9920635.72
C_5	6247439.48	-6256063.92	-400372.22	5131351.82	-24930987.93	63518064.50	-88927307.96	64653620.82	-19069014.39
C_6	8396532.21	-8393904.69	249288.84	-3018336.82	14486023.68	-36713644.08	51252728.94	-37195437.91	10956809.26

on the left panel and for various maximum inclination angles on the right panel. In the left panel, each of the curves represent a different value of $\theta_{\max}$. The range of correction factors increases dramatically as $\theta_{\max}$ approaches edge-on. However, all mean correction factors converge to near $f(\theta_{\max}, a) \sim 1.0$ for the highest spins. At $60° \leq \theta_{\max} \leq 80°$, the mean correction factor is fairly flat with relatively little deviation across all spins, except for near-maximal spin. On the right panel, the mean anisotropy correction is shown for the range of maximum inclination angles. As with Figure D2, most of the parameter space is covered by the highest 10% of spins.

If all black hole spins in a sample of QSOs are assumed to be uniformly probable, the mean curve is best represented by the $a = 0.4$ spin case, and the $a = 0.65$ curve best reflects the mean curve for all positive spins. These single-spin curves can reproduce the values of their respective mean curves to better than 1% precision. For instance, if a sample of QSOs was observed with unknown spins and orientations, but an opening angle of $\theta_{\max} = 65°$ is assumed as in this study, then the right panel of Figure D3 can be used to evaluate a mean anisotropy correction factor for this sample of $\langle f(65°, a) \rangle_a = 0.75$, which should then be applied to the isotropic luminosity of QSOs in this sample following Equation D.3. This correction factor is similar to the 25% bolometric luminosity suppression adopted by Runnoe et al. (2012) to correct for their orientation bias.
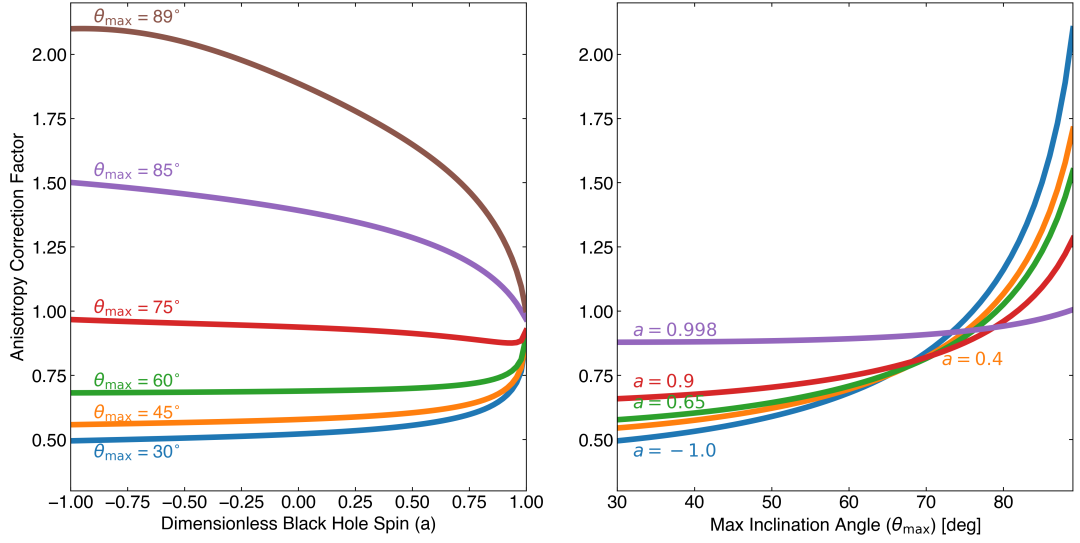
Figure D3: Mean anisotropy correction factor for different spins and uniform inclination up to θ_{max} (left) and for maximum inclination angle with uniform spin distribution (right). On the right panel, the $a = 0.4$ (or $a = 0.65$) spin case best represents the mean curve if all spins (all positive spins) are uniformly probable. For any QSO sample with randomly distributed spins and an estimated opening angle of the obscuring torus, the right panel can be referenced to estimate a mean anisotropy correction.

D.2 QSO J102325.31+514251.0

The QSO J102325.31+514251.0, $z = 3.477$, was measured to host a black hole of mass $\log(M_{SE}/M_\odot)_{Mg\,II} = 10.52 \pm 0.08$ using the SE virial mass estimate with the Mg II line (Zuo et al. 2015), which would make it one of the most massive black holes ever measured. However, that estimate is in contention with the Hβ-based virial mass estimate in the same study which suggested a black hole mass of $\log(M_{SE}/M_\odot)_{H\beta} = 9.58 \pm 0.14$ (Zuo et al. 2015). These cases where the virial mass estimates from different emission lines differ by more than 0.5 dex are rare, constituting about 3% of QSOs in the Shen et al. (2011) QSO catalogue and about 1% in the Rakshit et al. (2020) catalogue.

As an independent method of estimating black hole masses, AD fitting is useful for disentangling these ambiguous cases. Even if only limited to cases for which $\log(M_{SE}/M_\odot) > 8$, where the $f_{col} = 1$ assumption is reasonable (see Section 6.3.2), we find > 1000 QSOs in each of the Shen et al. (2011) and Rakshit et al. (2020) QSO catalogues. Here, we show how AD fitting can be used to measure the black hole mass of J1023+5142, using only publicly available photometric data.

We crossmatch J1023+5142 with AllWISE, 2MASS, and PanSTARRS DR1, obtaining data from the optical to infrared. Following the procedure from Section

6.3.2, we fit data between rest-frame 1 μm to 1600Å. Like J2157–3602, we determine the Galactic extinction based on the rescaled SFD extinction map to be $E(B - V) = 0.013$ and we assume no host galaxy extinction. We adopt the `slimbh` slim accretion disc models and flat uninformative prior probability distributions for all free parameters: black hole mass M_{BH}, disc luminosity L_{disc}, spin a, and inclination θ_{inc}. Figure D4 presents the corner plot of the MCMC posterior distributions. Although neither spin nor inclination are constrained by the data, the black hole mass estimate is $\log(M_{\mathrm{AD}}/M_\odot) = 9.55^{+0.20}_{-0.17}$, using the maximum likelihood and uncertainties determined by the 68% iso-likelihood line. This result strongly disfavors the Mg II-based virial mass estimate, suggesting nearly 1 dex lower mass. If the Hβ mass estimate is unavailable and the Mg II SE mass estimate is used as the mass prior, the AD fitting mass estimate is $\log(M_{\mathrm{AD}}/M_\odot) = 9.71^{+0.19}_{-0.20}$, which is sufficient to exclude the Mg II result at $> 4\sigma$ even if there is no alternative SE M_{BH} estimate.

We calculate the bolometric luminosity of J1023+5142 following the methods outlined in Appendix D.1, finding $\log(L_{\mathrm{bol}}/\mathrm{erg\,s^{-1}}) = 47.47 \pm 0.17$, 0.3 dex lower than in Zuo et al. (2015), which used a fixed correction of $k_{5100\text{Å}} = 9.26$ (Richards et al. 2006). Instead, we find our bolometric luminosity to be consistent with $k_{5100\text{Å}} = 4.68$ and $k_{3000\text{Å}} = 4.27$. Higher mass BHs such as J1023+5142 are more likely to have lower bolometric correction factors (e.g. Trakhtenbrot & Netzer 2012) than those derived from mean SEDs of lower-mass black holes. With the newly measured black hole mass bolometric luminosity using AD fitting, we find an Eddington ratio of $\epsilon = 0.7^{+0.4}_{-0.4}$. We also estimate the mass accretion rate from the `kerrbb` thin disc model following Section 6.4.4, finding $\dot{M} = 52^{+42}_{-23}\,M_\odot\,\mathrm{yr^{-1}}$, which implies a radiative efficiency of $\eta = 0.10^{+0.08}_{-0.05}$, consistent with the Sołtan argument (e.g Yu & Tremaine 2002).

Similar to J2157–3602, the SDSS spectra of J1023+5142 shows characteristics of a HiBAL QSO, which are, on average, found to be only slightly reddened by host galaxy dust compared to a non-BAL sample (e.g. Brotherton et al. 2001; Reichard et al. 2003). We find that, even with photometry alone, increasing the assumed host galaxy extinction decreases the estimated black hole mass from the AD fitting method, so M_{AD} could not be boosted to the $\log(M_{\mathrm{SE}}/M_\odot)_{\mathrm{Mg\,II}}$ mass through an intrinsic reddening correction. Because our M_{AD} estimate is not overestimated compared to the Hβ SE virial mass, we find that our assumption of no internal reddening for luminous QSOs is not contradicted.

This result motivates a future study to investigate cases for which the virial mass estimates are discrepant in additional detail using AD fitting. It also demonstrates

that AD fitting can be used to discover cases for which the SE virial mass estimate may have resulted in erroneous measurements.
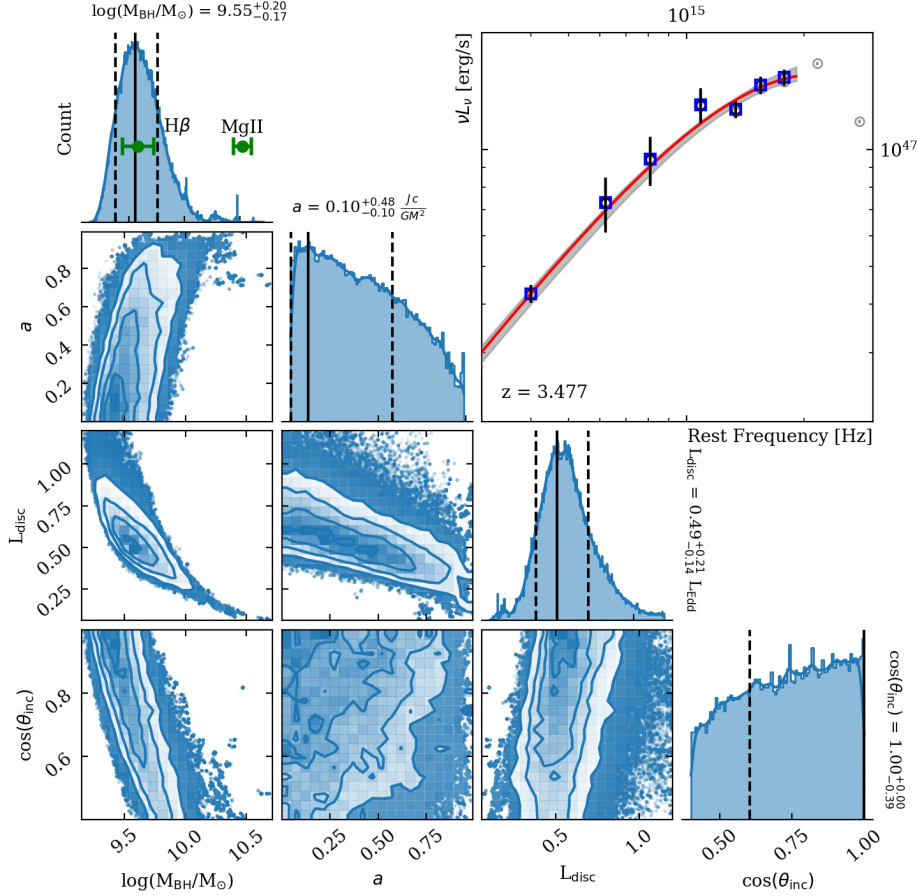
Figure D4: Corner plot for the accretion disc fit to QSO J102325.31+514251.0 photometry using the `kerrbb` model. The frequency is presented in the rest-frame. The final estimate of each parameter is determined by the maximum likelihood of the posterior distribution, with uncertainties determined by the 68% iso-likelihood line. The top-right panel shows the photometry in black, and masked data in light grey. The red model is the highest likelihood model and the one-sigma spread from a random sample of posterior models is similar in width to the red model line. The black hole mass is estimated to be $\log(M_{\mathrm{AD}}/M_\odot) = 9.55^{+0.20}_{-0.17}$ and we show each of the SE virial mass estimates in green.